5-29-2009

Plasma And Cold Sprayed Aluminum Carbon Nanotube Composites: Quantification Of Nanotube Distribution And Multi-Scale Mechanical Properties

Srinivasa R. Bakshi
Florida International University, sbaks003@fiu.edu

FLORIDA INTERNATIONAL UNIVERSITY

Miami, Florida

PLASMA AND COLD SPRAYED ALUMINUM CARBON NANOTUBE COMPOSITES: QUANTIFICATION OF NANOTUBE DISTRIBUTION AND MULTI-SCALE MECHANICAL PROPERTIES

A dissertation submitted in partial fulfillment of the

requirements for the degree of

DOCTOR OF PHILOSOPHY

in

MATERIALS SCIENCE AND ENGINEERING

by

Srinivasa Rao Bakshi

2009

To: Dean Amir Mirmiran
College of Engineering and Computing

This dissertation, written by Srinivasa Rao Bakshi, and entitled Plasma And Cold Sprayed Aluminum Carbon Nanotube Composites: Quantification Of Nanotube Distribution And Multi-Scale Mechanical Properties, having been approved in respect to style and intellectual content, is referred to you for judgment.

We have read this dissertation and recommend that it be approved.

(for Dr. K. Jones)
W. Kinzy Jones

Norman D. H. Munroe

Wenzhi Li

(For Dr. Agarwal)
Arvind Agarwal, Major Professor

Date of Defense: May 29, 2009

The dissertation of Srinivasa Rao Bakshi is approved.

Dean Amir Mirmiran
College of Engineering and Computing

George Walker
Dean George Walker
University Graduate School

Florida International University, 2009

DEDICATION

This dissertation is dedicated to my parents who have supported me through all the stages of my life. Their constant encouragement has provided me the strength to complete this dissertation.

ACKNOWLEDGMENTS

I would like to extend my sincere gratitude to Dr. Arvind Agarwal, my major advisor and chair of my dissertation committee for his support and guidance. This dissertation would not have been possible without his efficient planning, management and supervision. His perseverance and diligence had always been a motivation for working even harder towards achieving higher goals. His advice and innovative thoughts and pace of working have been very inspiring. I have learned a lot about leadership and management from him. I am also thankful to him for involving me in different projects simultaneously, which has widened my knowledge and scope of research work. I am thankful for the effort and time he has dedicated towards the completion of this thesis as well as development of my career. I thank him for giving me the opportunity to conduct research at the University of Nottingham by means of the NSF IREE grant; it is one of the memorable times of my life.

I would like to thank my committee members Dr. W. Kinzy Jones, Dr. Norman D. H. Munroe and Dr. Wenzhi Li for serving on my dissertation committee. Their advice and suggestions on the various aspects of my dissertation and the possible areas to look into have been very helpful. I received several ideas and encouragement from them which has helped in shaping my research plan. They have been a source of inspiration by acting as role models.

I would like to thank Dr. Graham McCartney of University of Nottingham for his extreme support and guidance. He has been very helpful during my stay in Nottingham during summer of 2007 during which the cold spray experiments in this research were carried out. I would like thank him for valuable suggestions and support. The congenial

and learning environment made the time spent in Nottingham memorable. I would also like to extend my gratitude to Dr. Sudipta Seal for his support and suggestions with various experiments notably HRTEM.

I would like to acknowledge Advanced Materials Engineering Research Institute (AMERI) for providing the various facilities used in this research work. I would like to thank Center for Study of Matter at Extreme Conditions (CeSMEC) for Raman spectroscopy. I would like to thank Dr. Surendra Saxena and Dr. Yanqing Liu for their support and encouragement with the experiments.

I would like to thank Dr. Kantesh Balani, Dr. Tapas Laha and Dr. Yao Chen for their help and suggestions. Almost all the equipments that I learnt to operate were taught to me by Kantesh. I was amazed how he could have time for everything. I would like to sincerely thank Tapas to have helped me personally and professionally. His dexterity with experiments was amazing and his hard working nature was inspiring. Dr. Yao Chen has been very friendly and the discussions with him on various topics have been enlightening. I extend my gratitude to Dr. Deen Zhang and Dr. Timothy Price of University of Nottingham. They taught me and had been extremely helpful in the cold spray experiments. They were always ready to help. I would like to thank Mr. Anup Kumar Keshri for being there whenever needed. I would like to acknowledge help from Ms. Debrupa Lahiri in preparing the review paper. Her hardwork in putting most of the data together helped a lot. I would like to Mr. Virendra Singh of University of Central Florida for helping with HRTEM imaging. His hard work and skill has brought lot of value to the present work. I would like to thank Mr. Riken Patel and Ms. Tanisha Richard for helping me with schematics. I would like to thank Mr. Riken Patel especially for

helping with SolidWorks™. I would also like to thank Mr. Ruben G. Batista for his help with Matlab programming.

I would like to thank my friends Shiv Narayan Sahu, Bajrang Agarwal, Rohit Khanna, Bibhu Narayan Rath and Manoj Mohapatra for always encouraging me to pursue higher studies and boosting my confidence and morale at various points of my career.

I would like to acknowledge financial support from Florida International University in terms of Presidential Enhanced Assistantship and Dissertation Year Fellowship. I also acknowledge funding from NSF CAREER Award (NSF-DMI-0547178) for funding this research.

I want to extend my thanks to my friends and colleagues Amit Kumar, Jorge Tercero, Venkata Pasumarthi, Sunil Anand Musali, Di Wang, Yamini Parikh, Puneet Gill, Sushma Amruthaluri, Anant Kanaparti, Srinivas Koneti, Uday Bhaskar Reddy, and many more who have always cheered me up during low times. The times spend with them will always we remembered.

Lastly, I would like to thank my family for being so supportive throughout the course of this research work.

ABSTRACT OF THE DISSERTATION

PLASMA AND COLD SPRAYING OF ALUMINUM CARBON NANOTUBE COMPOSITES: QUANTIFICATION OF NANOTUBE DISTRIBUTION AND MULTI-SCALE MECHANICAL PROPERTIES

by

Srinivasa Rao Bakshi

Florida International University, 2009

Miami, Florida

Professor Arvind Agarwal, Major Professor

Carbon nanotubes (CNT) could serve as potential reinforcement for metal matrix composites for improved mechanical properties. However dispersion of carbon nanotubes (CNT) in the matrix has been a longstanding problem, since they tend to form clusters to minimize their surface area. The aim of this study was to use plasma and cold spraying techniques to synthesize CNT reinforced aluminum composite with improved dispersion and to quantify the degree of CNT dispersion as it influences the mechanical properties.

Novel method of spray drying was used to disperse CNTs in Al-12 wt.% Si pre-alloyed powder, which was used as feedstock for plasma and cold spraying. A new method for quantification of CNT distribution was developed. Two parameters for CNT dispersion quantification, namely Dispersion parameter (DP) and Clustering Parameter (CP) have been proposed based on the image analysis and distance between the centers of CNTs. Nanomechanical properties were correlated with the dispersion of CNTs in the

microstructure. Coating microstructure evolution has been discussed in terms of splat formation, deformation and damage of CNTs and CNT/matrix interface. Effect of Si and CNT content on the reaction at CNT/matrix interface was thermodynamically and kinetically studied. A pseudo phase diagram was computed which predicts the interfacial carbide for reaction between CNT and Al-Si alloy at processing temperature. Kinetic aspects showed that Al_4C_3 forms with Al-12 wt.% Si alloy while SiC forms with Al-23wt.% Si alloy. Mechanical properties at nano, micro and macro-scale were evaluated using nanoindentation and nanoscratch, microindentation and bulk tensile testing respectively.

Nano and micro-scale mechanical properties (elastic modulus, hardness and yield strength) displayed improvement whereas macro-scale mechanical properties were poor. The inversion of the mechanical properties at different scale length was attributed to the porosity, CNT clustering, CNT-splat adhesion and Al_4C_3 formation at the CNT/matrix interface. The Dispersion parameter (DP) was more sensitive than Clustering parameter (CP) in measuring degree of CNT distribution in the matrix.

TABLE OF CONTENTS

LIST OF TABLES

LIST OF FIGURES

LIST OF SYMBOLS

SYMBOL	: QUANTITY
E	: Elastic Modulus
θ	: Contact angle
θ	: Total included angle of scratch cross section
θ	: Orientation angle of elongated CNT cluster
γ_{SV}	: Solid vapor interfacial energy
γ_{LV}	: Liquid vapor interfacial energy
W_A	: Work of adhesion
t_{Crit}	: Critical thickness of carbide nuclei
V_M	: Molar volume of carbide
$\Delta\gamma$	: Change in interfacial energy
$\gamma_{MC/CNT}$	: Carbide-CNT interfacial energy
$\gamma_{MC/Alloy}$	: Carbide-Alloy interfacial energy
$\gamma_{Alloy/CNT}$	: Alloy-CNT interfacial energy
ΔG_f	: Free energy change of carbide formation
l_f	: Length of fiber
D_f	: Diameter of fiber
σ_f	: Fracture strength of fiber
τ_{mf}	: matrix-fiber interfacial shear stress
l_c	: Critical length of fiber
σ_c	: Strength of composite
σ_m	: Strength of matrix
σ_{Shear}	: Shear strength of interfacial product
b	: Width of interfacial product
D	: Diameter of fiber
σ_c^{Frac}	: Fracture strength of composite
σ_m^{Frac}	**:** Fracture strength of matrix
S	: Aspect Ratio

S_{eff} : Effective aspect ratio

S_{eff}^{Av} : Average value of S_{eff}

$\sigma_{y,1}$: First yield strength of composite

$\sigma_{y,2}$: Second yield strength of composite

$E_{\parallel}$: Elastic modulus of composite parallel to fiber direction

$E_{\perp}$: Elastic modulus of composite perpendicular to fiber direction

E_f : Elastic modulus of fiber

E_m : Elastic modulus of matrix

ε_{11}^{m} : Longitudinal elastic modulus of matrix

ε_{11}^{CNT} **:** Longitudinal elastic modulus of CNT

E_{11} : Longitudinal elastic modulus of Composite

k_{dsc} : Bulk modulus of composite with dilute suspension of CNT clusters

$k_{Cluster}$: Bulk modulus of CNT cluster

k_m : Bulk modulus of the matrix

μ_{dsc} : Shear modulus of composite with dilute suspension of CNT clusters

$\mu_{Cluster}$: Shear modulus of CNT cluster

μ_m : Shear modulus of the matrix

ν_m : Poisson's ratio of matrix

c_f : CNT volume fraction in a cluster

c_c : Volume fraction of CNT clusters

h_c : Contact depth during nanoindentation

h_{max} : Maximum depth during nanoindentation

h_s : Surface displacement at maximum depth in nanoindentation

P_{max} : Maximum load applied in nanoindentation

S : Contact stiffness of material

ε : Geometric constant

H : Hardness

E_r : Reduced elastic modulus

A : Projected area of indent

μ_e : Effective kinematic viscosity CNT- molten alloy mixture

μ : Kinematic viscosity of molten alloy

R_C : Size of CNT cluster

R_P : Size of molten droplet

ϕ : Volume fraction of CNT in droplets

h : Infiltration depth of molten metal

k_p : Intrinsic permeability of the compact

P : Infiltration pressure

P_0 : Threshold pressure for infiltration

V_p : Volume fraction of porosity of compact

D : Pore size in compact

V : Velocity of gas in cold spraying

V_p : Velocity attained by particle in cold spraying

C_D : Drag coefficient

A_p : Cross sectional area of the particle

ρ : Density of the particle

x : Axial position

m : Mass of the particle

ν_p : Velocity of the particle

ρ_p : Density of the particle

H_p : Hardness of particle

DP : Dispersion parameter

CP : Clustering parameter

x : Variable

μ : Arithmetic mean

σ : Standard deviation

ΔG^f : Free energy of formation

ΔG^0 : Standard free energy of formation

a_{Al} : Activity of aluminum

a_{Si} : Activity of silicon

λ : Spacing between the ripples in CNT

r : Radius of CNT

t : CNT wall thickness

t_c : Contact time between colliding elastic spheres

$c_{\|}$: Velocity of longitudinal waves in particle

U(R) : Lennard Jones potential

R : Interlayer distance

W_E : Elastic work of indentation

W_T : Total work of indentation

σ_y : Yield strength

$\sigma_{0.29}$: Stress at a strain of 0.29

h_r : Residual depth of indentation

h_{inst} : Instantaneous depth during nanoscratch test

h_{true} : True depth during nanoscratch test

C : Area factor

ϕ : Included half angle of the scratch groove

α : Orientation angle of the indenter

V_C : Contact volume of scratch

V_T : True volume of the scratch

V : Wear Volume

l : Sliding distance

R_s : Recovery resistance parameter

$\sum A_{asp}$: Total contact area of asperities

F_f : Frictional force

μ : Coefficient of friction

μ_{adh} : Coefficient of friction due to adhesion

μ_{plough} : Coefficient of friction due to ploughing

F_{adh} : Force of Adhesion

$\sigma_{Al\text{-}Si}$: Tensile yield strength of Al-Si

$E_{Al\text{-}Si}$: Tensile modulus of Al-Si

1. INTRODUCTION

The aim of the present work is to investigate *Plasma spraying* and *Cold spraying* techniques in fabricating CNT reinforced aluminum matrix nanocomposites having *improved nanotube dispersion*. Figure 1.1 summarizes the overall research work that has been carried out.

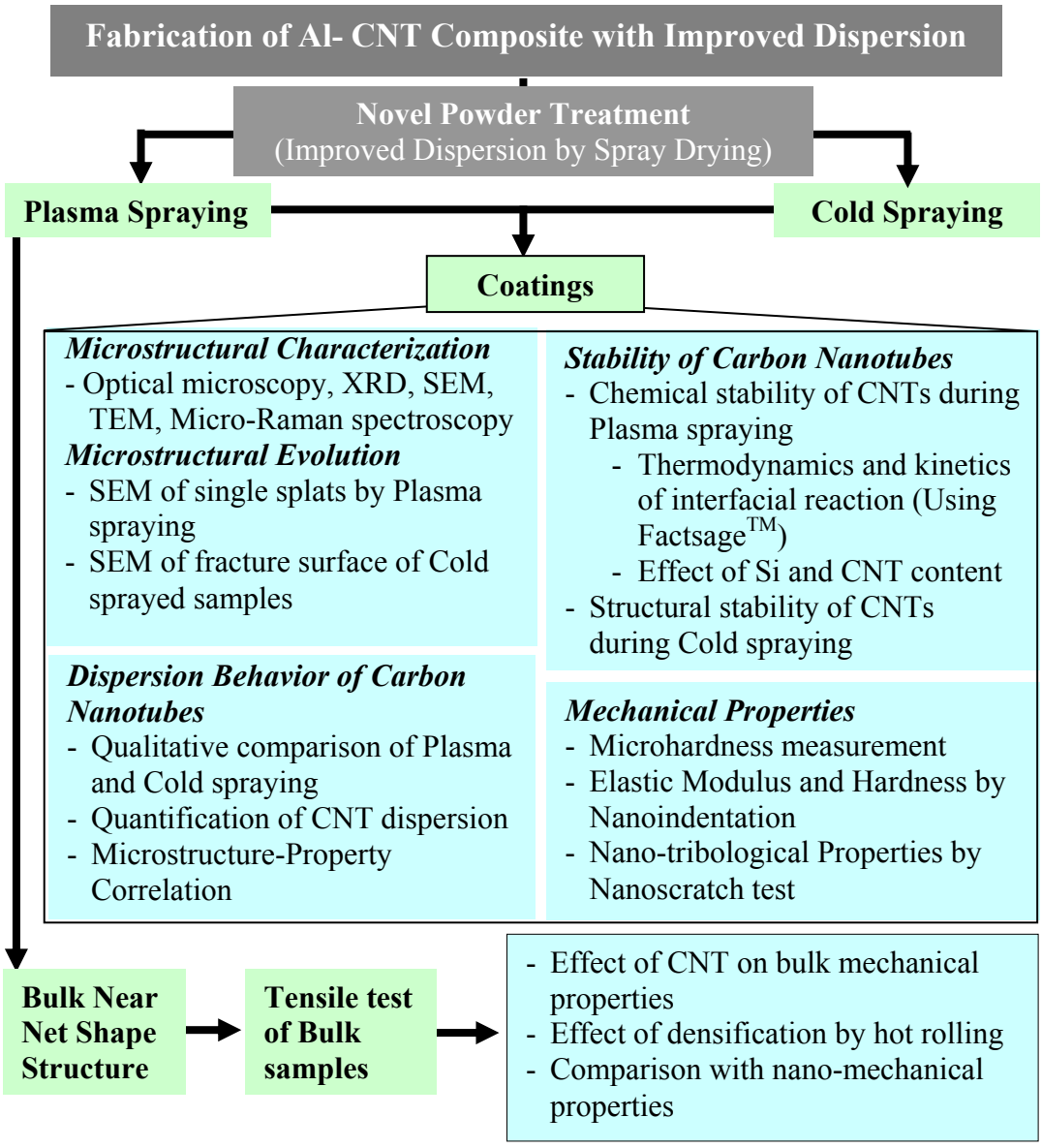

Fig. 1.1: Summary of Research Work

The need for lightweight, high strength materials has been realized since the invention of airplane. As the strength and stiffness of a material increases, the dimensions and consequently the mass of the material required for a certain load bearing application reduces. This leads to several advantages in the case of aircraft and automobiles like increase in payload and improvement of the fuel efficiency. The inadequacy of metals and alloys to provide both strength and stiffness to a structure has led to the development of metal matrix composites (MMC). In a MMC, the strength and ductility is provided by the metal matrix and the strength and/or stiffness is provided by the reinforcement which is either a ceramic or high stiffness metal based particulate or fiber. MMCs can also be designed to possess qualities like low coefficient of thermal expansion and high thermal conductivity which make them suitable for use in electronic packaging applications. Metal matrix composites today are extensively used for automobile and aerospace applications [1-4].

Extensive research has been carried out in the area of carbon fiber reinforced metal matrix composites. Since 1970, carbon fiber reinforced composites have been extensively used in wide array of applications like aircraft brakes, space structures, military and commercial planes, lithium batteries, sporting goods and structural reinforcement in construction. The new Virgin Galactic aircraft WhiteKnightTwo (WK_2) which will ferry the spacecraft SpaceshipTwo boasts to be the largest all carbon composite aircraft with a 140 ft wing made of carbon composite [5]. Research in the field of carbon was revolutionized by the discovery of carbon nanotubes (CNTs) by Iijima in 1991 [6]. Although CNTs might have been synthesized in 1960 by Bacon [7], it took the genius of Iijima to realize that they are tubes made by rolling a graphene sheet onto itself.

A multiwalled carbon nanotube (MWCNT) is made up of many single walled carbon nanotubes (SWCNT) arranged in a concentric manner. Experiments and simulations showed that CNTs have extraordinary mechanical properties over carbon fibers, e.g. stiffness up to 1000 GPa, strength of the order of 100 GPa [8-12] and thermal conductivity of up to 6000 $W.m^{-1}K^{-1}$ [13, 14]. These investigations showed that CNTs were the strongest fibers known to mankind. The use of CNTs could lead to tremendous improvement in the mechanical properties over the carbon fiber reinforced metal matrix composites. However, there are certain critical issues in this area and challenges to be overcome.

1.1. Challenges in Fabrication of CNT Reinforced MMCs

1.1.1. Dispersion of CNTs in Metal Matrix

This is by far the most important as well as difficult challenge in the fabrication of CNT composites. CNTs have large specific surface area up to 200 $m^2.g^{-1}$ and hence they tend to agglomerate and form clusters due to van der Waals forces. Good dispersion of the reinforcement is a necessity for efficient use of the properties as well as for obtaining homogeneous properties. CNT clusters have lower strength, higher porosity and serve a as discontinuities. Thus they increase the porosity of the composite. Several researchers have shown decrease in mechanical, electrical or thermal properties of the composite due to clustering phenomena [15-18]. Several methods have been suggested to improve the dispersion of CNTs which have their own advantages and limitations [19-22]. Improvement in mechanical properties has been reported due to improvement in

dispersion. Still a lot of work is needed to be done to improve dispersion during bulk composite fabrication.

1.1.2. Stability of CNTs

The next issue that is of concern is the stability of CNTs during the fabrication of the composite. Various processing routes like casting [23-25], hot pressing [26-28], extrusion [29-31] and thermal spraying [32-35] employ high temperatures which may cause damage to the CNT structure. Successful retention of CNTs during high temperature processes like plasma spraying and high velocity oxy-fuel spraying has been reported by our group in several previous works [32, 35]. Contact with the molten matrix could lead to interfacial reactions which may or may not be beneficial in transferring stresses to the CNT and in pinning CNTs to the matrix [31]. A good and strong interface makes a good composite. On the other hand, it could also lead to total conversion of the CNTs and deterioration of mechanical properties of the CNT [36, 37]. Several other processes like mechanical milling [22, 28], HVOF [32, 38] and equal channel angular pressing [39-41] could result in mechanical damage of the CNT structure. So it is necessary to assess processes based on the damage/changes they introduce in the CNTs.

1.2. Focus of the Present Research Work

The overall aim of the present research is to improve the dispersion of CNTs in the aluminum composite. Following are the specific objectives of this work.

- Improve the dispersion of CNTs in the composite by employing a novel method of spray drying metallic powders with CNTs.

- Utilize plasma spraying and cold spraying for fabrication of the composite coating from spray dried powders.
- Fabricate bulk near net shape structures using plasma spraying.
- Study microstructural features and evolution for the two processes.
- Study mechanism and quality of dispersion of CNTs in coatings synthesized from both the processes.
- Development of a method for quantification/comparison of the quality of CNT distribution in composites.
- Study the chemical and structural stability of CNTs in the coatings by thermodynamics and kinetic analysis of interfacial reactions and high resolution transmission electron microscopy.
- Study the effect of CNT content on nano-mechanical properties of the coatings measured from nanoindentation of nanoscratch testing.
- To study the bulk mechanical properties of plasma sprayed CNT composites through tensile and compressive testing of bulk samples in aas-sprayed and hot rolled conditions.

The research work carried out in this study will be documented in this dissertation in various sections namely, introduction, literature review, experimental procedure, results and discussion, conclusion and recommendations for future work. The appendix includes the first page of the publications in peer reviewed international journals arising out of this research work.

2. LITERATURE REVIEW

2.1. Development of Metal Matrix Composites (MMCs)

It is difficult to obtain a single homogeneous material with all the desirable properties. Though metals and alloys have sufficient strength and large toughness, they have lower stiffness. From the design point of view in any structural application, the width of the parts/members is decided based on the elastic modulus and strength of the material. While the strength of the metal and alloys determine the forces that a structure can withstand, the deflections and deformation undergone under elastic loadings are dependent directly on the elastic modulus. A higher elastic modulus is essential for dimensional stability of the overall structure. One of the strategies to increase the strength of metals/alloys has been to decrease the grain size leading to the development of nanocrystalline materials [42-44]. However, there are a lot of challenges with fabrication of bulk materials having nanocrystalline structure like inhibition of grain growth [42]. The other method of increasing the strength of metals/alloys, which is widely in use, is by modification of the microstructure by suitable heat treatment. But increase in elastic modulus is not easy to achieve since for a homogeneous material it is related to the forces between atoms. Ceramics materials on the other hand have a higher stiffness but a lower toughness. Great technological advance was brought about by the discovery and development of polymers in the fist half of twentieth century. They had the advantage of easy mold-ability and high specific strength and they were cost effective. However, the strength was lower it degraded very rapidly with increase in temperature. The need for materials with tailored properties has led to development of composite materials.

A composite material may be defined as one containing two or more physically distinct phases, with a matrix phase which is in large proportion and percolating and reinforcement phase(s) to bring about the desired property improvement. The reinforcement could be in the form of particulates, short fibers, whiskers or long fibers. Examples of composites are found in nature itself in the form of wood and bone. A lot of research has been carried out on particle and fiber reinforced metal matrix composites which can be partly ascribed to the development of ceramic fibers and whiskers of high strength and stiffness during the 1950s and 1960s. The metallic matrix provides ductility and toughness while the reinforcement provides strength and stiffness. The aim was to develop composites with desired properties like high strength, stiffness, wear resistance, machinability, high seizure resistance, large thermal conductivity and low coefficient of thermal expansion (CTE) coefficient. Table 2.1 shows typical properties of reinforcements in use [2, 45, 46]. The properties of pure aluminum and AA-2024 alloy have been included for sake of comparison. It is observed that the reinforcement phases have very high strength and elastic modulus and a lower CTE compared to the matrix.

Aluminum and aluminum alloys have been the choice of material in automobile and aerospace industry due to their light weight and sufficient strength [1, 47]. Aluminum matrix composites have been developed and proposed for many applications. In the automobile industry they are proposed for connecting rods, bearings, cylinder inserts, piston rings, gears, brake pads and many more. The properties desired for such applications include high specific strength, wear and seizure resistance and machinability. In aerospace industry they have been used for truss elements, bus panels, antennas, wave guides, and parabolic reflectors. Aluminum matrix composites having low CTE are

suitable for these applications which see a lot of thermal cycling from temperature between +125^{o}C to -125^{o}C during a day. They have been also used extensively in sporting industries in the fabrication of light weight bicycles and rackets, and for electronic packaging as thermal management materials due to their increased thermal conductivity and low CTE.

Table 2.1: Typical properties of some reinforcements used in MMCs

Reinforcement	**Density, g/cc**	**Ultimate Tensile Strength, MPa**	**Elastic Modulus, GPa**	**Thermal Conductivity, W/m.K**	**Coefficient of Thermal Expansion, 10^{-6} /K**
Al_2O_3 (Saffil), short fibers	3.29	2000	300	-	-
Boron Carbide (B_4C), fibers	2.35	2690	425	39	3.5
SiC fibers	3.46	2280	450	-	-
SiC particulates	3.21	-	448	120	3.4
AlN	3.26	2100	310-345	150	3.3
Si_3N_4	3.8	-	207	28	1.5
Vapor Grown Carbon Fibers	2.1	7000	700	1950	-1
AA1010 alloy	2.71	90	69	222	23.6
AA 2024 Alloy	2.78	485	73	193	23.2

2.2. Carbon Nanotubes as Reinforcement

In 1960, Roger Bacon [7] demonstrated the formation of graphite whiskers (diameters ranging between fractions of a micron to couple of microns) which were flexible and had a tensile strength of up to 20 GPa. Subsequent research led to development of processes for large scale production of these fibers by carbonization of Rayon, poly-Acrilonitrile (PAN) or pitch. Manufacture of carbon fibers of high strength in the 1960s and 1970s made them the first choice for the manufacture of advanced composites for use in rocket nozzle exit cones, missile nose tips, re-entry heat shields, packaging and thermal management. Extensive research has been carried out in the area of carbon fiber reinforced metal matrix composites [48]. Since 1970, carbon fiber reinforced composites have been extensively used in wide array of applications like aircraft brakes, space structures, military and commercial planes, lithium batteries, sporting goods and structural reinforcement in construction. The new Virgin Galactic aircraft WhiteKnightTwo (WK_2) which will ferry the spacecraft SpaceshipTwo boasts to be the largest all carbon composite aircraft with a 140 ft wing made of carbon composite. Such a thing has been possible due to the development of high strength composites employing carbon fibers.

Research in field of carbon was revolutionized by the discovery of carbon nanotubes (CNTs) by Iijima in 1991 [6]. Oberlin et al. have reported carbon filaments by decomposition of benzene [49]. They reported hollow tubular like morphology of diameters 2-50 nm with carbon layers arranged parallel to the tube axis similar to “annual ring structure of a tree”. Figure 2.1 shows the images of carbon fibers/nanotubes obtained by Bacon, Oberlin and Iijima. Although CNTs might have been synthesized earlier [7,

49], it took the genius of Iijima to realize that they are tubes made by rolling a graphene sheet onto itself. A multiwalled carbon nanotube (MWNT) is made up of many single walled carbon nanotubes (SWNT) arranged in a concentric manner. *Unless otherwise mentioned, CNT in this thesis refers to multi walled carbon nanotube.*

Multiwalled carbon nanotubes have emerged as potential reinforcement for novel nanocomposites due to their extraordinary strength and elastic modulus [50-53]. Mechanical properties of carbon nanotubes have been experimentally measured by several methods viz. thermal vibrations in TEM, electromechanical resonance and in situ testing inside SEM using an AFM. A summary of experimentally measured mechanical properties of carbon nanotubes is presented in Table 2.2. Of all the tests mentioned in Table 2.2 only the last two have studied the fracture behavior of CNTs. Rest of the studies probed the CNT properties in the elastic regime only.

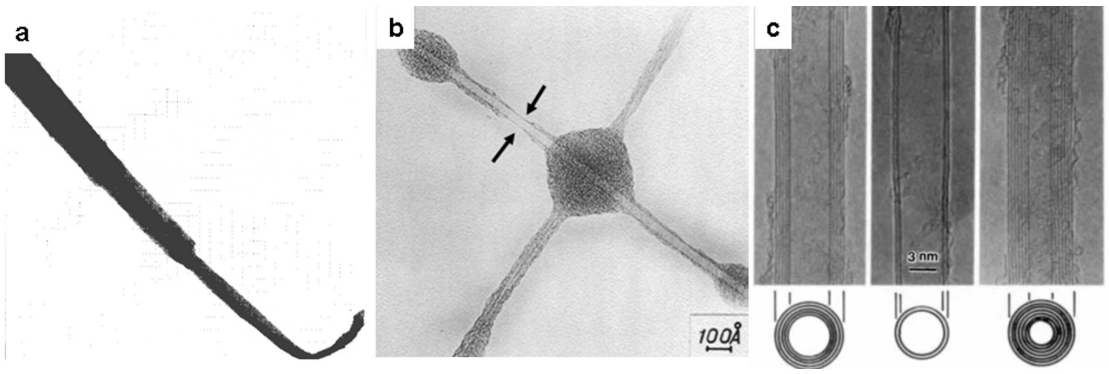

Fig. 2.1 Carbon nano-fibers/nanotubes synthesized by a) Bacon [7], b) Oberlin et al. [49], and c) Iijima [6]

Table 2.2: Summary of experimental measurements of Young's modulus of CNTs

Sl. No.	Method	Remarks	Reference
1	Amplitude of thermal vibrations of MWNTs at different temperatures in a TEM	E = 0.4-4.15 TPa Avg. = 1.8 TPa	Treacy et al. [8]
2	Same as 1 for SWNTs	E = 1.3-0.4/+0.6 TPa	Krishnan et al. [12]
3	Force-displacement curve of pinned MWNT using AFM	E = 1.28±0.59 TPa	Wong et al. [9]
5	Shifts in D* peaks of the Raman spectra of CNT in epoxy composites	E = 2.8-3.6 TPa for SWNT and 1.7-2.4 TPa for MWNT	Lourie and Wagner [54]
6	Frequency of electromechanical resonances	E = 1-0.1 TPa for MWNT	Poncharal et al. [55]
7	Bend test of simply supported MWNT	E = 870 GPa for arc MWNT and 27GPa for CVD MWNT	Salvetat et al. [56]
8	Same as 7 for SWNT ropes	E = 1 TPa	Salvetat et al. [57]
9	Tensile test of MWNT in SEM	E = 270-950 GPa Strength = 11-63 GPa	Yu et al. [10]
10	Same as 9 for SWNT ropes	E = 320-1470 GPa Strength = 13-52 GPa	Yu et al. [11]

It is observed that multiwalled carbon nanotubes have strength up to 63 GPa and elastic modulus up to 970 GPa showing that they are strongest material known to mankind next to single walled carbon nanotubes. Also they have been shown to have a large thermal conductivity of 3000 $W.m^{-1}K^{-1}$ [14]. These properties make them excellent candidate for reinforcement in place of graphite fibers. A lot of work has been carried out on reinforcing polymer, ceramic and metal matrices with carbon nanotubes. Figure 2.2 shows the number of publications in CNT reinforced polymer, ceramic and metal matrix composites in during 1997-2008.

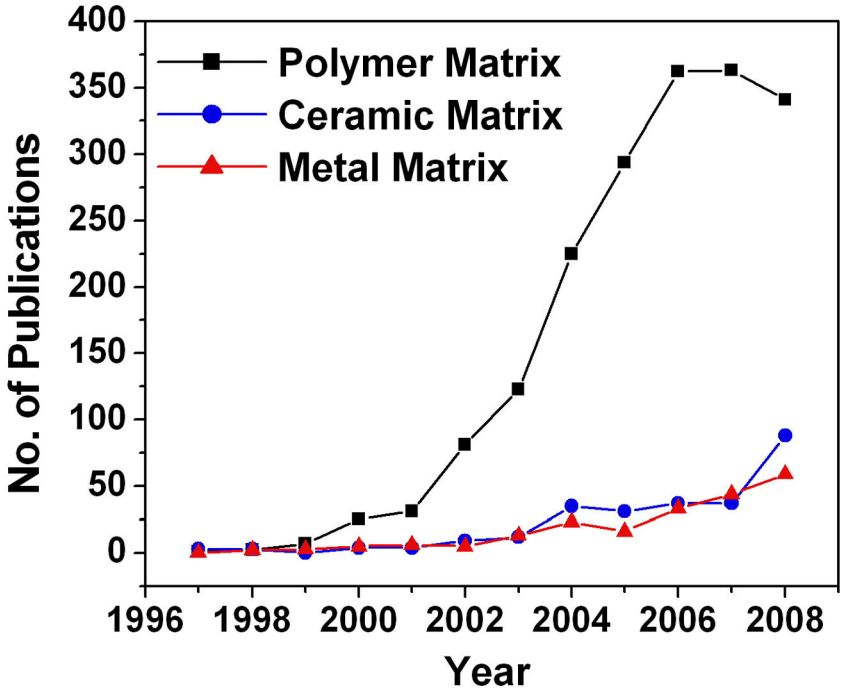

Fig. 2.2: Number of journal articles published in the area of CNT reinforced polymer, ceramic and metal matrix composites during 1997-2008. (source: www.scopus.com)

It is seen that majority of the research work is performed in the area polymer-CNT composites. This is due to the low processing temperatures and forces required for fabrication and ease of dispersion of reinforcement. Extensive research has helped in developing graphite fiber reinforced plastics (GFRP) as an established technology and today most of the aircraft interior is made of GFRP. However, the interest and efforts in synthesis of ceramic and metal matrix CNT composites have been steadily increasing in last five years as seen in Fig. 2.2.

2.3. Processing of CNT Reinforced Metal Matrix Composites

Metal matrix carbon nanotube (MM-CNT) composites are prepared through a variety of processing techniques. The main challenges include the retention of undamaged CNTs, achievement of homogeneous dispersion of CNTs, achievement of good interfacial bonding between CNTs and the matrix, elimination of porosity and fabrication of bulk composite. The various processes used for fabrication of MM-CNT composites have been summarized in Fig. 2.3. Powder metallurgy is the most popular and widely applied technique for preparing MM-CNT composites. Electrodeposition and electroless deposition are second most important techniques for deposition of thin coatings of MM-CNTs as well as deposition of metals on to CNTs. For low melting metals like Mg and bulk metallic glasses, melting and solidification is a viable route. *Our research group has pioneered thermal spray techniques for fabrication of CNT reinforced aluminum composites.* Apart from these techniques, scattered efforts have been made on indigenous methods for preparing MM–CNT composites. The following subsections will present all of these processing techniques.

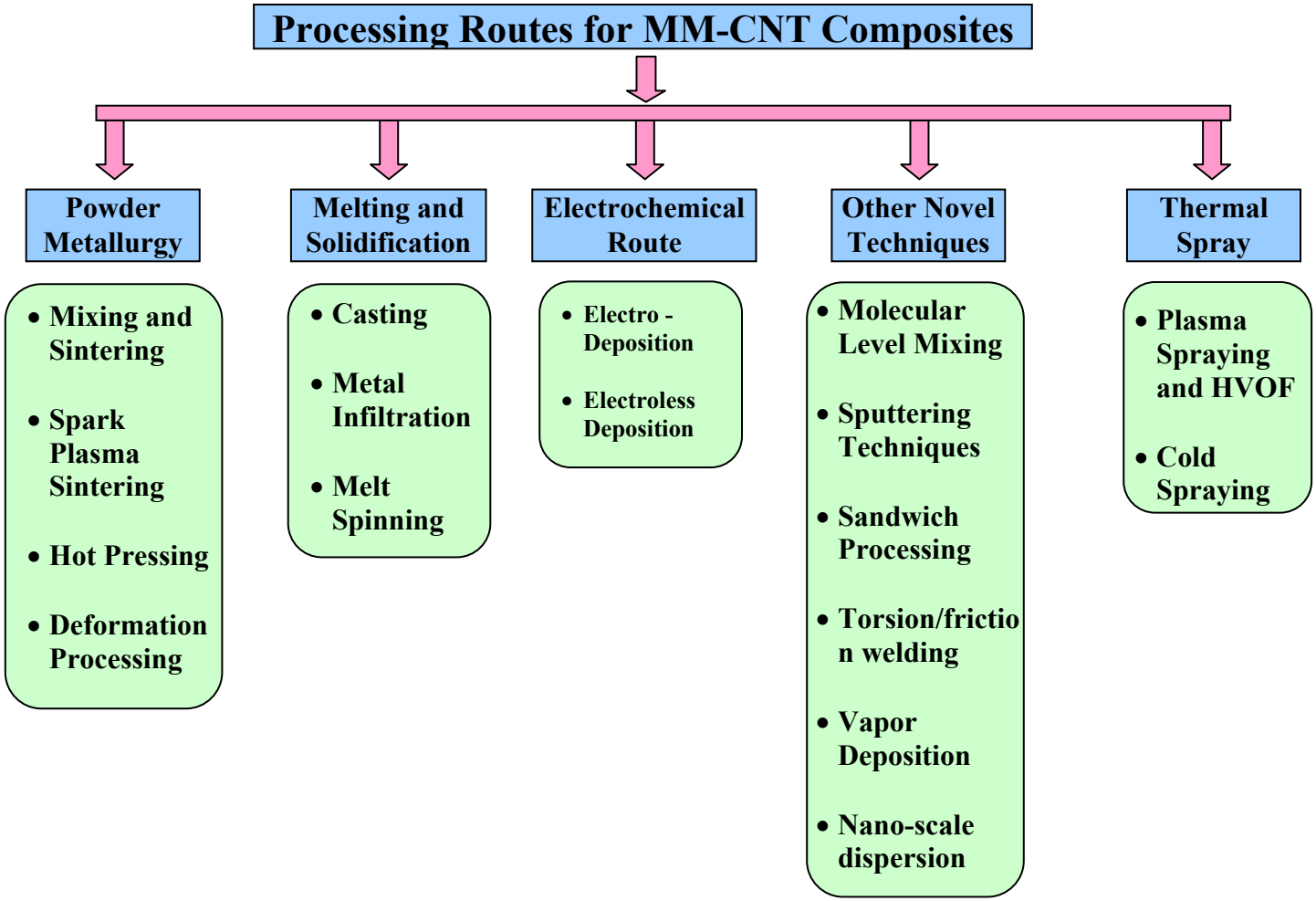

Fig. 2.3: Processing routes used for fabrication of CNT reinforced metal matrix composites

2.3.1. Powder Metallurgy Techniques

Most of the studies on Al-CNT and approximately half of the research work on Cu-CNT composites have been carried out using powder metallurgy method. A few researchers have also prepared CNT composites based on Mg, Ni, Ti, Ag, Sn, and intermetallics through this route. The basic process steps consist of mixing CNTs with metal powder by grinding or mechanical alloying followed by consolidation by compaction and sintering, cold isostatic pressing (CIP), hot isostatic pressing (HIP) or spark plasma sintering.

2.3.1.1. Mixing and Sintering

Some of the MM-CNT composites prepared using sintering route are Cu-CNT [17, 58], Al-CNT [21], W-Cu-CNT [18], Mg-CNT [59] and Ag-CNT [60]. In some cases [22, 61-64], only mechanical alloying was used to prepare composite powder particle as the final product. In the preparation of Cu-CNT composites [17, 58] through mixing, compaction and sintering route, CNTs were coated with Ni using electroless deposition to achieve good interfacial bond strength. Density of the composites was comparable up to 8 wt.% CNT addition beyond which it decreased drastically due to agglomeration. No interfacial product formation was observed. In order to obtain homogeneous dispersion of CNTs, He et al. [21] have grown CNT by chemical vapor deposition (CVD) process on Al powders which were subsequently compacted and sintered at 913 K to obtain Al-5wt.% CNT composite of high relative density of 96% and homogeneous dispersion of CNTs. CNT pullouts and bridges, revealed at fracture surface were responsible for increased hardness (4.8 times) and tensile strength (2.8 times) over pure Al. Yang et al.

[59] achieved homogeneous distribution of CNT in Mg matrix by mechanical mixing of the powders in alcohol and acid mixture followed by sintering at 823 K. In order to enhance adhesive bonding at the surface, CNTs have also been treated by acid to roughen the surface through oxidation and used for Ag matrix composite [60]. CNTs were shortened in length due to this treatment, but no damage on the wall was reported. Morsi and Esawi [22, 64] have used ball milling to disperse CNTs in Al matrix. Milling for up to 48 hrs lead to good dispersion of CNTs but resulted in formation of large spheres (> 1 mm) due to cold welding.

2.3.1.2. Spark Plasma Sintering

Spark plasma sintering (SPS), a comparatively new and novel sintering technique, has also been explored by some researchers for synthesizing CNT-metal matrix composites. In this process, a pulsed direct current is passed through a die and the powder, producing rapid heating and thus greatly enhancing the sintering rate [65]. Efficient densification of powder can be achieved in this process through spark impact pressure, joule heating and electrical field diffusion. This method is, generally, suitable for consolidation of nano powders, without allowing sufficient time for grain growth. Most of the studies using SPS have been carried out in Cu-CNT [19, 66-68] and Al-CNT system [31]. Kim et al. [66] were the first to report SPS of Cu-CNT composites fabricated at 1023K at 40 MPa with better dispersion and improved density (97-98.5%). Sintered microstructure consisted of dual zones of CNT free matrix and CNT rich grain boundary regions.. Extraordinary strengthening of more than 3 times was achieved by SPS of molecular level mixing powder of Cu and 10vol.% CNT [19]. Microstructures of

the samples prepared by SPS of ball-milled powders and molecular level mixed powders are shown in Fig. 2.4. Enhancement in mechanical strength by 129% with addition of 5 vol.% CNT has been reported for Al-CNT composite synthesized by SPS followed by hot extrusion of powders prepared by a nano-scale dispersion method (described in section 2.3.4) [31]. Good dispersion and alignment of CNTs clusters in the matrix as well as improved interfacial bonding by formation of minor amounts of Al_4C_3 at the CNT-matrix interface were the prime reasons for improvement is mechanical properties. SPS has also been explored for synthesis of CNT reinforced Ni-Ti based shape memory alloys [69] and Fe_3Al -CNT composites [70] with enhanced mechanical properties.

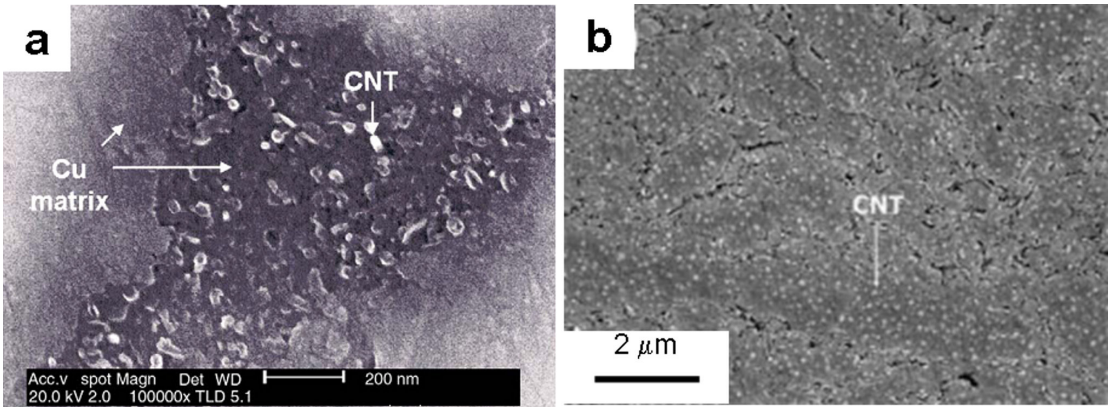

Fig. 2.4: Microstructure of Cu-CNT samples prepared by SPS of a) ball-milled nano-sized Cu-CNT mixtures [71] and b) Molecular level mixed Cu-CNT powder [19]

2.3.1.3. Hot Pressing

Instead of sintering, some researchers have used hot pressing consolidation of powder mixtures. Researchers have found hot pressing method to be inappropriate for fabricating Al-CNT composites as it results in clustering of CNTs [26, 72]. Kuzumaki et

al. [28] have optimized the milling time for mechanical mixing at 5 hrs to avoid damage to CNTs and fabricated Ti-CNT composite by hot pressing.

Mg-CNT composites [73] and Fe_3Al-CNT composites synthesized via hot-pressing [74] have shown improved mechanical properties (hardness, compressive strength and bend strength) due to uniform distribution of CNTs. Hot pressing route has also been explored for processing CNT reinforced Ti-based BMG composite [75, 76]. Addition of CNT has been shown to increase in the glass transition and crystallization temperature in this composite which further assisted in decreasing the required cooling rate for glass formation, thus assisting BMG formation.

2.3.1.4. Deformation Processing

In most of these works, the composite compacts were subjected to post-sintering deformation processes like rolling, equi-channel angular processing (ECAP), extrusion etc. However, the approach was mainly confined to Cu-CNT [41, 71, 77-80] and Al-CNT [29, 30, 81-86] composites. Kuzumaki et al. [29] have synthesized Al-CNT composite through hot extrusion of powder compacts, at 873K. It was found that the CNTs were aligned along the extrusion direction and were strong enough to withstand the extrusion load. Rolling of Cu-CNT composites resulted in alignment of CNT clusters in the matrix [67, 77, 80]. Improvement in wear resistance and coefficient of friction was also observed in rolled samples [83]. Equal-channel angular processing (ECAP) was employed to successfully to synthesize Cu-CNT composites from powder compacts [41, 78, 79], with CNT content varying between 1-5 vol.%. ECAP, being a severe plastic deformation

technique, is expected to induce high amount of deformation to the constituent phases, thus damaging the CNTs.

It is observed that most of the processing for all major MM-CNT systems except Ni-CNT has been done by powder metallurgy route. Application of high temperature deformation by hot pressing and hot extrusion lead to large improvement in properties. This indicates that the density and CNT-matrix bonding of the composites is very important factor in strength enhancement.

2.3.2. Melting and Solidification Route

Melting and solidification, the most conventional processing techniques for MMCs, has also been utilized for synthesizing CNT reinforced composites. The limitations of this route is that it is favored for composites having low melting point matrix and suspended CNTs tend to form clusters due to surface tension forces. Bian and co-workers were the first to synthesize CNT reinforced Zr-based bulk metallic glass (BMG) by this route [23, 87]. Pre-alloyed powders, mixed with CNTs and compacted into cylinders, were melted and cast to form Zr-BMG-10 vol.% CNT composite rods. Increase in crystallinity of the matrix has been attributed to ZrC formation at the CNT matrix interface as well as depletion of Zr from amorphous matrix. Mg, being a low melting point metal, has been suitably processed through melting and casting route [24, 88-90].

Yang and Schaller [59] have used infiltration technique to prepare Mg-CNT composite. CNTs were grown by CVD on a structure made by Al_2O_3 fibers and then the same was infiltrated with molten Mg under pressurized gas. This study reported

improvement in the high temperature (500K) shear modulus by 20%. Al-CNT composite has been synthesized by Zhou et al. [91] through infiltration of a porous preform made by pressing a ball milled mixture of Al, Mg powders and CNTs at 1073 K for 5 h. In a recent study, Uozumi et al. [92] have explored the possibilities of squeeze casting to fabricate CNT reinforced Al and Mg alloy composite with good dispersion of CNTs and without pores.

Melt spinning involves pouring a molten alloy drop by drop on to a rotating Cu wheel. The droplets are converted into ribbons which are amorphous due to the large cooling rates. CNT-$Fe_{82}P_{18}$ – bulk metallic glass composite ribbons of 40 μm thickness have been prepared in this manner [93]. Retention of undamaged CNTs and amorphous nature of the composite was reported. One study by Hwang et al. [94] reports about Ni-10 vol.% CNT composite processed through laser deposition technique after roller mixing of CNT and Ni powder. Though the process incurs very high temperatures, still CNTs were retained.

Melt processing could be used for casting alloys having low melting points. Novel materials like bulk metallic glasses which are prepared by casting method have also been explored. Most of the metals and alloys do not wet CNT and hence this could lead to poor infiltration. Chemical stability of the CNTs during this kind of processing might be an issue due to the higher reactivity of molten metal/alloy.

2.3.3. Electrochemical Route

In terms of number of publications on metal matrix-CNT composites, electrochemical deposition is the second most popular route after powder metallurgy

techniques. The main difference between the two is that electrochemical method is primarily used for formation of thin composite coatings with a reported thickness of 20 to 180 μm [95], though some of the studies on electrochemical deposition do not report coating thickness. This technique has also been used for coating CNTs with metals to produce one-dimensional composites– the projected application for which includes, but not limited to, different types of nano-sensors, electrodes, inter-connects and magnetic recorder head in computer applications. Both electrodeposition and electroless deposition have been used for MM-CNT fabrication.

2.3.3.1 Electrodeposition

Electrodeposition technique has been reported as a processing route for mainly Ni-CNT [95-112] and Cu-CNT [113-116] composites. Fig. 2.5 shows the mechanism of formation of coatings by electrodeposition. The first ever report on electrochemical deposition of MM-CNT composite coating was by Chen et al. [98] on co-deposition of a Ni- 14 vol.% CNT composite coating from electrolytic bath at a current density of 15 A/dm^2 and CNT concentration of 2 g/l. It was found that the CNT content increased with an increase in CNT concentration of the electrolyte, current density and agitation rate of the bath [98, 99]. Guo et al. [109] have shown that pulse deposition produces smother surface and the CNT content of the Ni-CNT composite coating increases with increasing pulse frequency and reverse ratio. Ultrasonication and magnetic stirring have been used to keep the CNTs in suspension.

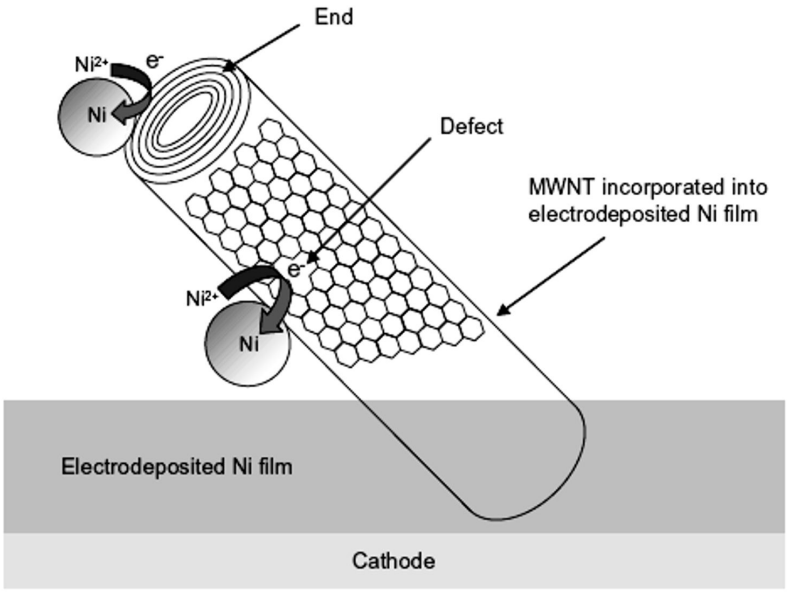

Fig. 2.5: Schematic showing composite coating formation during electrodeposition [101]

Arai et al. have added polyacrylic acid to the bath to keep the CNTs in suspension [101, 105, 107]. Ball milling of CNTs has been used to decrease their aspect ratio to help them being dispersed in the bath [96, 99, 103]. Acid cleaning and adding surfactants has also improved suspension of CNTs [100, 102]. Metal ions deposit on CNT surfaces by absorbing electrons [108, 117] and hence the large surface area provided by CNTs serves as a mechanism for reduction of grain size of electrodeposited coatings. Shi and co-workers [102] have reported 250% reduction in grain size (42 nm to 17nm) of Ni-Co co-deposited coatings. Guo et al. [109] have shown increase in the microhardness of Ni-CNT composite coating by AC-deposition with increasing pulse reverse ratio and current density up to 8 A/dm^2 of the bath. Another processing approach is filling the voids of aligned arrays of CNTs, used as cathode, with Cu by electrodeposition [118]. Composites with up to 40 vol.% CNT were produced having lower thermal resistance and electrical

resistivity than unreinforced matrix making them suitable for interconnect and thermal management applications.

2.3.3.2. Electroless Deposition

Electroless deposition is a chemical technique in which a metal or its alloy is decomposed by catalytic action and deposited, without application of any current. This technique is mostly developed and employed for Ni-P or Ni-B alloys [17, 118-135]. There are only few studies on Co-CNT [21], Ni-Fe-P alloy [136] and Ni-Cu-P alloy [135]. Agitation of the bath during processing and ball milling of the CNTs prior to mixing in the bath have been proposed as solution for improved CNT dispersion [120, 121, 124, 128]. The mechanism of deposition in electroless process is based on thermo-chemistry of the system. Hence, the bath temperature and pH value plays a very critical role on the coating composition and morphology. Increasing beyond the optimized bath composition resulted in reduction of CNT content of coating due to agglomeration of CNTs in the bath. Uniformly distributed and deeply embedded CNTs were reported in some of the studies [127, 128, 130, 135], while some studies report presence of CNT-clusters [118]. Other than coatings, synthesis of one-dimensional composites of CNT coated with Co [123] and Ni and Ni-alloys [121, 129] by electroless deposition technique have also been reported.

2.3.4. Other Novel Routes

It is evident from the complexity of the length scales involved in the CNT composite systems that novel processing routes need to be developed. Several researchers

have adopted novel approaches for enhancement of dispersion and bonding in MM-CNT composites. Molecular level mixing is one such method which has been mostly used for Cu-CNT Composites [19, 68, 137-139], except one that deals with Sb and $SnSb_{0.5}$ matrix composites [140]. This method is capable of producing composite particles or one dimensional nanostructure of CNT coated with metal. In this process, a CNT metal suspension is subjected to drying, calcination and reduction process, in series, to produce metal-CNT composite powder [19]. These nanocomposite powders are then used for bulk processing through powder metallurgy route [19, 68, 138, 139]. The aim is to obtain good dispersion and better bonding of CNTs with matrix in the final composite structure.

Huang et al. [141] have tried to deposit several metals on CNT bundles using sputtering. Au, Ag and Cu form array of nano crystals of ~10Å on the surface of CNTs, whereas Ti, Zr and Mo forms nanowires at the grooves of the CNT bundles. This difference in morphology has been explained in terms of interactions between carbon and respective metal atoms. Particle formation in Au, Ag and Cu indicates a weak interaction of those metals with C, whereas strong interaction of C with Ti, Mo and Zr helps them in forming elongated islands. Ci et al. [37] have sputtered Al at the bottom surface of vertically grown CNTs detached from the quartz surface. Subsequent annealing in the temperature range of 723- 1223K leads to Al_4C_3 formation. It was shown that carbide formed at defect sites and amorphous regions of CNTs.

Researchers have also tried to prepare MM-CNT composites by putting alternate layers of CNT and metal like a sandwich structure and then consolidating by applying severe pressure [142, 143]. Li et al. [142] have arranged 20 layers of 10 μm Cu foil with alternate CNT layers of 450 nm thickness and cold rolled the assembly with intermittent

annealing steps to form a Cu-CNT composite. They have reported good bonding between CNT and Cu, and improvement of young's modulus by 13±5% by addition of 3.1 vol.% of CNTs. Salas et al. [143] have explored shock wave consolidation of alternate layers of Al powder and CNTs to produce composite with 2 wt.% and 5 wt.% CNT content. Deterioration of mechanical properties was observed due to clustering of CNTs at splat boundaries.

There have been few studies on application of torsion or frictional force to weld CNT and metal together to form MM-CNT composite [144-146]. Tokunaga et al. [144] have severely deformed ultrasonicated mixture of Al powder and CNT under a torsion force of 2.5 GPa and rotation speed of 1 rpm. They could produce Al-5 wt% CNT composite of 98% theoretical density. A decrease in grain size by 80% was also reported, which has been attributed to the presence of CNTs in the matrix causing constrained movement of dislocation towards grain boundary and subsequent annihilation [124]. Morisada and co-workers [145] have adopted a similar process for producing Mg-alloy-CNT composite. CNTs were kept in a groove of a bulk piece of Mg alloy. Subsequently, frictional force was applied inside the groove with a probe rotating at 1500 rpm with various travel speeds.

Few research groups have used physical /chemical vapor deposition (PVD/CVD) techniques for processing one dimensional or particulate type of MM-CNT composites [21, 147-150]. Zhang et al. [147] coated CNTs by tungsten through PVD of a W filament heated to 2473K in H_2 environment. They obtained non-uniform coating formation. Shu et al. [148] and Kim et al. [149] have reported processing of Si-CNT composite, to be used as Li-ion battery anode, by CVD technique. Both the studies have grown CVD on

Si particles using Ni as catalyst. Wang et al. [151] have produced Si-coated CNT composite by decomposition of Silane (SiH_4) in order to increase thermal stability of CNTs. Ishihara and co-workers [150] have produced Si particles coated with nanotubes by chemical decomposition and vapor deposition of tetramethyl silane ($(CH_3)_4Si$). CVD process has also been used to produce Al-CNT composite powder by growing CNT on Al particle using Ni catalyst. He et al. [21] have used this composite particle with 5 wt.% CNT to prepare bulk composite structure through powder metallurgy route. Hardness and tensile strength of these composites have also increased by 200% and 180%, respectively, than the composite made with blended powders.

A nanoscale dispersion method has also been proposed that utilizes natural rubber (NR) to improve dispersion of CNTs in metallic powder [20]. A perform of CNT in NR and CNTs and metal mixture in NR is stacked alternatively. The stacks are compression molded into slabs at 80^oC which are subsequently heated in N_2 atmosphere at 800^oC. This treatment burns off the rubber and melts the Al incorporating the CNTs into the composite in a dispersed manner. A seven-fold increase in compressive yield strength was reported by addition of 1.6 vol.% CNTs. In another study [31], NSD process was used to produce precursor Al powder on which CNTs were distributed uniformly. This powder was subjected to spark plasma sintering followed by hot extrusion for synthesizing 5 vol.% CNT composites which has a tensile strength (194 MPa) twice that for pure aluminum.

2.3.5. Thermal Spray

To the best of our knowledge, all of the work on thermal spraying of CNT reinforced metal matrix composites have been carried out by our research group. Thermal spraying can be defined as the spraying of molten or semi-molten particles onto a substrate to form a coating/deposit by way of impact and solidification. Thermal spraying is now a 100 years old technique with the first patent being filed in early 1900 by Dr. Schoop [152]. Thermal spraying methods offer the advantage of large cooling rates as high as 10^8 $K.s^{-1}$ during solidification which often result in the formation/retention of nanocrystalline structure in the coatings [153-155]. Based on the heat source, thermal spray processes can be classified into flame spraying, plasma spraying, high velocity oxy-fuel spraying (HVOF) or cold spraying.

2.3.5.1. Plasma and High Velocity Oxy-Fuel Spraying

In Plasma spraying, the heat source is a plasma created by the ionization of an inert gas by an arc struck between a tungsten cathode and concentric copper anode (DC plasma spraying) or by high frequency radio waves (RF plasma spraying) [152]. Powders injected into the plasma (temperature ≈ 10000 – 15000K) absorb the heat as well as gain kinetic energy and are projected at high velocities onto the substrate to form coating. Particle velocities can be subsonic or supersonic in plasma spraying. In HVOF, the source of heat is high pressure combustion of fuel oxygen mixture. The fuel could be gaseous like propylene, methane, propane and hydrogen or liquid like kerosene. The velocities of the particles are considerably higher (up to 1500 $m.s^{-1}$) in case of HVOF which leads to formation of dense coatings. Thermal spraying can also be used for near

net shaping of bulk nanocrystalline components [156, 157]. By spraying on rotating mandrels of complex geometries, parts with intricate shapes can be generated. The faster rate of deposition and the fabrication of components having shape close to the final shape offers tremendous advantages by way of savings in the machining costs.

Laha et al. have studied the feasibility of spraying CNTs with Al-Si powders to form composite coatings [35]. Successful retention of undamaged CNTs in plasma sprayed aluminum coatings was observed. Laha et al. have also fabricated bulk free standing cylindrical structures of CNT reinforced Al-23% Si alloy using Plasma Spray Forming (PSF) and HVOF as shown in Fig. 2.6 [32]. These cylinders were prepared by spraying on a rotating 6061 aluminum mandrel.

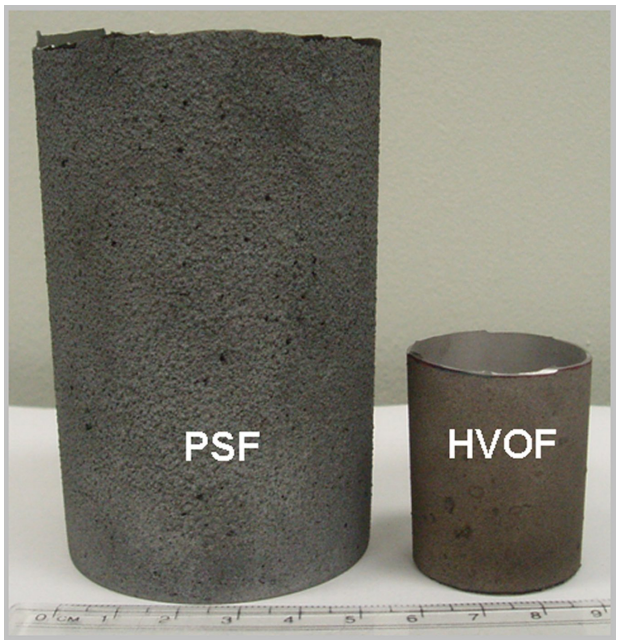

Fig. 2.6: Free standing structures of Al-23 wt.% Si alloy containing 10 wt.% CNT produced by Plasma spray forming (PSF) and HVOF

The thickness of the PSF and HVOF cylinders were 0.64 mm and 1.24 mm, respectively. The thickness of the cylinders was limited due to the fact that the flowability for blended (Al + CNT) powders was not good and lead to clogging of powder feed pipes. HVOF resulted in higher density coating (2.54 $g.cm^{-3}$) compared to PSF (2.45 $g.cm^{-3}$) due to the fact the higher velocities of the particles during HVOF lead to better compaction. Elastic modulus and hardness were found to be higher for the HVOF coating compared to the PSF which was attributed to the lower degree of porosity and higher dislocation density in HVOF coatings [32]. Interfacial phenomenon in PSF composite was studied and will be reviewed in detail in section 2.4.2. It was shown that 2-5 nm layer of SiC is formed at the interface of the CNTs in case of Al-23 wt. % Si alloy [33].

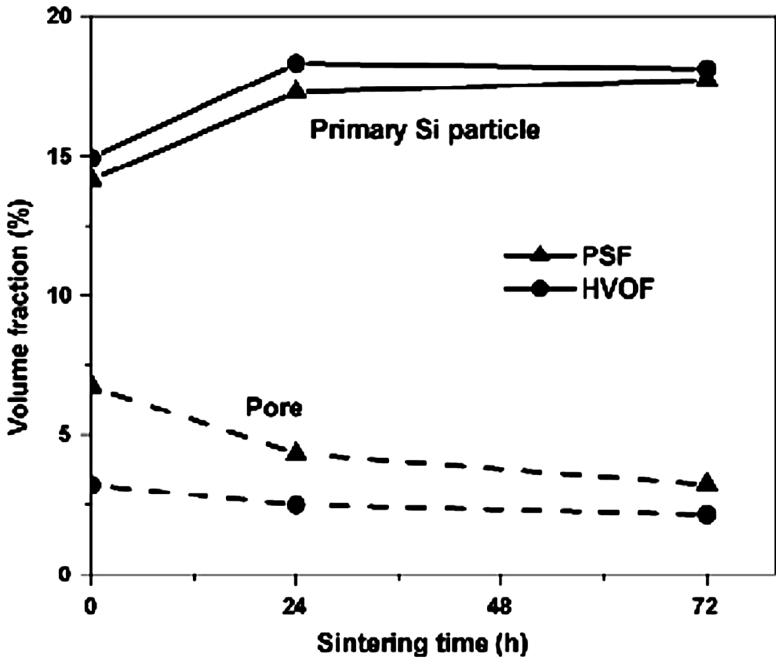

Fig. 2.7: Effect of sintering time on primary silicon porosity content of plasma and HVOF sprayed Al-23 wt.% Si coatings containing 10wt.% CNT [158].

Sintering of the HVOF and PSF composites in argon atmosphere at 400^{o}C for up to 72 hrs resulted in densification and increase in the size and fraction of primary silicon as shown in Fig. 2.6 [158]. No noticeable effect on the interfacial carbide morphology was observed.

2.3.5.2. Cold Spraying

Cold spraying is a relatively new coating technique wherein powder particles are accelerated to supersonic velocities (600-1500 m/s) by a carrier gas flowing under large pressure difference (up to 3.5 MPa) through a de-Laval type of nozzle and made to impact onto a substrate [159]. It has unique advantages like minimal effects on the material sprayed like oxidation, grain coarsening or phase changes, produces highly dense coatings and that the substrate is not affected during the coating process. The disadvantage is that a large amount of carrier gas is lost, unless recycled, and that only plastically deformable materials can be deposited. There is no melting of the particles and the bonding is believed to be due to adiabatic shear instabilities arising from thermal softening at the particle/substrate and particle/particle interfaces which have been modeled using finite element method [160, 161]. Figure 2.8 shows the schematic of shear instabilities leading to curvature generation. The constitutive relations for plastic flow used in modeling the deformation and bonding take care of the dependence of the flow stress on the strain, strain rate, temperature and pressure. The parameters affecting the process and spraying efficiency are particle size, density of particles, temperature of gas, density of gas and spraying angle, and various models have been proposed for the effect of various parameters [162-164].

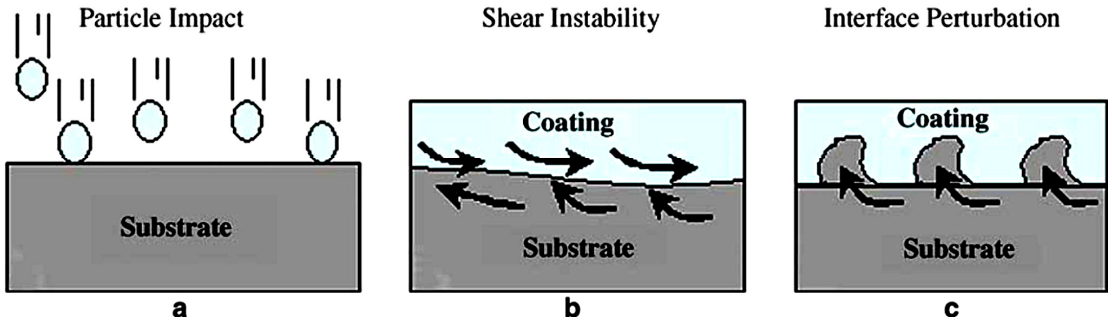

Fig. 2.8: Schematic showing curvature generation due to shear instability resulting in mechanical interlocking [165]

Cold spraying has been used to deposit many types of materials including pure metals like Al, Cu and Ti [166-170], alloys like Al-Cu, Cu-Ni and Al-Si [171-174] and composite materials like TiB_2-Cu, Al-Al_2O_3 and W-Cu [175-178]. In all the above cases of spraying composite coatings, it was observed that the second phase was distributed uniformly within the matrix. Recently, there has been interest in cold spraying composites containing nano fillers as reinforcements by cold spraying [177, 178]. Cold spraying has not been used for spraying CNT composites. It is interesting to study the feasibility of high impact processes for CNT composite fabrication. The effect of impact and plastic deformation processes on CNTs has not been studied.

2.3.5.3. Comparison of Plasma and Cold Spraying

Plasma and cold spraying have been used in this dissertation for fabrication of coatings and composites reinforced with CNTs. So a comparison of the basic nature of the processes in terms of the energy imparted to the particles is necessary. Thermal spray

provides an efficient way of incorporating and dispersing CNTs into coatings and bulk components as it is a layer by layer deposition technique. Addition of CNTs could lead to improvement in the wear resistance and thermal conductivity of the coatings. Also possibilities of rapid prototyping exist with thermal spray methods. Plasma and cold spraying are different processes in many fundamental aspects. The important parameters that influence the property of coatings are the particle temperature and velocity.

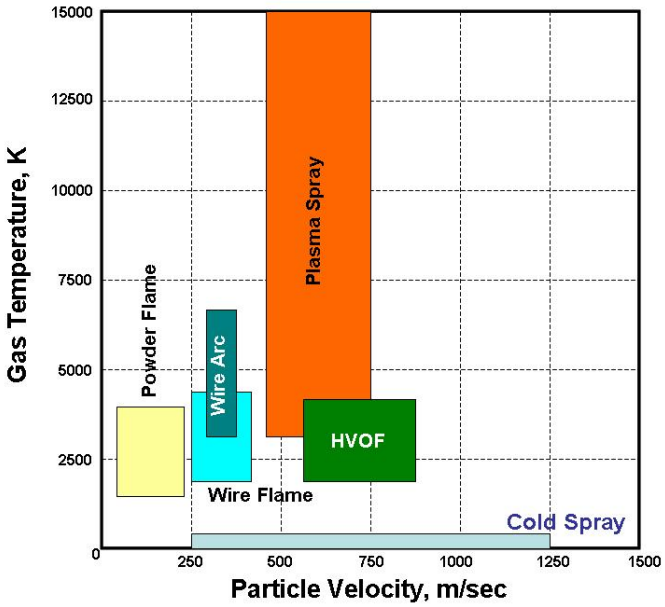

Fig. 2.9: Comparison of various thermal spray processes

Figure 2.9 shows a comparison of various thermal spray processes based on the gas temperature and particle velocities. It is observed that the plasma and cold spraying represent extreme processes in terms of gas temperature and particle velocities respectively. Table 2.3 compares the various aspects of the two processes.

Table 2.3: Comparison of various aspects in plasma and cold spraying for CNT composites

Feature	Plasma Spraying	Cold Spraying
Particle Temperature	> 2000K	RT-600K
Particle velocity	100-200 m/s	> 600 m/s
Particle state	Molten or semi-molten	Solid
Mechanism of coating formation	Layer by layer deposition of splats from solidification of impacting droplets	Plastic deformation of particles due to impact leading to splat formation
Oxidation of matrix material	Possible	Not possible
Retention of powder microstructure	Not retained	Retained
Thermal damage to CNTs	Possible	Not possible
Chemical stability of CNTs	Reaction with the matrix material possible	No chemical reaction possible
Mechanical damage to CNTs	Moderate damage possible	Severe damage possible

From Table 2.3 it is noted that there are several interesting phenomena that needs to be studied in fabrication of these coatings by the two processes. While oxidation and phase changes could occur during plasma spraying of Al-Si powders, cold spraying produces little change in the phase composition of the powder feedstock. Plasma spraying could cause changes in morphology of the CNTs due to thermal damage and chemical interaction with the molten matrix, while in cold spraying there is no melting involved.

Cold spraying involves extremely high velocity impact which can cause mechanical damage to CNTs whereas mechanical damage, though possible in plasma spraying is but less severe. The research work carried in this study addresses these issues.

It is observed that interest in MM-CNT composite fabrication is increasing. Figure 2.10 shows pie chart of number of publication in various metal matrices.

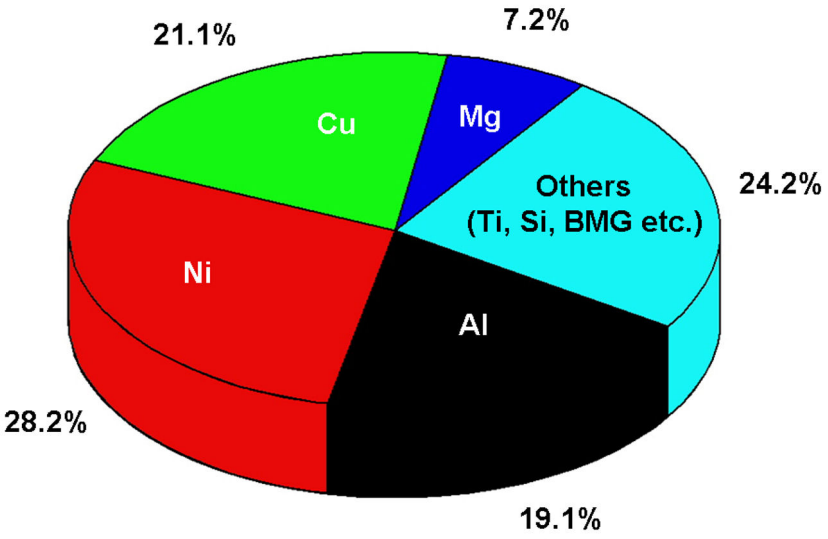

Fig. 2.10: Pie chart of no. of publications till 2008 on various MM-CNT systems

Most of the work has been carried out on Ni-CNT composites where the effort has been mainly to synthesize coatings by electrochemical means. Aluminum and Copper are comparable and interest in this field has been in developing novel CNT reinforced composites for structural, electronic or thermal management applications. Novel methods are being designed to meet the challenges and overcome the issues. Table 2.4 shows the summary of major processing routes for fabrication of MM-CNT composites. As has been seen from the discussion on processing, the main objective is to achieve

homogeneous dispersion and good reinforcement of CNTs in the matrix. Electrochemical deposition techniques are the best for achieving the same. But, the main limitation for those techniques is that they can produce thin coatings and not thick coatings and free standing bulk composite structures. Casting techniques are suitable for only low melting point materials or amorphous structures though uniform dispersion of CNTs in the melt pool is still a challenge. Powder metallurgy is, by far, the most widely used and feasible route for preparing MM-CNT composites, but it needs immediate attention for both the dispersion and reinforcement issues. Molecular level mixing technique and CVD method have shown promising improvement in preparation of starting powder for powder metallurgy route. If they are combined with SPS technique for sintering, MM-CNT composite with better mechanical properties may be produced. But, these techniques are still in their nascent stage and further studies are required to explore their possibilities as suitable method for preparing MM-CNT composites. Thermal spray methods like plasma spraying and HVOF have been shown to produce CNT reinforced coatings and near net shape structures. CNTs were shown to retain during high impact processes like cold spraying and explosive shock-wave consolidation. Thermal spray methods offer the advantages of rapid solidification and rapid prototyping for bulk composite fabrication as compared to extrusion or casting.

Table 2.4: Summary of Processing Techniques utilized for MM-CNT composite fabrication

Processing	**Sub-type**	**Method summary**	**Alloy systems**	**Property Enhancement**
Powder Metallurgy	Sintering	(Powders + CNT) mechanically alloyed/mixed followed by compaction and sintering	Cu-CNT [17, 58] Al-CNT [21] W-Cu-CNT [18] Mg-CNT [59] Ag-CNT [60]	91% reduction in COF and 140% reduction in the wear rate in Cu-16vol.% CNT [58] Wear rate and Friction coefficient decreased by 60% for Cu-12wt.% CNT [17] Increased hardness (4.8 times) and tensile strength (2.8 times) in Al- 5wt.% CNT [21]
	Hot pressing	(Powders + CNT) mechanically alloyed/mixed followed by hot pressing	Al-CNT [26, 72], Cu-CNT [179], Ti-CNT [28] Mg-CNT [73] Fe_3Al-CNT [74] Ti-BMG-CNT [75, 76]	450% increase in hardness and 65% increase in elastic modulus in Ti-CNT [28] 9% increase in elastic modulus in Mg-2wt.% CNT [73] Increased thermal stability and hardness (30%) in Ti-BMG-10wt.% CNT [75]
	Spark plasma sintering (SPS)	SPS of powders prepared by Mechanical alloying/novel dispersion methods	Cu-CNT[19, 66-68] Al-CNT [31]	129% increase in tensile strength in Al-5vol.% CNT [31] 200% increase in yield strength and 70% increase in elastic modulus of SPS of molecular level mixed Cu-5vol.% CNT [19]

	Deformation Processing	Compacts processed by hot extrusion, rolling, ECAP	Cu-CNT[41, 67, 77-80] Al-CNT[29, 30, 81-86] Mg-CNT [90, 180]	100% increase in tensile strength in hot extruded Al-10vol.% CNT [29] 71% reduction in wear loss in (sintered + rolled) Cu-12vol.% CNT [80] 15% increase in yield strength in (sintered + hot extruded) Mg 0.3wt.% CNT [87]
Melting and Solidification	Casting	Pre-alloyed powders melt and cast	Zr-BMG-CNT [23, 87] Mg-CNT [24, 88-90]	12% increase in elastic modulus of Zr-BMG-4vol.% CNT [87]
	Melt Infiltration	Infiltration of porous CNT-metal powder compacts	Mg-CNT [59] Al-CNT [91]	20% increase in 500K shear modulus in Mg-CNT [59] 67% increase in hardness, 28% decreas in wear rate in Al-20vol.% CNT [91]
Thermal Spraying	Plasma and HVOF spraying	Spraying CNT-metal powder blends to form coatings/bulk structures	Al-CNT [32, 35, 38, 181]	72% increase in hardness and 78% increase in elastic modulus in Al-10wt.% CNT [35, 181]
Electro-	Electro-deposition	Deposition of Metal-CNT coating from metal electrolyte containing CNTs by passing electric current (Pulsed + DC)	Ni-CNT[95-112] Cu-CNT[113-116]	250% reduction in grain size in Ni-Co-CNT co-deposited coatings [102] 320% and 270% increase in tensile strength of Ni-SWNT and Ni-MWNT [108]. 65% decrease thermal resitance and negligible electrical resistance in Cu-40vol.% CNT [114]

chemical Techniques	Electroless deposition	Deposition of Metal-CNT coating by spontaneous decompostion of salt solution containing CNTs	Ni-P-CNT or Ni-B-CNT [17, 118-135]	44% increase in hardness in Ni-2 vol.% CNT [118, 132] 300% increase in hardness and elastic modulus in Ni-P-28.2vol.% CNT [133, 134] 83% reduction in wear volume and 60% reduction in COF in Ni-P-2vol.% CNT coating [118, 132]
Novel Routes	Molecular Level Mixing	Dispersion of CNTs in salt solution followed by drying, calcination and reduction.	Cu-CNT [19, 68, 137-139]	200% increase in yield strength and 70% in elastic modulus Cu-5vol.% CNT [19] 76.9% decrease in wear loss with 10 vol.% CNT addition [68]
	Nanoscale Dispersion	Mixing natural rubber (NR), CNTs and metal powders followed by curing to remove NR	Al-CNT [31, 182]	Seven-fold increase in compressive yield in Al-1.6vol.% CNTs [31] 128% increase in tensile strength in SPS compacted and hot extruded Al-CNT [31]

2.4. Critical Issues in CNT reinforced MMCs

2.4.1. CNT Dispersion

Uniform dispersion of CNTs has been the main challenge in CNT-reinforced composites be it polymer, ceramic or metal matrix. This is due to the fact that CNTs have tremendous surface area of up to 200 $m^2.g^{-1}$ which leads to formation of clusters due to attractive van der Waals force. The elastic modulus, strength and thermal properties of a composite are related to the volume fraction of the reinforcement added. Hence, a homogeneous distribution of reinforcement is essential as it translates into homogeneous properties of the composite. Clustering leads to concentration of reinforcement at certain points and this could lead to lowering of overall mechanical properties.

Most of the early research on fabrication of CNT composites used blending/mixing for adding CNTs to metals [35, 58, 60]. Blending is not effective in dispersing the CNTs. Several researchers have observed that mechanical properties (wear, hardness, tensile strength) deteriorate for composited made by blending of larger concentration of CNTs [58, 60, 80, 183]. The reduction in the properties is due to the inability to obtain uniform distribution of CNTs at large volume fractions. Several methods have been developed to uniformly distribute the CNTs in metal matrices. Noguchi et al. have suggested nanoscale dispersion (NSD) process which results in uniform dispersion of CNTs on Al powder [20]. A seven fold increase in the compressive yield strength was observed for 1.6 vol.% CNT addition. Esawi et al have shown that excellent dispersion of CNTs in Al powders can be achieved by ball milling [22]. However, large particles up to 1 mm in diameter resulted from the milling action, which can cause difficulty during consolidation. Choi et al. used hot extrusion for consolidating

ball milled powders and aligning the CNTs in the extrusion direction [30]. Cha et al. have developed a novel molecular-level mixing method for dispersing CNTs [19]. He et al. [21] have used CVD method to grow CNTs on Al powders which were then used to fabricate a 5 vol.% composite by pressing and sintering. Figure 2.11 shows the dispersion achieved by different methods.

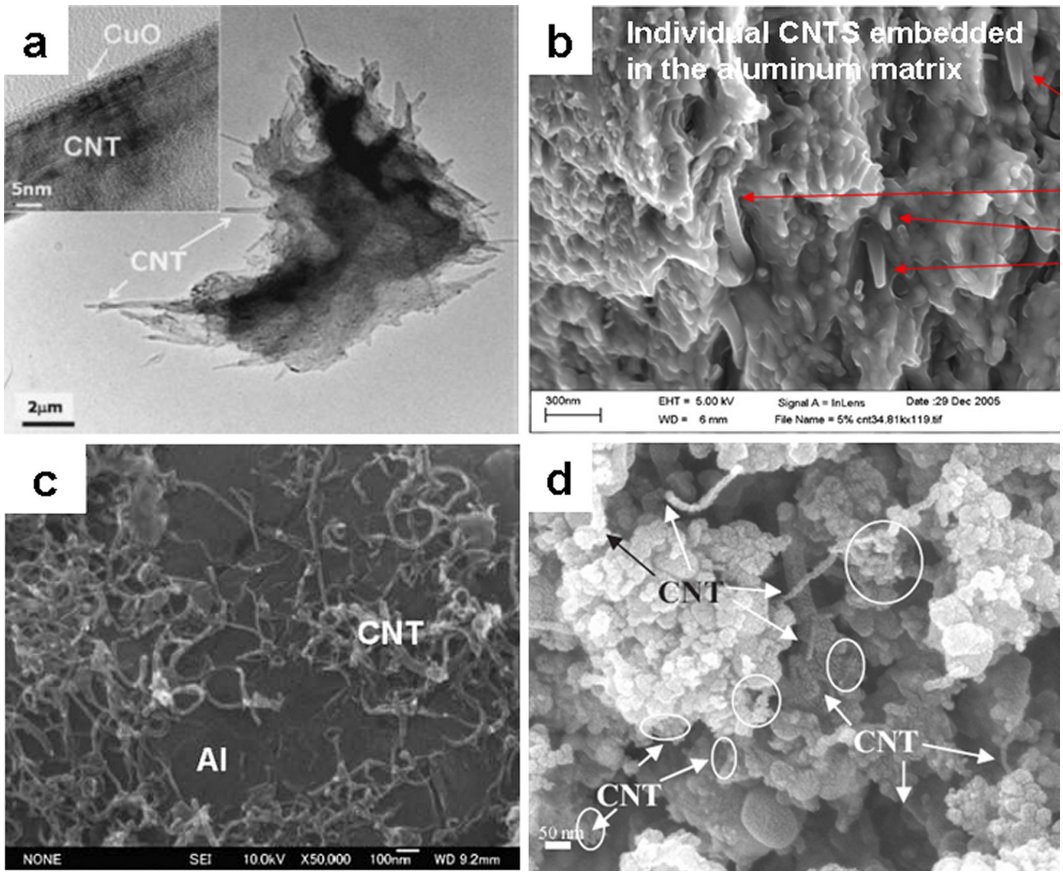

Fig. 2.11: a) TEM image of CuO/CNT powder prepared by molecular level mixing method [19], b) SEM image of the fracture surface of Al/CNT powder prepared by ball milling for 48 hours [22], c) SEM image of Al-5 wt.% CNT powder prepared by nanoscale dispersion method [31], and d) SEM image of CNTs grown on aluminum powder [21]

The methods suggested above have their own drawbacks. The NSD process leads to good dispersion of CNTs on the particle surface. So the level of dispersion is dependent on the particle size used. Ball milling leads to excellent dispersion but might result in the damage to CNTs. Molecular level mixing method might lead to oxide impurities due to incomplete reduction of the powders. While the quality of dispersion is important, the processes used should also be amenable for large scale production of powders.

Quantification of the degree or quality of CNT reinforcement is also important. It helps in comparing various microstructures and the effectiveness of various methods for dispersion of CNTs in composites. Dirichlet tessellation has been used in the quantification as well as to study the effect of dispersion in composite materials [184-186]. But there has been hardly any study in the quantification of dispersion in carbon nanotube composites. Majority of the researchers mention uniform CNT dispersion in the composites which is based on mere visual examination of the microstructure. Recently, Luo and Koo proposed a method based on the statistical distribution of horizontal and vertical separation distances between the peripheries of the particles/carbon fibers in a cross sectional image of the composite [187]. A lognormal distribution was found to fit the distribution obtained. Two parameters $D_{0.1}$ and $D_{0.2}$ were defined representing the probability that the values lied between $\mu \pm 0.1\mu$ and $\mu \pm 0.2\mu$ of the values respectively, μ being the average distance. The larger the values of $D_{0.1}$ and $D_{0.2}$ the better the distribution was since it means uniform separation of the filler materials. Recently, Pegel et al. [188] have used spatial statistics on TEM images of polymer CNT composite to study the variation of the area fraction of CNTs as a function of radius of the nanotubes. They show that the variation of the area and spherical contact distribution function

converged to 100% faster in case of clustered CNT configurations. Use of the above methods is very useful in differentiating processes based on their ability to disperse CNTs in the microstructure. However, there is a necessity to develop simpler methods for quantification of CNT distribution.

2.4.2. Interfacial Phenomena and Chemical stability of CNTs

Interfacial phenomena and chemical stability of the CNTs in the metal matrix is critical for several reasons. The fiber-matrix stress transfer [189] and the interfacial strength [53] play an important role in strengthening. The applied stress is transferred to the high strength fiber through the interfacial layer. So a strong interface would make the composite very strong but at the expense of ductility of the composite. A weak interface would lead to lower strength and inefficient utilization of fiber properties by facilitating pullout phenomena at low loads due to interface failure. Wetting of the fiber by the liquid metal is essential. Non-wetting will lead to poor interfacial bonding. Interfacial reactions leading to formation of interfacial phase can improve wetting if the liquid has a lower contact angle with the phase forming due to the reaction. A lot of work has been carried in reinforcing aluminum matrix with carbon fibers. Interfacial reactions and degree of wetting of the fibers have been shown to affect the properties of the composite [190-192]. Formation of aluminum carbide (Al_4C_3) has been observed at the interface in liquid metal infiltrated Al-Si alloy composites reinforced with carbon fibers containing 7 wt.% [193] and 13 wt.% Si [194]. Vidal-Setif et al. have shown reduction in the strength and premature failure of 75 vol.% carbon fiber reinforced A357 alloy due to formation of Al_4C_3 and presence of brittle Si particles [195]. So formation of Al_4C_3 needs to be

avoided. However, there have been reports of improvement of properties of Al-SiC_p composites due to limited amounts of Al_4C_3 [196]. In case of CNT reinforced aluminum composites, Kwon et al. suggest that the Al_4C_3 helps in load transfer by pinning the CNTs to the matrix [31]. The extent and nature of chemical reactions can be changed by either by controlling the chemistry of the matrix [197] or by using coatings on reinforcements [198, 199].

CNTs are expected to be quite stable chemically compared to carbon fibers due to their perfect structure. *Unless otherwise specified CNT in this section refers to multi-walled CNT.* It is obvious that reaction of single walled CNTs with metal leading to carbide formation would lead to destruction of the tubular structure. Comparison of the intensity of (111) peak of the XRD pattern of Cobalt, after a 10 hr annealing treatment with various forms of carbon at 1000^oC shows that the chemical interaction of layered graphite was the lowest followed by single walled CNT, multi-walled CNT and activated carbon in respective order [200]. Layered graphite has perfect structure of sp^2 hybridized carbon atoms arranged in ABABAB… stacking sequence which would make it less reactive chemically. Defects in activated carbon and in CNTs provide sites for chemical reactions to occur. Reaction of CNT with metal matrices leading to carbide formation has been observed by many researchers. In fact, Dal et al. have utilized reactions between volatile oxides/halides with CNTs as a means of synthesis of various carbide nanorods viz. TiC, NbC, Fe_3C, SiC and BC_x [201]. Shi et al. have synthesized WC-CNT composites by reduction and carbonization of WO_3 precursors produced after a molecular level mixing followed by calcination [202]. Kuzumaki et al. have observed formation of TiC in hot pressed Ti-CNT composites [28]. Ci et al. have shown the formation of Al_4C_3

on annealing CNTs, on which aluminum was deposited by magnetic sputtering process, at temperatures above the melting point of aluminum [37]. It was found that carbide formed at amorphous areas of CNT due to incomplete graphitization. The small size and amount of Al_4C_3 formed was due to the smaller availability of defective sites and amorphous carbon. The formation of carbide also depends on the processing techniques. Some researchers have reported no formation of Al_4C_3 in case of solid state processes like extrusion [30]. In our research group, Laha et al. has shown formation of SiC due to reaction between Al-23 wt.% Si alloy and CNTs [33]. SiC formation was justified based on the fact that its free energy of formation was lower than Al_4C_3. But when molten Al-Si alloy is in contact with CNTs the free energy of formations will depend on the activities of each constituent which was not taken into account. An in-depth study is required for the effect of Si content on interfacial reaction. A study on the chemical stability of CNT with temperature in Al (2024 alloy)-CNT composite has been carried out by Deng and co-workers [36]. They found no existence of CNT in the matrix when heated up to 1073K and XRD results show that CNT fully converts to Al_4C_3. Figure 2.12 shows the TEM images of CNT matrix interfaces in various composites. Different interfacial carbides may result in significantly different mechanical properties of the composites since the shear strength of the carbides determines the stress that could be transferred to the CNTs.

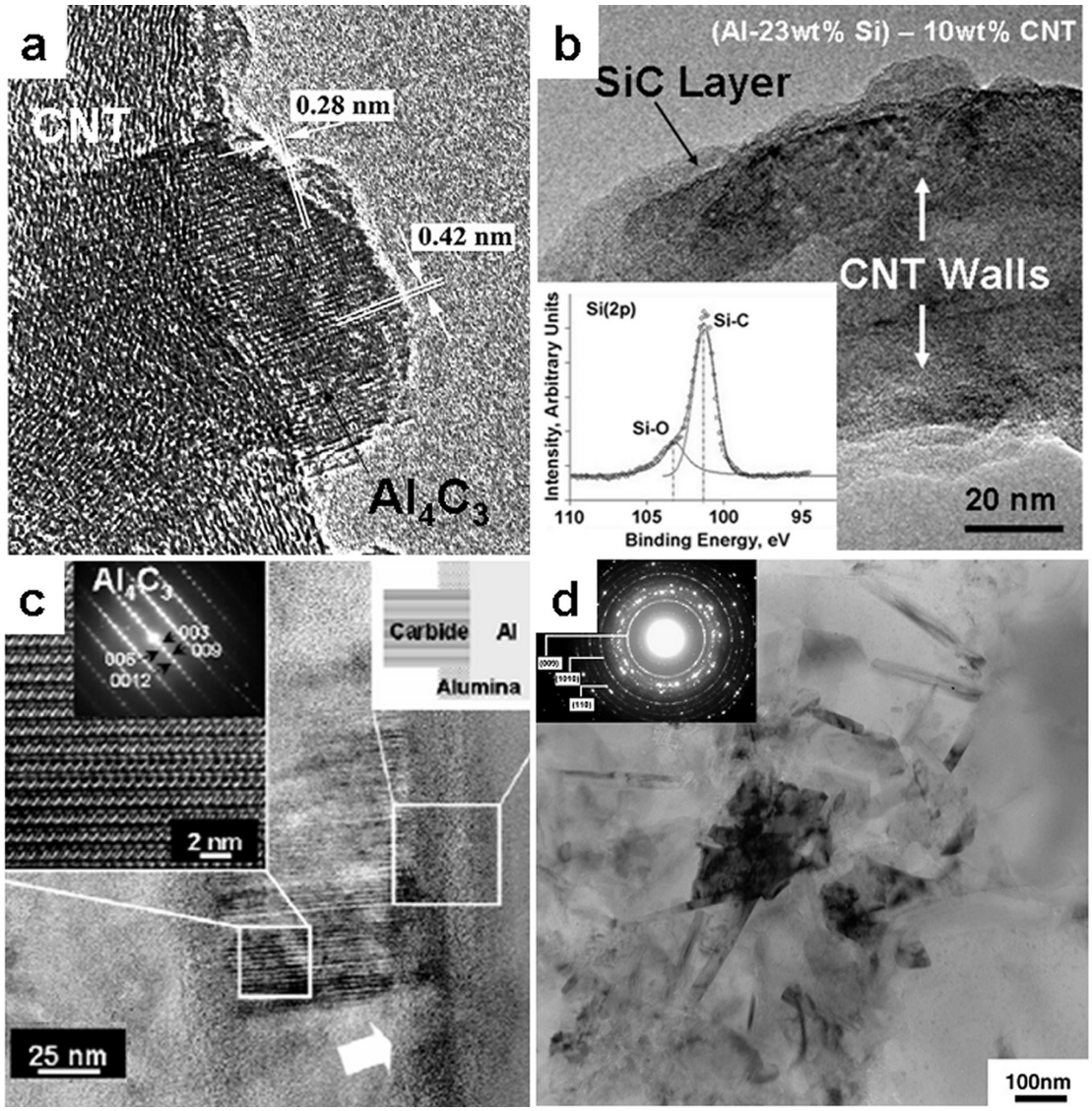

Fig. 2.12: TEM images of CNT-Matrix interface from various composite systems namely a) annealed Al-deposited on CNT showing Al_4C_3 [37], b) SiC layer in Al-23 wt.% Si composite containing 10wt% CNT [33], c) Al_4C_3 in composites obtained by hot extrusion of spark plasma sintered samples [31], and d) Al4C3 formation in a mixture of CNT and 2024 alloy heated to 1000K in DSC [36]

An important aspect of composite fabrication is wetting of the reinforcement by the liquid alloy. Wetting is related to the surface energies of the interacting species by the Young's equation and the Young-Dupre relation given below.

$$\cos\theta = \frac{\gamma_{SV} - \gamma_{LS}}{\gamma_{LV}} \qquad \text{Equation 2.1}$$

$$W_A = \gamma_{LV}(1 + \cos\theta) \qquad \text{Equation 2.2}$$

Here θ is the contact angle and γ_{SV}, γ_{LS} and γ_{LV} are the solid-vapor, solid-liquid and liquid vapor surface energies and W_A is the work of adhesion between the liquid and the substrate. Carbide nucleation and growth was discussed by Landry et al. [203] and it was applied to Al-23 wt.% Si composites reinforced with CNTs by Laha et al. [33] The critical thickness for carbide nucleation is given by the equation

$$t_{Crit} = -V_M \frac{\Delta\gamma}{\Delta G^f} \qquad \text{Equation 2.3}$$

Here V_M is the molar volume of the carbide formed, ΔG^f is the free energy of formation per mole of carbide and $\Delta\gamma = \gamma_{MC/CNT} + \gamma_{MC/Alloy} - \gamma_{Alloy/CNT}$ is the increase in total surface energy as a result of formation of new interfaces. MC stands for metal carbide. When carbide thickness reaches t_{Crit}, further growth is energetically favorable. This might result in the decrease in contact angle and improvement in wetting. Smaller t_{Crit} values therefore indicate easy formation of carbide as well as better wetting. The surface tension of CNTs (γ_{SV}) is 45.3 $mJ.m^{-2}$, which is similar to carbon fiber [204]. It has been shown that a liquid with surface tension between 100-200 $mN.m^{-1}$ results in good wetting with CNT [205, 206]. Molten Al-Si alloys have surface tension of ~800 $mN.m^{-1}$. Hence, it is expected that the wetting between Al-Si alloys and CNTs will be poor. It has been

experimentally observed in the sessile drop experiments by Landry and co-workers that Al-Si alloys do not wet graphite in the beginning and exhibit a large contact angle of ~160^o [203, 207]. Al_4C_3 and SiC formation reduces contact angle to 45^o and 38^o respectively. Hence, formation of interfacial carbides favors wetting which would promote infiltration of liquid melt into CNT performs. The reaction at the triple point between liquid alloy and CNT leads to formation of carbide and subsequent spreading of metal. Minimal reaction of CNT is desirable in order that efficient stress transfer can occur without much damage to the CNT structure.

2.4.3. Strengthening Mechanisms in MM-CNT Composites

The objective of addition of fibrous reinforcements like CNTs is twofold: (i) to increase the tensile strength and (ii) to increase the elastic modulus of the composite. Both these effects are due to the fact that the CNTs have higher stiffness and strength compared to the metal matrix. The mechanisms for enhancement of mechanical properties will be discussed below.

2.4.3.1. Tensile Strength of MM-CNT Composites

Understanding the strengthening mechanisms in fiber reinforced composite materials has been a focus of research for almost 50 years now. The shear lag models[208] used in case of conventional fiber reinforced composites have also been applied to CNT composites. The stress is transferred to the fiber (σ_f) via the interface and is related to the shear stress (τ_{mf}) between the fiber and matrix given by:

$$\frac{l_f}{D_f} = \frac{\sigma_f}{2\tau_{mf}} \qquad \text{Equation 2.4}$$

where l_f and D_f are the length and diameter of CNT respectively. CNTs with a larger aspect ratio will assist larger load transfer and hence efficient utilization of reinforcement. For a critical length l_c, the value of σ_f becomes equal to the fracture strength of CNTs. For nanotube lengths $l < l_c$, the fracture strength of the composite (denoted by superscript *Frac*) is given as

$$\sigma_c^{Frac} = V_f \sigma_f^{Frac} \left(\frac{l}{2l_c} \right) + V_m \sigma_m^{Frac} \qquad \text{Equation 2.5}$$

Choi et al [30] concluded that equation 2.5 holds good for Al-CNT composites prepared by extrusion of ball milled powders. Coleman et al. [53] reviewed the strengthening models for CNT composites. In case of MM-CNT composites, reaction with the metal matrix might lead to interfacial carbide product. The stress transfer to the CNT is then affected by the shear strength of the carbide phase. When the stress exceeds this value, the fracture occurs along the carbide layer leading to fiber pull out phenomena. Coleman et al. have derived the strength of the composite in the presence of an interfacial layer as follows[209]

$$\sigma_c = (1 + 2b/D)[\sigma_{Shear} l / D - (1 + 2b/D)\sigma_m]V_f + \sigma_m \qquad \text{Equation 2.6}$$

Where σ_{Shear} is the shear strength of the interface and b is the width of the interfacial layer and D is the diameter of CNT. Laha et al. [181] have found that the value of strength calculated by this formula (226 MPa) is quite large compared to experimentally measured value (83.1 MPa) which is due to reasons like porosity, uniformity of interfacial product, and clustering of CNTs which are not considered in the model. Kim et

al. have observed elongated clusters of CNT in the microstructure of Cu-CNT composites produced by spark plasma sintering of ball milled powders followed by cold rolling [67]. The stress-strain curve of the composite showed a two stage yielding process. Figure 2.13a shows the microstructure and 2.13b shows the corresponding stress strain curve.

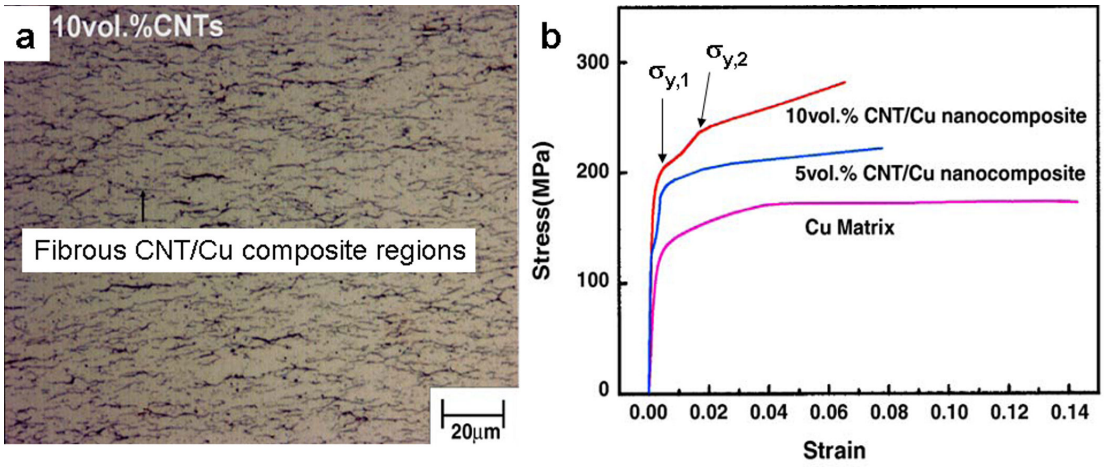

Fig. 2.13: a) Microstructure of CNT-Cu composites produced by spark plasma sintering and cold rolling and b) Stress strain curves showing two stage yielding process [71]

The first ($\sigma_{y,1}$) was matrix yielding and second ($\sigma_{y,2}$) yield strength was CNT cluster yielding and both could be modeled by following equations

$$\sigma_{y,1} = \frac{V_f \sigma_m}{2} S_{eff} + \sigma_m \qquad \text{Equation 2.7}$$

where $S_{eff} = S\cos^2\theta + \left(\frac{3\pi - 4}{3\pi}\right)\left(1 + \frac{1}{S}\right)\sin^2\theta$ is the effective aspect ratio of an elongated CNT cluster oriented at an angle θ to the loading direction. The average S_{eff} is given as

$$S_{eff}^{Av} = \int_{o}^{\pi/2} S_{eff}(\theta) F(\theta) (2\pi \sin\theta) d\theta \qquad \text{Equation 2.8}$$

Where $F(\theta)$ is the probability distribution function of the misorientation of the CNT/Cu clusters which was obtained by image analysis. The second yield stress is given as

$$\sigma_{y,2} = \sigma_{y,1}(1 - V_f) + \sigma_f V_f \qquad \text{Equation 2.9}$$

Yeh et al. [210] have shown that a modified Halpin-Tsai equations fits the properties of phenolic-based composites well which could be used for MMC-CNT composites too.

$$\sigma_c = \frac{1 + \xi\eta V_f}{1 - \eta V_f}\sigma_m, \text{ where } \eta = \frac{\alpha(\sigma_f / \sigma_m) - 1}{\alpha(\sigma_f / \sigma_m) + \xi} \qquad \text{Equation 2.10}$$

The coefficients ξ and α can be determined and are influenced by the degree of dispersion of the CNTs in the matrix. The properties of the CNT composites are also affected by nanotube waviness as suggested by some FEM simulations [211]. Strengthening due to dislocation generation by thermal expansion mismatch and precipitate strengthening by Orowan looping mechanism has been suggested as a mechanism of strengthening in Al-CNT composites [81] although observance of such mechanisms have not been made yet. But the most important factor in achieving the predicted theoretical strengths is uniform dispersion of CNTs in the matrix [19].

2.4.3.2. Elastic Modulus of MM-CNT Composites

Improvement in the elastic modulus of the composite is a result of the large tensile modulus of 350-970 GPa of CNTs [10]. Most of the research has been done on polymer CNT composites which can be applied to metal matrices too. Various

micromechanical models have been proposed to predict the elastic modulus of composite materials and they have been applied to CNT composites also [53, 186, 212, 213]. Some of the most commonly used models are discussed below. In the equations that follow, E stands for elastic modulus, σ stands for yield strength, V stands for volume fraction, *k* stands for bulk modulus, μ stands for rigidity modulus, ν stands for Poisson's ratio and the subscript *m* corresponds to matrix while *f* corresponds to fiber (CNT).

a) Combined Voigt – Reuss Model

The elastic modulus for randomly oriented fibre composites is given by

$$E = \frac{3}{8}E_{\parallel} + \frac{5}{8}E_{\perp} \qquad \text{Equation 2.11}$$

Where $E_{\parallel} = V_f E_f + (1 - V_f)E_m$ is the longitudinal modulus (along the direction of the fibers) and $E_{\perp} = \frac{E_f E_m}{E_f(1 - V_f) + E_m V_f}$ is the transverse modulus (along the direction normal to the fibers).

b) Cox Model

Elastic modulus of the composite according to this model is given by[212, 214]

$$E = \frac{1}{5}\eta_L E_f V_f + E_m(1 - V_f) \qquad \text{Equation 2.12}$$

Where $\eta_L = 1 - \frac{\tanh(\beta s)}{\beta s}$, $s = \frac{2l}{r}$, and $\beta = \frac{2\pi E_m}{E_f(1 + \nu_m)\ln(1/V_f)}$

Where *l* and *r* are the length and radius of the fiber reinforcement.

c) Halpin-Tsai Equations

Qian et al. [215] have used the Halpin-Tsai equations[216] to obtain the elastic modulus of randomly oriented fibre composites as follows:

$$E = \frac{3}{8}\left[\frac{1+(2l/D)\eta_L V_f}{1-\eta_L V_f}\right] + \frac{5}{8}\left[\frac{1+2\eta_T V_f}{1-\eta_T V_f}\right] \qquad \text{Equation 2.13}$$

Where $\eta_L = \frac{E_f/E_m - 1}{E_f/E_m + 2l/D}$, $\eta_T = \frac{E_f/E_m - 1}{E_f/E_m + 2}$ and l and D represent the length and diameter of the CNT respectively. Halpin Tsai equations have been found to closely predict mechanical property in case of small CNT concentrations in polymer and metal matrix CNT composites [53, 210, 217].

d) Hashin Strikman Model

This model based on variational principles[218, 219] provides the upper and lower bounds for the elastic modulus of a composite. It is independent of the shape of the particle. Laha et al. [32] found that experimental elastic modulus for Al-CNT composites prepared by PSF and HVOF and sintered for various times ranged between the upper and lower bounds.

e) Modified Eshelby Model

Chen et al. [220] have used modified Eshelby model to relate the properties in CNT composites to the volume fraction of CNTs as well as porosity. The longitudinal elastic modulus value is given by the formula

$$E_{11} = E_m \varepsilon_{11}^m \left(\varepsilon_{11}^m + V_f \varepsilon_{11}^{CNT}\right)^{-1} \qquad \text{Equation 2.13}$$

The values predicted by the model were higher than those observed experimentally which were ascribed to the poor bonding between CNT and matrix.

f) Dispersion Based Model

All the above equations assume that the CNTs are distributed uniformly which is seldom the case, especially at large concentrations. Recently, Villoria and Miravete[221] have developed a model to take into account clustering phenomena in CNT composites. They have developed a model to compute the properties of CNT clusters which could be applied to any type of fiber reinforcement where clustering is present. The overall properties of the composite are obtained by considering it as a dilute suspension of the clusters (properties with subscript *dsc*) in matrix.

$$k_{dsc} = k_m + \frac{(k_{Cluster} - k_m)c_c}{1 + \frac{(k_{Cluster} - k_m)}{k_m + 4\mu_m / 3}} \qquad \text{Equation 2.14}$$

$$\mu_{dsc} = \mu_m \left[1 - \frac{15(1-\nu_m)\left(1 - \frac{\mu_{Cluster}}{\mu_m}\right)c_c}{7 - 5\nu_m + 2(4 - 5\nu_m)\frac{\mu_{Cluster}}{\mu_m}} \right] \qquad \text{Equation 2.15}$$

Where c_c refers to the volume fraction of clusters which is related to the overall CNT fraction by $V_f = c_f . c_c$, c_f being the CNT concentration in of a cluster. This model has been shown to predict the values more accurately compared to Cox model in case of epoxy CNT composites [221].

2.5. Mechanical Properties of MM-CNT Composites

2.5.1. CNT Reinforced Aluminum

Kuzumaki et al. [29] were the first researchers to show a 100% increase in the tensile strength with 10 vol.% CNT addition. Deng et al. have reported a 41% increase in elastic modulus and 36% increase in tensile strength in 2024 alloy reinforced with 1 wt.% CNT prepared by cold pressing and hot extrusion [83]. On the contrary, Salas et al. [143] have reported deterioration in hardness in shock wave consolidated Al-5 vol.% CNT composite. Agglomeration of CNTs in the matrix and weak interface bonding led to drop in properties. CNT reinforcement to composite coatings prepared by Laha et al. [32, 35, 181] using thermal spraying methods, have been shown to improve the hardness by 72%, elastic modulus by 78%, marginal improvement in tensile strength and 46% decrease in ductility with 10 wt.% CNT content. Sintering (673 K, 72 hrs) of the sprayed coating has been reported to further increase the elastic modulus of the composite coating by 80%, which has been attributed to reduction in porosity and residual stress [158].

Noguchi et al. [20] have reported 350% increase in the compressive yield strength with 1.6 vol.% CNT addition, which, is due to a very homogeneous distribution of CNTs obtained by the nano-scale dispersion method. He et al. [21] have achieved 333% increase in hardness and 184% increase in tensile strength with 6.5 vol.% CNT addition in a composite prepared by using powders on which CNTs were grown by CVD technique [21]. Hence, it is clear that homogeneous distribution of CNTs and strong bonding with the matrix are the main areas to control the mechanical properties of the MM-CNT composites. The only report on wear properties of Al-CNT composite

processed through pressureless infiltration technique shows 22% decrease in COF and 25% decrease in the wear rate with 20 vol.% CNT addition [91].

2.5.2. Other metallic systems

Reports on Cu-CNT systems deal with improvement in mechanical as well as electrical properties. Powder metallurgy technique, comprising of compaction and sintering, helps increasing the hardness up to 20% with 15 vol.% CNT addition [77, 80].CNT reinforcement coated with Ni improved bonding with the Cu matrix and resulting in ~80-100% increase in the hardness for 9-12 vol.% CNT addition [17, 222, 223]. Spark plasma sintering (SPS) of Cu-10 vol.% CNT composite has improved the hardness by 79% with a further improvement up to 207% resulted from rolling of the SPS composite. This improvement is attributed to better dispersion and reinforcement induced by SPS and rolling [66, 67]. Molecular level mixing resulted in an improvement of 200% in the yield strength and 70% in elastic modulus. Cu-CNT composite, processed by cold rolling of sandwiched layers of metal and single walled CNT shows 8% improvement in tensile strength and 12.8% increase in elastic modulus [142]. Tu and co-workers [17, 103] have reported a maximum improvement of wear properties in a Cu-CNT composite processed through powder metallurgy technique using Ni-coated CNTs.. They have obtained 91% reduction in COF and 140% reduction in the wear rate with 16 vol.% CNT addition. Molecular level mixing technique has also helped improving the wear properties of Cu-CNT composite by resulting 76.9% decrease in wear loss with 10 vol.% CNT addition [68].

C.S. Chen et al. [128] and X. Chen et al. [122] have reported the maximum improvement in the hardness by 68% for the Ni-CNT composite coating deposited by electroless technique. Deng and co-workers have reported improvement of hardness of the electroless composite coating by 44% with addition of 2 vol.% CNT. [118, 132] On the contrary, Chen et al. [124] have reported to improve the hardness by only 11% with 12 vol. % CNT addition. This might have been caused by agglomeration of CNT in the bath due to increase in concentration. Shen et al. [133, 134] observed an extraordinary 300% improvement in the hardness and elastic modulus of Ni-CNT composite coating prepared by electroless deposition technique for MEMS application. The improvement in mechanical properties is attributed to the acid oxidative method used for surface modification of the CNTs that keep them dispersed and suspended uniformly in the bath and in the coating. Sun et al. [108] achieved a significant increase in the ultimate tensile strength of 320% for SWCNT and 270% for MWCNT addition in electro-deposited Ni films. Deng and his group [118, 132] have reported a maximum of 83% decrease in the wear volume for electroless plated Ni-P-CNT composite coating with 2 vol.% CNT content, whereas the coefficient of friction (COF) reduced by 60%. It has been noted that COF continues decreasing with increasing CNT content in the composite but the wear rate starts increasing after a critical concentration [17].

Number of reports on Mg-CNT composite is fewer as compared to Al, Cu and Ni-CNT composites. Some of these studies are restricted to effect of CNT addition on hydrogen storage properties of the composite [63]. Li et al. [88] have reported a maximum of 150% increase in the tensile strength of the Mg-CNT composite with 0.55 vol.% CNT prepared through melting and casting route. Such high increase in mechanical

properties is attributed to Ni-coating on CNTs before addition which helps in improving wetting with the matrix. Morisada et al. [145] have prepared Mg-CNT composite through friction stir welding and reported 90% increase in hardness, though the CNT concentration and its gradient is not mentioned. Goh et al have reported 15% increase in yield strength for 1 vol. % CNT composite prepared through casting route [24]. They have also studied to fatigue behavior of Mg-CNT composite to find out that CNT addition decreases number of cycle to failure [90]. A recent study on Mg- 0.1 wt% CNT composite through casting route have reported 36% increase in the compressive strength [25].

Ti-CNT composite, produced by powder metallurgy, shows 450% improvement in the hardness and 65% increase in elastic modulus, though the CNT content of the composite was not mentioned [28]. Zeng and colleagues also have observed 200% increase in the hardness of Ti-Ni shape memory alloy with 4.5 wt.% CNT addition [224]. Researchers have used CNTs as reinforcement in bulk metallic glasses (BMG) also. Ti-based BMG-CNT composites, processed by powder metallurgy, have shown 53% increase in hardness [75, 76]. CNT reinforced Zr-based BMG prepared by melting and casting technique, show ~10% improvement in hardness and elastic modulus [23, 87]. Kumar et al. [225] have achieved 50% increase in tensile strength for their soldering alloy with only 0.01 wt.% SWCNT content. Pang and co-workers have reported 30% and 11% increase in hardness and compressive strength, respectively, of Fe_3Al intermetallic, with 3 wt.% CNT addition through powder metallurgy[70, 74].

Figure 2.14 plots the improvement in the mechanical properties for various MM-CNT systems. It is observed that novel techniques seem to be more successful in

improving mechanical properties of the composites due to improved dispersion and interface bonding. In general, there is lot of scatter in data and there is poor correlation between CNT content and improvement in mechanical property which is due to presence of defects induced by various processing techniques and lack of uniformity in mechanical testing methods.

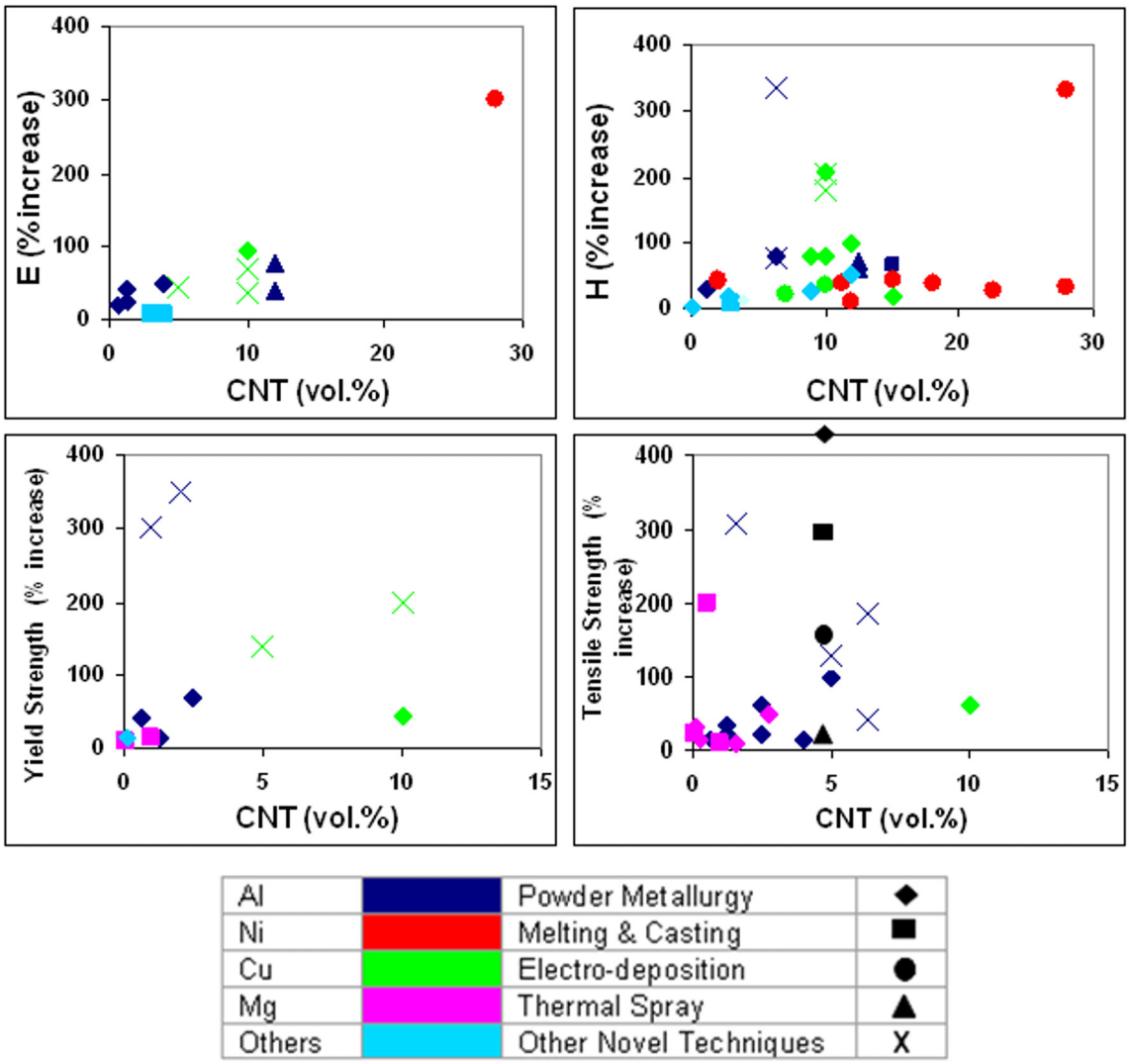

Fig. 2.14: Improvement in mechanical properties of different MM-CNT composites as a function of CNT content classified depending on processing routes employed

Most of the mechanical property data reported on CNT reinforced nanocomposites has been based on microhardness, nanoindentation, miniaturized sample or computational theories. Though CNTs have excellent properties, but the nanoscale properties are not translated into bulk mechanical properties of the composite. Inhomogeneous CNT distribution and insufficient CNT metal bonding are some of the reasons and these are affected by the processing techniques. Kuzumaki et al [29] obtained the yield strength of 80 MPa for 5-10 vol% CNT whereas Deng et al. [84] reported yield strength of 336 MPa for mere 1 wt. % CNT addition to Al matrix. It is evident that the tensile properties of CNT reinforced aluminum composites synthesized by different processes display a wide scatter in the mechanical properties attributed to the variance in the microstructural features, defects, porosity level caused by processing and lack of consistency in mechanical testing techniques and samples.

2.6. Other Properties of MM-CNT Composites

Owing to excellent electrical properties, evinced by the current carrying density of $\sim 4 \times 10^9$ A.cm^{-2} (three orders of magnitude higher than Cu or Al),[226] CNTs have been used for enhancement of electrical properties. Al- 12.5 vol.% CNT composite prepared by powder metallurgy [26] displayed increased electrical resistivity by 66%. Authors have also reported an abrupt drop in resistivity to almost '0' at 80K– though no suitable explanation for this behavior was provided. A recent study by Yang et al. [110] shows that the electrical resistivity of Cu-CNT composite remains same as that of pure Cu, up to 10 vol.% single walled CNT addition. The observation by Feng et al. [60] for Ag-CNT

composites also shows marginal increase in the electrical resistivity up to 10 vol.% CNT addition. The sharp increase in the electrical property beyond 10 vol.% CNT is attributed to the increase in interfacial area and strain in the matrix due to presence of CNT cluster – both of which hinders electron transfer through the composite.

CNTs are known to have very high thermal conductivity[18] of 1812 ± 300W/mK and very low coefficient of thermal expansion [85] (CTE) ~ 0. Hence, MM-CNT composites have a great potential to be used for thermal management. Tang and co-workers [16] reported 63% decrease in CTE with 15 vol.% CNT addition to Al matrix. Further increase in CNT content increases CTE, which has been attributed to the agglomeration of CNTs. Deng et al. [85] have obtained 12% reduction in CTE with 1.28 vol.% CNT addition in Al, which has been attributed to the larger surface area of CNTs that creates larger interface and thus restricts thermal expansion of the metal matrix. Goh et al. [90] have shown the gradual decrease in CTE of the Mg matrix composite with CNT addition up to 0.30 wt. % where the CTE is decreased by 9% of the base material. Increase in the thermal conductivity of Ni- 0.7 wt.% CNT composite by 200% with has been attributed excellent dispersion and bonding of CNTs forming defect free interface with matrix by electro-deposition technique. W-Cu alloy also shows 27.8% increase in thermal conductivity with 0.4 wt.% CNT addition [18]. Ngo et al. [116] and Chai et al. [114] have shown decrease of thermal resistance by ~ 62% when Cu is filled up in the voids of CNT arrays.

Another important effect of CNT addition is on corrosion resistance. Most of the corrosion studies are preformed on electrodeposited Ni-CNT composite coatings [62, 63, 100, 109, 125, 126] with a single study on Zn-CNT composite coating [227].

Electrodeposited coatings are more prone to corrosion due to the presence of pores and voids. All the studies have shown increase in the corrosion resistance of the composite coatings with CNT addition. Yang et al. [125, 126] have reported increase in pitting potential by 24% with 5 wt.% CNT addition, whereas, Chen and colleagues [100] have reported a 75% increase of the same without mentioning CNT content. Chen et al.[103] have also measured the corrosion rate of the composites to be 5 times lower than the Ni coating. Praveen et al. [227] have reported the service life of Zn-CNT composite to be more than double of that of only Zn coating. All these studies indicate the improvement in corrosion resistance due to two reasons. Firstly, the chemical inertness of the CNTs that helps forming a passive layer on the coating surface. Secondly, CNTs help filling up voids and pores of electrodeposited coatings leaving no place for initiation of localized corrosion.

Hydrogen storage capacity has been studied for MM-CNT composites by very few researchers. Chen et al. [63] reported the effect of CNT content on the hydrogen storage capacity of Mg-CNT composite. Mg-CNT composite has better hydrogen storage capacity and absorption-desorption rate than other hydrogen storage materials. At higher temperatures, composite with 5 wt.% CNT shows better hydrogen storage capacity than 20 wt.% CNT, which has been attributed to the breakage and amorphous carbon content of the CNTs in the latter. However, Huang and co-workers [62] did not observe any improvement in hydrogen storage capacity of Mg-based composite with addition of CNT over carbon black and graphite. Ishihara et al. [150] have reported large hydrogen storage capacity of Si-CNT composite material formed by chemical vapor deposition of

tetramethylsilane. Research about the hydrogen storage capacity of metal matrix -CNT composites is at an early stage with very little available information [46].

It is observed that efforts to develop MM-CNT composites have significantly increased in last 5 years. Several novel methods have been developed to address the issues like obtaining uniform dispersion of nanotubes. In this research work, novel CNT dispersion method by spray drying has been used for developing high strength Al-CNT coatings and bulk structures. The details of the experimental methods used will be described in the next section.

3. EXPERIMENTAL PROCEDURE

This section focuses on the processing details for synthesis of the CNT reinforced aluminum coatings and bulk structure. The various characterization techniques and the respective equipment used for obtaining information on microstructure and mechanical properties are also described.

3.1. Powder Feedstock

The powder feedstock characteristics are very important for thermal spraying as it determines the coating properties. Powder characteristics like particle size distribution, particle shape and phase composition determine many aspects like flowability of the powder, temperature and velocity attained by the powder and the degree of melting of the powder.

3.1.1. Materials

Aluminum – silicon (Al-Si) eutectic alloy powder of composition Al – 11.6% Si - 0.14% Fe by weight obtained by inert gas atomization process and having a mean particle size 2.4±1.2 μm (D90 = 3.8 μm) was obtained from Valimet Inc. (Stockton, CA, USA). These fine sized Al-Si powders were utilized for spray drying as described in next section. Gas atomized Al-Si powder of the same composition as above but particle size 14 ± 9 μm (D90 = 26 μm) was used for fabrication of pure Al-Si coating without any nanotubes and will be referred to as Al-Si hereafter. Al powder of purity 99.7% and particle size 26±13 μm were obtained from Alpoco (Minworth, UK). Multiwalled carbon

nanotubes (CNT), obtained from Inframat Advanced Materials (Willington, CT, USA), had a purity of more than 95% and diameter of 40-70 nm and length 1-3 μm.

3.1.2. Spray Drying

Spray drying process transforms a feed of liquid or slurry material (solution, dispersion or paste) into a dried particulate agglomerate by spraying the feed into a hot drying medium. Figure 3.1 shows a schematic of the processes.

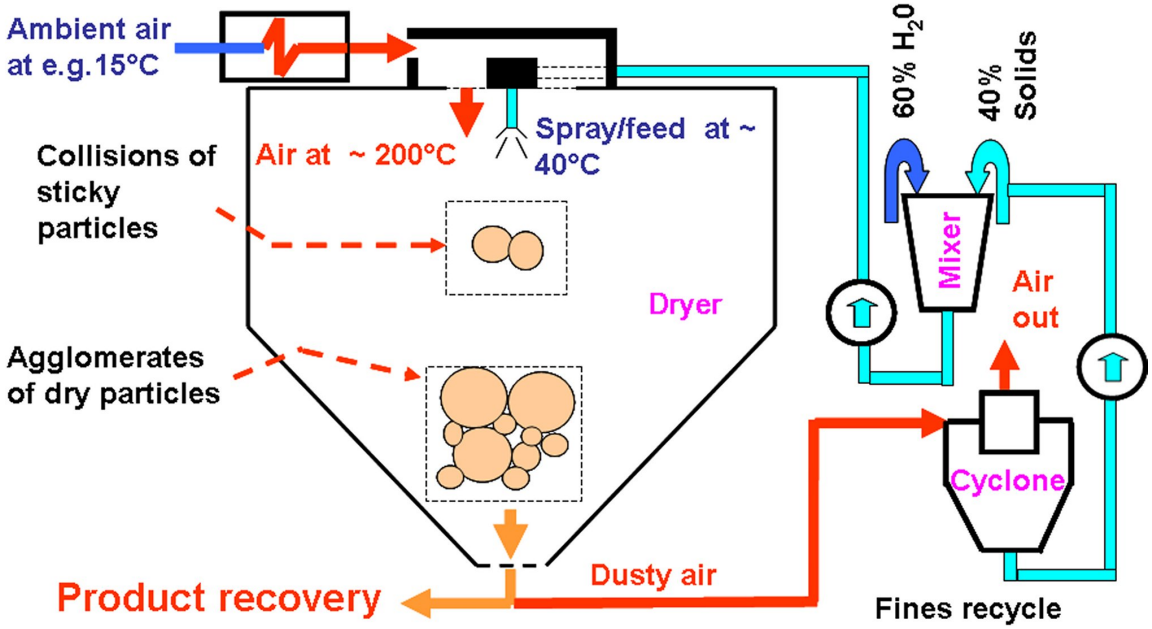

Fig. 3.1: Schematic of spray drying process

Spray drying is a very popular technique in food and pharmaceuticals industry. Spray dried powders are usually spherical in shape and thus have good flowability. Balani et al.

from our research group has used spray drying to disperse CNTs in nanocrystalline aluminum oxide particles [228]. Uniform dispersion of CNTs in the powders was observed. Spray drying has not been used for dispersing CNTs in metallic powders. In the present work, an aqueous slurry is made with the fine size Al-Si powders and CNTs with a little amount of poly vinyl alcohol (PVA) as binder. Two compositions containing 5 wt.% CNT and 10 wt.% CNT were prepared. The slurries are then subjected to spray drying which results in formation of agglomerated powder particles. The resulting agglomerates were named SD Al-5CNT and SD Al-10CNT powder based on their CNT content. The agglomerated powders are utilized for coating fabrication. Spray drying was performed at a commercial facility Inframat Advanced Materials (Farmington, CT, USA).

3.2. Plasma Spraying of Al-Si-CNT Coatings

3.2.1. Coatings

The agglomerated Al-Si-CNT powders (SD Al-5CNT and SD Al-10CNT) were used for plasma spraying to obtain coatings on the mild steel substrate. The substrate was grit blasted in order to make it rough for the coating to stick. A Praxair SG-100 gun (Praxair Inc., Danbury, Connecticut, USA) was used. Powders were internally fed in radial direction into the plasma. Figure 3.2 shows a schematic of the gun. It has a thoriated tungsten cathode (Part # 02083-730) and a concentric copper anode (Part # 01083A-720). Table 3.1 shows the plasma processing parameters. The powder feed rate was calculated by spraying without the plasma power switched on and collecting the powder in a bag. The gun was mounted on a Velmex robot which was programmable

using software. Several passes were carried out to generate the coating of desired thickness. Coatings obtained from Al-Si, SD Al-5CNT and SD Al-10CNT powders are named as Al-Si, Al-5CNT, and Al-10CNT coatings respectively.

Table 3.1: Plasma processing parameters for the coating synthesis

Item	**Type**	**Quantity**
Plasma gas	Argon	40 psi (42.5 SLPM)
Secondary gas	Helium	80 psi (30.5 SLPM)
Carrier gas	Argon	30 psi (11.9 SLPM)
Stand off distance	-	4 in (100 mm)
Plasma power	-	~22 kW (550 Amps 40 Volts)
Powder feed rate	Praxair 1264 feeder	Al-SI: 12 $g.min^{-1}$, SD Al-5CNT: 7 $g.min^{-1}$ and SD Al-10CNT: 6 $g.min^{-1}$

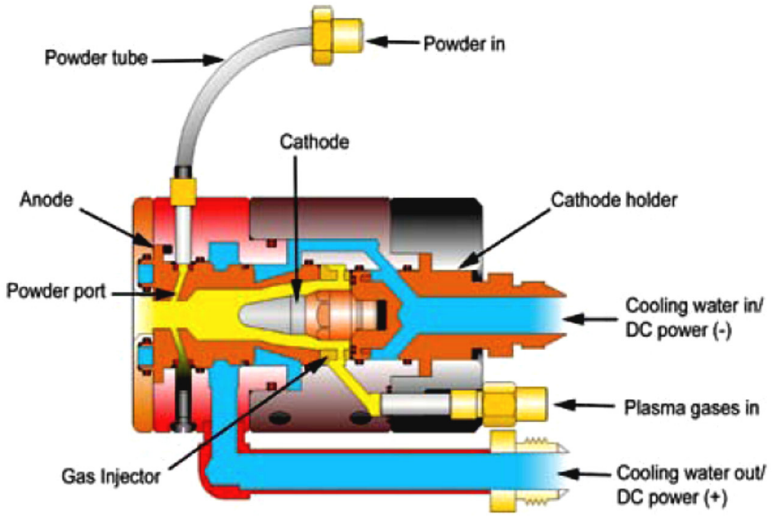

Fig. 3.2: Schematic of the SG-100 plasma spray gun

3.2.2. Single and Multiple splats

Molten droplets form splats on impacting the substrate. It is very important to understand the microstructure of the single and multiple splats in order to understand the evolution of the coating microstructure. Single splats from individual powder agglomerate were obtained by making a single sweep of the plasma gun on a glass substrate. The plasma parameters were kept same as that for the coating so that splats were representative of those present in the coating.

3.2.3. Near Net Shape Fabrication

One of the aims of the study was to fabricate the bulk near net shape CNT composites using plasma spraying. Mechanical testing of bulk samples will provide the insight into over all effect on properties due to CNT addition. Bulk cylinders were fabricated by plasma spray forming (PSF) on a rotating mandrel using the same processing parameters as in table 3.1. The spraying time was up to 20 minutes which led to the formation of 5 mm thick coating on the mild steel pipe used as the mandrel. The pipe surface was grit blasted prior to deposition of coating.

3.3. Cold Spraying of Al-CNT Composites

Cold spraying experiments were carried out at the University of Nottingham, Nottingham, UK, which has an in-house built system comprising a high pressure gas supply, high pressure powder feeder, a converging-diverging nozzle and a X-Y traverse unit [229]. Figure 3.3 shows a picture of the cold spray set up.

The powder feeder used was a Praxair 1264HP (Praxair Surface Technologies, Indianapolis, IN) which has a maximum pressure capability of 3.4 MPa.

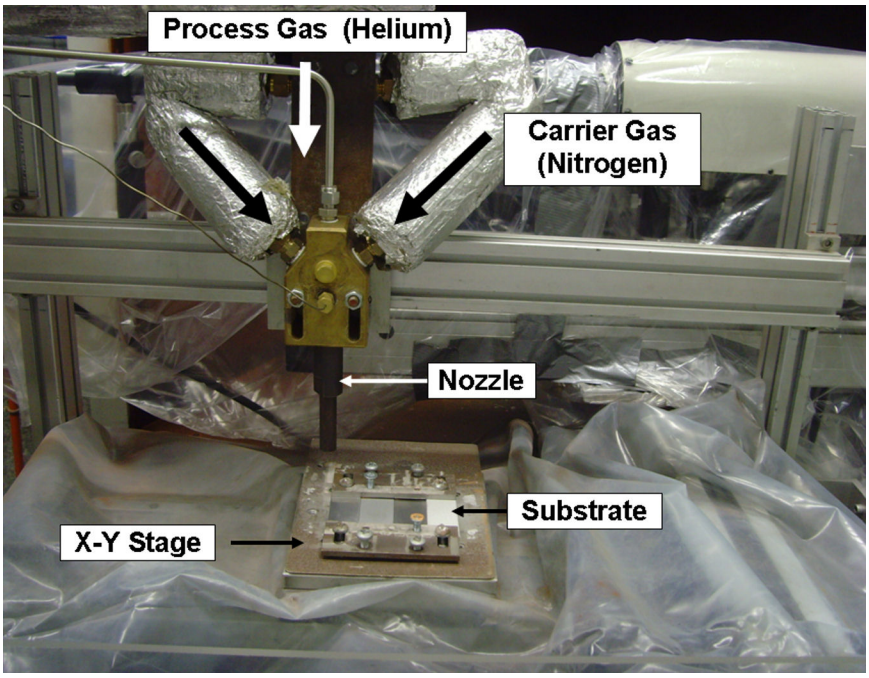

Fig. 3.3: Picture of the cold spray nozzle set up

Helium gas was used as the main gas and for the current work, a main gas stagnation pressure of 2.9 MPa was employed. Nitrogen gas was used as the powder carrier gas and the pressure was kept 0.1 MPa higher than that of the main gas in order to facilitate the injection of the powder into the jet. The nozzle was fixed to a frame and the substrate was fixed onto an X-Y traverse table, the movement of which was programmable using a computer. Cold spraying was carried out with various powder mixtures given below in Table 3.2. Eight layers were sprayed to build up the coating thickness. The substrate used was 6061 aluminum alloy which was grit blasted prior to spray deposition.

Table 3.2: Composition of powder blends used for cold spraying

Powder Mixture	Coating Nomenclature
Pure Al	Al
Al-Si + 10wt.% SD Al-5CNT	Al-Si-0.5CNT
Al-Si + 20wt.% SD Al-5CNT	Al-Si-1CNT
Pure Al + 10wt.% SD Al-5CNT	Al-0.5CNT
Pure Al + 20wt.% SD Al-5CNT	Al-1CNT

3.4. Microstructural and Phase Characterization

In this section, the procedure for various microstructural and physical property measurement methods will be outlined.

3.4.1. Density Measurement

Density was measured using the water displacement method which works on the Archimedes principle. This method gives the apparent density of the sample which takes into account the closed porosity present in the sample. The density of calculated using the following

$$\rho_{app} = \frac{X}{X - Y}$$

Where ρ_{app} is the apparent density in $g.cm^{-3}$, X is weight of the sample in air and Y is the weight of the sample when immersed in water. Special care is taken while measuring Y, since it takes time for water to fill into the open pores. Sufficient time was allowed for the

weight to stabilize before noting the value. Also samples were taken as large as possible so that errors in measurement had little effect on the values. A Denver instruments microbalance with a precision of 1 mg was used.

3.4.2. Optical Microscopy

To examine and study the microstructure of the cross sections of cold sprayed Al-CNT composite coatings, samples were cut using a high speed cutting saw and were mounted in hot mounting resin. They were then ground and polished to a 0.1 μm finish using colloidal silica. For examination in an optical microscope they were etched in Keller's reagent (5 ml HNO_3, 3 ml HCl, 2 ml HF and 190 ml H_2O). Porosity was determined from the optical micrographs of the polished cross-sections of the coatings by calculating the fractional area occupied by the pores. A total of seven micrographs at magnifications ranging from 100x to 400x were analyzed using image analysis software Image J. For plasma sprayed composites, samples were prepared by grinding and polishing up to a 0.1 μm finish using diamond suspension. Samples were etched with Keller's reagent before observing under the microscope.

3.4.3. X-ray Diffraction

X-ray diffraction was carried out to study the phase composition of the sprayed coatings. Coating top surfaces were ground using a 600 grit paper to remove the top layer. XRD was carried out using CuKα (λ=1.542Å) radiation in a Siemens D-500 X-ray Diffractometer operating at 40kV and 20mA at a scan rate of 1.2 deg./min. XRD was carried out only for plasma sprayed coatings since there was no scope for phase changes

in cold sprayed samples. The peaks obtained were matched with Al, Si, Al_2O_3, SiO_2, Al_4C_3, SiC and various aluminum silicon carbides and aluminum silicon oxy-carbides to see what phases were present in the coating. Phase fractions were calculated by taking the ratio of the sum of the area under the X-ray peak for all peaks of a phase to the total area under the XRD plot.

3.4.4. Scanning Electron Microcopy (SEM)

SEM was carried out to study the powder and CNT morphology and particle size distribution. SEM was also used to study the coating cross sections. The main use of SEM was in studying the fracture surfaces of the coatings and tensile specimens fabricated out of them. The large depth of focus of SEM at low magnifications makes it the only technique to obtain information from rough fracture surfaces on the mechanisms of failure of the composite. The large depth of focus also helps in getting good images of the powders for determination of particles size distribution while optical images are always blurred and inaccurate. Coating fracture surfaces were prepared by breaking a part of the coating under tension. Some of the microscopy for cold sprayed coatings and powder morphology were carried out using a FEI XL 30 FEG – SEM. All the SEM characterization of plasma sprayed coatings and some of the cold sprayed coatings were carried out using a JEOL JSM 630OF FEG-SEM. Samples were sputter coated with gold for 30 sec prior to investigation inside SEM to avoid artifacts due to charging.

3.4.5. Transmission Electron Microscopy (TEM)

TEM is very important characterization tool for CNT reinforced composites. It gives information on the structure of CNTs. The mechanical damage to CNTs can be studied using high resolution TEM images. Lattice fringe images show the reactions occurring at CNT metal interface. . Selected area diffraction images can be obtained to identify and confirm the crystal structure of various phases obtained. A Philips/FEI Tecnai F30 field emission gun transmission electron microscope (TEM) operating at an accelerating voltage of 300 kV was used to study the high resolution microstructure of the matrix and the nanotubes. The samples for TEM were in the form of a 3 mm disc, which were punched from the coating less than 100 μm thick prepared by grinding on a 600 grit abrasive paper, followed by dimpling at the center using a dimple grinder (Model 656 Mk3, Gatan, Inc., CA, USA). The final thinning was carried out by twinjet polishing (Model 110, E.A. Fischione Instruments, Inc., PA, USA) using a 30 vol.% mixture of 6N HNO_3 in ethanol as the electrolyte until a hole was formed.

3.4.6. Raman Spectroscopy

Raman spectroscopy has emerged as a very important technique for studying CNTs in composites. Raman spectra originate due to the interaction of radiation with the vibrational modes of a molecule. It is very weak and the Raman intensity is around 10^{-5} to 10^{-7} of the incident beam. Incident beam energy is reduced by the atomic bond vibrational energies characteristic of the molecule and the reflected beam consists of beams which have wavelengths shifted by the amount characteristic of the bond vibration. The intensity of the reflected radiation can be plotted against the shift in the

wave number compared to incident wave. This plot known as Raman spectra provides lot of information on the species present in the sample and stress state of the CNTs. Micro-Raman spectroscopy was carried out in the backscattering mode using an Argon ion laser of wavelength 514.5 nm and 18 mW to compare CNT structure in powder and coating. The spot size is typically 5 μm. Thus, this technique enables study of Raman spectra from various microstructural features like CNT clusters.

3.5. Mechanical Property Testing

3.5.1. Vickers Microhardness

Increase in the hardness of the composites reflects the resistance to plastic deformation and provides an idea about the strengthening due to addition of CNTs. Microhardness measurements were made on metallographically polished coating cross sections. Microhardness measurements on cold sprayed coatings were made using a LECO M-400 microhardness tester. A load of 200 g and a dwell time of 15 sec were chosen so that the indent formed was of sufficiently large size so that hardness values represented the average values. Microhardness of the plasma sprayed coatings was measured using a Vickers microhardness Tester (Shanghai Taiming Optical Instrument Co. Ltd., model HXD-1000 TMC, Shanghai, China). A load of 200 g was applied for a dwell time of 15 seconds for the purpose. The average value of at least 6 indents was reported.

3.5.2. Nanoindentation

Nanoindentation technique is a relatively new technique which has been brought about by the advancements in precision measurement of forces and displacements in the range of few micro-Newtons and nanometers respectively. In nanoindentation, the load and depth of penetration are recorded during loading and unloading. Figure 3.4 shows the indent formed underneath a Berkovich tip and the typical load displacement curve. Oliver and Pharr have proposed a simple method to for calculating the reduced elastic modulus and hardness from the initial slope of the unloading portion of the curve [230].

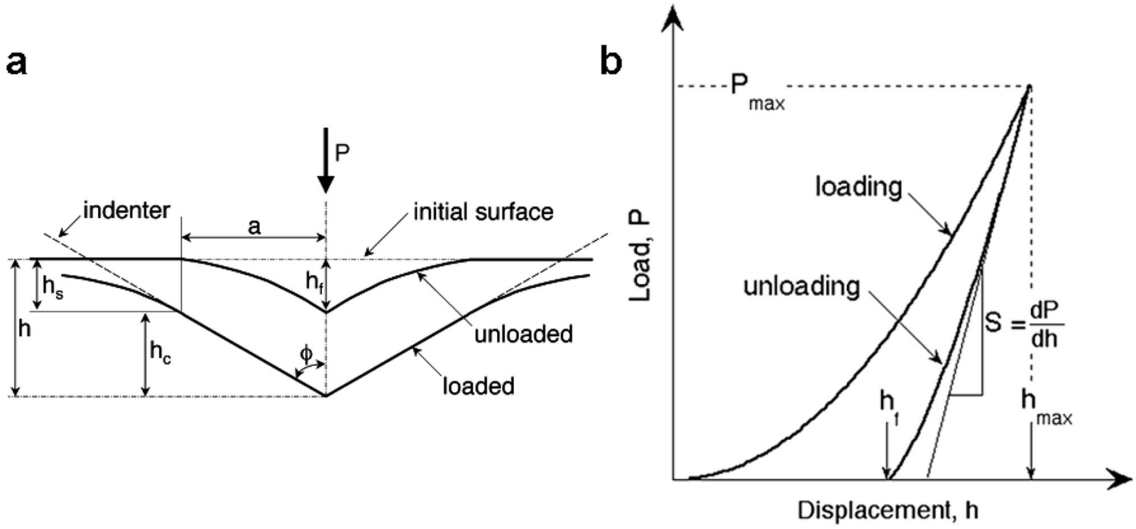

Fig. 3.4: a) Schematic of the indent formed by a Berkovich tip, and b) typical load depth curve obtained in nanoindentation

We have

$$h_c = h_{\max} - h_s = h_{\max} - \varepsilon \frac{P_{\max}}{S} \qquad \text{Equation 3.1}$$

where ε is is a constant that depends on geometry (ε = 0.72 for conical, 0.75 for paraboloid of a revolution and 1 for flat punch) and S is the slope of the unloading portion of the curve at maximum load. The reduced modulus and hardness are given by the following equations:

$$H = \frac{P_{\max}}{A} \qquad \text{Equation 3.2}$$

$$S = \beta \frac{2}{\sqrt{\pi}} E_r \sqrt{A} \qquad \text{Equation 3.3}$$

where H and E_r refer to hardness and elastic modulus and β is a correction factor close to unity.

The nano-mechanical properties were measured by carrying out nanoindentation using a Hysitron Triboindenter TI 900 (Hysitron Inc., Minneapolis, MN, USA). A Berkovich type diamond indenter having tip radius of 100 nm was used. Nanoindentation was carried out on polished cross section of both coatings. For cold sprayed coatings, indentations were carried out at a load of 600 μN. The load function comprised a linear increase in load up to 600 μN in 10 s followed by a 10 s halt at maximum load and followed by a linear decrease in load to zero in 10 s. A matrix of 7 x 7 indentations (49 indents) was made for cold sprayed for Al-0.5CNT coating. Each indent was 10 μm apart. Hence these values are obtained from an area of 70 μm x 70 μm. A matrix of 5 x 5 indentations (25 indents) representing an area of 50 μm x 50 μm was made for Al-1CNT coating. Fewer indents were made for the Al-1CNT coating because there was a lower spread in the values. For the plasma sprayed coatings, indentations were carried out at loads of 2000 μN, 3000 μN and 4000 μN. The load was applied linearly up to the

maximum load in 5 s followed by a halt of 2 s at the maximum load followed by unloading in 5 s. Nine indents were made for each load on the matrix part of the nanocomposite coating, which makes it a total of 27 values of hardness and elastic modulus per sample. It was found that the results were consistent and nine values at each load were sufficient to generate an average value for the properties.

Scanning probe microscopy (SPM) images of the indent were obtained using the same Berkovich tip by rastering over the surface with a contact load of 2 μN. The resultant scanning probe microscopy (SPM) images were analyzed using the SPM image processing software SPIP^{TM} (Image Metrology A/S, Horsholm, Denmark).

3.5.3. Nanoscratch Testing

Nanoscratch testing was also carried out on the polished cross sections using Hysitron Triboindenter TI 900 (Hysitron Inc., Minneapolis, USA). It has a horizontal capacitive transducer for applying normal load and two vertical capacitive transducers for measuring the lateral force experienced by the indenter during scratching. From plasma sprayed coatings, scratches of length 20 μm were made at loads of 1000, 2000 and 3000 μN using a Berkovich tip. During the loading cycle, the indenter moves 10 μm to one side of the mean position after which the load is applied. During this movement the indenter records the surface profile from which the tilt of the sample is measured. The correct instantaneous depth is obtained by subtracting the tilt from the measured values. After the load has reached the set value, the indenter starts scratching at a speed of 0.67 μm s^{-1}. When the scratch length has reached 20 μm, the load is released. The Berkovich tip is in the form of a triangular pyramid with total included angle of 142.3^{o} and has a tip

of radius of curvature equal to 100 nm. After the scratching has been performed, the same tip was used to image the surface by applying a contact load of 2 μN. The resultant scanning probe microscopy (SPM) images were analyzed using the SPM image processing software SPIP^{TM} (Image Metrology A/S, Horsholm, Denmark). Depth profiles were taken along lines parallel and perpendicular to the scratch using SPIP^{TM}. The scratches were also examined using a JEOL JSM 630F scanning electron microscope employing a field emission electron gun in the secondary electron imaging mode. For cold sprayed samples, 10 μm scratches were made using a Berkovich tip at a load of 1000 μN.

3.5.4. Bulk Tensile Testing

Samples for tensile testing were machined out from the bulk cylindrical samples fabricated by plasma spray forming. Tensile specimens (all dimensions in mm) were machined along the axis as shown in Fig. 3.5 using wire electro-discharge machining (EDM). The spray direction was perpendicular to the axis of the specimens. Tensile samples were obtained from plasma-sprayed Al-Si, Al-5CNT and Al-10CNT cylinders. Tensile tests were carried out using an MTS model 858, servo-hydraulic test system. Hydraulic wedge grips were used to clamp the sample. The tests were run at a constant crosshead rate of 0.0085 mm.s^{-1}. The engineering stress in the sample was calculated by dividing the load by the original area of cross section. To measure the strain in the sample, a strain gage was attached to the center of the specimens using glue. Minimum amount of glue was used in order to not add to the strength of the composite. A total of 4 samples were tested for each composition for getting an average value and to check

reproducibility. The fracture surface of the tensile samples was examined under SEM to study the mechanism of failure under tension.

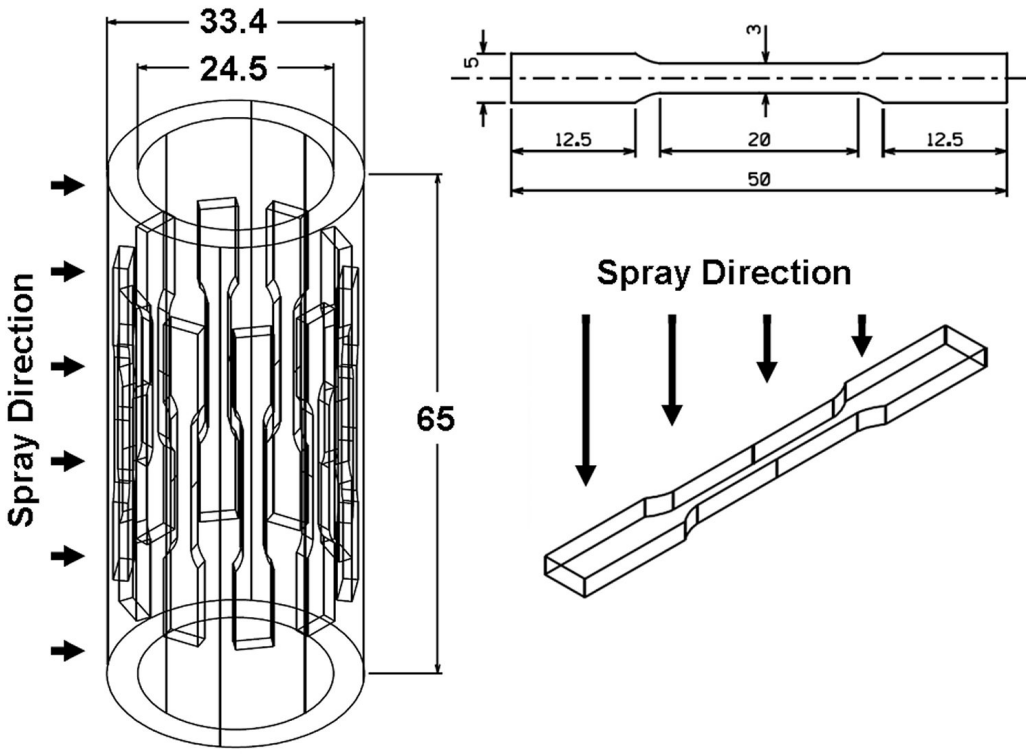

Fig. 3.5: Schematic of the tensile specimen prepared from the bulk spray formed cylinder (all dimensions are in mm)

3.5.5. Compression Testing

Compression testing was carried out cube shaped samples of edge 4mm cut from the bulk cylinder as shown in Fig. 3.6. Tests were carried out on Al-Si, Al-5CNT and Al-10CNT Samples. Tests were carried out on three samples each and the best results were reported. The loading direction was along the cylinder axis so that load was applied parallel to the splats.

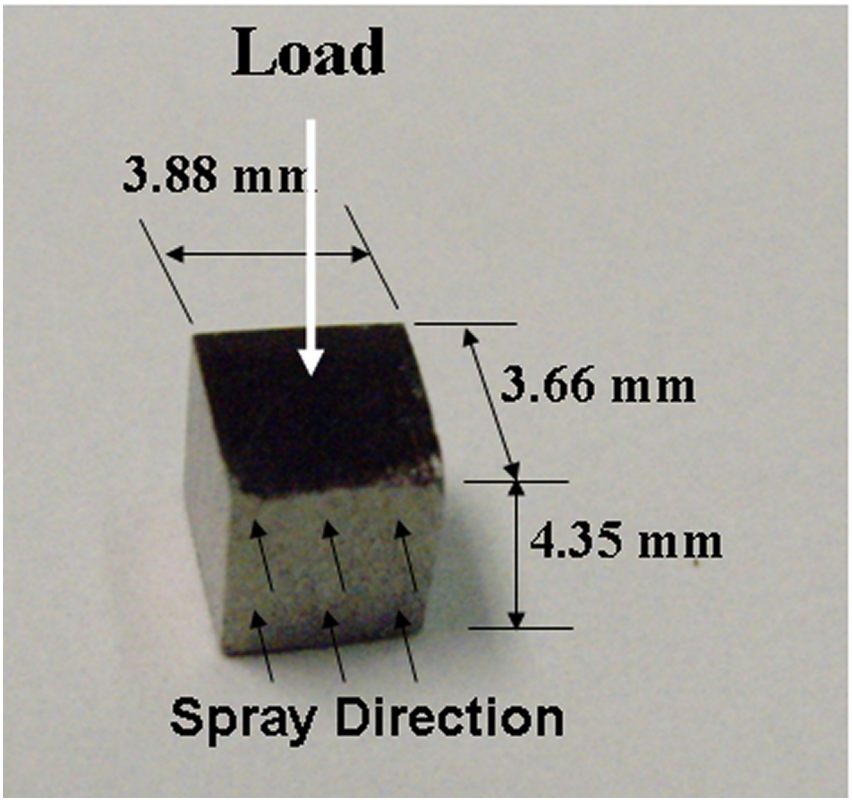

Fig. 3.6: Picture of the compression sample. The loading direction is parallel to the axis of the hollow cylinders.

As the specimen is loaded, the load varies linearly with displacement. When failure occurs, there is sudden drop in load. The engineering stress was calculated by the dividing the load by original area of cross section. The strain was calculated by dividing the distance moved by the crossheads by the original height of the cube. The proportional limit and the fracture strength of the materials under compression were used to compare the strength of the three materials. The fractured pieces were obtained and observed under SEM to study the deformation and failure mechanisms in compression.

4. RESULTS AND DISCUSSION

4.1. Characterization of Feedstock Powders

Powder feedstock morphology and its characteristics have very significant effect in thermal spraying. The distribution of CNTs in the powder feedstock will influence the coating characteristics which will be reflected in the microstructure. Figure 4.1 shows the SEM micrographs of the gas atomized fine sized Al-11.6 wt.% Si alloy powders and the multiwalled carbon nanotubes.

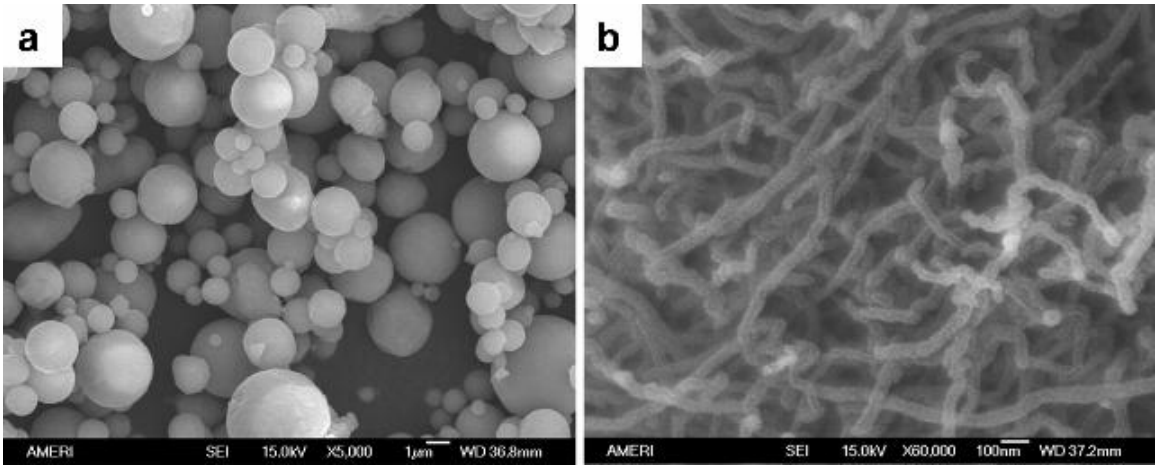

Fig. 4.1: SEM images of the a) fine sized Al-Si alloys powder, and b) multi-walled carbon nanotubes

The fine sized Al-Si particles have a mean particle size of 2.4±1.2 μm. Aqueous slurry of fine sized Al-Si powder and multi-walled carbon nanotubes shown in the figure above was subjected to spray drying. Figure 4.2 shows SEM images of the large size Al-Si particles used for plasma spraying of Al-Si coating without nanotubes and the spray dried

agglomerates. The Al-Si powders are almost spherical. The spray dried agglomerates are roughly spherical in shape and are made up the fine sized Al-Si particles.

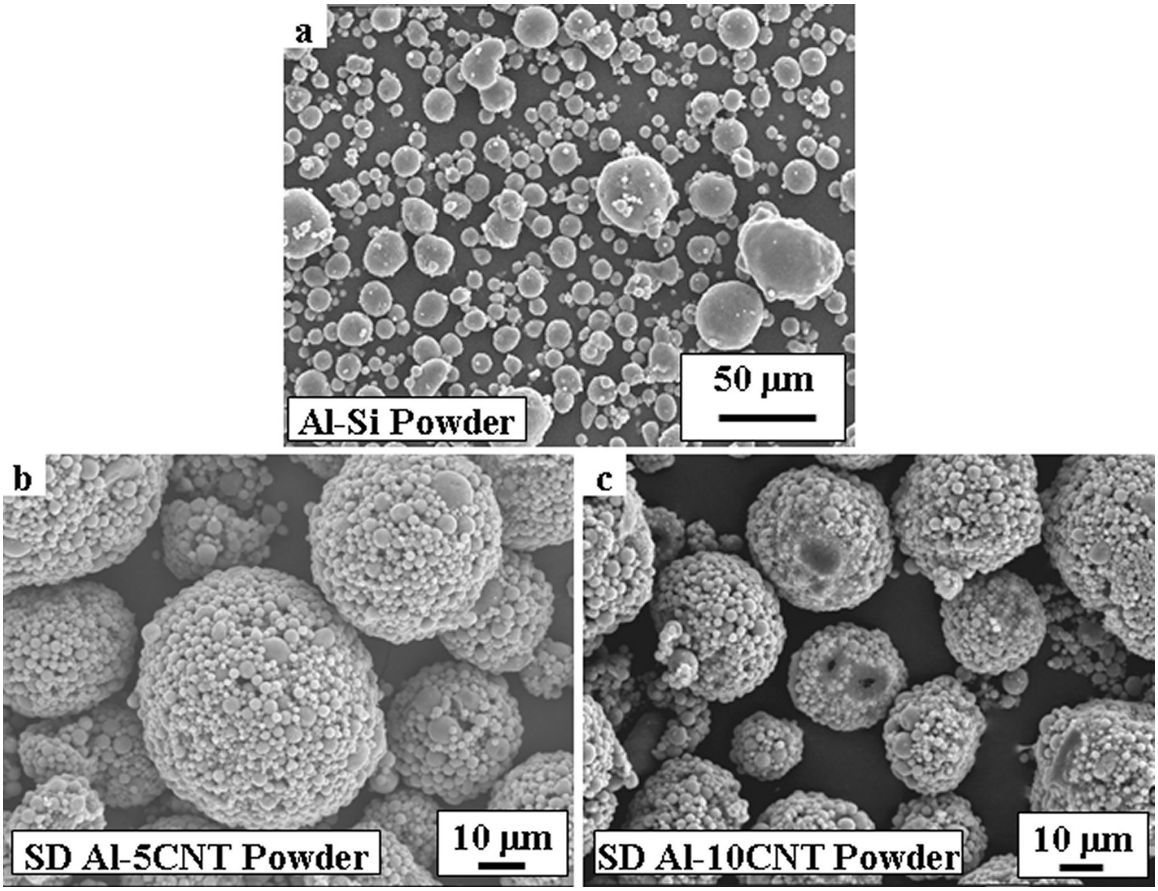

Fig. 4.2: SEM images showing the powder morphologies of a) Pure Al powder, b) Al-Si powder, c) SD Al-5CNT powder, and d) SD Al-10CNT powders

The particle size distribution of the three powders has been shown in Fig. 4.3. The average particle size of Al-Si, SD Al-5CNT and SD Al-10CNT powder was found to be equal to 14 ± 9 μm, 57 ± 21 μm and 39 ± 15 μm respectively. A more rigorous way of specifying the particle size distribution is by the size of particles such that a certain fraction of the total particles are less than or equal to it. Typically, the fractions specified

are 10% (named D10), 50% (named D50) and 90% (named D90). Table 4.1 shows the particle size distribution parameters in detail.

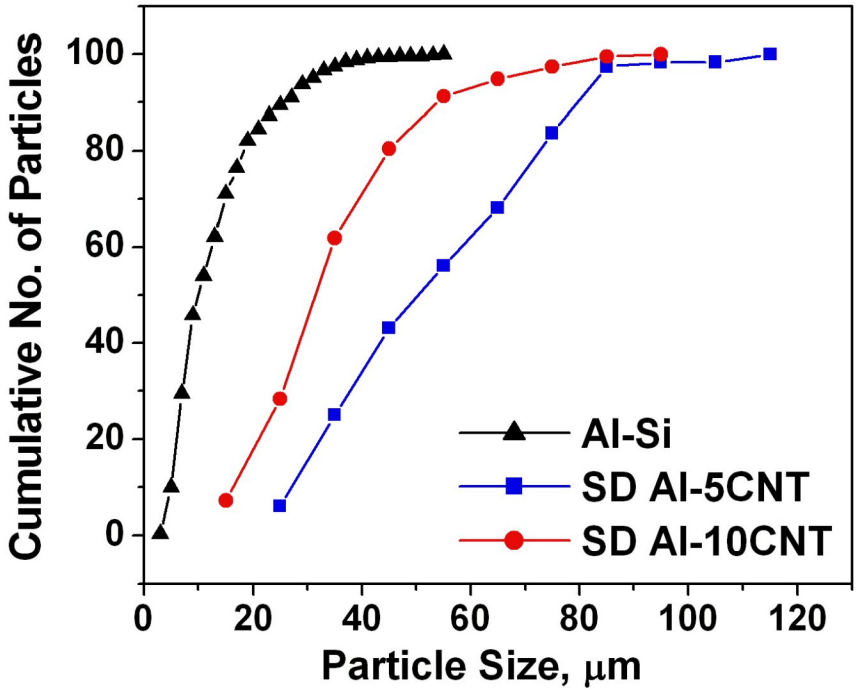

Fig. 4.3: Particle size distribution of powders

Table 4.1: Particle size distribution of the powders

Powder	D10, μm	D50, μm	D90, μm	Mean size, μm	Standard Deviation, μm
Pure Al	9	22	40	26	13
Fine size Al-Si	0.8	1.9	3.8	2.4	1.2
Al-Si	5	10	26	14	9
SD Al-5CNT	28	50	80	57	21
SD Al-10CNT	17	31	54	39	15

Figure 4.4 shows the XRD plot of the powders. It is observed that the peaks correspond to Al and Si. There is a peak corresponding (002) basal plane of graphite in SD Al-10CNTcoating that is due to presence of CNTs.

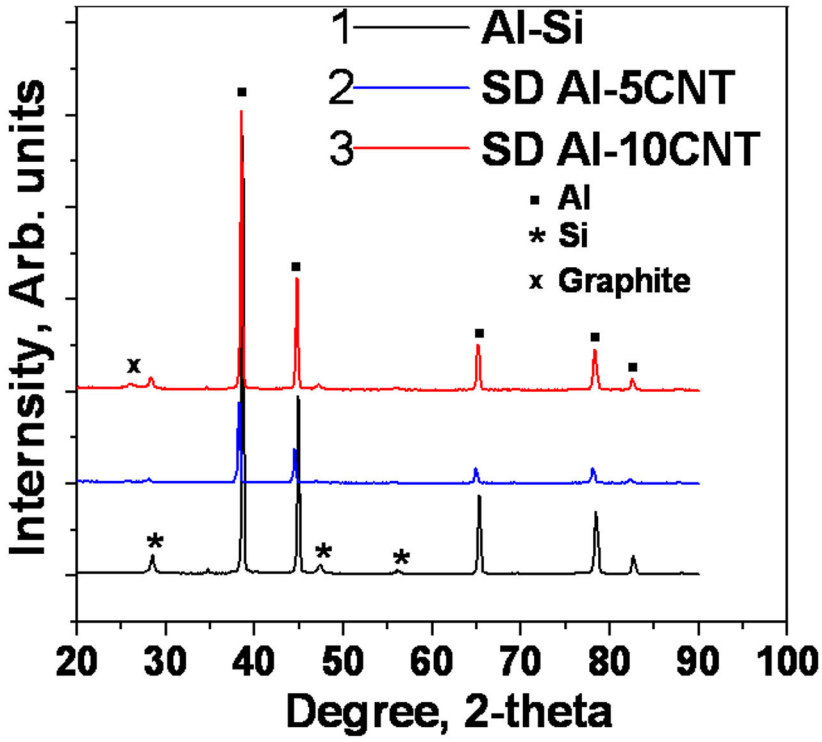

Fig. 4.4: XRD plots of the powders showing peaks for Al, Si and graphite

Spray drying results in formation of large spherical agglomerates of sizes up to 50 times of the constituent particles. Spherical shape of the particle causes low inter-particle friction and hence leads to excellent flowability. Figure 4.4a and 4.4b show the high magnification SEM image of the outer surface of SD Al-5CNT and SD Al-10CNT agglomerate. Figure 4.4c and 4.4d show the inside of broken agglomerate of SD Al-5CNT and SD Al-10CNT powders, respectively.

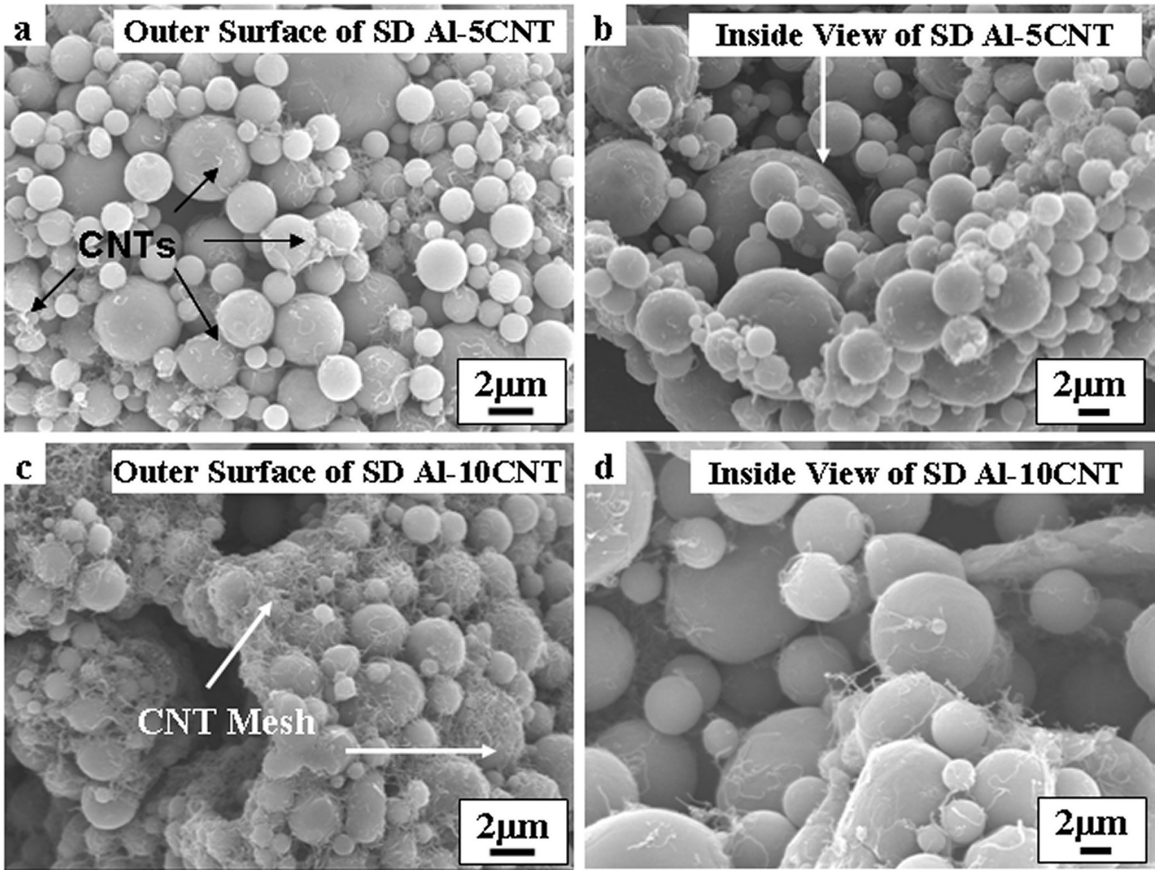

Fig. 4.5: SEM micrographs showing a) outer surface of a single SD Al-5CNT powder, b) inside view of fractured SD Al-5CNT powder, c) outer surface of a single SD Al-10CNT powder, and d) inside view of fractured SD Al-10CNT powder.

It is concluded from figure 4.5a and 4.5b that in case of SD Al-5CNT powder, CNTs are distributed uniformly on the surface as well as inside of the agglomerate. From figure 4.5c, it can be seen that there is dense network of CNTs forming a mesh on the outer surface of the SD Al-10CNT agglomerate that holds Al-Si particles on the surface. There is no mesh formation on the inside of the agglomerate (Fig. 4.5d). During spray drying, where the CNT-metal slurry is atomized into droplets, the CNTs have a tendency to

segregate on the surface of the droplets, owing to their non wetting property. Shrinkage caused by drying of the droplets brings CNTs closer. Also during drying, the movement of vapor from inside the droplet to outside would lead to transport of low density CNTs to the surface. This leads to mesh formation in the SD Al-10CNT powder. Mesh formation is not seen in SD Al-5CNT due to the lower concentration in CNTs.

In powder metallurgy route, dispersion of the carbon nanotubes in the starting powder is one of the most critical steps that affect the CNT distribution in the final product. Physical blending [35], nanoscale dispersion [182], molecular level mixing [19] and mechanical alloying [22] have been used for dispersing CNTs in the metallic powder. Blending often uses a turbula mixer or a rotating mill which is not effective in dispersing CNTs in the matrix powder [22, 35]. It has been reported that ball milling of the blended aluminum-CNT powders [22] for 48 hours resulted in excellent dispersion. However, the particle size reached in excess of 1 mm after the ball milling process, which cannot be used for thermal spraying as well as most powder metallurgy based fabrication methods. Also, CNTs break and undergo damage due to impact from the milling media. Molecular level mixing and nanoscale dispersion method were described in section 2.3.4. Though molecular level mixing provides promising results in terms of CNT dispersion [19], it is a multi-step process which is time consuming and expensive. Also there are chances of presence of oxide inclusions due to improper reduction. Nanoscale dispersion method [182] is effective in dispersing CNTs in larger particles (~28 μm), which are an order of magnitude larger than those used in the present study. Since the starting powder in this study is finer (1-3 micron), the CNT dispersion can be considered at a better resolution in the present case of spray drying. Spray drying not only provides improved CNT

dispersion but also improves the flowability of the powder due to the spherical nature of the agglomerates which is very advantageous in thermal spraying. Thus we can conclude that spray drying offers a simple and economical process for dispersing CNTs uniformly at the scale of a micrometer which can be utilized for large scale manufacturing of CNT reinforced nanocomposites by thermal spraying as well as other methods.

For cold spraying, mixtures of powders as shown in table 3.2 were prepared by blending a mixture of Al, Al-Si and SD Al-5CNT powders. The samples were mixed in a turbula mixer for 1 hour. Figure 4.6 shows the SEM images of the powder mixtures. The mixing was found to be very effective and a homogeneous mixture was obtained. The Al powders are elongated as compared to the near spherical Al-Si powders. Also it is observed that mixing has not caused damage to the spray dried agglomerates indicating that these agglomerates have some green strength.

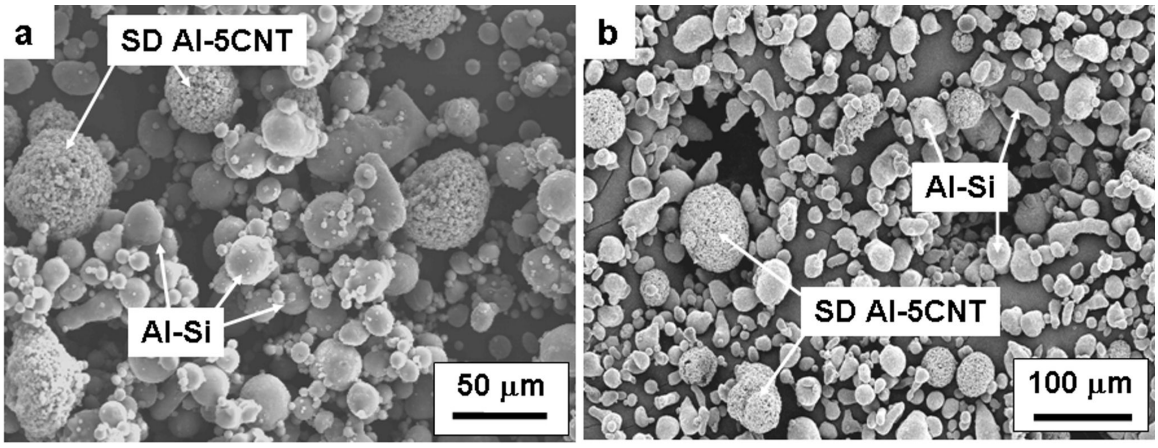

Fig. 4.6: SEM images of mixtures of a) Al-Si and 10 wt.% SD-Al-5CNT and b) Al and 10 wt.% SD-Al-5CNT

4.2. Plasma Sprayed Al-Si-CNT Composites

The Al-Si, SD Al-5CNT and SD Al-10CNT were used for plasma spraying with the parameters shown in Table 3.1. Coating, single splats and bulk structures were generated which will be discussed below.

4.2.1. Microstructure of Plasma Sprayed Al-Si-CNT Coatings

The coatings containing 0 wt.%, 5 wt.% CNT and 10 wt.% CNT will be referred to as Al-Si, Al-5CNT and Al-10CNT respectively. Figure 4.7 shows the picture of the plasma sprayed coatings.

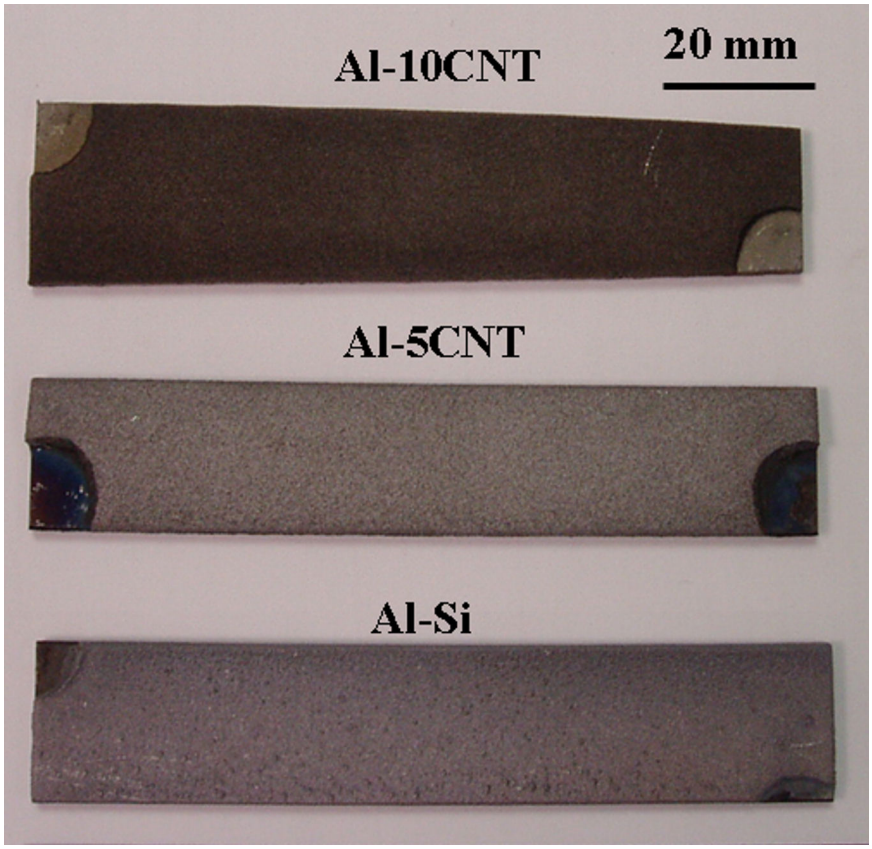

Fig. 4.7: Picture of plasma sprayed coatings on to mild steel substrate

It is observed that as the CNT content goes on increasing, the coatings become more dark in color. Figure 4.8 shows the SEM micrograph of the cross sections of the three coatings. The coatings are uniform, dense and adherent to the substrate. The thickness of the Al-Si, Al-5CNT and Al-10CNT coatings was equal to 580, 1100 and 550 μm respectively.

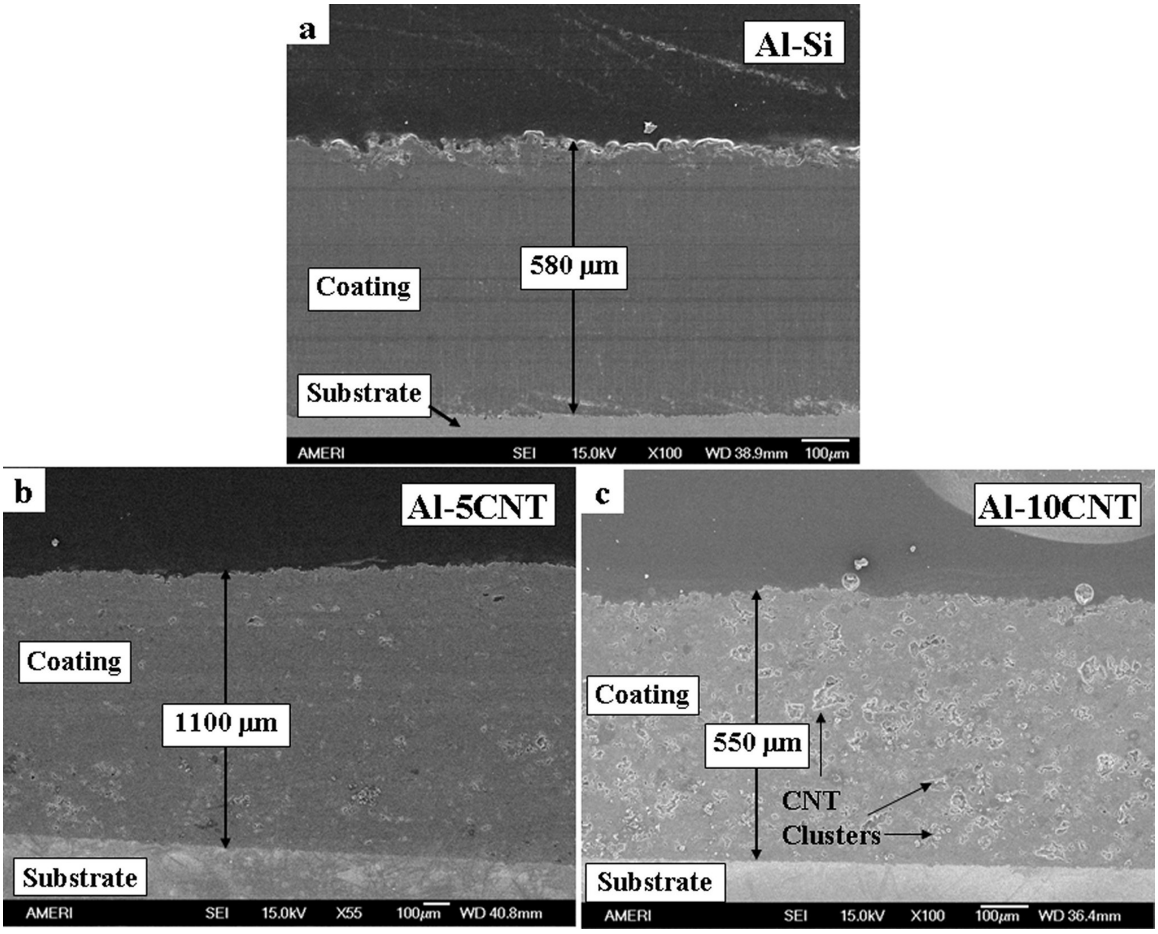

Fig. 4.8: SEM images of the coating cross sections showing the microstructure and thickness of a) Al-Si, b) Al-5CNT and c) Al-10CNT coatings

The microstructure of Al-5CNT and Al-10CNT is two phase and the CNT dispersion is bimodal in nature. It consists of (i) matrix containing dispersed CNTs and (ii) CNT rich clusters. The degree of CNT clustering is higher in the Al-10CNT coating as compared to Al-5CNT coating. The higher degree of clustering in Al-10CNT coatings is attributed to mesh formation in the corresponding SD Al-10CNT powder. When the spray dried powder gets molten, the poly vinyl alcohol binder evaporates. The surface tension of molten Al-Si alloy generates capillary forces which lead to collapse of the mesh structure by agglomeration of CNTs to form CNT cluster. This is schematically shown in Fig. 4.9. The degree of CNT clustering is low in Al-5CNT coating due to lower concentration of CNTs in SD Al-5CNT powder. The porosity present in the coatings is located in vicinity of CNT clusters. The densities of the Al-Si, Al-5CNT and Al-10CNT coating as measured by water immersion technique was found to be 2.44, 2.36 and 2.35 g/cc which corresponds to a density of 90%, 88% and 90% of the theoretical density respectively.

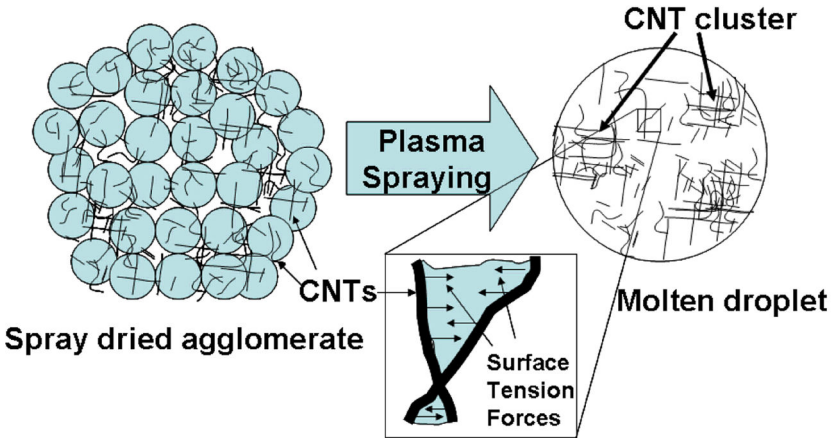

Fig. 4.9: Schematic showing mechanism of cluster formation during plasma spraying of spray dried powders

Figure 4.10 shows high magnification images of the CNT clusters in Al-5CNT and Al-CNT coating. It is observed that the CNT clusters and neighborhood surrounding clusters contain lot of porosity.

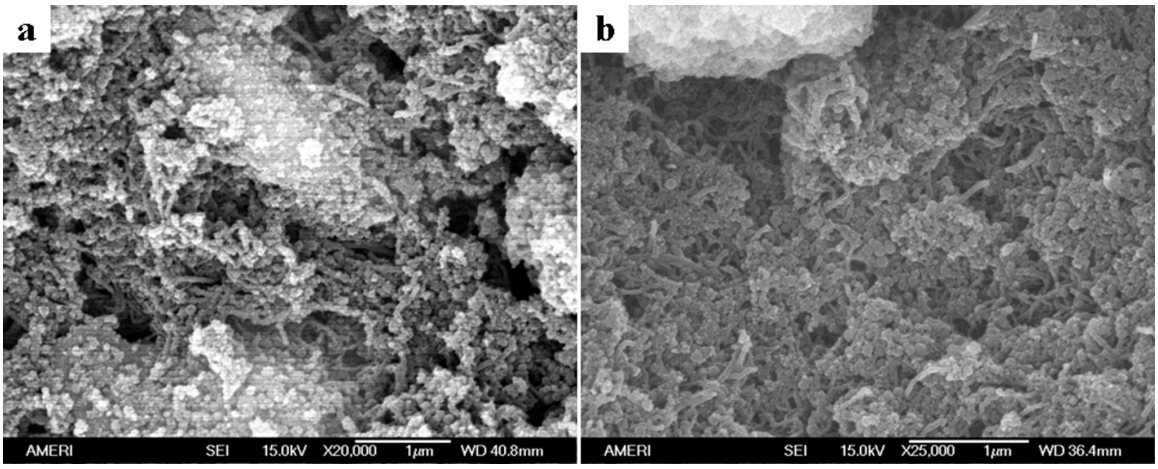

Fig. 4.10: SEM images showing a) metal infiltrated CNT cluster in Al-5CNT coating, and b) a CNT rich cluster in Al-10CNT coating

The CNT cluster in Al-5CNT shown in Fig. 4.10a is infiltrated with molten Al-Si alloy, while the CNT rich cluster from Al-10CNT coating in Fig. 4.10b is not. Micro-Raman spectra were taken from the matrix, the clustered CNT region of the cross section of the coating and corresponding spray dried powder agglomerates and are shown in Fig. 4.11. The micro-Raman spectra of the CNT cluster in Al-5CNT coating shows a strong Si peak at a Raman shift of 520 cm^{-1} while the CNT cluster in Al-10CNT has a weak Si peak. This indicates that the CNT cluster in Al-5NT was metal infiltrated while the cluster in Al-10CNT was not. The presence of D and G peaks in the powder, coating matrix and

CNT clusters indicates that the CNT structure remains intact after spray drying and plasma spraying. Most of the clusters in both the coatings were not infiltrated with metal.

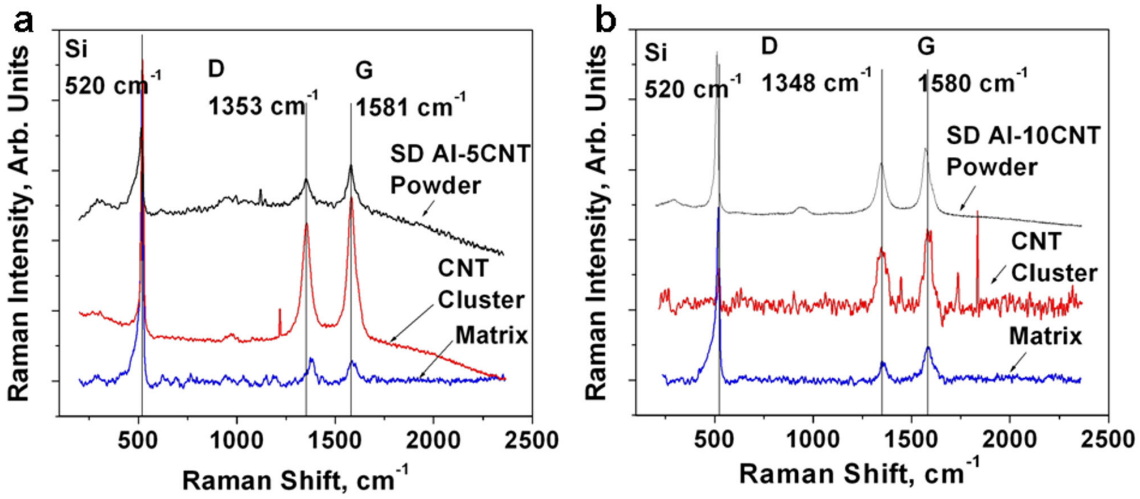

Fig. 4.11: Micro-Raman Spectra taken from matrix, CNT cluster and spray dried powder for a) Al-5CNT and b) Al-10CNT coating

SEM was further carried out on the fracture surfaces of the coatings. Small portion of the coating was broken under tension and bending forces for the purpose. Figure 4.12 shows the SEM images of the fracture surfaces of the coatings. It is observed that the CNTs are distributed uniformly within the splats as well as splat interfaces in Al-5CNT coating. In case of the Al-10CNT coating, CNT clusters can be seen on the fracture surface and in the splat interfaces. At some places where the fracture occurred under tensile stresses, strengthening phenomena like CNT pullout and crack bridging were observed as shown in Fig. 4.13. XRD patterns of the top surface of the coating are shown in Figure 4.14. Aluminum carbide (Al_4C_3) formation was observed. The fraction of Al_4C_3 formed was calculated by ratio of the sum of the area under all the peaks of a

given phase to the area under all the peaks. The amount of Al_4C_3 formed was found to be 7.8% and 15.8% by vol. for Al-5CNT and SD Al-10CNT coatings respectively. From the SEM of fracture surface or the coating cross section, no typical features corresponding to Al_4C_3 formation were found for Al-5CNT coating. But for Al-10CNT coating, Al_4C_3 could be exclusively seen. Figure 4.15a and 4.15b show the SEM images of Al-10CNT coating's cross section and fracture surface respectively. Al_4C_3 needles are formed near CNT clusters where the activity of carbon is high.

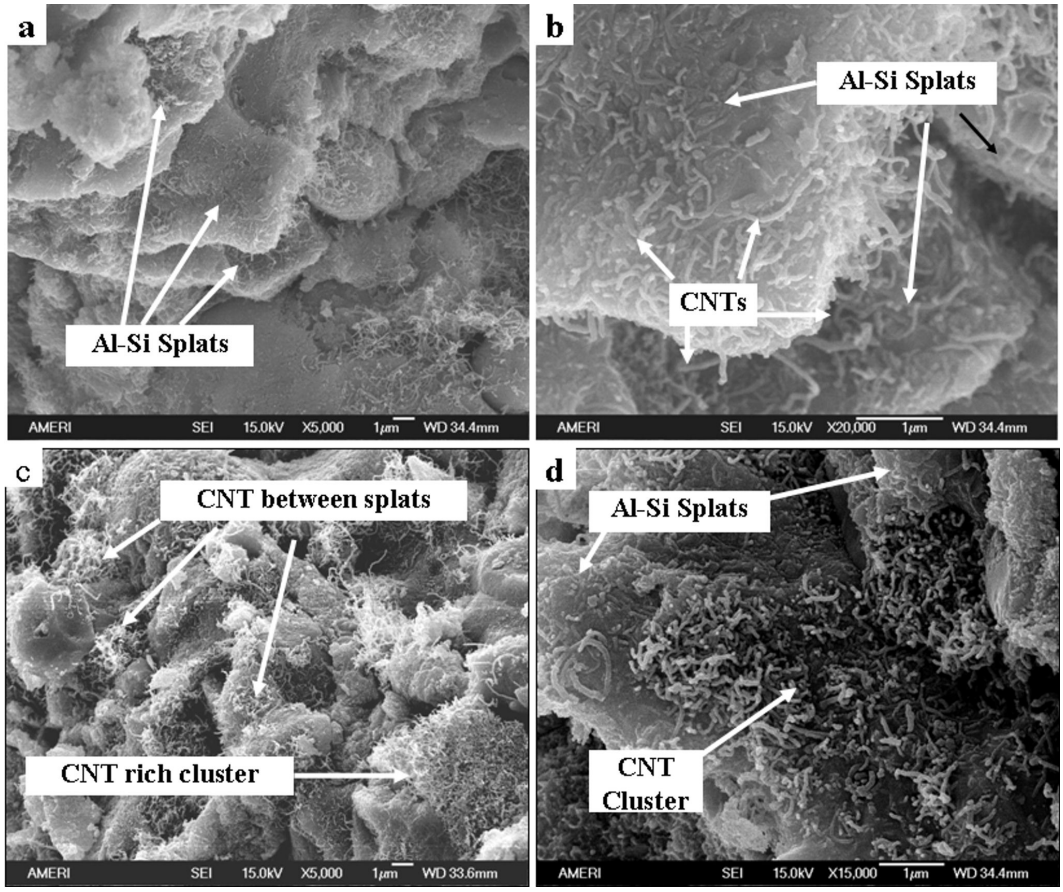

Fig. 4.12: SEM images of fracture surfaces showing the a) and b) splats of Al-Si in the Al-5CNT coating with CNTs uniformly distributed within the splats and in the intersplat region, and c) and d) CNT clusters on the fracture surface and intersplat regions

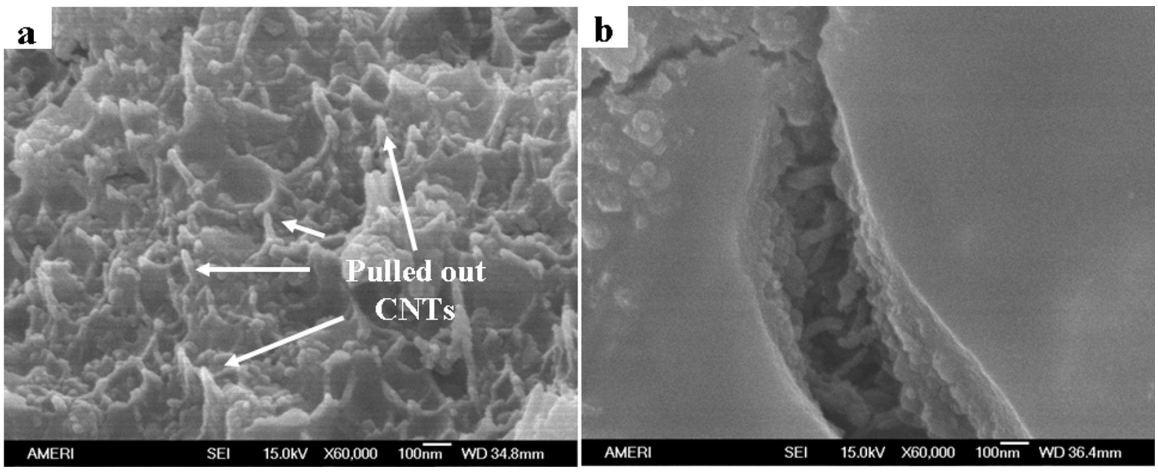

Fig. 4.13: SEM images of fracture surface showing a) CNT pullout in Al-5CNT coating, and b) CNTs bridging a crack in Al-10CNT coating

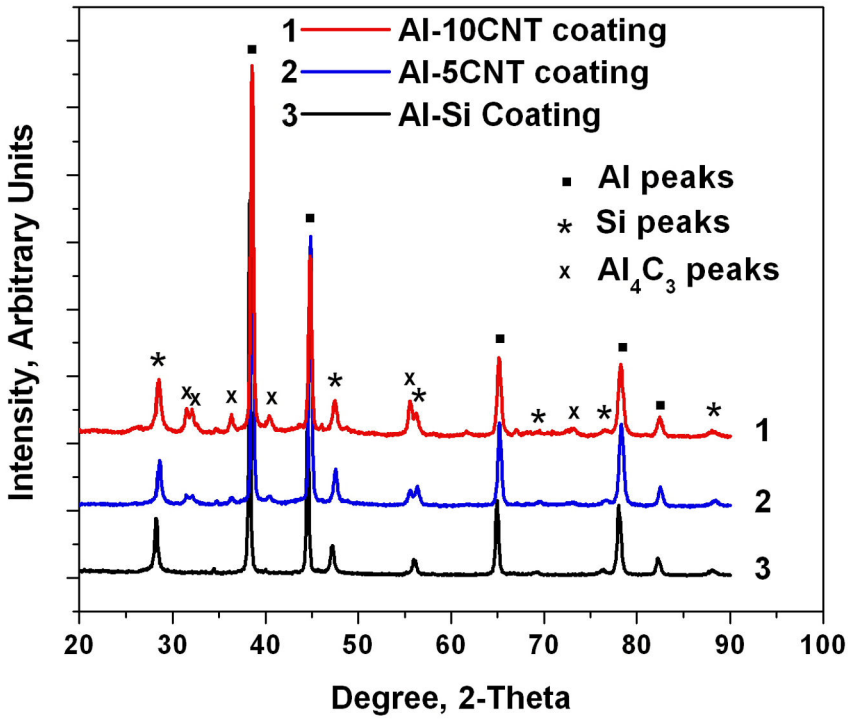

Fig. 4.14: XRD plots taken from the top surface of the three coatings showing Al_4C_3 formation

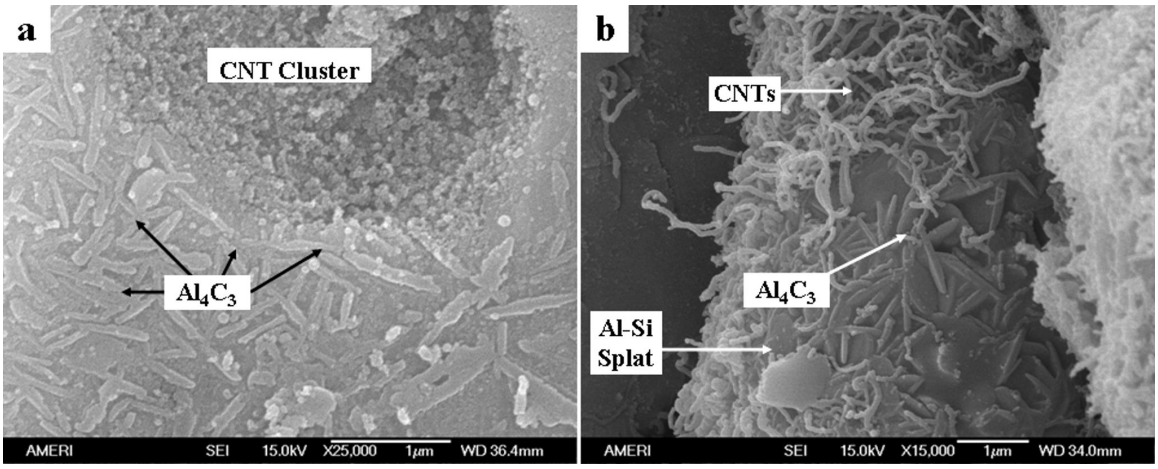

Fig. 4.15: SEM images showing Al_4C_3 formation in Al-10CNT coating on a) Cross section, and b) fracture surface

It is observed in Fig. 4.15a that the surface of the cluster seems to be made of carbonaceous mass resulting from damaged CNT due to reaction. In case of SD Al-10CNT powder, the large CNT content leads to mesh formation and there is large surface area available for reaction. The CNT rich clusters which are poorly infiltrated with metal undergo more damage due to direct interaction with the plasma plume. This will lead to generation of more defects on the CNTs which will lead to increase in reaction sites for carbide formation. These are the reasons for increased amount of Al_4C_3 formed in Al-10CNT coating.

For further study of the microstructure, transmission electron microcopy was carried out on the coatings. Figure 4.16a shows TEM image of fine grained structure in Al-10CNT coating. Inset shows the SAD pattern confirming the presence of Al_4C_3.

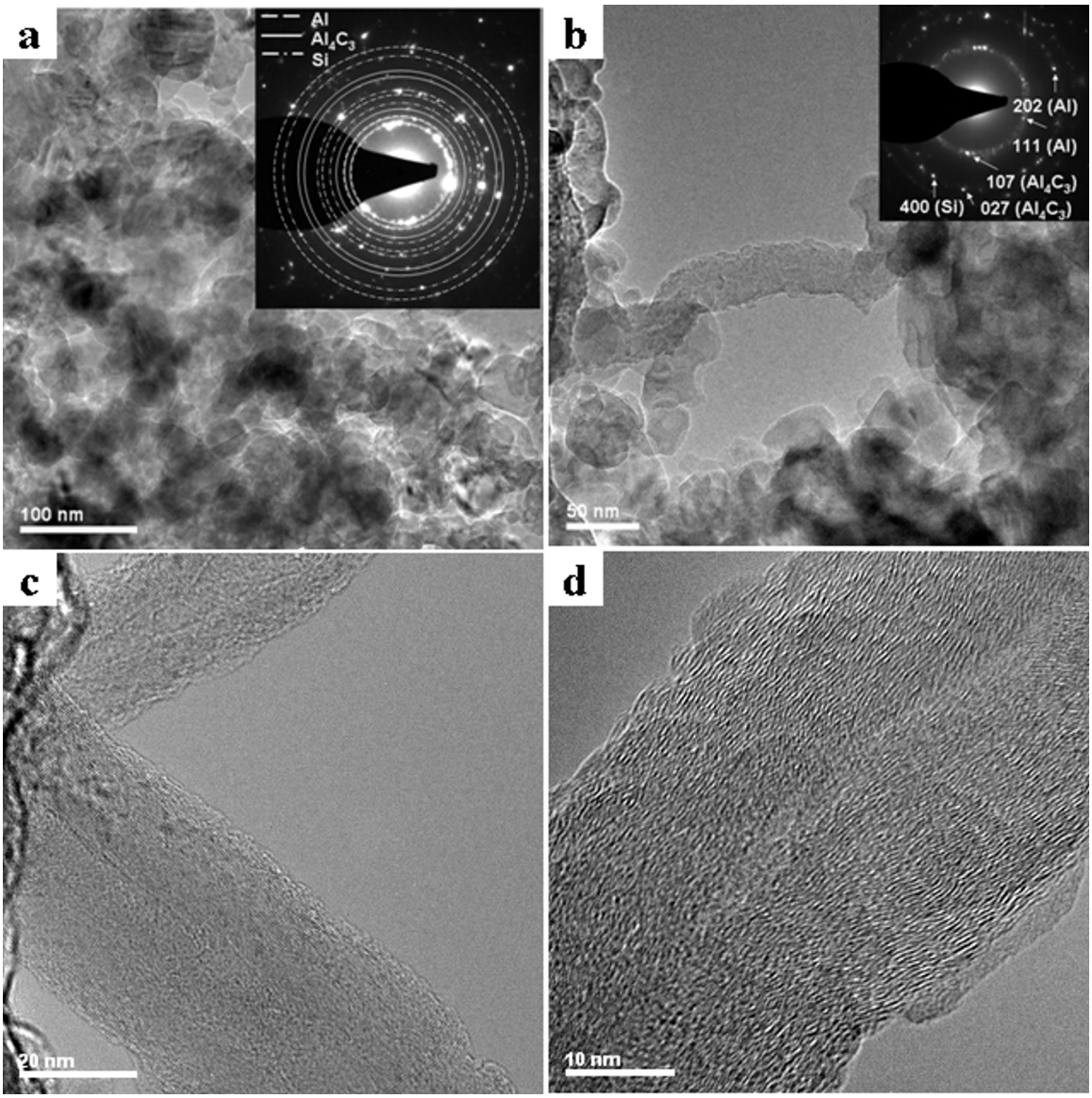

Fig. 4.16: TEM images showing a) fine grained microstructure of Al-10CNT coating, inset shows the diffraction pattern showing Al_4C_3, Al and Si b) metal coated and reacted CNT in Al-10CNT coating, inset shows the diffraction pattern indicating Al_4C_3 formation, c) undamaged CNT in Al-5CNT coating, and d) undamaged CNT in Al-10CNT coating with some reaction products on the surface

Fig. 4.16b shows a metal coated CNT in Al-10CNT coating which has undergone some reaction with the matrix The inset shows the diffraction pattern which indicates Al_4C_3 formation. Figs. 4.16c and 4.16d show HR-TEM images of undamaged CNTs in Al-5CNT coating and Al-10CNT coating, respectively. CNT surface is smooth in case of Al-5CNT coating (Fig 4.16c) whereas discontinuous reaction product is formed on the CNT surface in Al-10CNT coating (Fig. 4.16d). Surface walls of CNT shows slightly damaged structure in case of Al-10CNT as compared to Al-5CNT coating. Table 4.2 shows the in-flight properties of the particles and indicates that the SD Al-10CNT powder experienced higher temperature and velocity. This was due to the smaller size of the powders and CNT mesh formation which increased the thermal conductivity and emissivity of the powder, resulting in damage to outer walls of CNTs.

Table 4.2: Properties and in-flight temperature and velocity of the particles

Powder	**Specific Surface Area m^2/g**	**Temperature K**	**Velocity m/s**	**Particle Size, µm**	**Approximate Flight Time ms**
Al-Si	1.44	2309 ± 34	109 ± 3	14 ± 9	0.9
SD Al-5CNT	4.50	2287 ± 3	168 ± 1	57 ± 21	0.6
SD Al-10CNT	5.90	2308 ± 6	180 ± 2	39 ± 15	0.6

The high thermal conductivity of CNTs [14] helps in conducting heat to the interior of the cluster thereby assisting the damage. It was shown earlier that metal infiltration into the CNT cluster was more prominent in Al-5CNT coating. The molten

layer acts as a protective layer shielding the CNT clusters and helps prevent damage to CNTs in Al-5CNT coating. Figure 4.17 shows a schematic of the heat transfer in metal coated and uncoated clusters. The heat transfer in coated clusters would be only by conduction and convection and the metal layer will shield the CNTs from the radiation of the plasma plume. So it can be concluded that wetting of CNTs by molten alloy is critical in establishing dispersion as well as stability of CNTs.

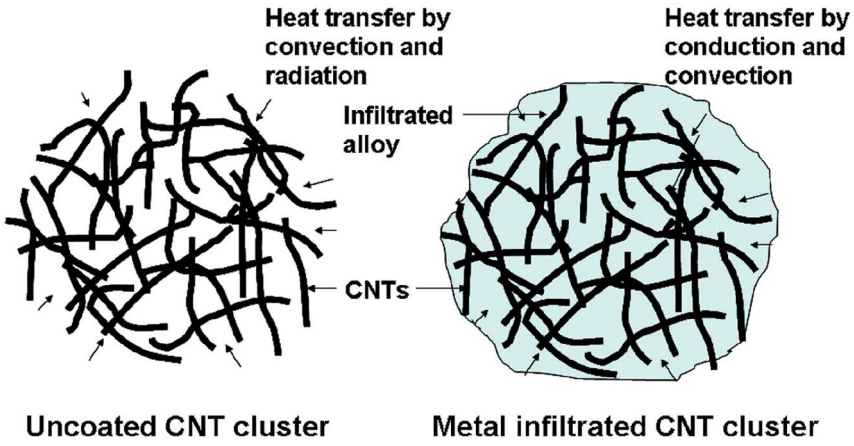

Fig. 4.17: Schematic showing heat transfer mechanisms in the clusters

In the present study, fabrication of bulk structures were also carried out using plasma spray forming. Plasma spraying was carried out on a rotating mandrel to generate thick cylindrical structure of bulk CNT reinforced composite. Figure 4.18 shows a composite cylinder made by plasma spraying of SD Al-10CNT powder. The dimensions of spray deposited cylinder are: 27 mm inner diameter, 5 mm wall thickness and 100 mm length. This cylinder was spray formed in 20 minutes which proves that composite with high (10 wt.%) CNT content can be rapidly fabricated by plasma spraying. Similar cylindrical structures were spray deposited using SD Al-5CNT and Al-Si powder. It is emphasized

that thick coatings could be deposited due to the fact that spray dried spherical agglomerates assist the plasma spraying process without clogging the powder feeding system. Thick coating could not be deposited in our previous work [35] where blended CNT and aluminum powder feedstock caused clogging and inconsistent powder flow due to high surface forces between CNTs.

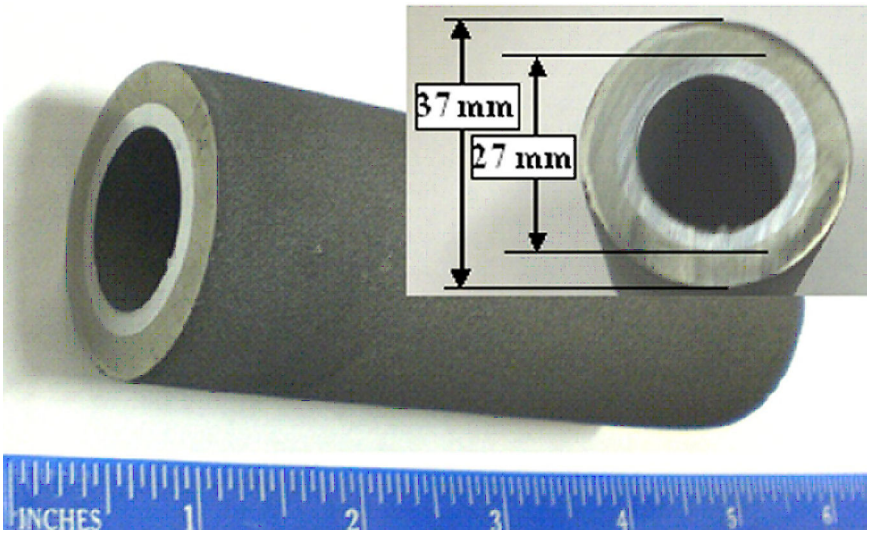

Fig. 4.18: Plasma spray formed Al-10CNT cylinder with a wall thickness of 5 mm and 100 mm length

To understand the mechanism of formation of the microstructure and clustering of CNTs single splats for the spray dried particles were studied which is described in next section.

4.2.2. Microstructural Evolution in Single Splat

Studying the mechanism of microstructure evolution is essential as it gives knowledge about clustering. A thorough understanding of the clustering phenomena is

essential for creating new strategies to avoid it. Plasma sprayed coatings are formed by a layer by layer deposition of splats. Splats are formed when the molten/semi-molten droplets impact the substrate and solidify. Two kinds of splat morphologies namely *fingered* and *disc* shaped splats are observed for the SD Al-5CNT powder as shown in Figures 4.19 and 4.20 respectively.

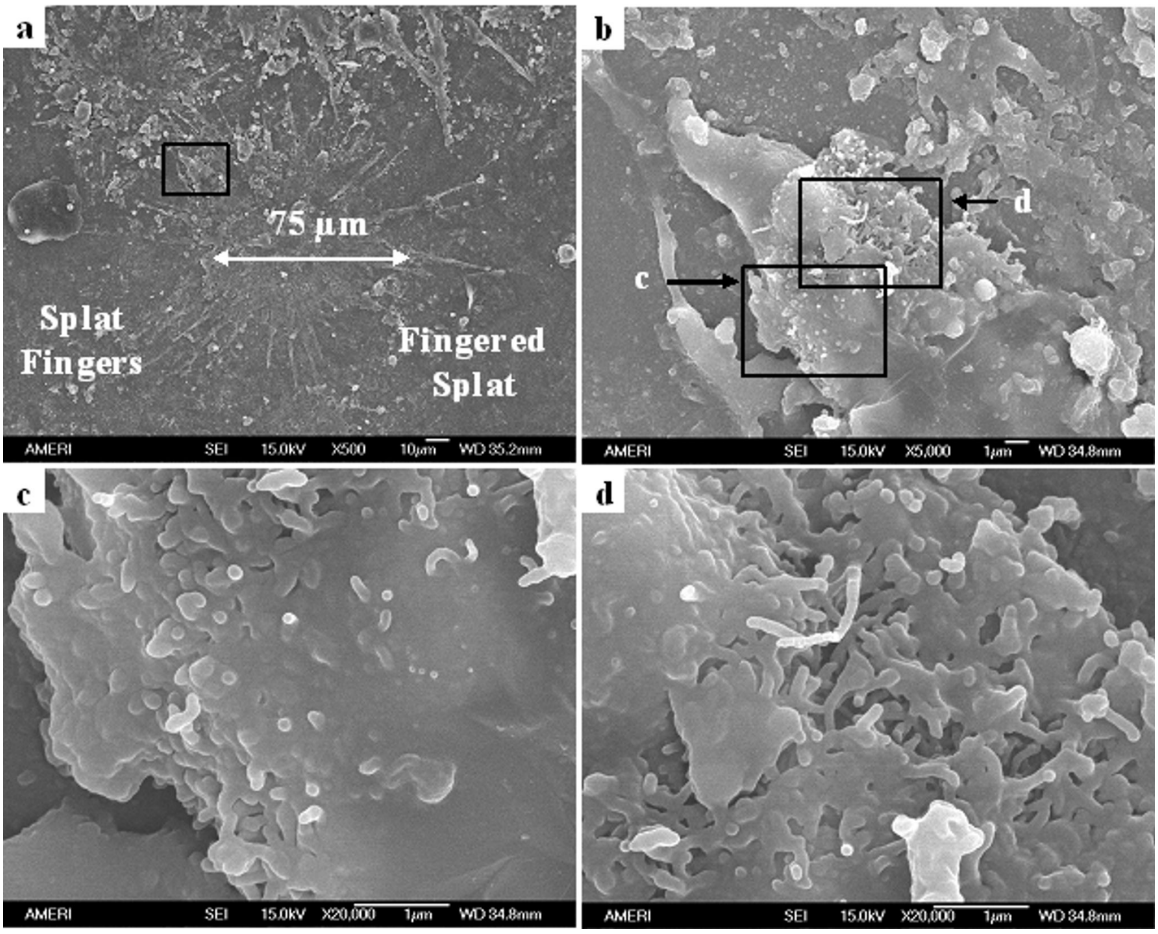

Fig. 4.19: SEM images showing a) Fingered splat from SD Al-5CNT powder, b) splat finger showing CNT cluster infiltrated with metal marked by rectangles, c) and d) high magnification images of the CNT infiltrated cluster

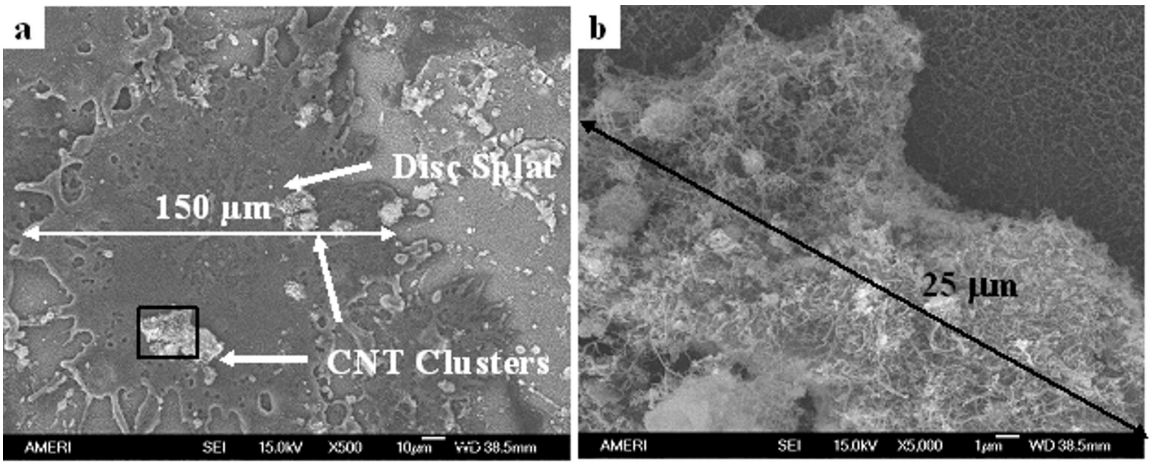

Fig. 4.20: SEM images showing a) Disc splat of Al-5CNT powder showing CNT rich cluster, and b) CNT rich cluster with poor metal infiltration

Splats were mostly irregular disc type for Al-10CNT powders as shown in Fig. 4.21. A CNT rich cluster that has not been infiltrated with metal is also seen.

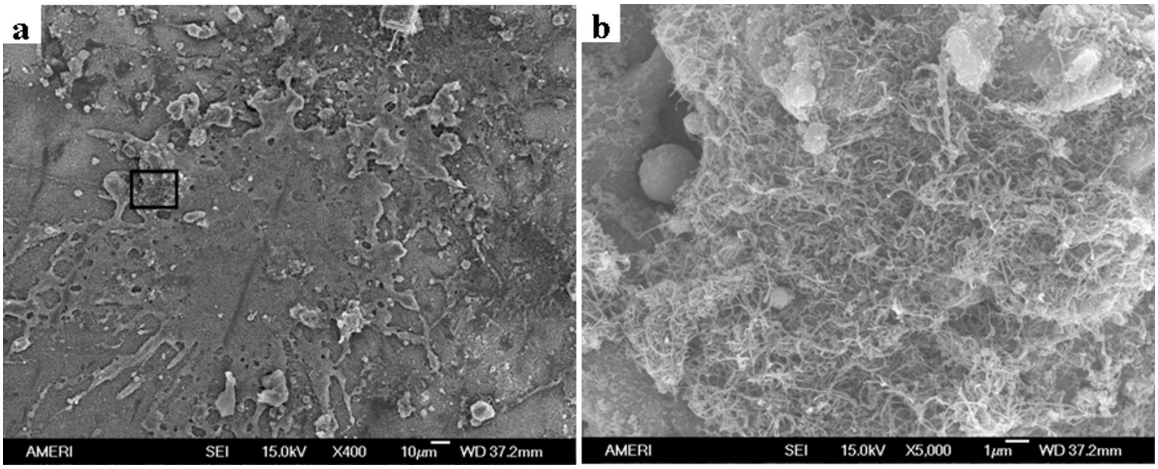

Fig. 4.21: SEM images showing a) Disc splat from SD Al-10CNT powder showing CNT rich cluster, and b) high magnification image of the CNT rich cluster with poor metal infiltration

It was observed that the fingered splats are smaller than the disc splats indicating that they are formed from smaller powder particles. This could be due to the fact that small particles undergo complete melting and contain low CNT content due to which the viscosity is low. Larger particles could exhibit higher viscosity due to higher CNT content which inhibits spreading and splashing. Viscosity of the droplet from composite particles can be given as [231]

$$\mu_e = \frac{\mu}{1-\phi\left(1+R_C/R_P\right)} \qquad \text{Equation 4.1}$$

Where μ_e is the effective dynamic viscosity, μ is the dynamic viscosity of the liquid phase, R_C is the radius of CNT clusters and the R_P is the droplet size and ϕ is the CNT fraction. Considering $R_C/R_P<<1$, equation 4.1 predicts 6.5% and 13.8% increase in viscosity of the molten Al-Si alloy due to addition of 5 wt.% and 10 wt.% of CNTs respectively. Most of the splats in Al-10CNT are disc shaped which is due to the increase in the viscosity of the melt caused by increased CNT content. The splat sizes ranged from 70 – 190 μm for Al-5CNT and 50 – 160 μm for Al-10CNT powder. This is in accordance with the starting powder sizes. The fingers represent the last material that solidifies during splat formation. The CNTs flow in radial outward direction along with the molten particle on impact. It is seen from Fig. 4.19b that CNTs are found in the finger area indicating that they retain the thermal energy and keep the melt molten. This is deduced from the fact that the specific heat capacity of C (Graphite) and Al-12%Si alloy at 2300K is equal to 2.145 $J.g^{-1}.K^{-1}$ and 1.152 $J.g^{-1}.K^{-1}$ (taken from thermo-chemical software and database FactSage) respectively. It is concluded from the magnified images (Fig. 4.19c and 4.19d) that the CNT clusters in the fingers have been infiltrated by the molten alloy.

Distribution of CNTs in each of the fingers is very uniform. Figure 4.20 shows a disc splat of SD Al-5CNT and a CNT rich cluster (Fig. 4.20b) which has been partially infiltrated with molten Al-Si alloy. The disc splat is larger (150 μm) compared with fingered splat (75 μm) for reasons explained earlier. Figure 4.21 shows a disc splat from SD Al-10CNT particle showing CNT clusters which are partially infiltrated with metal. The size of the CNT clusters observed within a splat is between 10 -30 μm which is same as the size of CNT clusters observed in the coating cross sections Fig. 4.8). A few clusters of size up to 50 μm are observed in the Al-10CNT coating cross section, which form due to contiguity of the CNT clusters from individual splats.

Landry et al. [232] have shown that the wetting of Al-Si alloys on graphite improves with time i.e., the contact angle diminishes from 160 to 40 degrees with time due to formation of interface carbide layer over a period of 10^5 s at a temperature of 1190K. This indicates that reaction products forming at the interface promote wetting and hence infiltration. The pressure induced infiltration of porous compacts is governed by the Darcy's law given by [233]

$$h^2 = \frac{2k_p t}{\mu(1-V_p)}(P - P_0) \qquad \text{Equation 4.2}$$

where h is the infiltrated depth of the metal into the porous compact, k_p is the intrinsic permeability of the compact, μ is the viscosity of melt, t is the infiltration time, V_p is the particulate volume fraction and P is the applied pressure. P_0 is the threshold pressure for infiltration to occur and is governed by the capillary forces and is given by [234]

$$P_0 = \frac{6\lambda}{D}\gamma_{LV}\cos\theta\frac{V_p}{(1-V_p)} \qquad \text{Equation 4.3}$$

where λ is a parameter dependent on the particulate shape, γ_{LV} is the liquid vapor surface tension of the infiltrating liquid and θ is the contact angle. From eq. 4.2 and 4.3 it can be seen that lower the viscosity and surface tension of the infiltrating liquid, larger will be the infiltration depth. During plasma spraying, the impact of molten particles on the substrate could also lead to pressure infiltration of the CNT clusters. P_0 was computed ~ 67-200 MPa with following values used for computation: CNT diameter (D) = 60 nm, λ = 1 for spherical shape particle, $\theta = 40^o$ [232], V_p assumed ~ 0.50-0.75 and γ_{LV} = 0.889 $N.m^{-1}$ (for A356 alloy [235]). Assuming that an Al-Si droplet of 50 μm diameter travelling at 200 $m.s^{-1}$ comes to rest in 1 μs forming a splat of 100 μm, the pressure generated due to impact is found to be ~4 MPa, which is orders of magnitude smaller than P_0. Hence, it is concluded that infiltration of the CNT clusters during impact is rather unlikely. Table 4.1 showed the powder properties along with the in-flight temperature and velocity. Considering the stand-off distance as 100 mm, the flight time has been calculated and shown in Table 1. The particle flight time is less than 1 ms. The measured temperature of the particles during flight is of the order of 2300 K. It is anticipated that infiltration would be limited due to the small interaction time between the CNT cluster and the molten metal. But under such high superheated conditions, the viscosity and surface tensions would be very low which will promote infiltration. Since in Al-10CNT a larger amount of CNT clusters are observed (due to higher CNT content), it is expected that there would be more clusters which have not been infiltrated with metal (Figure 4.21b). Also it is observed that there is lot of porosity within each CNT cluster. This accounts for the low density of the coatings.

So in order to improve the dispersion of CNTs in the coatings, CNTs must wet the molten alloy and remain dispersed during the melting stage. This can be possible if there is a limited reaction between the alloy and the CNT so that the CNTs wet the alloy. Plasma spraying can be used for obtaining densified powders. However, air plasma spraying is not suitable as it will lead to oxidation the powders.

4.3. Cold Sprayed Al-CNT Composites

The other process used for synthesizing CNT composites in this study was cold spraying. Cold spraying has its own advantages compared to plasma spraying which were highlighted in table 2.3. There are some studies on cold spraying of metallic composites with nano-sized fillers. But there is no study on cold spraying of metal-CNT composites. So this study has been carried out to study the feasibility of using cold spraying for depositing CNT-reinforced coatings. Several powder mixtures as specified in table 3.2 have been cold sprayed to synthesize coatings on 6061 alloy.

4.3.1. Microstructure of Cold Sprayed Al-Si-CNT Coatings

There are some studies on cold spraying Al-Si alloys. Table 4.3 shows the parameters used in this study. The SD Al-5CNT was sprayed onto 6061 steel substrates. But it did not result in formation of a deposit. This was attributed to the fact that the agglomerates fractured on impact and disintegrated. A part of the kinetic energy was absorbed in the process. The resulting fines did not have much kinetic energy and the impact was not enough to cause plastic deformation. Al-Si powders could be easily

sprayed to form coatings. So these SD-Al-5CNT powders were mixed with Al-Si powders and sprayed. This resulted in coating formation.

Table 4.3: Cold spraying parameters used in the present study

Item	Quantity
Process gas (Helium)	29 bar pressure
Powder carrier gas (Nitrogen)	30 bar pressure
Rotation speed of powder feeder	4 RPM
Vibration pressure of feeder	2 bar
Stand off distance	20 mm

Figure 4.22 shows the SEM image of the cross section of Al-Si-0.5 wt.% CNT coating. It is observed that the thickness of the coating is just 80 μm.

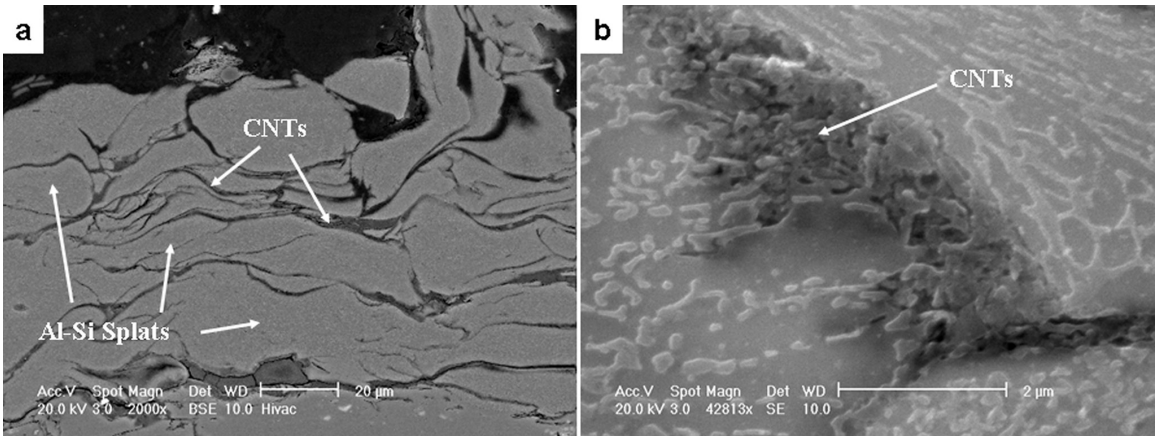

Fig. 4.22: SEM image of cross section of Al-Si-0.5 wt.% CNT coating showing a) back scattered image of coating microstructure, and b) CNTs at inter-splat boundaries

The coating is made up of splats of Al-Si particles with CNTs/carbonaceous materials at the splat interfaces. The coating thickness did not increase beyond 80 μm. The coating was successively forming and getting removed due to poor interfacial adhesion between the splats. Figure 4.23 shows SEM images of the fracture surface of the coating indicating very uniform distribution in the coatings. This is brought about due to the fact that the spray dried agglomerates disintegrate on impact and release the CNTs in an uniform manner which are then trapped by the particles impacting at that instant. Since the thickness was limited to only 80 μm, due to limited ductility of Al-Si powders, the Al-Si powders were replaced by pure Al and cold sprayed. These coatings will be discussed in the next section.

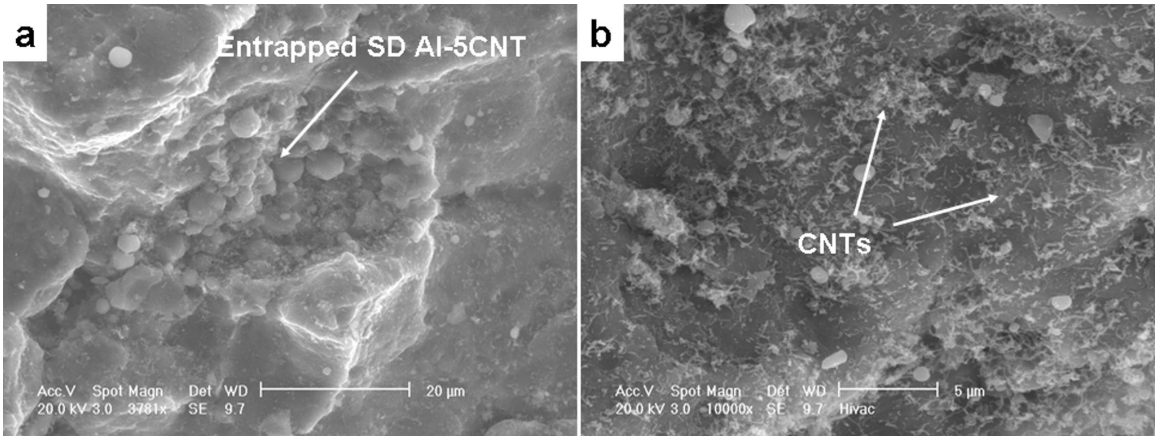

Fig. 4.23: SEM images of fracture surface of Al-Si-0.5 wt.% CNT coating showing a) an entrapped spray dried particle and b) uniformly distributed CNTs on the fracture surface

4.3.2. Microstructure of Cold Sprayed Al-CNT coatings

Cold spraying of the powder mixtures were carried out onto AA6061 substrate. The mixture of Al and SD Al-5CNT sprayed well. This is attributed to the high

deposition efficiency of non-porous and readily deformable Al powder. It is possible to entrap the Al-Si particles and the nanotubes resulting from the disintegration of the spray dried agglomerates in between the deforming Al particles. Composite coatings containing an overall nominal CNT content of 0.5 wt.% and 1 wt.% and having a thickness of ~ 500 μm were successfully prepared as shown in Fig. 4.24.

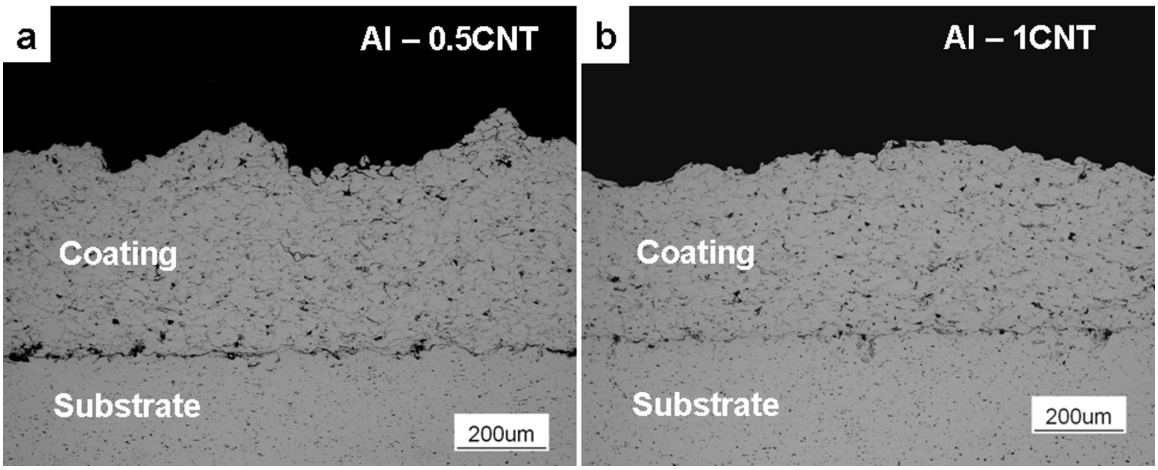

Fig. 4.24: Optical micrographs of polished and etched cross sections of a) Al-0.5CNT and b) Al-1CNT coatings

These cold sprayed coatings will be referred as Al-0.5CNT and Al-1CNT hereafter. Figure 4.25 shows a schematic illustration of the powder pretreatment steps involved in the fabrication of the composite coating. The velocity attained by the particles during cold spraying is given by Dykhuizen [236] as

$$V_p = V\sqrt{\frac{C_D A_p \rho x}{m}} \qquad \text{Equation 4.4}$$

Where V is the gas velocity, C_D is the drag coefficient, A_p is the cross section area of the particle, m is the mass of the particle and x is axial position. The energy of the impact is

absorbed in disintegration of the agglomerates with only a fraction of the kinetic energy available for plastic deformation of individual Al-Si particles.

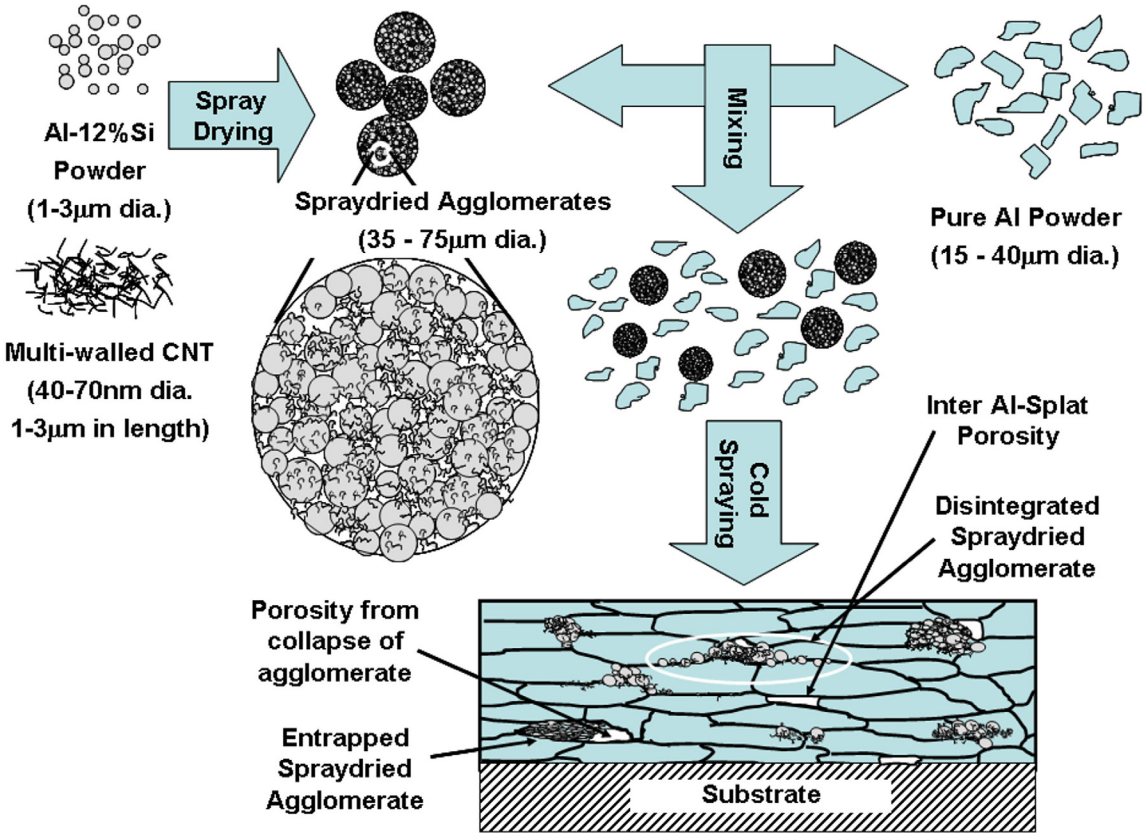

Fig. 4.25: Schematic of the steps involved in the fabrication of the composite

There are only a few studies on the impact breakage of agglomerates [237, 238]. In these studies, breakage of agglomerates has been simulated using Distinct Element Method (DEM). Thornton and co-workers [237] have simulated the breakage of an agglomerate of 1000 particles having a radius, solid density, Young's modulus and Poisson's ratio of 100 μm, 2650 kgm^{-3}, 70 GPa and 0.3 respectively which are close to the properties of the Al-Si eutectic alloy. The coefficient of friction and surface energy were assumed as 0.35

and 3.0 Jm^{-2} respectively. It was concluded that for velocities of impact of 1 ms^{-1} there is extensive damage to the structure [237]. Hence, it is expected that under the high velocity (~600 ms^{-1}) impact in cold spraying the spray dried particles will disintegrate.

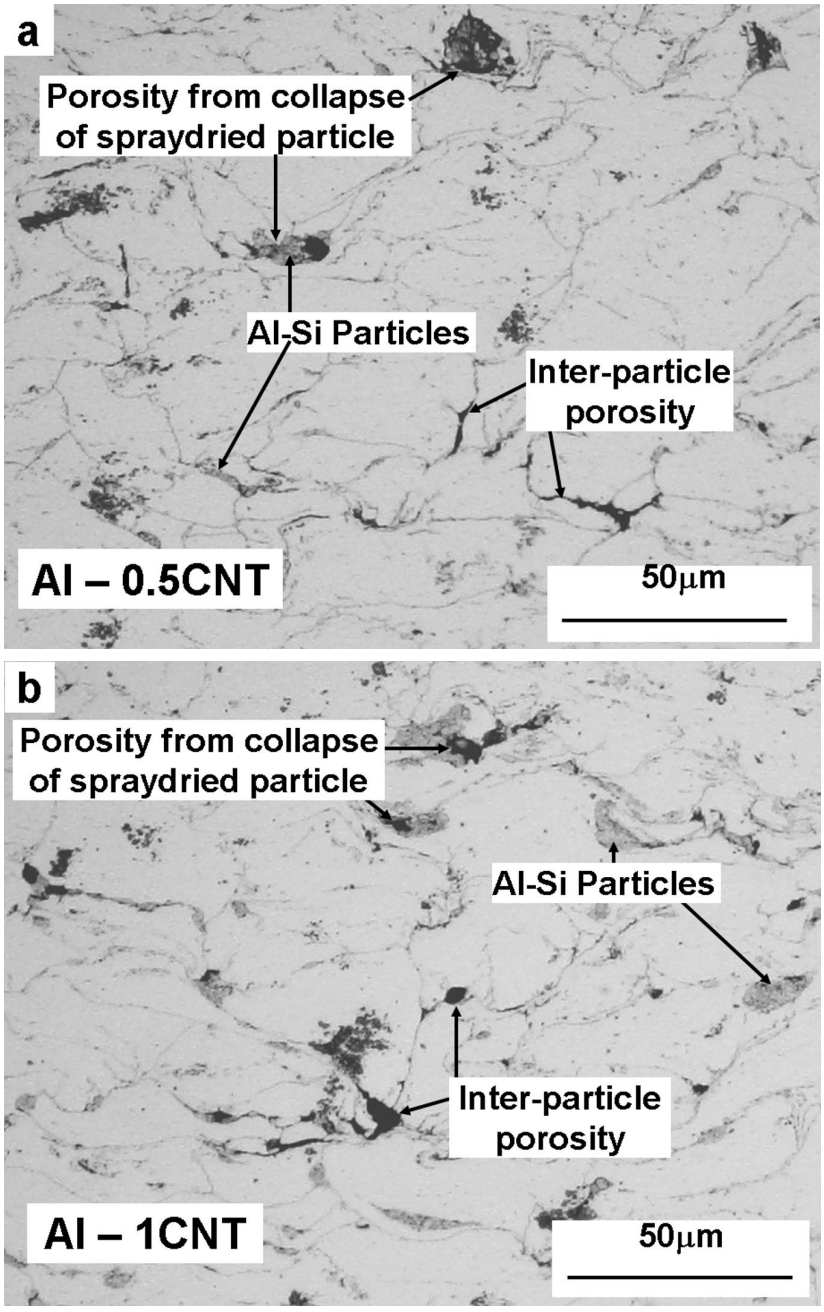

Fig. 4.26: High magnification optical micrographs of the cold sprayed coatings

Figure 4.26 shows the high magnification optical micrographs of the polished and etched cross sections of the Al-0.5CNT and Al-1CNT coatings. It can be seen that thick and dense coatings were formed by cold spraying. Three distinct features seen in the optical micrographs are: deformed Al particles; Al-Si particles from collapse of the spray dried particles; and porosity. The Al-Si particles were found in between the deformed Al particles. Al particles had undergone a large amount of plastic flow to form elongated disc like particles which are often referred to as splats. Papyrin and coworkers [239] have measured the plastic strain (ε_p) in the individual particles from the deformed shape of cold spray deposited single particles and have correlated it empirically to the material properties and the velocity of the particles as follows.

$$\varepsilon_p = \exp\left(-1.4\frac{H_p}{\rho_p v_p^2}\right) \qquad \text{Equation 4.4}$$

Here ε_p is the strain in the particle, H_p is the hardness of the particle (MPa) and ρ_p and v_p are the density and velocity of the particles on impact respectively. The velocity of the Al particles measured by laser particle image velocimetry under similar conditions was found to be 636±20 ms^{-1} [240]. The measured hardness of the aluminum powder particles was found to be 315 MPa and so from equation 4.4 the corresponding plastic strain in the particles comes out to be 0.66 which is a very significant degree of plastic deformation. Under similar conditions, the strain of an Al-Si particle having a hardness of 1260 MPa comes out to be 0.19. So it is expected that the Al-Si particles will have undergone much lower amounts of deformation due to impact (assuming that the particles adhered and did not disintegrate or rebound).

The porosity for the Al-0.5CNT and Al-1CNT coatings were found to be 1.6±0.5% and 2.3±0.9% respectively. This indicates that dense coatings can be sprayed which is one of the main advantage of cold spraying. Two types of pores are seen. The first type is between the Al particles and the second type which happens to be the major one is present adjacent to locations where the spray dried agglomerate is entrapped. When the spray dried particles get entrapped between deforming Al splats, the porosity is squeezed out which gets entrapped as the second type of porosity. Kang et al. [175] have used cold spraying to deposit spray dried agglomerates of tungsten and copper. It was found that the porosity was mostly found at the coalesced tungsten particles and that while the spray dried particle had 75 wt.% W, the coating had only 37 wt.% W in it.

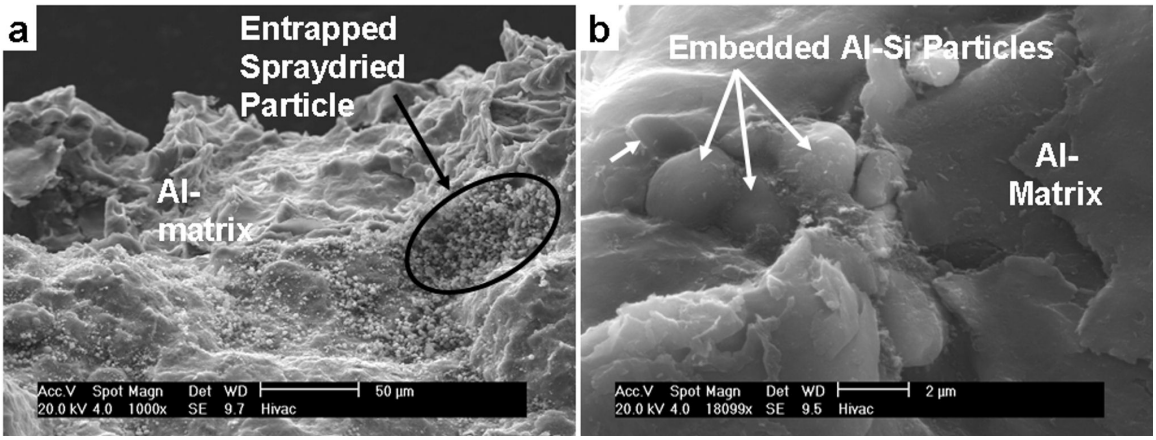

Fig. 4.27: SEM micrograph of Al-0.5 CNT coating showing a) entrapped spray dried particle in Al matrix, and b) high magnification image showing embedding of Al-Si particles in Al matrix

Figure 4.27 shows the SEM of the fracture surface of the Al-0.5CNT coating. Figure 4.27a shows an entrapped spray dried particle. Many Al-Si particles are also seen

due to disintegration of spray dried particles. Figure 4.27b shows Al-Si particles embedded in aluminum matrix with a mechanical bond apparently existing between the two. It is seen that the Al-Si particles penetrates into the Al matrix (marked by the arrow) owing to their high hardness of 1260 MPa, which has an effect of indenting the softer Al matrix. However, most of Al-Si particles are not well bonded to the Al matrix due to the lower amount of energy available after disintegration of the agglomerate.

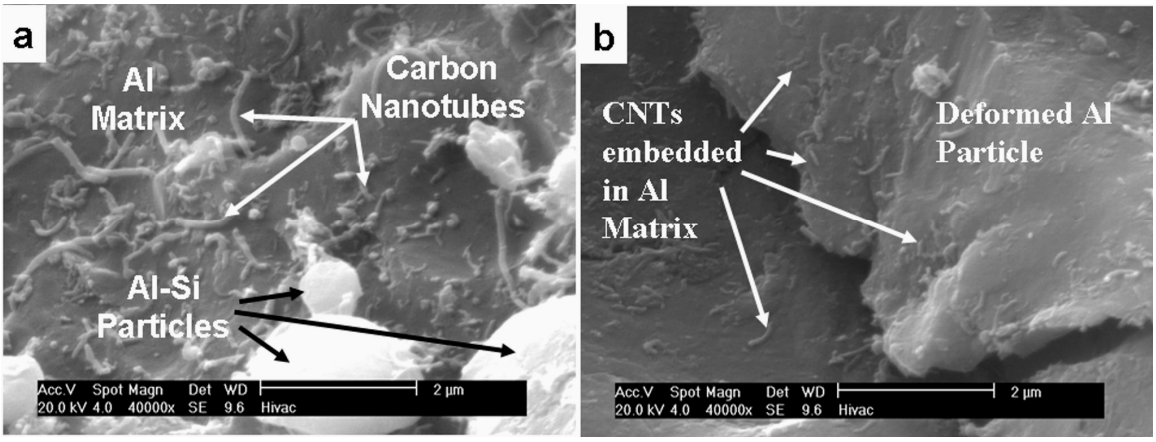

Fig. 4.28: SEM of fracture surface showing a) good distribution of nanotubes, and b) CNTs embedded in Al particle

As a consequence of the disintegration of the spray dried powder, CNTs are fragmented and are evenly distributed in the matrix. It is seen from figure 4.28a that CNTs appear to be homogeneously distributed between the Al splats. Figure 4.28b shows CNTs embedded in Al matrix forming a mechanical bond. The bonding between Al and CNTs might not be strong. This is expected since there is no thermal energy input and the occurrence of a chemical reaction between Al and CNT will require some minimum activation energy. Interfacial bond formation is a prerequisite for shear stress

transfer and reinforcement of the matrix which is the basis of the shear-lag theory for short fiber reinforced composites. In a recent research, Salas et al. have consolidated Al – CNT mixtures using a shock wave technique [143]. It was observed that most of the CNTs were found at the Al particle triple points. CNTs formed an agglomerated carbonaceous mass and displayed extensive damage. Cold spraying also involves high impact consolidation though less aggressive than shock wave techniques.

Figure 4.29 shows high magnification TEM images of the cold sprayed Al-1CNT coating. The microstructural characteristics of cold sprayed aluminum were discussed by Balani et al. in case of cold sprayed Al 1100 alloy [165]. From Fig. 4.29a it is observed that there is sub-cell type structure formation. Cold spraying is a high velocity impact severe deformation process and leads to generation of lots of dislocations. These dislocations might rearrange to form cell structure. An inter-splat interface between two deformed particles is also seen. There are a lot of free graphene sheets too. These are more clearly visible in Fig. 4.29b. These graphene sheets are a result of mechanical damage of CNTs due to shearing forces between particles. The deformation and damage of carbon nanotubes in cold sprayed coating is discussed in the section 4.6.2.

It has been shown that cold spraying can be successfully used for generating CNT-reinforced coatings. Spray dried powders could not be directly deposited. Advantage of the high ductility and deposition efficiency of pure aluminum powders was made use of and the spray dried powders were entrapped between deforming Al particles. Very good CNT distribution was obtained due to disintegration of the spray dried agglomerates.

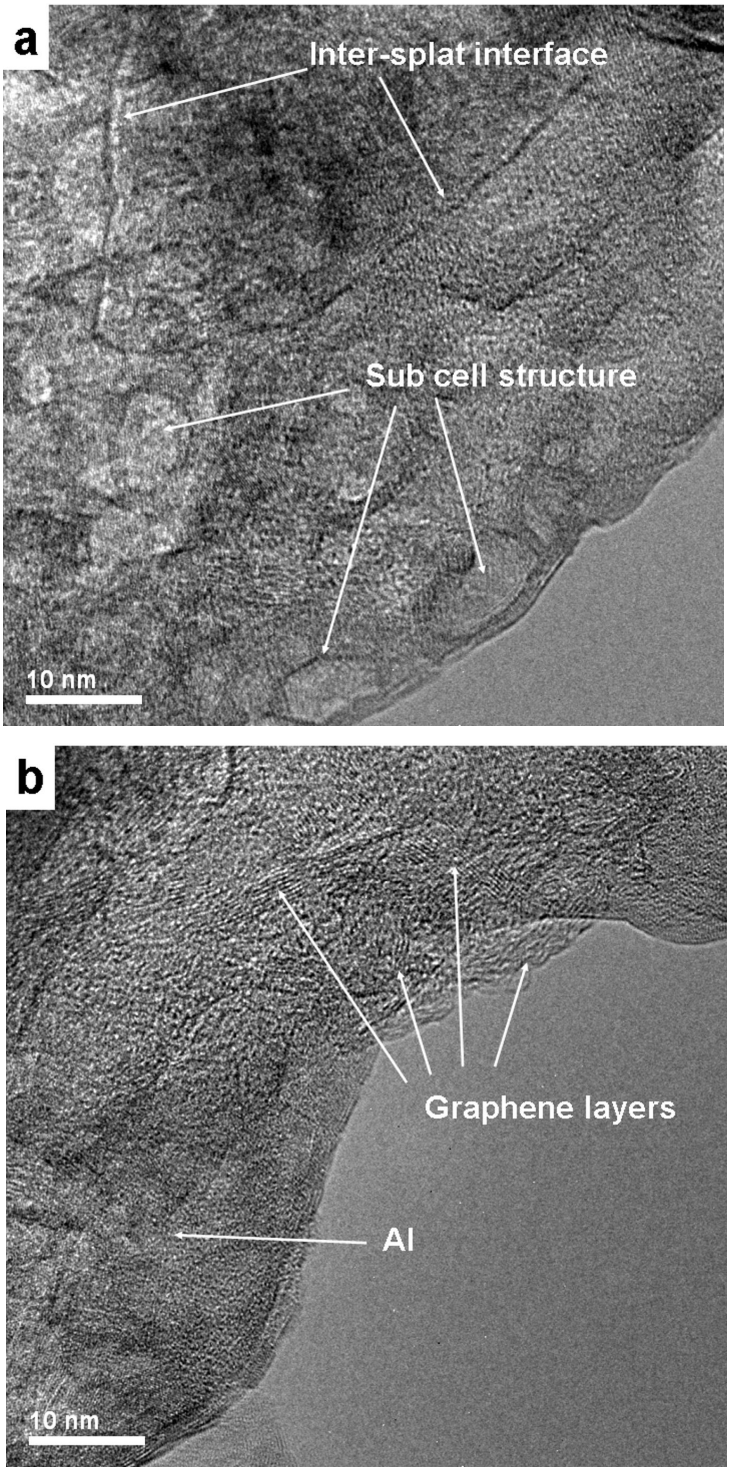

Fig. 4.29: TEM micrographs of Al-1CNT coating showing a) sub-cell structure and inter-splat interface and b) free graphene layers generated due to damage of CNTs

4.4. Quantification of CNT Distribution in Composites

The main challenge in processing CNT composites remains to obtain homogeneous distribution of CNTs in the matrix. It has been shown that there is deterioration of properties due to clustering and inhomogeneous distribution of CNTs at large fractions of reinforcement [60, 80]. Cha and coworkers [19] have obtained more than 200% increase in yield strength by employing powders obtained using a molecular-level mixing method. They have attributed the success to the homogeneous distribution of carbon nanotubes obtained by molecular mixing. However, the degree of distribution of CNTs was not defined or quantified. The elastic modulus, strength and thermal properties of a composite are related to the volume fraction of the reinforcement added. Hence, a homogeneous distribution of filler/reinforcement is essential as it translates into homogeneous properties of the composite. The quantification of dispersion of second phase materials is of interest in many fields of science. There has been hardly any study in the quantification of dispersion in carbon nanotube composites. Majority of the researchers mention uniform CNT dispersion in the composites which is based on visual examination of the microstructure. Attempts to quantify the CNT distribution have not been made in any of the works.

In the present study, two methods are suggested to quantify the spatial distribution of carbon nanotubes in nanocomposite. Two dispersion parameters are presented, one based on the image analysis and the second based on the distance between nearest neighbors (obtained by constructing the Delaunay triangulation of the centers of the nanotubes). We believe this is more appropriate as well as effective while studying the

extent of clustering. The CNT dispersion scheme has been developed using SEM images of cold sprayed coatings and will be finally applied to plasma sprayed coatings.

4.4.1. Image Analysis Method

The CNT distribution in a given micrograph has been quantified using image analysis. It is difficult to obtain binary image of micrographs for CNT composites using thresholding since the contrast is generally low and thresholding leads to errors in demarcation of CNTs from the matrix. Figure 4.30 shows the fracture surface of a cold sprayed Al-0.5CNT coating. The fracture surface represents the splat surfaces since the fracture occurred between the splats. It can be seen that the carbon nanotubes (CNTs) are distributed *"uniformly"*. Figure 4.30b shows a binary image obtained by manually drawing over the CNTs. The black lines represent the CNTs. Only intact and undamaged CNTs were taken into account. Carbonaceous matter or highly damaged CNTs are not taken into account which is another advantage of the present method. The thickness of all the lines was taken to be same and approximately equal to the average value of the CNT diameter (66 nm). Figure 4.30b has been used for further analysis. Figure 4.30b can be converted into a binary image file, which consists of values of 0 or 1 for each pixel depending on whether it was white or black respectively. Then the image is divided into a number of parts or cells and the carbon nanotube (CNT) fraction in each cell is measured in terms of the fraction of pixels that are black. The CNT fraction in each cell is then plotted as a function of the location of the cells on the micrograph. This gives an idea of how the CNTs are spatially distributed in the micrograph.

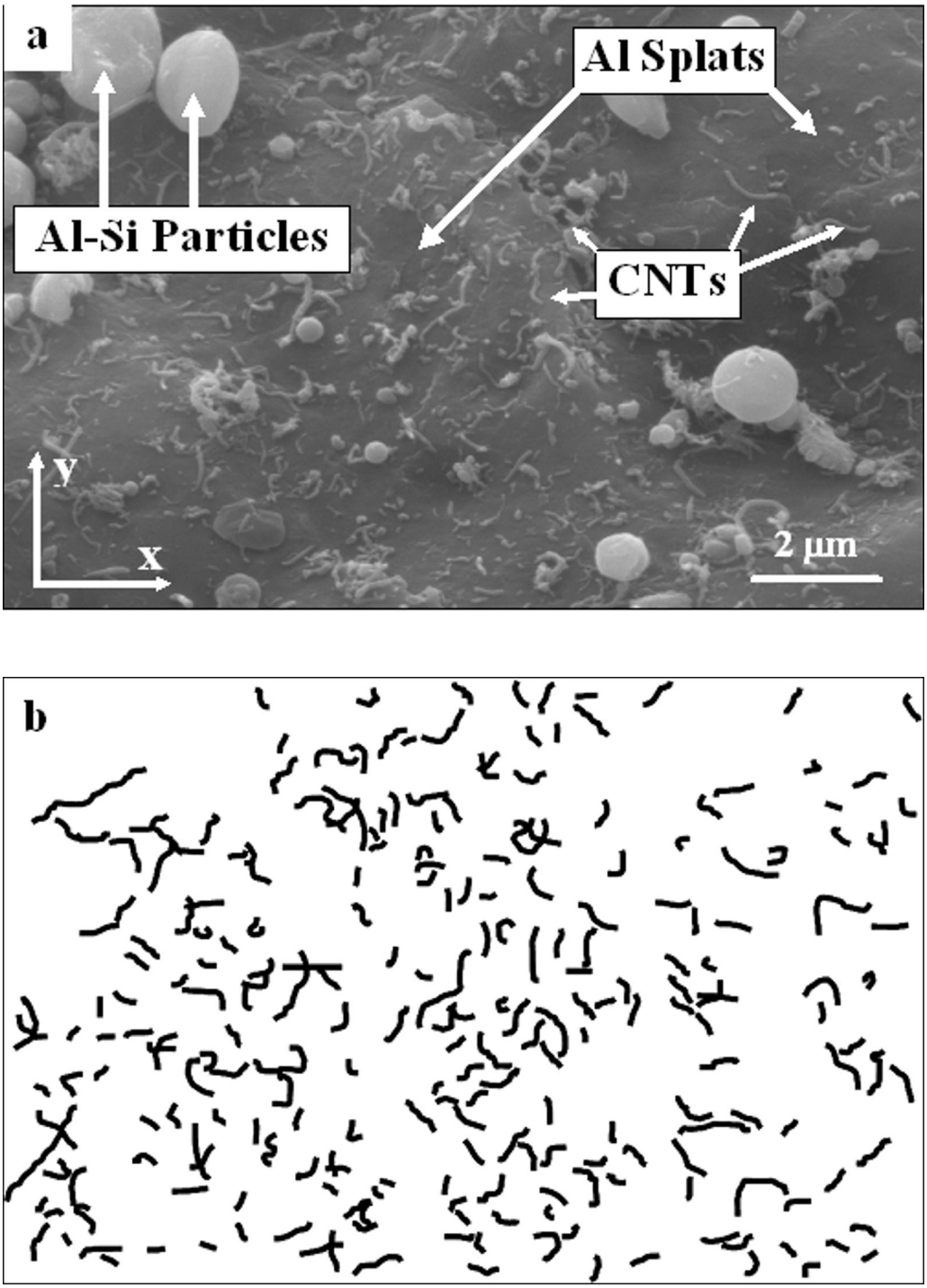

Fig. 4.30: a) SEM micrograph of the fracture surface of the CNT reinforced Al coating, and b) schematic of the CNTs distributed in the micrograph

The number of divisions used in the present case was 225. So each cell has a width and height that is $1/15^{th}$ that of the total width and height of the micrograph. The number 225 was chosen because it leads to a maximum cell dimension of approximately 1 μm. So it can be said that the CNT distribution was quantified down to an area of 1 square micrometer. The spatial distribution of the area% occupied by CNT has been plotted in Figures 4.31a and 4.31b that represent 3-dimensional surface plot and 2D contour maps, respectively. All dimensions in the contour maps are in micrometers. The x-dimension represents the width while y-dimension represents the height of the micrograph. The contour lines in Fig. 4.31b are the traces of the planes cutting the surface shown in Fig. 4.31b at the respective CNT area%. This provides a way of quantifying the CNT area% at various locations in a micrograph. It can be seen that CNT percent varies from 0 to 40% over the micrograph on the scale of a micrometer. Figures 4.32 and 4.33 represent the same analysis carried out on two more SEM micrographs of the same composite. The overall CNT area% in figures 4.30a, 4.32a and 4.33a are 9.4%, 9.1% and 9.1% respectively. Microstructures shown in figures 1a, 3a and 4a will be referred to as micrograph 1, 2 and 3 respectively from now onwards.

(i) Effect of Number of Divisions

It is obvious that a uniform distribution of CNT would result in the area fraction of CNT in each of the cells to be nearly equal. In such a case, a statistical analysis of the CNT area fraction of all the cells would result in the variance close to zero. The variance of the values of CNT area fraction of the cells depends on the scatter of the data and hence is an indicator of the quality of the distribution. A higher value of variance

indicates a poor distribution since it indicates a large scatter in the values of CNT fraction in different parts or cells of the microstructure.

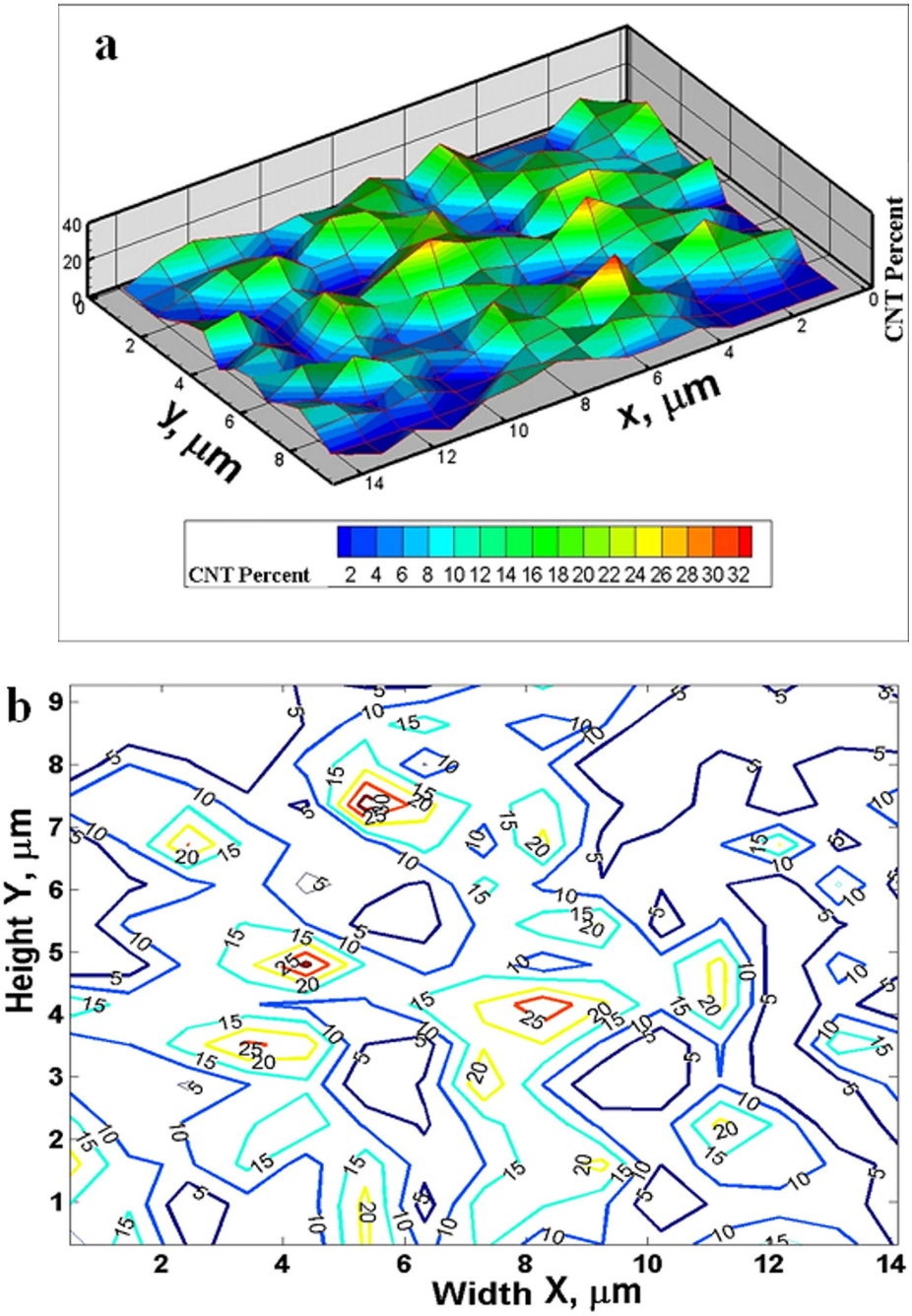

Fig. 4.31: Plots showing a) 3D surface of the CNT fraction variation across the micrograph, and b) 2D contour map of the CNT fraction distribution

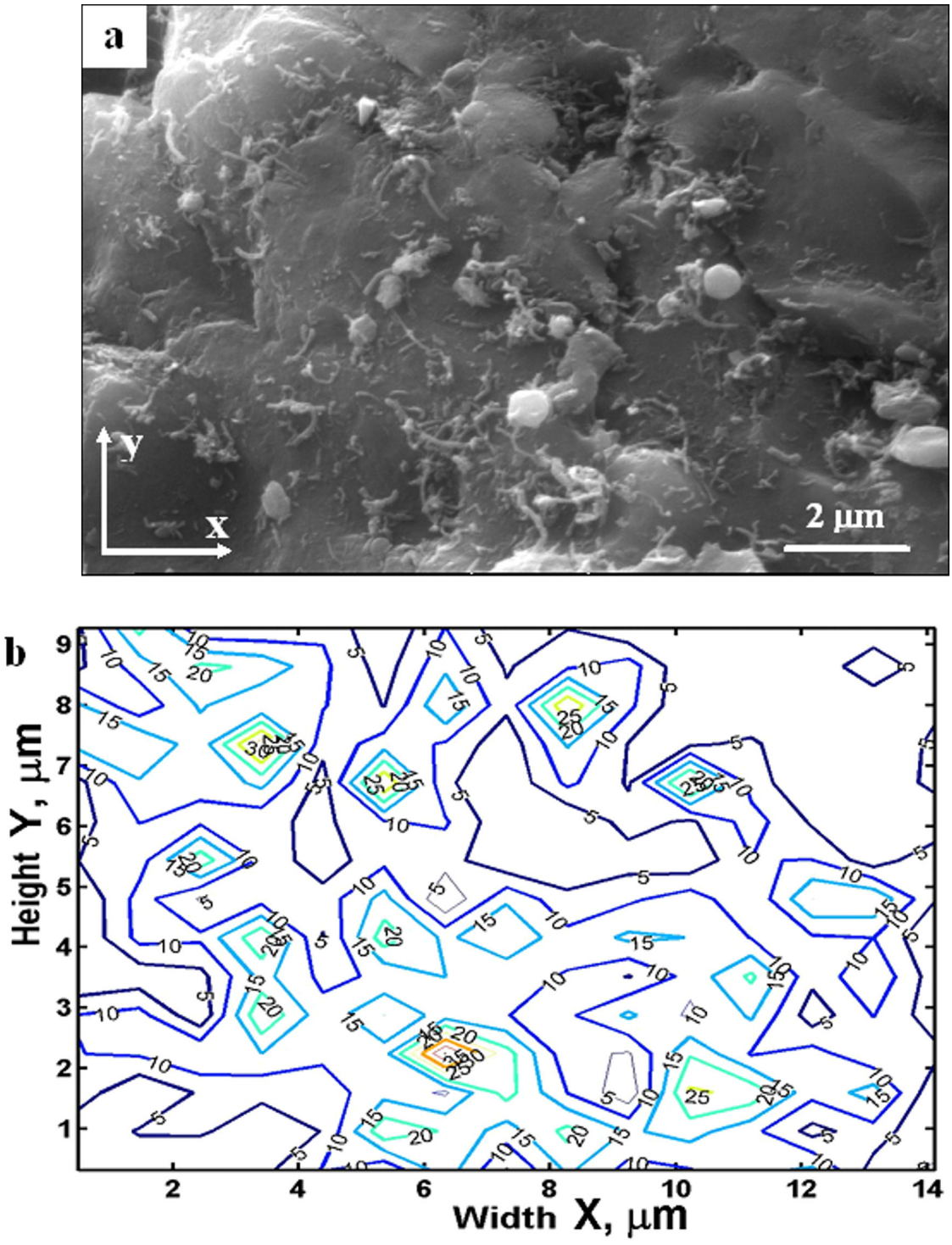

Fig. 4.32: a) SEM micrograph of the fracture surface, and b) contour map of CNT fraction distributed in the micrograph

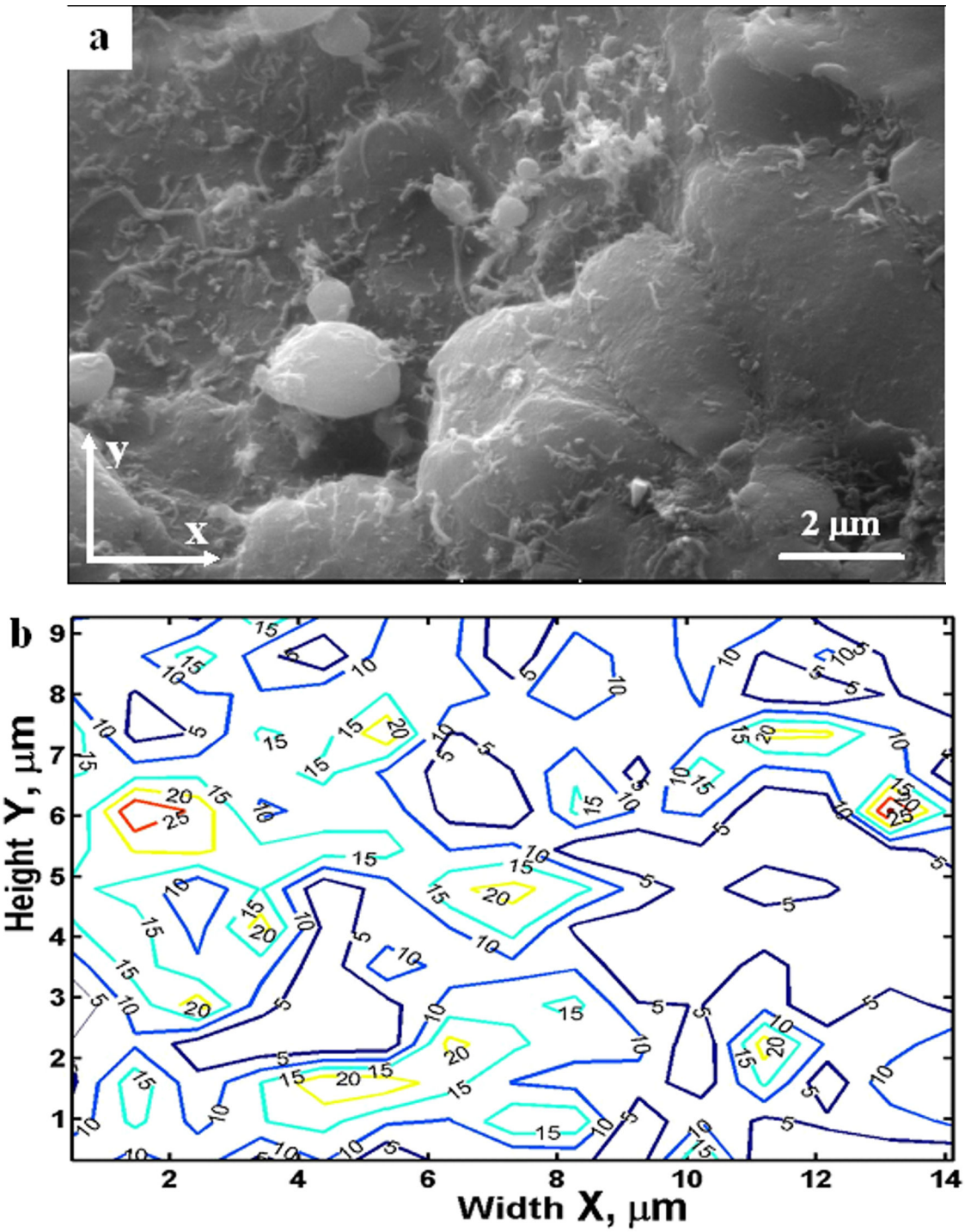

Fig. 4.33: a) SEM micrograph of the fracture surface, and b) contour map of CNT fraction distributed in the micrograph

As the number of cells into which a micrograph is divided increases, the dimension of each cell reduces. Since the dimension of CNT remains the same, the fraction of a cell that is occupied by the CNT will increase with an increase in number of cells. Thus the range of measured values for CNT fraction in a cell will increase on increasing the number of divisions. Also the maximum CNT fraction recorded for a cell will increase as the cell size is reduced. But, the mean value of the CNT fraction of all the cells would remain same, which is equal to the overall CNT content regardless of the number of divisions. Consequently, the variance of the values of the CNT fraction in a cell also increases with the number of cells.

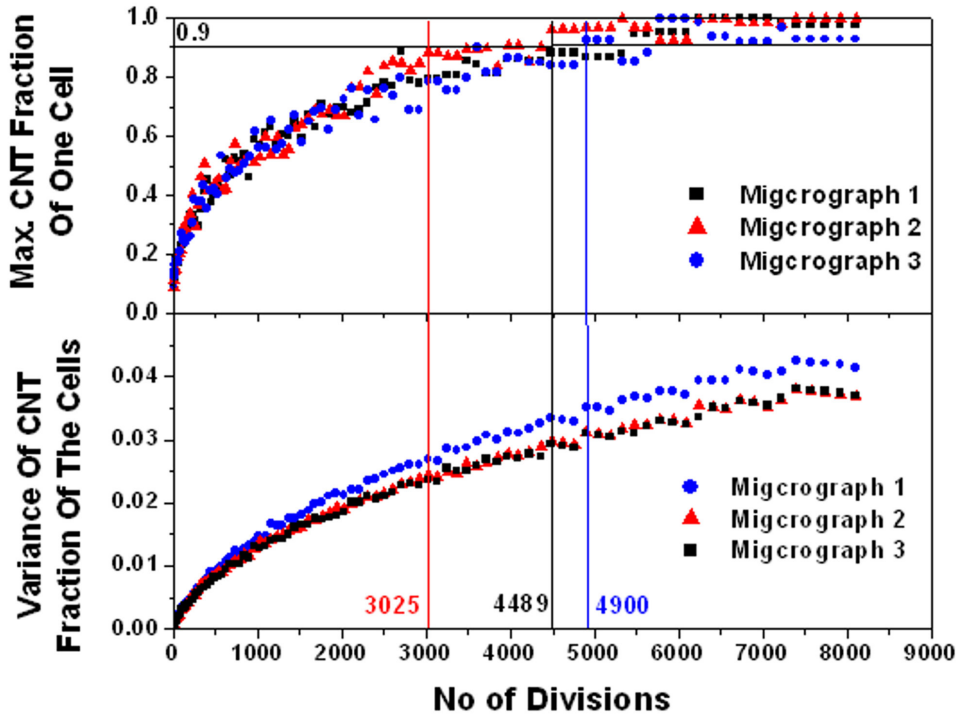

Fig. 4.34: Plots showing the standard deviation of CNT volume fraction in the cells and maximum CNT fraction in a cell with the number of divisions carried out

Figure 4.34 shows the plot of the variance and maximum volume fraction measured for a cell as a function of number of divisions of the micrograph. It is seen that the values of variance and maximum CNT fraction of a cell increases rapidly with the number of divisions during initial stages but the rate decreases afterwards. The curves are almost similar for the three micrographs indicating similar and consistent kind of distribution.

We define CNT cluster as an area/cell containing more that 90% CNT. The extent to which the micrograph must be divided in order that one or more cells show a CNT fraction of 0.9 indicates the size of CNT cluster. The higher is this number of divisions, the smaller is the cell and hence CNT cluster size and hence better is the distribution. Further divisions of the micrograph after that are expected to result in more and more cells having 90% CNT area or more. *So for a given overall CNT fraction, the critical number of divisions leading to observance of clustering indicates the extent of distribution of CNT.* The width of the image is 14.6 μm and the mean diameter of the nanotube is 66 nm which is approximately $1/220^{th}$ part of the width. This means that if the image is divided 220 x 220 = 48400 times, at least one cell would cover a CNT and will show a CNT fraction of 100%. This is the case of uniform distribution when all the CNTs are not touching and are separated. But when they are clustered, a lesser number of divisions would result in at least one cell having 100% CNT. The extent of dispersion or distribution can be estimated by a dispersion parameter DP which is defined below taking into account the overall CNT fraction.

$$DP = \frac{N\left(At\ Least\ One\ Cell\ has\ CNT\ \ fraction = 0.9\right)}{N\left(Cell\ size\ equals\ CNT\ diameter\right) x\ Overall\ CNT\ Fraction} \quad \text{Equation 4.5}$$

Here N refers to number of divisions. Division by the overall CNT fraction makes the parameter independent of the CNT fraction. From Fig. 4.34 it is seen that the number of divisions for which CNT fraction of a cell reaches 90% is approximately 4489, 3025 and 4900 for three microstructures in Figs. 4.30a, 4.32a and 4.33a respectively. Thus, DP equals 1.07, 0.74 and 1.20 for three micrographs respectively. It can be concluded that Figure 4.33a has *most uniform* distribution amongst all and micrographs Figure 4.32a has *least uniform* CNT distribution. The average value of DP for the Al-CNT nanocomposite is 1.0. This value indicates an *overall uniform* distribution as also observed in the three micrographs. The exact dependency of DP on CNT fraction is difficult to be determined since it will require the analysis of micrographs of similar dispersion but different overall CNT fractions, which are hard to obtain due to processing technique limitations.

(ii) Effect of Aspect Ratio and Orientation

Carbon nanotubes have a varying aspect ratio and random orientation in most of the nanocomposites. To study the effect of the aspect ratio and orientation of the CNT filler material, model structures were drawn as shown in Fig. 4.35. Figures 4.35a, 4.35b, and 4.35c have uniformly aligned reinforcement with increasing L/D ratio from 1 to 4 while filler material has random orientation in figure 4.35d. The fraction of filler material is kept the same in all the schematics and is equal to 9.5 area % which is close to the CNT fraction in the actual micrographs 1, 2 and 3. This will help in comparing values of the dispersion parameters obtained for experimental micrographs (Fig. 4.30a, 4.32a and 4.33a) and the schematics (Fig. 4.35).

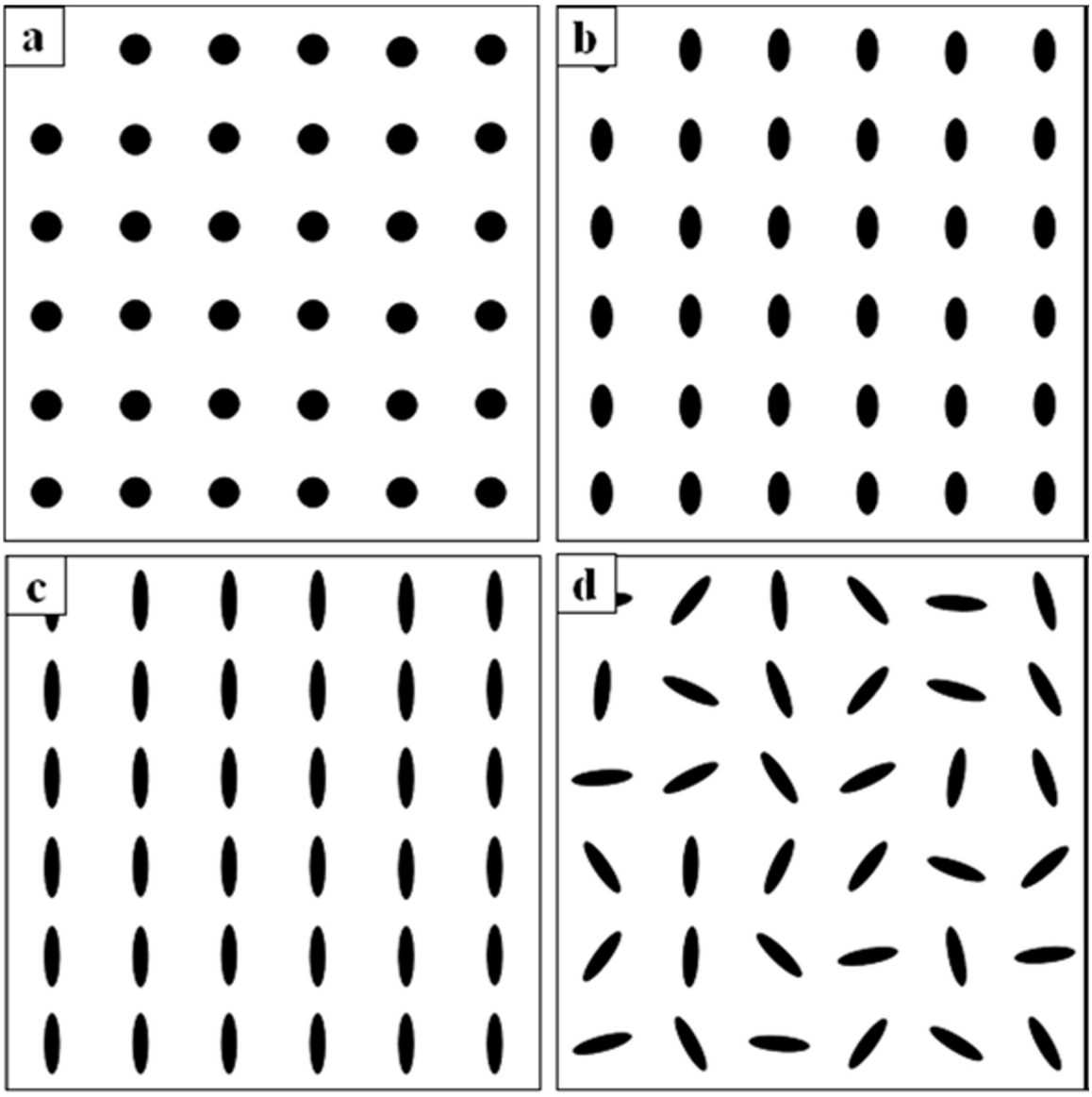

Fig. 4.35: Model microstructures of composites of filler materials having a) L/D = 1 aligned, b) L/D = 2 aligned, c) L/D = 4 aligned, and d) L/D = 4 random orientation

Figure 4.36 plots the maximum CNT fraction measured for a cell and the variance of the values of CNT fraction in the cells as a function of number of divisions of the

figures. It is seen that the graphs of maximum CNT fraction in a cell vs. number of divisions for L/D = 1 and L/D = 2 are significantly different from L/D = 4.

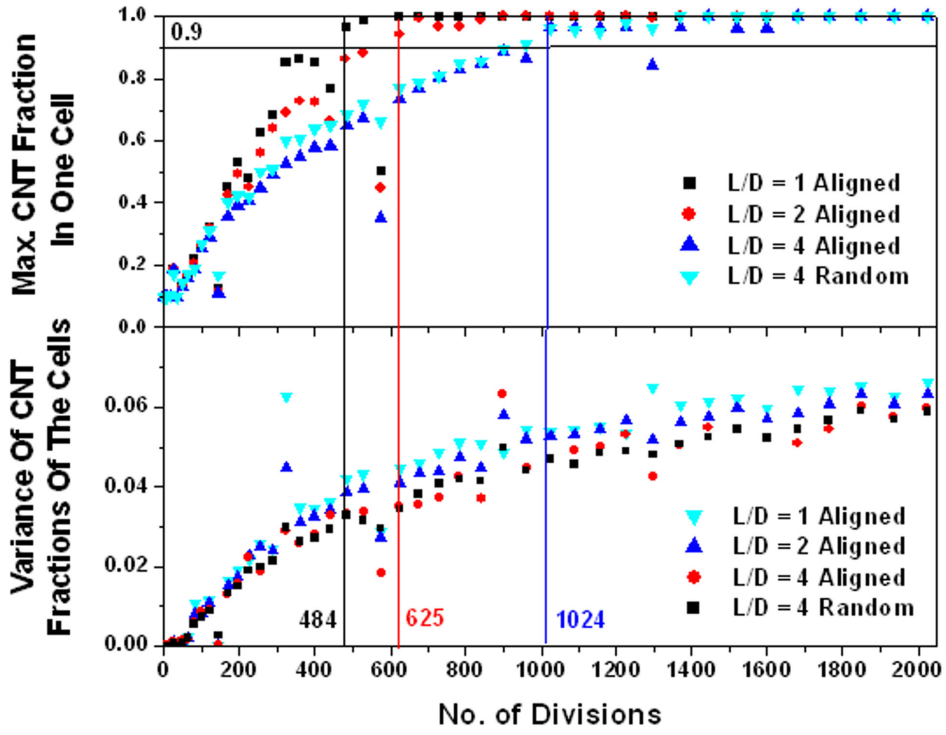

Fig. 4.36: Plot of the variation of standard deviation and maximum CNT fraction in a cell with no. of divisions for the model structures

The diameter of the reinforcement is more significant in determining the dispersion parameter. It is obvious that it takes less number of divisions for the CNT fraction in a cell to reach 100 percent when L/D =1 as compared to when L/D = 4 since the size of a square that just fits into a circle is larger than that for an ellipse of same area. Hence, it will affect the value of dispersion parameter DP. It indicates that our analysis holds accurate for nanocomposites with narrow diameter range for the CNTs. Most of the CNTs found in the microstructure had a diameter between 40 – 80 nm which is a spread

of 40 nm (less than 0.5% of the width of the micrograph). Hence, assuming that all the CNTs have a diameter same as the mean value of 66 nm does not affect the calculations significantly. The spatial arrangement of the CNTs will be reflected in the value of DP when long CNTs are curved or broken down so that they form clusters. It is observed that orientation does not have much affect on the curves as seen in the plots for Figs. 4.35c and 4.35d which almost overlap in Fig. 4.36. The value of DP for Figs 4.35a, 4.35b and 4.35c are equal to 9.3, 10.5 and 9.6 respectively, which are quite large as compared to that calculated for the micrographs 4.30a, 4.32a and 4.33a. This is attributed to the uniform distribution and the small aspect ratio of the filler materials in Fig. 4.35.

4.4.2. Delaunay Triangulation Method

Delaunay triangulation of a set of points is the construction of triangles connecting the points such that no point falls inside the circumcircle of any triangle. This gives rise to triangles connecting a point to its nearest neighbors. The sides of the triangles then represent the distances between nearest neighbors. These distances are related to the manner in which the points are distributed in space. Also the number of nearest neighbors gives information about the coordination. Delaunay triangulation has been used extensively in fields for characterizing distribution in particulate reinforced composites [241], distribution of pores [242] and in hard sphere packing [243]. However, such studies have been made on model microstructures and there is no study on the use of Delaunay triangulation for CNT composites. In the present work, a simple method is proposed to quantify clustering phenomena in CNT composites based on the actual micrographs. Here, points are taken at the center of the nanotubes as shown in Fig 4.37a.

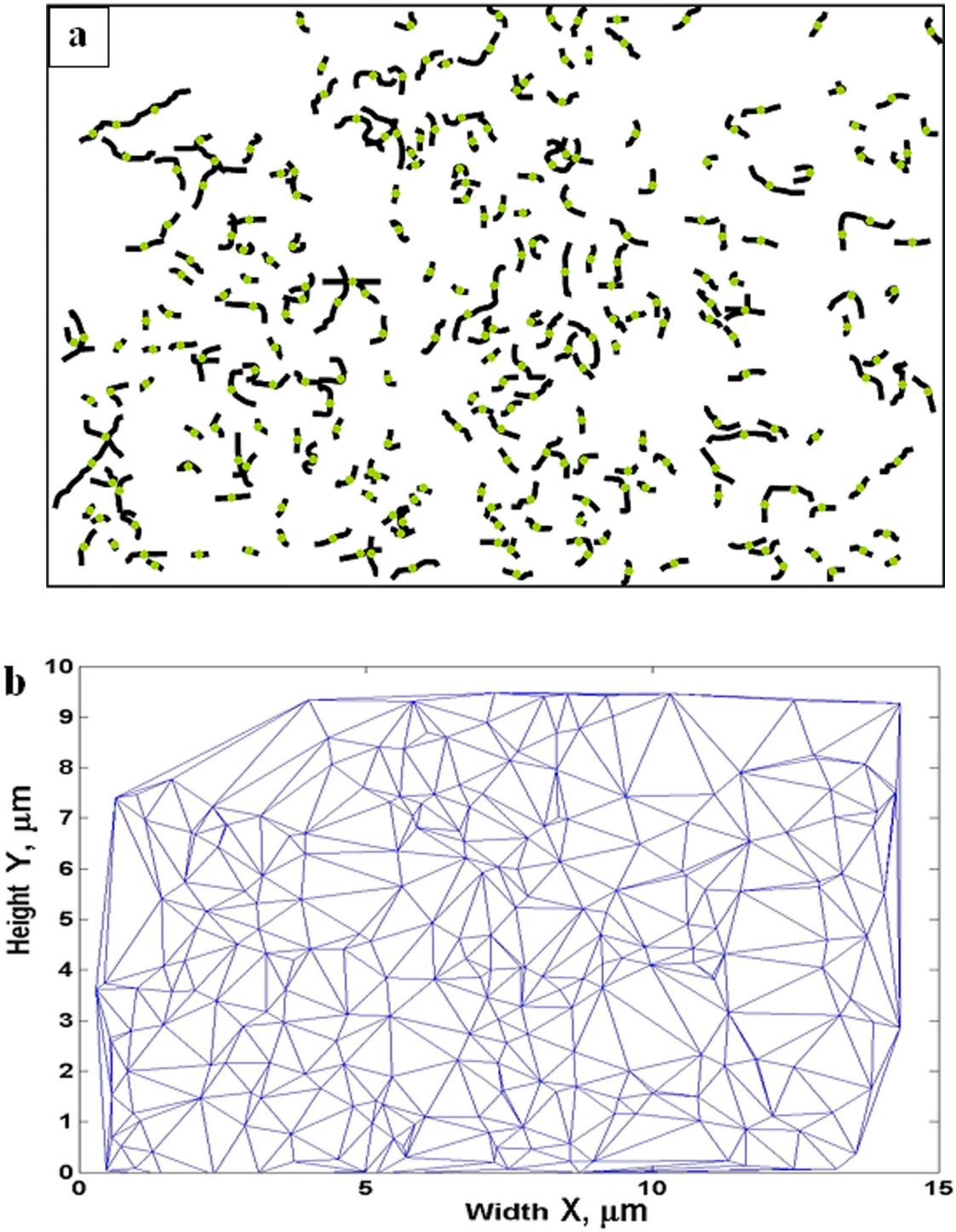

Fig. 4.37: a) Schematic of the way the points are taken for the nanotubes, and b) the Delaunay triangulation of the points

In cases where the nanotube is long and curved, points are taken on the center of each linear part of the nanotube. Then a Delaunay triangulation is performed as shown in Fig. 4.37b. The sides of the triangles when collected give the distance between nearest neighbors counted twice. But for the triangles situated at the periphery, the side making the periphery is counted only once. So a convex hull operation is carried out which gives the polygon making up the periphery. Then the sides of the polygon are measured and included in the group containing the sides of the triangles. This leads to a group containing the distance between all nearest neighbors counted twice. A statistical distribution of this group is then carried out. The mean and standard deviation of the values then characterize the distribution of the points or nanotubes. *For a given overall CNT fraction, the large value for the mean spacing of the points and a small value of the standard deviation indicate a better and uniform distribution.*

Delaunay triangulation was carried out on the three micrographs shown in Fig. 4.30a, 4.32a and 4.33a. Subsequently, statistical analysis is performed to analyze the distribution of the values of the sides of the triangles. Figure 4.38 plots the distribution of the distances between the nanotubes for the three micrographs. It can be seen that a lognormal distribution fits the distribution well. The lognormal distribution is defined by the following.

$$f(x) = \frac{1}{xn\sqrt{2\pi}} \exp\left[-\frac{1}{2}\left(\frac{\ln x - m}{n} \right)^2 \right] \quad \text{for } x > 0, \text{ and} \qquad \text{Equation 4.6}$$

$$= 0 \quad \text{for } x \le 0$$

Where

$$m = \ln \frac{\mu^2}{\sqrt{\mu^2 + \sigma^2}} \quad \text{and} , \quad n = \sqrt{\ln \frac{\mu^2 + \sigma^2}{\mu^2}}$$

μ is the mean and σ the standard deviation.

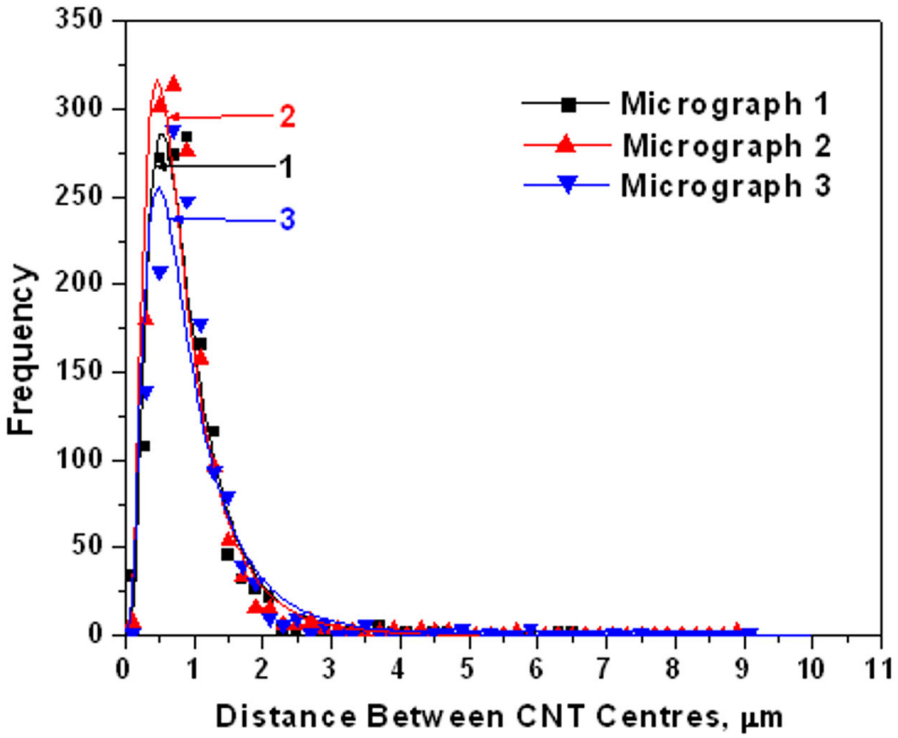

Fig. 4.38: Plots showing the distribution of distance between CNT centers for the three micrographs

It is interesting to note that Luo and Koo [187] also found that the lognormal distribution fitted well for the values of the inter-particle spacing as defined by them. In their analysis, the distances were chosen in horizontal or vertical directions, due to which there is a sense of directionality involved. But when clustering is considered, the distances between particles or fibers must be considered irrespective of the direction. To be more precise, nearest neighbor distances must be considered. A uniform distribution

corresponds to a uniform separation between nearest neighbors. Also the nearest neighbor concept presented here can be extended to three dimensions while the distances used by Luo and Koo are strictly for two dimensional analysis.

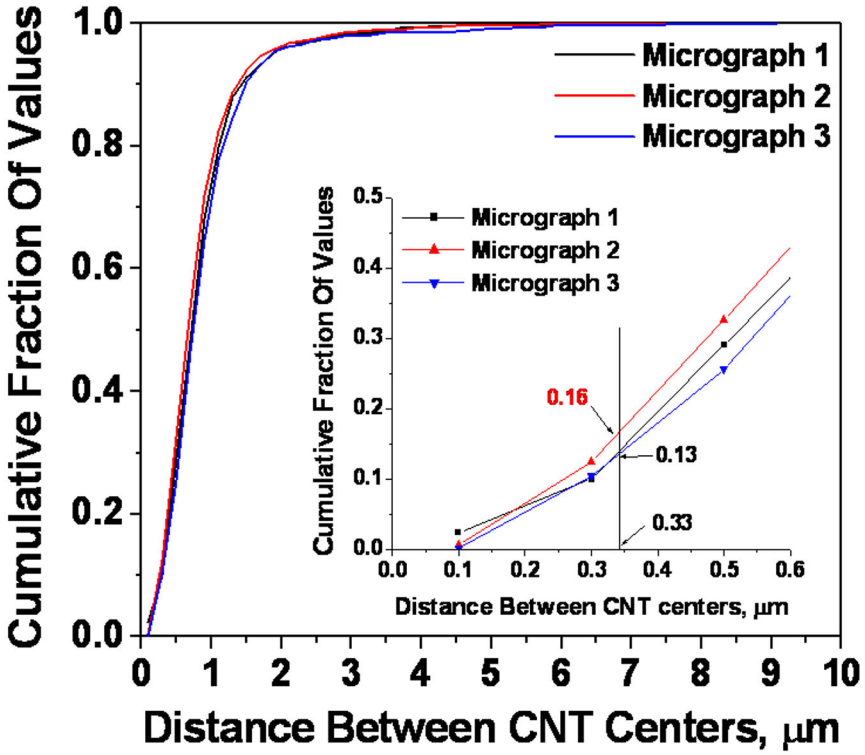

Fig. 4.39: Calculation of clustering parameter for distribution of the distance between CNT centers

A new parameter is defined here which defines the degree of clustering observed in a micrograph. This clustering parameter, CP, is defined based on the fraction of the distances between CNT centers which are less than or equal to 5 times the CNT diameter. A larger value of overall CNT fraction will ensure that the CNTs are closely packed and will lead to an increase in the CP. Hence, CP can be defined as following:

$$CP = \frac{\left(Cumulative\ Fraction\ Of\ \ Distances\ Less\ Than\ Or\ Equal\ To\ 5.D_{CNT}\right)}{Overall\ CNT\ \ Fraction}$$

Equation 4.7

where D_{CNT} is the mean diameter of CNT (66 nm in the present case). A large value of CP will indicate the presence of more clustering. Figure 4.39 shows the plot of the variation of cumulative fraction of values with distance between CNT centers. The inset is a magnified view of the graph at low values of the distance between CNT centers. It can be seen that the fraction of values less than or equal to 0.33 μm for micrograph 1, 2 and 3 is 0.13, 0.16 and 0.13 respectively which leads to a value of CP of 1.38, 1.76 and 1.43 respectively. It is observed that micrograph 2 which had relatively poor CNT distribution shows the highest value of CP too. T

Comparison of the Two Methods

Table 4.4 represents the ***dispersion*** and ***clustering*** parameters (***DP*** and ***CP***) for three microstructures in figures 1a, 3a and 4a.

Table 4.4: Dispersion and Clustering parameter for CNT distribution in the micrographs

Micrograph	**Overall CNT %**	**DP**	**CP**
1 (Fig. 4.30a)	9.4	1.07	1.38
2 (Fig. 4.32a)	9.1	0.74	1.76
3 (Fig. 4.33a)	9.1	1.20	1.43

DP is a parameter which is obtained from the image directly and represents dispersion, while CP is the derived parameter obtained from the distances between nanotubes and represents clustering. A higher value of DP and lower value of CP is indicative of good CNT distribution. Based on DP, it was earlier concluded that dispersion is relatively better in micrograph 3 (Fig. 4.33a) and relatively poor in micrograph 2 (Fig. 4.32a) which can be verified visually from the SEM micrographs. The CP values of micrographs 1 and 3 are low and nearly same (1.38 and 1.43) suggesting better and similar degree of dispersion. The CP value of micrograph 2 is higher (1.76) showing relatively poor dispersion. Hence, it is concluded that DP and CP serve as consistent parameters in describing the extent of CNT dispersion and clustering in a given micrograph.

4.4.3. Comparison of CNT distribution in Plasma and Cold Sprayed Coatings

The CNT distribution quantification was carried out for plasma sprayed coatings also. Figs. 4.12b and 4.12d were used and binary images file of CNT distribution on the microstructure was analyzed. Figure 4.40 shows the images obtained by quantification process. It is seen that the CNT fraction in a cell reaches 0.9 after 2116 and 2209 divisions for figs. 7a and 7b respectively. The overall CNT fraction in Figs. 4.40a and 4.40b are 0.18 and 0.14 respectively. Considering the CNT diameter to be 66 nm, DP values are 1.4 and 1.1 for micrographs Figs. 4.12b and 4.12d respectively. This indicates that distribution of CNT is better in case of Figs. 4.12b as compared to Figs. 4.12d. This is in accordance with the distribution observed in the splats. It is also observed in general that clustering is high in Al-10CNT (hence relatively poor CNT distribution) due to higher CNT content.

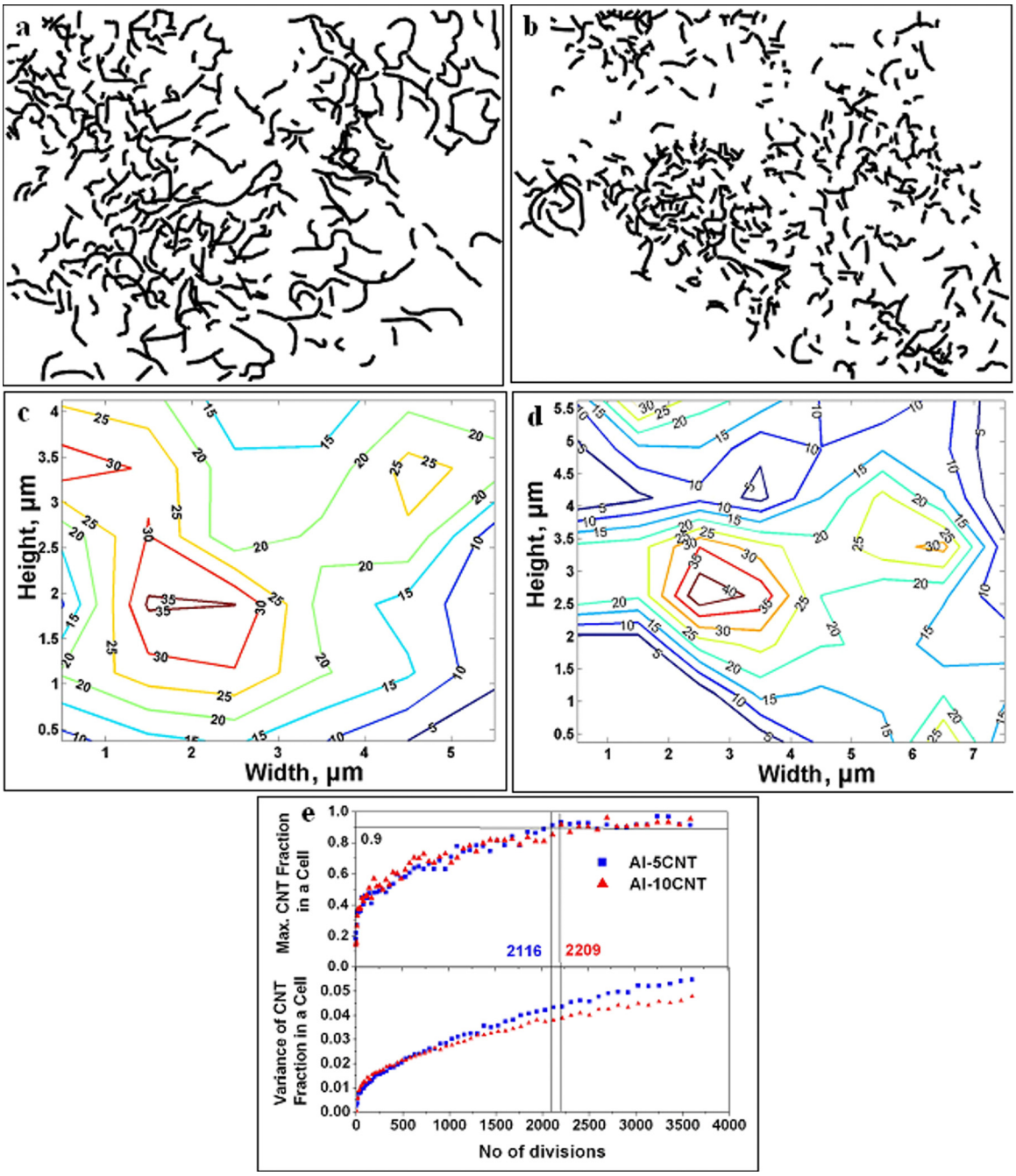

Fig. 4.40 a) and b) Binary schematic images of SEM images 4.12c and 4.12d, c) and d) plot of the corresponding CNT distribution with contours indicating areas of same CNT fraction, and e) plot of maximum CNT fraction in a cell and variance of the CNT fraction in one cell with the number of division carried out

When compared to cold spraying, plasma spraying involves molten alloy and there is larger chance of CNT agglomeration. The CNT distribution with splats indicates that distribution in Al-5CNT is good and comparable to cold sprayed coatings. The determination of CNT coatings requires good binary images to be obtained that resemble as close as possible to the actual micrographs. Use of advanced image processing techniques has to be explored to obtain such images. The proposed quantification technique based on such images would yield better results.

4.5 Chemical Stability of CNTs in Plasma Sprayed Al-Si-CNT Composites

In cold spraying, there is no thermal energy input. So reaction between CNT and aluminum cannot occur. The bonding is purely mechanical between the CNT and aluminum matrix. Aluminum carbide formation was observed from XRD peaks in Fig. 4.14 in plasma sprayed Al-5CNT and Al-10CNT coatings where the matrix was Al-11.6 wt.% Si alloy. Laha et al. had observed the formation of SiC in case of 10 wt.% CNT reinforced Al-23 wt.% Si alloy composite. So the alloy composition has a string effect on the interface. This study highlights the effect of CNT and Si content on the interfacial reaction in Al-Si composites. Thermodynamic and kinetic analysis is used to predict which carbide will form for a given processing temperature and alloy composition. Particular interest is devoted to the interfacial phenomena occurring in Al–11.6 wt.% Si alloy and CNT composite. Thermodynamic calculations were done using thermo-chemical software and database FactSage^{TM} [244]. Images of the crystal structures were obtained using the free software Mercury 1.4.2 developed by the Cambridge Crystallographic Data Centre (Cambridge, UK) while the crystallographic information

file for Al_4C_3 was obtained from the International Union of Crystallography (IUCr) database. High Resolution Transmission Electron Microscopy has been carried out to study the interfacial reactions to validate the theoretical predictions.

4.5.1. Thermodynamic Analysis of Carbide Formation

When molten aluminum silicon alloy reacts with carbon in CNT, there is a possibility of formation of silicon carbide (SiC) or aluminum carbide (Al_4C_3) at the matrix/reinforcement interface. The chemical reactions and the corresponding free energies have been represented by the equations below:

$$\frac{4}{3}[\mathrm{Al}] + \mathrm{C} = \frac{1}{3}\mathrm{Al_4C_3},\ \Delta G^{f}_{Al_4C_3} = \Delta G^{0}_{Al_4C_3} + \frac{1}{3}RT\ln\frac{a_{Al_4C_3}}{(a_{Al})^4} \qquad \text{Equation 4.7}$$

$$[\mathrm{Si}] + \mathrm{C} = \mathrm{SiC},\qquad \Delta G^{f}_{SiC} = \Delta G^{0}_{SiC} + RT\ln\frac{a_{SiC}}{a_{Si}} \qquad \text{Equation 4.8}$$

Here the square [ ] brackets represent that Al and Si are in the molten Al-Si solution and ΔG^0 refers to the standard free energy of formation per mol of carbon, 'a' denotes activity, R the universal gas constant and T the absolute temperature at which the reaction takes place. Representing the equations per mole of carbon makes it easy to study which carbide will form preferentially. For a given alloy composition and temperature, only one of the reactions 4.7 or 4.8 will occur depending on which has a more negative free energy change. The thermodynamic properties of CNTs were assumed equal to graphite due to lack of the data for CNTs. This gives us a comparative analysis for the two

competing reactions which might be accurate for the CNT-alloy system as well, because for both graphite and CNTs the reacting planes are the same (the (0001) basal and the $(10\bar{1}0)$ prism planes). It is assumed that CNTs are pure and activity of carbon can be taken as 1. The activity of Al_4C_3 and SiC can also be taken as unity since there was no evidence of formation of ternary aluminum silicon carbides which would affect the activity of any of them. The activity ('a') is equal to atom fraction ('X') only for ideal solutions. From the reported thermodynamic values for the Al-Si system [245, 246] it is observed that both Al and Si show negative deviation from ideality. Figure 4.41 shows the plot of activity vs. atom fraction for Al-Si alloy at 1700°C [245]. Using the activity of Al and Si for various alloy compositions at different temperatures [246], the free energy of formation of Al_4C_3 and SiC was computed using the 'Reaction' module of FactSage.

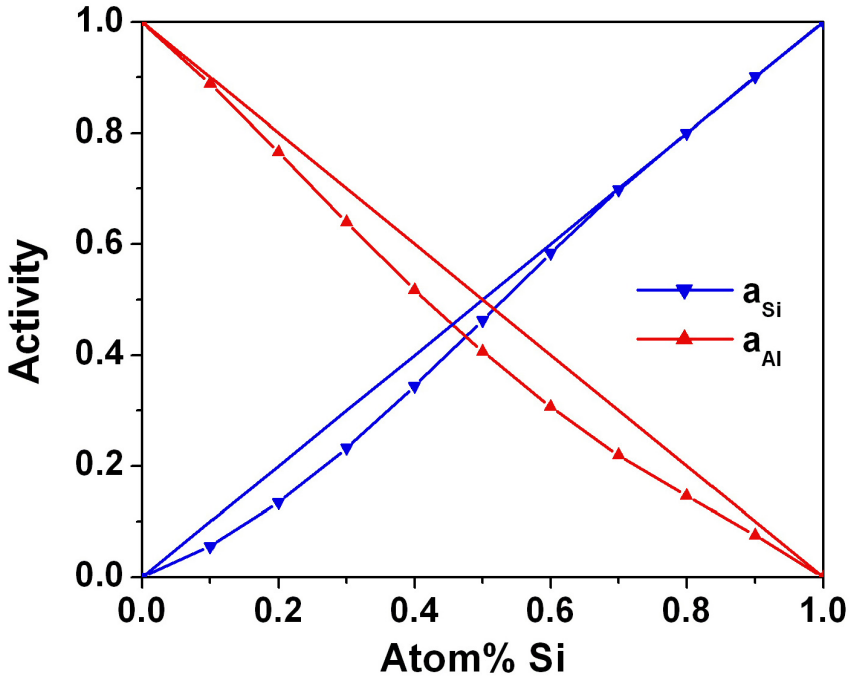

Fig. 4.41: Variation of activities of Al and Si with mole fraction at 1700°C

Figure 4.42 shows the free energy of formation of the carbides per mole of carbon as a function of alloy composition at different temperatures. It is observed that at an experimentally measured temperature of 2300K, which is typically attained by the molten particle during plasma spraying (Table 4.2), the free energy of formation of Al_4C_3 increases with increasing Si content and becomes positive for Si content > 34.8 wt.% (34 atom%). This indicates that Al_4C_3 formation is thermodynamically not feasible at 2300K for Si content > 34.8 wt.%. Also it is seen that the free energy of formation of SiC becomes more and more negative with increasing silicon content of the alloy. It is observed that at 2300K, for alloys with Si content < 21.6 wt.% (21 atom%), ΔG^f_{SiC} is positive which indicates that the formation of SiC is thermodynamically not feasible.

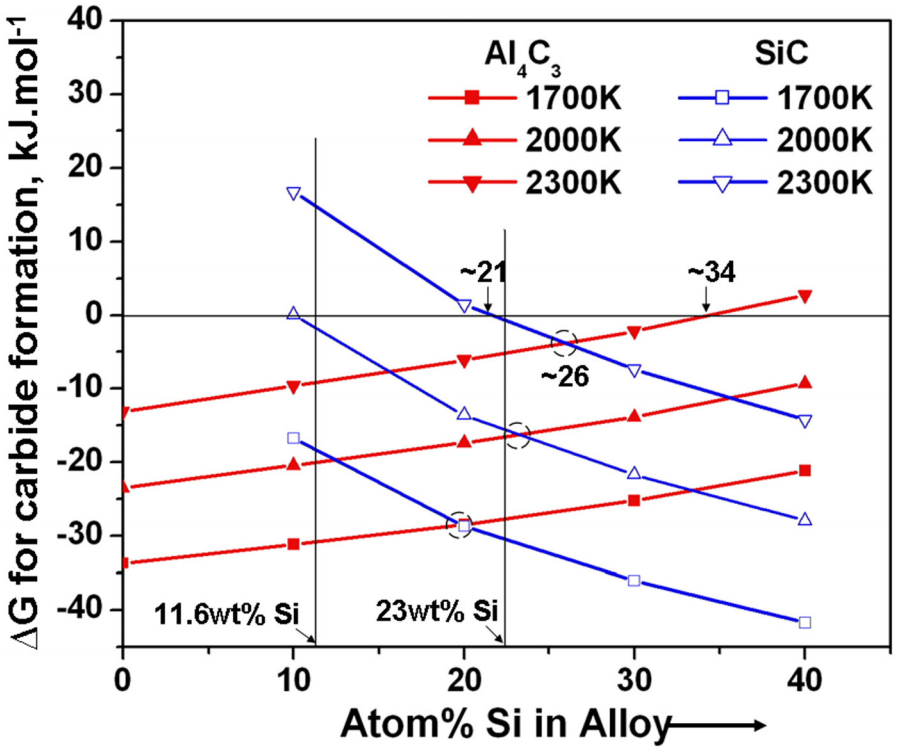

Fig. 4.42: Free energy of formation of Al_4C_3 and SiC per mole of carbon as a function of alloy composition at various temperatures

The open circles on Fig. 4.42 indicate the alloy compositions where the values of the free energy of formation of Al_4C_3 and SiC are equal for the given temperature. These points of intersection of the two curves have been obtained for a series of temperatures and plotted in Fig. 4.42. Figure 4.43 is a pseudo-phase diagram which shows the equilibrium carbide forming at the interface for a given alloy composition and temperature of processing. For any given temperature of reaction, Al_4C_3 will form with all alloy compositions to the left of this line while SiC will form for compositions to the right of the line.

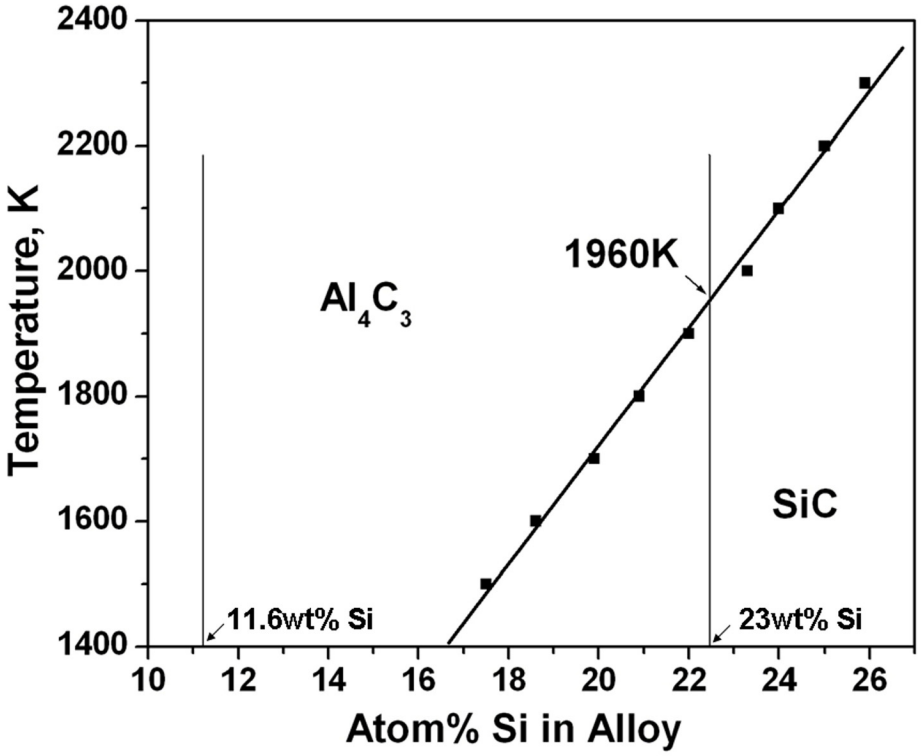

Fig. 4.43: Plot showing the alloy compositions for which free energy of formation of either carbide at various temperatures are equal. For a given temperature of reaction, all compositions to the left of the line will lead to formation of Al_4C_3 while alloy compositions to the right will show formation of SiC

It is seen that Fig. 4.43 predicts Al_4C_3 formation for Al-11.6 wt.% Si alloy. It also validates the observance by Landry et al. [232] of formation of SiC with Al-20 wt.% Si alloy with graphite at 1190K. It is observed that at 2300K, Al_4C_3 formation is predicted with 23 wt.% Si alloy. But for reactions occurring below a temperature of 1960K, SiC formation is predicted from the figure. Laha et al. from our research group previously observed SiC formation in case of 23 wt.% Si alloy [33]. Although the temperature of the particles was not measured experimentally in the Al-23 wt.% Si alloy case, it is expected to be lower than 2300K as observed for the spray dried agglomerates in present case. This is due to the fact that the uniform distribution of CNTs in the spray dried agglomerates particles would lead to better thermal absorption and hence higher particle temperature.

Further equilibrium analysis was carried out using 'Equilib' module of FactSage. This module calculates the equilibrium phases that would be present when a mixture of Al, Si and C is allowed to equilibrate at a given temperature. This is done by calculating the free energies for formation of all possible reaction products and then selecting the final reaction products that minimize the Gibbs free energy of the system. It is to be noted that when Al reacts with C to form Al_4C_3, the Si percent in the liquid melt increases. Increase in the activity of Si will tend to favor SiC formation. For example from Fig. 4.42, at 2300K Al will react and form Al_4C_3 until the wt.% of Si in the melt becomes equal to 26.7% (26 atom%). After that SiC formation is favored. Both the reactions will go on in this manner until all the carbon has been consumed. Various composition of Al-Si alloys were equilibrated with 5wt% and 10wt% CNTs at different temperatures and the final products formed were calculated using 'Equilib' module. It was found that at

temperatures above the liquidus temperature of the Al-Si alloy, the products formed were a mixture of SiC, Al_4C_3 and Al liquid containing dissolved Si and C. Figure 4.44 plots the equilibrium mol.% of SiC and Al_4C_3 vs. temperature for Al-11.6 wt.% Si alloy and Al-23 wt.% alloy. Al-23 wt.% Si with 10 wt.% CNT was chosen for the sake of comparison because it was the composition that was reported in previous research from our group [33].

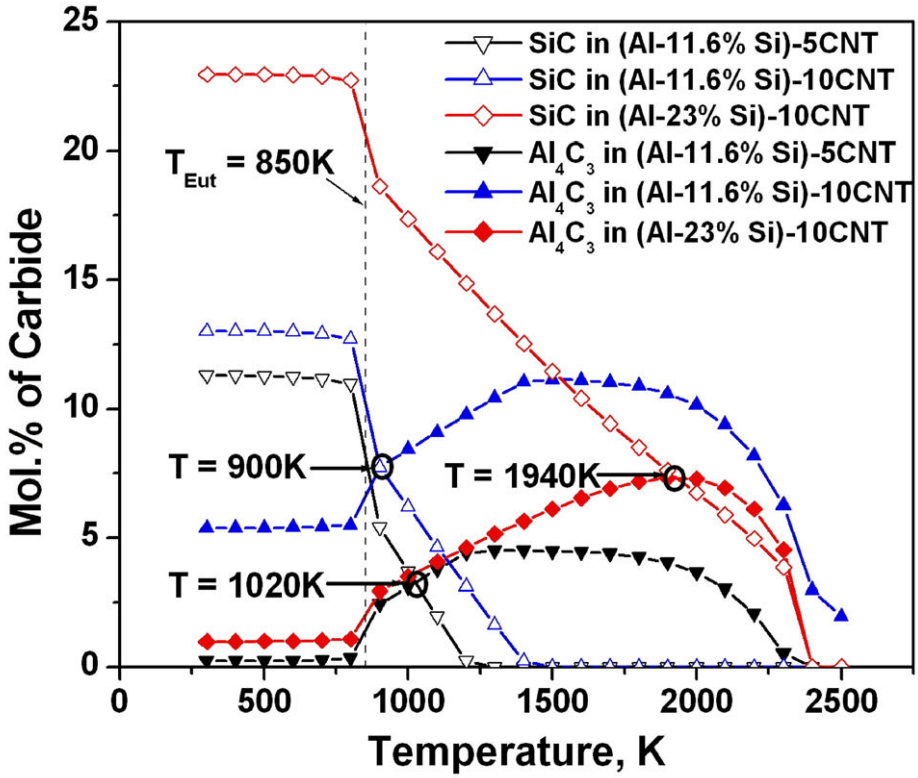

Fig. 4.44: Variation of mole fraction of Al_4C_3 and SiC for in different composite composition with temperature of processing

It can be seen for the Al-11.6% Si alloy that below the eutectic temperature of 850K, SiC is the major carbide formed. This is consistent with the observations in aluminum composites reinforced with SiC particulates produced by liquid metal

infiltration, where the reaction between aluminum and SiC leading to formation of Al_4C_3 is favored by increased temperature of molten aluminum [247]. It can be seen that as equilibrium temperature increases, the amount of Al_4C_3 formed increases and SiC decreases. But at higher temperatures solubility of carbon in Al increases. This will lead to dissolution of Al_4C_3 in molten Al-Si. The temperature of intersection of the Al_4C_3 and SiC mol.% curves are shown by the circles. It is seen that the cross over between the curves takes place at 1940K for 23 wt.% Si alloy while it take place at 900K for 11.6 wt.% Si alloy indicating that Si content plays an important role in the composition of the final product.

The equilibrium mole fractions of the two carbides were collected at different temperatures for different Al-Si alloy composition with 10 wt.% CNT. The fraction of total carbides that was Al_4C_3 is plotted as a function of Si content for various temperatures in Fig. 4.45. It can be seen that at any given temperature as the silicon percent goes on increasing, the Al_4C_3 fraction reduces. Also for a given silicon percent in the alloy, higher temperatures result in higher equilibrium fraction of Al_4C_3. All these results indicate that given sufficient time, CNTs will react with Al-Si alloy and result in formation of the carbide. This is undesirable as it leads to formation of Al_4C_3 and possible loss of the CNT reinforcement. In reality, only few outer walls of multi-walled CNTs react to form carbide of nanometer thickness. It has been shown through SEM images of fracture surface that a majority of CNTs are retained and intact without any damage. Retention of undamaged CNTs has been successfully observed by our group even when the matrix was a high temperature ceramic like hydroxyapatite [248] and aluminum oxide [228, 249, 250]. The retention of undamaged CNTs during plasma

spraying is attributed to rapid kinetics. The kinetic aspects of these reactions are discussed next.

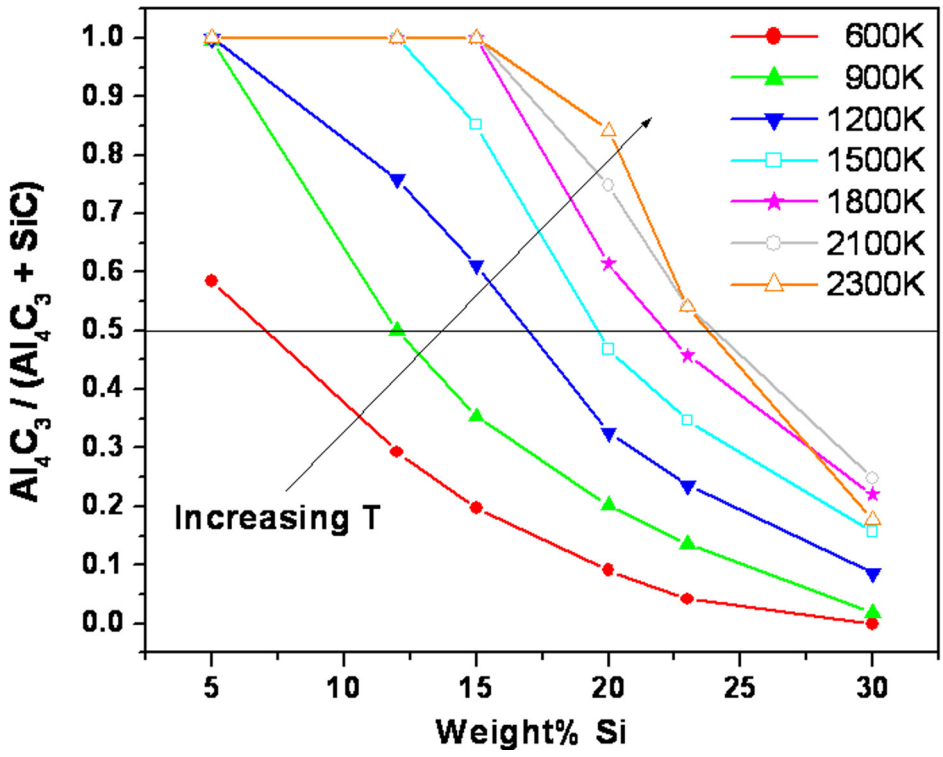

Fig. 4.45: Equilibrium mole fraction of Al_4C_3 v. Si wt% in the alloy at various temperatures for 10wt% CNT composites

4.5.2. Kinetics and Reactive Wetting

The interaction time of powder particle with the heat source during plasma spraying is very small (0.1-1 ms) compared to the time required for other synthesis processes (e.g. hot pressing, sintering, extrusion etc.). Hence, kinetics becomes very important in predicting CNT/Al-Si matrix interface reaction during plasma spraying. Landry and coworkers observed that Al-Si alloys do not wet graphite in the beginning and exhibit a

large contact angle of ~160^o. It is noted that contact angle strongly depends on the temperature, substrate surface roughness and the atmosphere during the test. In the case of Al-Si alloys and graphite, the contact angle reduces with the formation of Al_4C_3 or SiC as interfacial reaction product. Al_4C_3 and SiC formation reduces contact angle to 45^o and 38^o respectively [232]. Hence, formation of interfacial carbides favors wetting and infiltration of liquid melt into CNT clusters. Figure 4.46 shows a CNT cluster that has been infiltrated by Al-11.6 wt.% Si melt suggesting occurrence of reactive wetting. Thus reactive wetting is an important phenomenon for infiltration of the clusters.

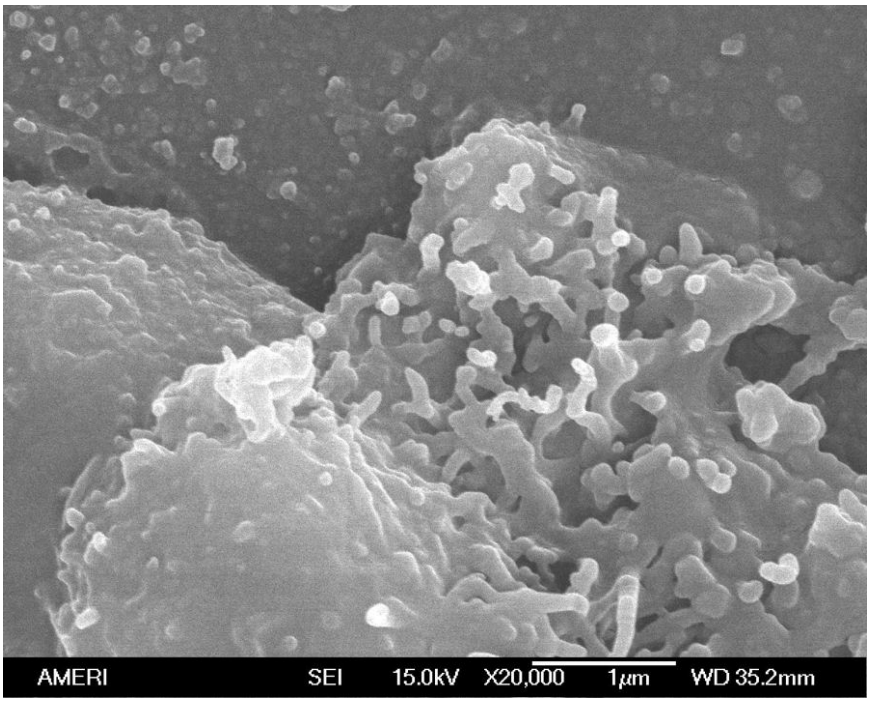

Fig. 4.46: SEM image of a splat finger in Al-5CNT showing Al-Si infiltrated CNT cluster

The mechanism of growth of SiC in case of Al-23 wt.% Si alloy was discussed by Laha et al [33]. A similar kind of mechanism will hold true for the growth of Al_4C_3 at the interface of Al-Si alloy and CNTs. This is illustrated in the schematic in Fig. 4.47. When

carbide thickness reaches t_{Crit} as defined by equation 2.3, further growth is energetically favorable this results in the decrease in contact angle and increase in reactive wetting.

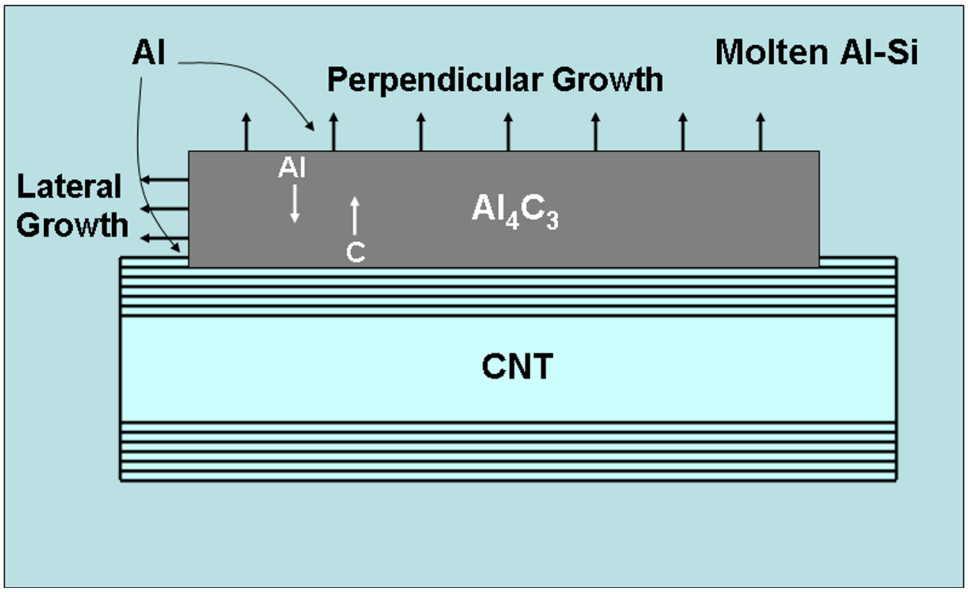

Fig. 4.47: Mechanism of growth of Al_4C_3

Smaller t_{Crit} values therefore indicate easy formation of carbide as well as better wetting. But once Al_4C_3 is formed, it acts as a barrier for further reaction to occur. Further reaction leading to growth of Al_4C_3 is possible by two mechanisms. The perpendicular growth of the carbide will occur by reaction at the a) Al_4C_3/CNT interface that will be governed by the diffusion of Al through Al_4C_3, and b) at the Al_4C_3/Al-Si alloy interface which will be governed by the diffusion of C through Al_4C_3. The atomic radius of Al atom is 0.125 nm while that of carbon is 0.07 nm. Hence, it is expected that diffusion of the smaller carbon atoms from the CNT to the Al_4C_3/ Al-Si alloy interface would be the dominating mechanism for perpendicular growth of Al_4C_3. The data on diffusion of Al and C in Al_4C_3 is not available. The lateral growth of the carbide is governed by the

reaction at the triple points. So the larger the spreading, the larger will be the area of the triple points and hence the extent of reaction and formation of Al_4C_3.

It is evident from equation 2.3 that large negative free energy (ΔG^f) of formation and small increase in interfacial energy ($\Delta\gamma$) will yield smaller t_{Crit} and better wetting. A lower value of carbide/CNT ($\gamma_{MC/CNT}$) and CNT/molten alloy ($\gamma_{MC/Alloy}$) interfacial energies will result in lower $\Delta\gamma$. Lower carbide/CNT interfacial energy is possible in case of coherent interfaces which will promote oriented growth of carbides over the CNT. There is a lack of experimental data for the interfacial energy values. The surface energies of a compound can be computed using ab initio methods [251] for crystallographic planes terminated by different kind of atoms.

From the compilation of activity vs. atom% by Desai [245] for Al-Si alloys and using FactSage, the value of ΔG^f per mole of Al_4C_3 and SiC were calculated and then t_{Crit} was calculated. $\Delta\gamma$ has been assumed to be 1000 $mJ.m^{-2}$ [33, 203]. Figure 4.48 shows the variation of critical carbide thickness with alloy composition at 1700K. It is observed that for Al-11.6 wt.% Si alloy, Al_4C_3 has lower critical thickness compared to SiC while the reverse is true for Al-23 wt.% Si alloy. The t_{Crit} values indicate that Al_4C_3 formation is favored from the kinetics point of view for an alloy composition of 11.6 wt.% Si while SiC is favorable when alloy composition is 23 wt.% Si. This justifies the experimentally observed formation of the type of carbide with different silicon content of matrix in our present study and Laha et al.

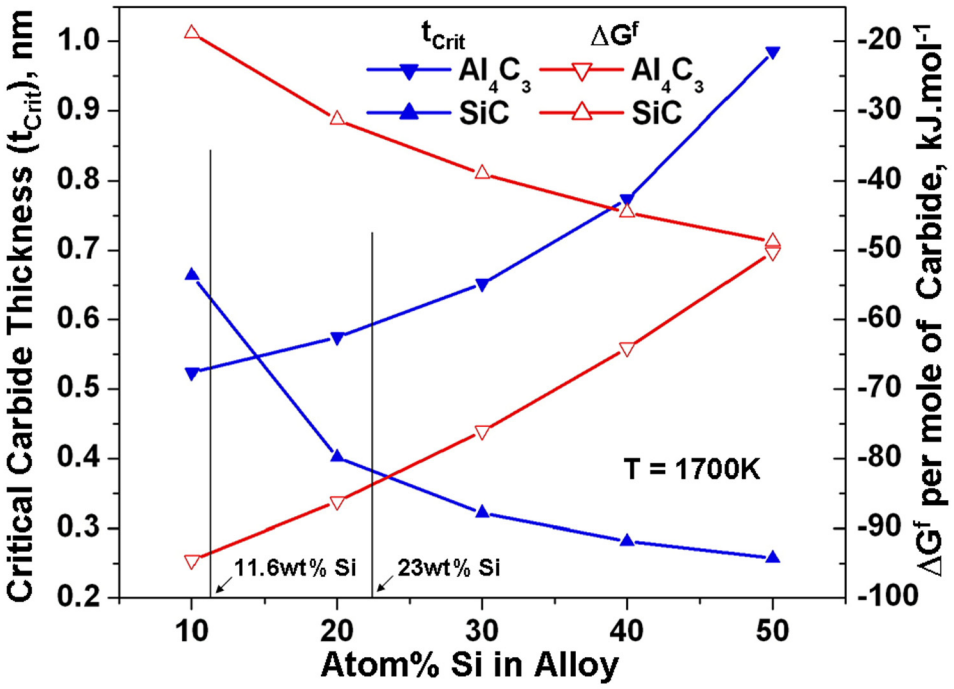

Fig. 4.48: Plots showing variation of critical carbide thickness and the free energy per mole of carbide formation with alloy composition for Al_4C_3 and SiC at 1700K

4.5.3. Experimental Validation of Results

It has been shown in our previous work that SiC is formed in case of Al-23wt% Si alloy [25] while Al_4C_3 is formed when matrix is Al-11.6wt% Si alloy. The amount of SiC formed was too low to be detected by XRD. Thin layer of SiC, 2-5 nm in thickness has been observed on the CNT surface in HRTEM images in case of Al-23wt% Si composites as shown in Fig. 2.11b. In the present case formation of Al_4C_3 is quite evident from XRD plots. This could be due to the fact that, in case of spray dried powders, the CNTs are uniformly distributed and have a higher probability of coming in contact with the molten alloy and reacting to form carbide phase. Further experimental verification of

Al_4C_3 formation in Al-11.6wt% Si matrix composites reinforced with 5wt% and 10wt% CNT was carried out using SEM of fracture surfaces and High-resolution Transmission Electron Microscopy (HRTEM). Figure 4.49 shows the SEM of the fracture surface of Al-11.6%Si coating containing 10wt% CNTs, in which formation of clusters of Al_4C_3 needles can be seen.

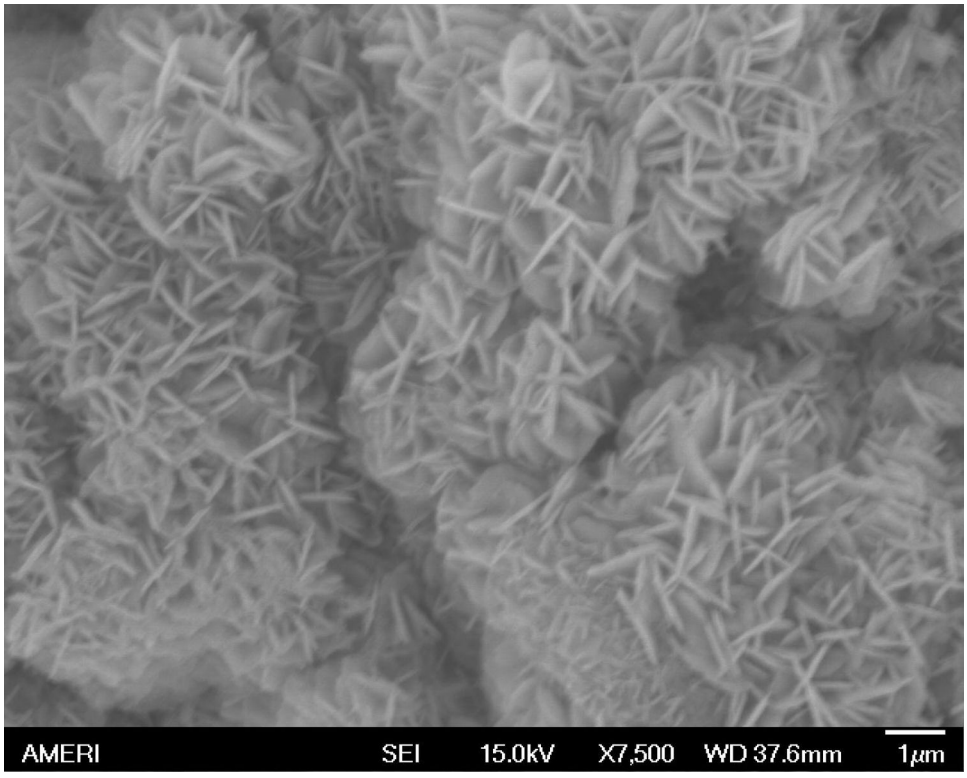

Fig. 4.49: SEM image of fracture surface of Al-11.6wt% Si coating containing 10wt% CNTs showing formation of clusters of Al_4C_3 needles

HRTEM images of the plasma sprayed Al-11.6wt% Si composite containing 5wt% CNT are shown in Fig. 4.50. A coated and reacted CNT is seen in Fig. 4.50a where the alloy and reaction products on the CNT are marked by the arrows. There is an approximately 6 nm thick coating on the nanotube surface which is more than the critical

thickness for Al_4C_3 formation at 1700K (~ 0.65 nm). This indicates that reactive wetting occurs resulting in uniform coating of the CNT with the molten alloy. Figure 4.50b shows an Al_4C_3 particle formed on the nanotube.

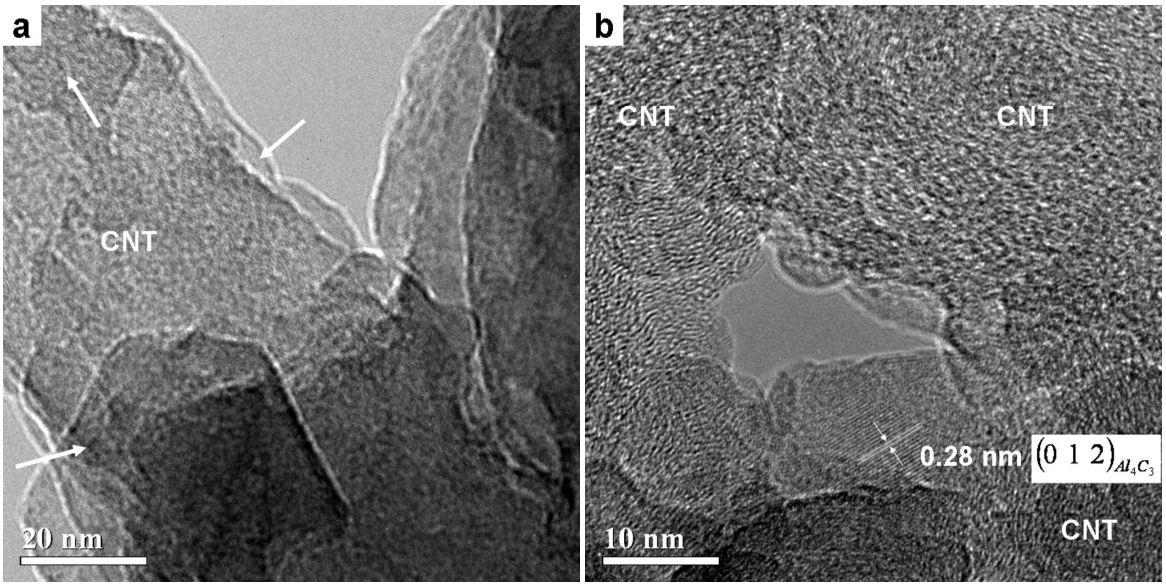

Fig. 4.50: TEM micrographs of Al-11.6wt% Si alloy reinforced with 5wt% CNT showing a) a coated CNT showing reaction products and adhering alloy marked by arrows, and b) Al_4C_3 layer on the CNTs

Figure 4.51 shows HRTEM images from plasma sprayed Al-11.6 wt% Si composite containing 10wt% CNT coating. A clean interface between Si and CNT in Fig. 4.51a is observed which indicates that no reaction has taken place between CNT and Si, even when they are in intimate contact. This proves the predictions from thermodynamic calculations presented previously. Figure 4.51b shows the formation of Al_4C_3 at the Al-

CNT interface in the composite. The thickness of the carbide layer as shown by the white arrow is found to be approximately 6 nm.

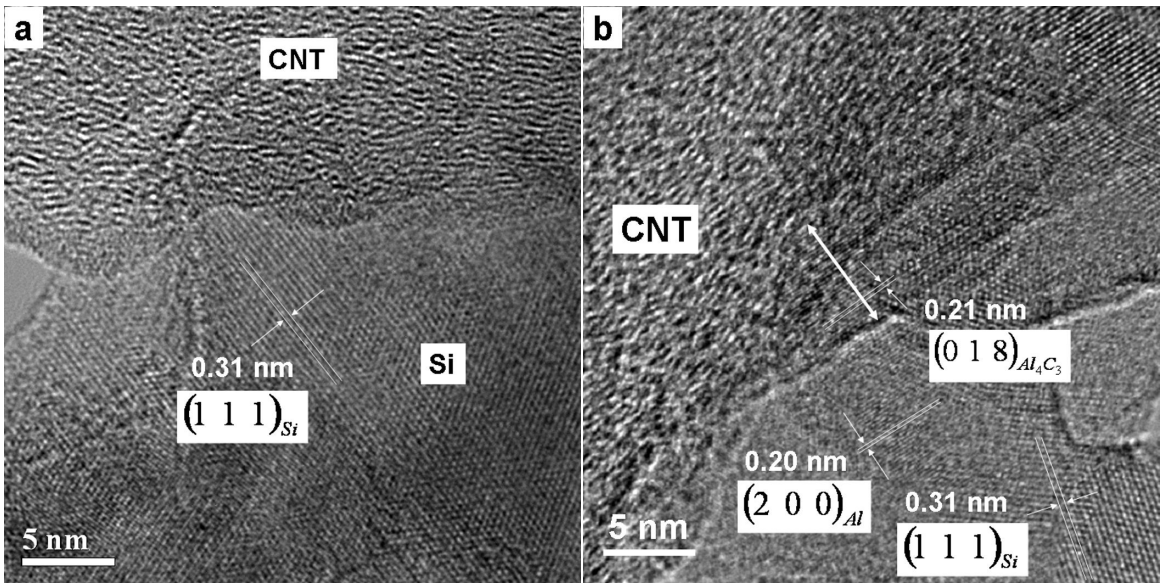

Fig. 4.51: TEM images showing a) CNT-Si interface, and b) Al_4C_3 formation at the interface of Al-11.6wt% Si alloy containing 10wt% CNT

No orientation relationship between Al_4C_3 carbide and CNTs was observed. This is in contradiction to observed orientation relationship of $(0002)_C \parallel (0003)_{Al4C3}$ [41] in carbon fiber aluminum composites. Growth of carbide phase is attributed to the crystal structure of Al_4C_3, which has a rhombohedral (space group $R\bar{3}m$) structure as shown in Fig. 4.52. It is made up of alternating layers of Al_2C and Al_2C_2 with Al atoms having tetrahedral C coordination. C atoms have octahedral (C_1 in Fig. 4.52) and trigonal

bipyramidal (C_2 in Fig. 4.52) coordination with Al atoms [252]. Al_2C layer is close packed with C in octahedral voids formed by close packed aluminum atoms. So it is expected that the lateral diffusion of carbon atoms by an interstitial mechanism would be favored through the Al_2C_2 layer. As seen from the figure, (0003) plane of Al_4C_3, has a hexagonal arrangement of carbon atoms similar to that in graphite. However, it is to be remembered that the C-C distance in graphite is 1.42 Å while it is 3.33 Å in Al_4C_3. Thus Al_4C_3/CNT interface is expected to be strained without any orientation relationship.

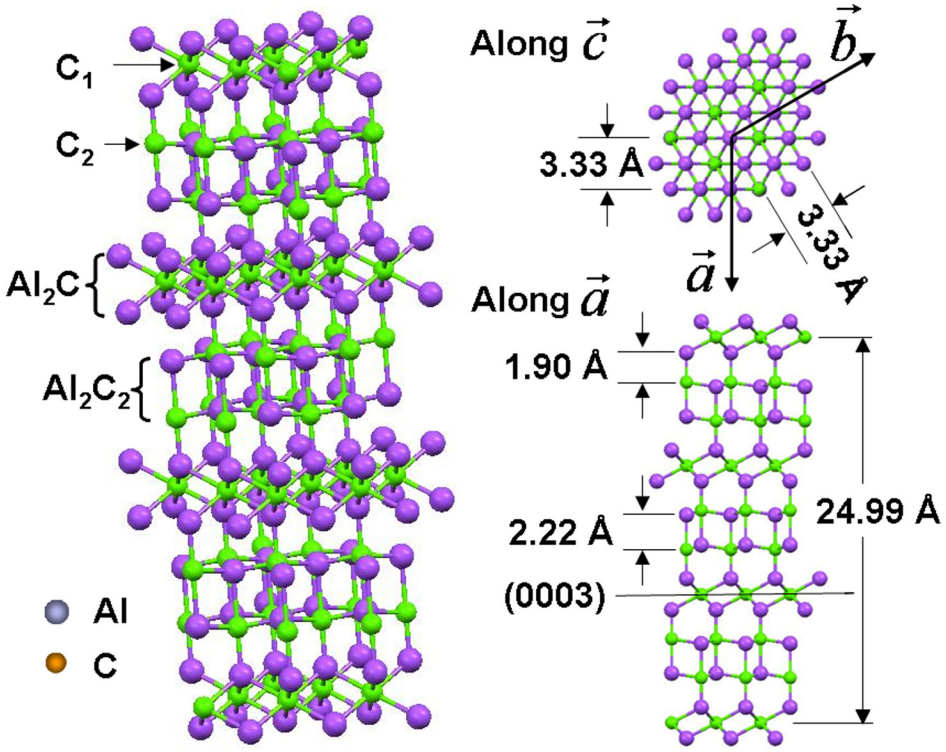

Fig. 4.52: Crystal structure of aluminum carbide showing alternate layers of Al_2C and Al_2C_2. Also it can be seen that the (0003) plane is the carbon terminated plane which is similar to the graphene layers of CNTs

Formation of limited amount of nano-size layer of Al_4C_3 at the interface has been shown to be beneficial for the mechanical properties for Al-SiC composites by increasing the interfacial bonding [253]. Kwon et al have suggested that Al_4C_3 formation helps in load transfer to CNTs by pinning the nanotubes to the matrix [31]. So the formation of controlled amount of interfacial products might help in the improvement of the mechanical properties. Tensile testing of bulk samples in future may answer the effect of Al_4C_3 on the macro-scale properties of the composites.

4.6. Structural Stability of CNTs in the Coatings

A lot of changes occur in the CNTs due to the nature of the fabrication process. Some of them may be desirable, like formation of thin carbide layer for instance, while some may deteriorate the properties of the CNTs. In this section the changes in CNT morphology due to thermal and mechanical interactions during plasma and cold spraying have been highlighted.

4.6.1. Structural Stability of CNTs in Plasma Spraying

The CNTs are subjected to very severe environment in plasma spraying. The temperature in the core of the plasma ranges between 10000 and 15000K. Direct exposure of CNTs to the plasma can cause evaporation of CNTs. This has been recently observed by Anup et al. our group [254]. When suspension of CNTs and alumina nanoparticles in ethenol was sprayed, no CNTs were observed in the deposit formed due to evaporation of the CNT. This was due to direct contact between CNT and plasma. However, in case of spraydried powders, the molten alloy shields the CNTs from the

plasma as shown in Fig. 4.17. Figure 4.53 shows the HRTEM image of two damaged CNTs.

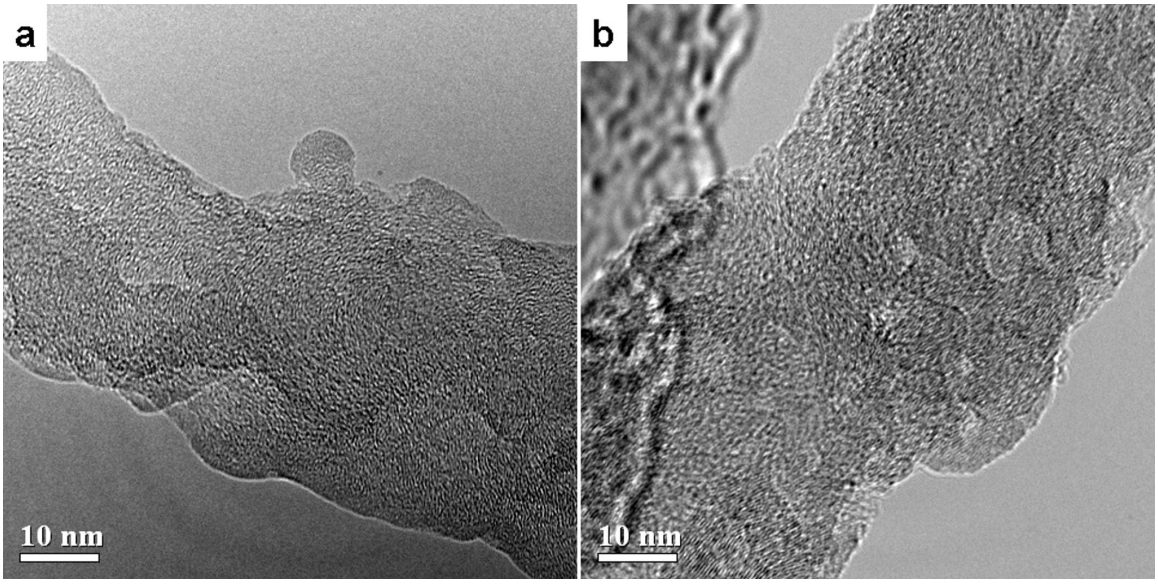

Fig. 4.53: HRTEM images of CNTs from a) Al-5CNT and b) Al-10CNT coating

It can be seen that the CNTs are not uniform and layers of graphene are quite distorted. This could be due to oxidation at the high temperatures. CNT layers can also be consumed in formation of Al_4C_3. It is quite possible that the damaged CNTs shown in these images are weak mechanically. High temperature may also cause amorphisation of the outer walls. There have been reports of synthesis of amorphous CNTs or CNTs with amorphous outer walls [255] due to high temperature synthesis by CVD. More damaged CNTs were found in case of Al-10CNT coating. This was due to the fact that there was CNT mesh formation in case of SD Al-10CNT powder. Most of the CNTs formed a mesh on the outer surface of the powder. This increases the probability of exposure of CNTs to the plasma and hence increased damage. It is to be noted that most of the CNTs were

retained without damage as can be seen from fracture surfaces were retained without damage.

4.6.6. Cold Spraying

During cold spraying, CNTs are subjected to severe mechanical stresses that include impact and shear. So there is likelihood of damage to the CNT structure. It was observed in most of the fracture surface micrographs that CNT could be retained and uniformly distributed. Most of the visible damage observed was shortening of the length of the nanotubes. Figure 4.54a and 4.54b shows the length and diameter of the nanotubes, respectively, as measured from the series of SEM micrographs.

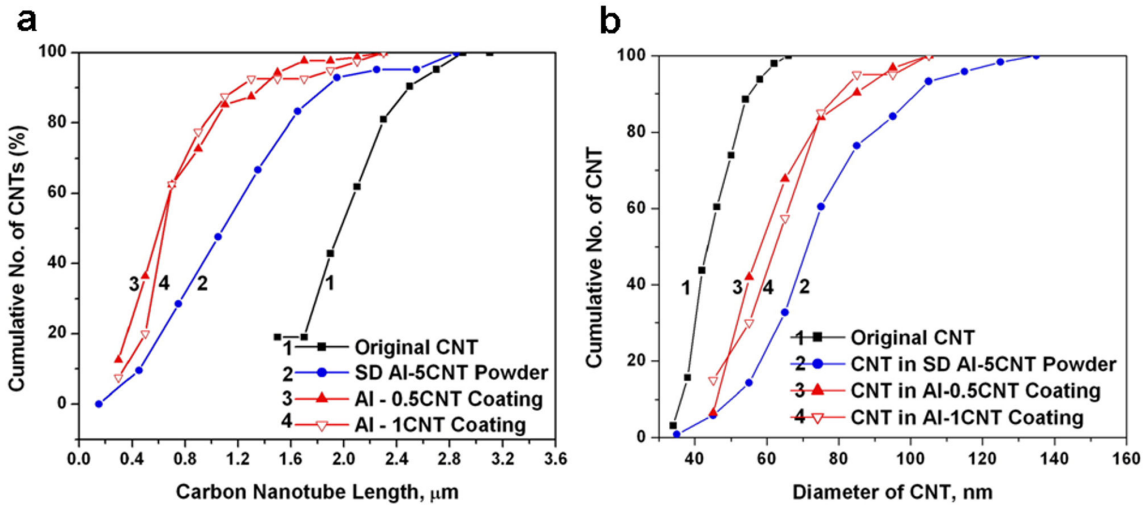

Fig. 4.54: Distribution of a) CNT length and b) CNT diameter in powder and cold sprayed coatings

The values of the mean and standard deviation of length and diameter of the CNTs during various stages of the processing are tabulated in Table 4.5. It can be seen

that there is a decrease in the length of CNT after spray drying. This shortening happens during mixing operation for the preparation of the slurry used in spray drying. The milling action due to rubbing Al-Si particles might cause breakage of CNT. Chen et al. [256] have also observed shortening of CNTs due to milling in a two roller mill, the extent of which increases by addition of PMMA particles. Also the CNT are observed to be thicker in the spray dried powder. This is because they are covered with the binder used for spray drying. After cold spraying, there is a decrease in the value of both the length and diameter of the CNT. The decrease in diameter means that the binder is ripped off the CNT due to the gas flow, impact and disintegration of the agglomerate and during the rubbing action between particles. There is a noticeable decrease (~30%) in length of the nanotubes.

Table 4.5 Length and diameter of CNTs during various stages of the processing

CNT considered	**Length, μm**	**Diameter, nm**
As-received CNT	2.1±0.4	47±7
In Spray dried agglomerate	1.3±0.6	78±19
In Al-0.5CNT coating	0.8±0.4	66±15
In Al-1CNT coating	0.85±0.4	68±15

Figures 4.55a and 4.55b show TEM micrographs of fractured end or tips of two different CNTs. As seen in Fig. 4.55a, after the impact there is a systematic fracture of the concentric tubes which progresses inward until the innermost tube has broken. On the

other hand, Fig. 4.55b shows the fractured tip of a CNT that is uneven or asymmetric with respect to tube axis. Two mechanisms are responsible for the fracture surfaces observed. They are by impact and by shear which are schematically described in Fig. 4.55c and 4.55d respectively.

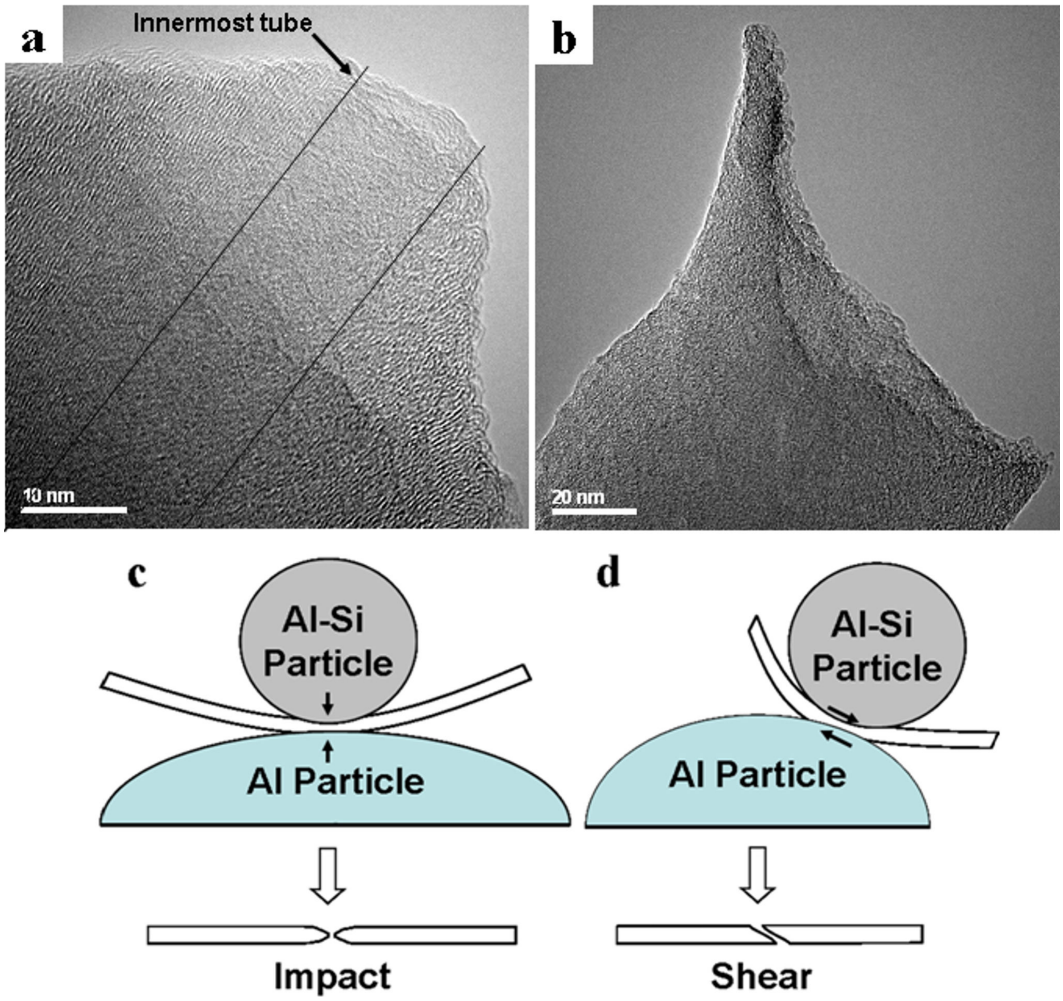

Fig. 4.55: Transmission electron microscope images showing a) tip of CNT broken due to impact, and b) tip of a CNT broken due to shearing. Schematic showing the two main mechanisms for fracture of CNTs during cold spraying namely by (c) impact and (d) shear

When the spray dried agglomerate strikes the substrate/coating, there is a possibility of a CNT being crushed in between the incoming Al-Si particle and the preceding splat. Depending on whether the Al-Si particle strikes a horizontal or an inclined surface, it will exert impact or shear forces on the nanotube. Both impact and shear is expected to cause fracture in CNT. Impact is expected to result in CNTs with fracture surface that is normal or symmetric to the longitudinal axis while shearing will result in broken CNTs with fracture surfaces that are inclined or asymmetric to the longitudinal axis. A CNT might undergo multiple events of fracture before getting embedded or entrapped within two particles or in porous area between particles created as a result of insufficient deformation.

Further analysis of the deformation and fracture mechanism under high velocity impact was carried out. Figure 4.56 shows the TEM of a MWNT that has undergone impact. It is seen that impact loading at the point shown by the white arrows lead to fracture at the point of impact and a generation and propagation of an axial shock wave or a ripple along the length of the MWNT. Ripple formation is seen marked by formation of kinks. Rippling has been observed by many researchers during bending of thick nanotubes [55, 257, 258]. This phenomenon has been attributed to the variation of elastic modulus in different directions [55]. It has been shown [257] that the rippling caused during bending leads to lower restoration forces than predicted by linear elasticity theory. Lourie et al. [258] observed buckling of MWNT embedded in a polymer matrix, under compressive stresses for MWNT having the ratio of wall thickness to the radius greater than 0.6. But it was not clear whether the deformation was plastic or recoverable

(elastic). Bower et al. [259] have also observed such ripples or buckle in the nanotubes. It was reported that the buckles formed were reversible and elastic for strains as high as 8%.

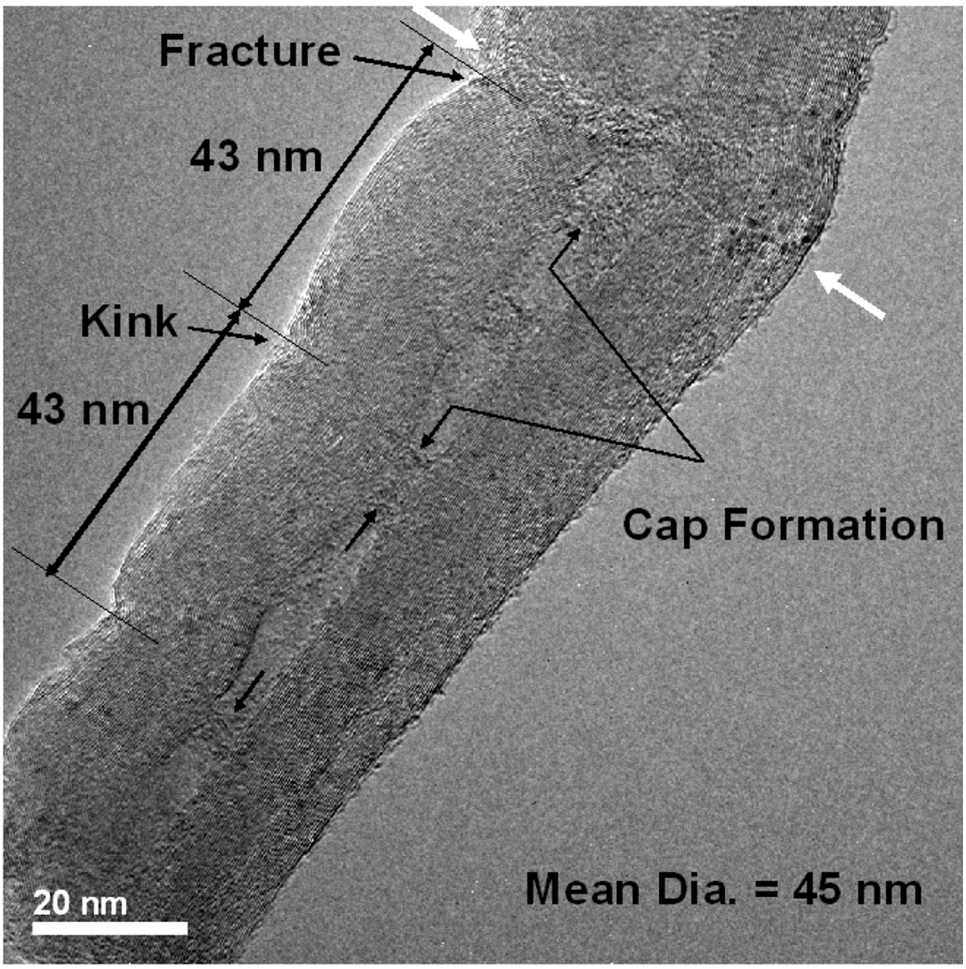

Fig. 4.56: TEM of CNT fracture due to impact and shockwave formation

The ripples observed in Fig. 4.56 are different compared to the ripples formed due to bending due to following reasons. Firstly, fracture of CNT due to bending has not been reported till date and the kinks here are observed to be permanent. Bending induced kinks should be recoverable after the release of stresses due to fracture. Secondly, there is a periodicity in the occurrence of the kinks which is measured to be around 43 nm which is

quite close to the average diameter of the tube which is equal to 45 nm. On the other hand, the spacing between the kinks occurring due to bending is small and up to 50% of the diameter of the tube [55, 258]. The $\lambda/\sqrt{rt}$ ratio (where λ is the periodicity of the ripples, r is the radius of MWNT and t is the wall thickness) has been found to be 1 for most of the MWNT in bending [259]. In the present case the $\lambda/\sqrt{rt}$ ratio is equal to 2.1 (λ =43 nm, r =22.5 nm, t =19 nm as shown in Fig. 4.56). It is acknowledged that the periodicity based on two wavelengths may lead to some ambiguity in lack of an image showing longer length of nanotube. Hence, there is a possibility that bending also plays a role in ripple formation. But the fracture is attributed to impact as observed by the curving of the CNT layers at the fracture point (top left in Fig. 4.56). The kinks might develop into deep cracks in case of severe shock loading. Internal cap formation is also observed just below the kinked regions attributed to axial compressive deformation. Internal cap cannot form due to bending and has not been observed in bent nanotubes in the literature. These observations indicate that under shock loading there is a possible tendency of MWNTs to breakdown into secondary pieces having length equal to their diameter. The internal cap formation at location of kink formation further indicates that there is a tendency of these pieces to form closed shell structures like carbon onions. It has been suggested that carbon onion structure is thermodynamically more stable [260] as compared to an open ended MWNT of aspect ratio equal to one since the latter would require the presence of many broken bonds. Li et al. [261] have in fact observed that ball-milling of MWNT with 1 μm sized iron particles for 15 minutes lead to formation of carbon onion like particles. Wei et al. [262] have also observed transformation of MWNT

into diamond under laser irradiation. It was proposed that disorder is created by the laser followed by ordering of the innermost layer to form a closed structure, which is followed by the successive layers resulting in formation of carbon onion. The internal capping observed in the present case is the first step in such a process.

Figure 3.57 shows a fractured MWNT due to impact. It can be seen that the MWNT has undergone plastic deformation prior to fracture. The MWNT had undergone a necking kind of phenomena followed by a cup and cone kind of fracture. This kind of failure is common in moderately ductile materials like low carbon steel. To the authors' knowledge, such kind of failure has not been reported till date for CNTs. It is to be kept in mind that the MWNT has not yet fractured into two parts although most of the layers of this nanotube have fractured. The link between the two parts might consist of layers that have undergone pull out. Also the angle at which these layers are inclined is around 35^{o}, as indicated by the arrow which suggests the presence of torsion forces after fracture. Yakobson et al. [263] have studied the high strain rate fracture of single and double walled CNT using molecular dynamics. It was observed that the nanotubes fracture and rearrange to form a single chain thus leading to large breaking strains. They also show that failure of double walled CNT occurs after formation of two monoatomic chains. It could be possible that there are some monoatomic chains connecting the two fractured parts. The reduction in area at fracture can be calculated from the initial area and the area of the necked region at failure. The diameter of the initial CNT is 59 nm while the diameter of the necked region is 33 nm which leads to a reduction in area of around 70%. The reduction in area for annealed 1020 mild steel is around 66% [264]. This indicates that MWNTs show ductility comparable to mild steel.

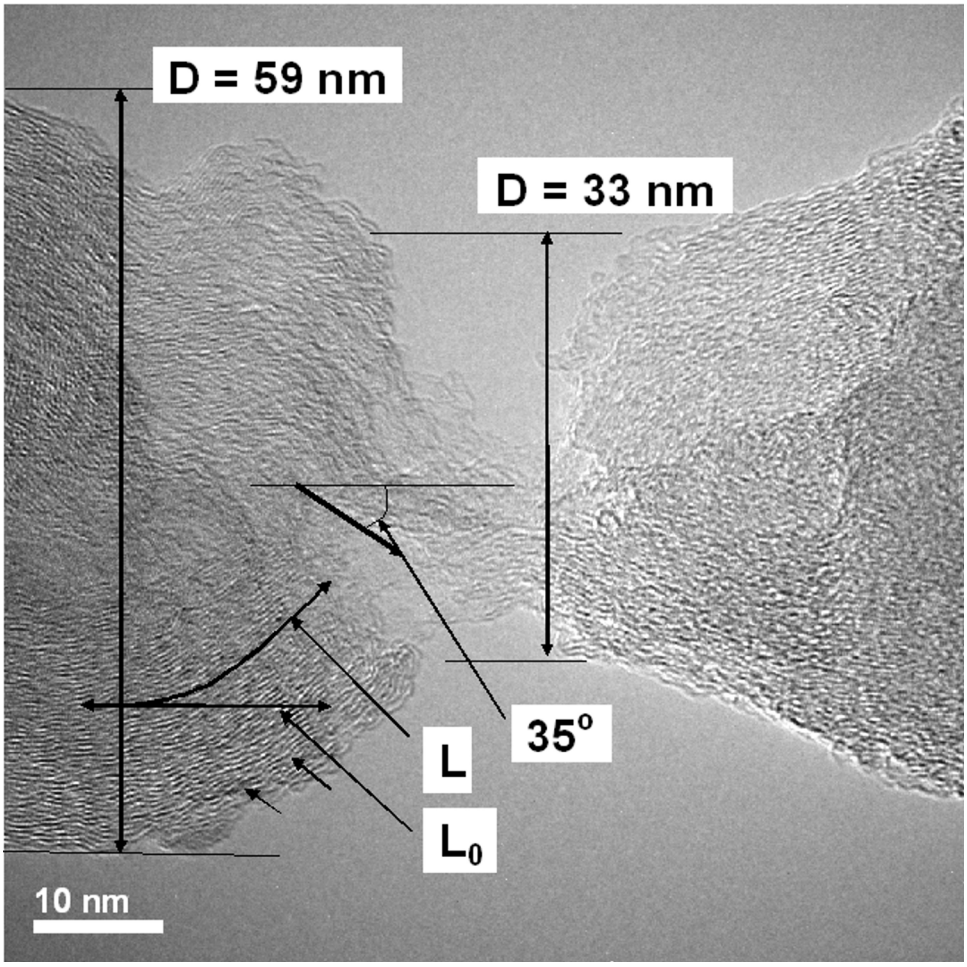

Fig. 4.57: TEM image showing necked CNT due to impact. The circle shows the plastic bending of individual layers

Cold spraying involves impact of successive powder particles (containing Al and MWNT in this case) onto the substrate at supersonic velocity. The contact time (t_c) between two colliding elastic spheres is approximated by Kil'chevskii [239] as

$$t_c = 2.9432\left[\frac{25\pi^2}{8}\frac{\left(1-\nu_p\right)^4}{\left(1-2\nu_p\right)^2}\right]^{0.2}\frac{d_p}{2\nu_p^{0.2}c_{II}^{0.8}} \qquad \text{Equation 4.9}$$

Where $c_{II} = \sqrt{\frac{E(1-\nu_p)}{(1+\nu_p)(1-2\nu_p)\rho_p}}$ is the velocity of longitudinal waves in the medium, ν_p is the Poisson's ratio, d_p is the diameter of the particles, E the elastic modulus and ρ_p is the density. For aluminum-silicon particles of average size 2.4 μm, E=70 GPa and ρ_p=2700 kg.m^{-3}, t_c is calculated to be the order of 10^{-7} s. Considering that the particle is moving at an average velocity of 636 m.s^{-1} (experimentally measured) and assuming that all the momentum is lost on impact, it corresponds to a force of impact of the order of ~100 μN. Assuming, that the load is applied over an area of d^2 on the CNT, where d = 66 nm is the average diameter of the CNT, an impact stress of ~20 GPa is obtained. This value is within the range of experimentally measured fracture strength of MWNTs [10]. It is seen from Fig. 4.57 that there is a gradual curving of the concentric graphene cylinders which results in the necking behavior. After a critical strain value is reached, the MWNT fractures due to fracture of the individual layers. In such loading conditions, the outermost tubes will experience tensile forces while the inner tubes would be in compression. So the fracture of outermost tubes is quite probable and such kind of fracture is seen at some points as marked by the arrows. The approximate average true strain in the nanotubes can be calculated by taking the natural logarithm of the ratio of the final curved length (L) and initial length (L_0, taken to be projected length on the axis of the tube) of the central tube. Using Image analysis software Image J, L and L_0 were found to be equal to 29.6 nm and 25.8 nm respectively, which gives a true strain of approximately 14%. The large reduction in the area before fracture suggests that nanotubes can be engineered under high strain rate conditions to design a nano-piping

network with varying diameters. Such structure could be utilized to design nano syringes for drug delivery and nanofluidic applications.

There are some reports on the fracture behavior of CNTs. Wagner et al. [265] reported the fragmentation of MWNT in polymer matrix composite with several breaks along the nanotube length. However, high magnification images were not obtained due to loss of contrast in the presence of the polymer. It was reported that the MWNT failed by telescopic fracture. Hwang et al. [266] have observed the fracture of a MWNT inside a TEM, bridging a crack in PMMA matrix, occurring due to tensile forces generated by electrostatic repulsion. A gradual increase in the length of the MWNT with time was observed. This was attributed to the breakage of the outermost layer followed by sliding between the layers to some distance followed by fusion of the outermost layer to the layer below. This *breakage, sliding and fusion* process continued until MWNT fractured. It was followed by termination of the broken ends due to cap formation. While this mechanism is significant, it remains to be understood what factors govern the sliding distance and fusion process and the number of tubes that undergo breakage in one instance. Troiani et al. [267] have observed the breakage of SWNT in TEM. It was found that SWNT thins down progressively until a single chain of carbon atoms are formed joining the broken ends. Marques et al. [268] have shown that MWNT formed from an amorphous carbon film using an electron beam in a TEM, thins down successively to form SWNT before fracturing into two. It is evident that the deformation mechanism of MWNT under high velocity impact conditions is significantly different compared to relatively slow strain rate conditions studied previously

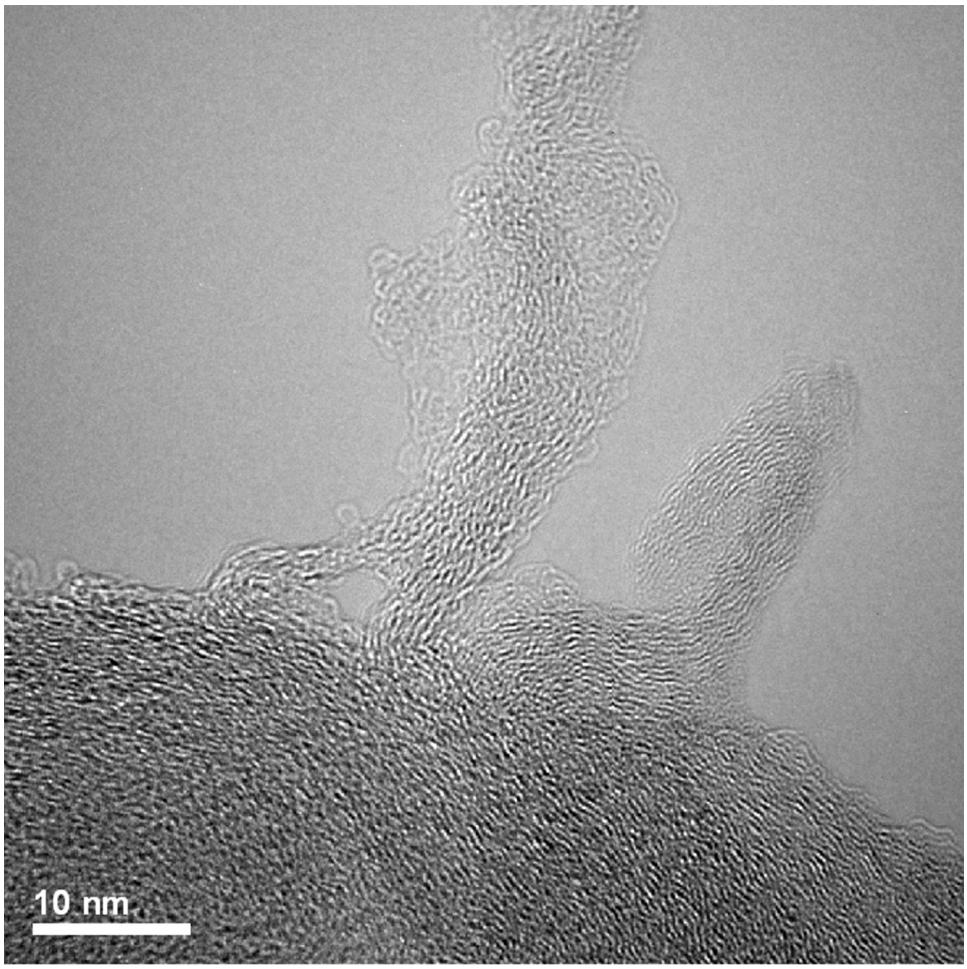

Fig. 4.58: Peeling mechanism in outer walls of MWNT due to shearing between aluminum particles

Figure 4.58 shows the high magnification TEM image of a MWNT that has undergone shearing between two aluminum particles. It is seen that peeling of MWNT layer can occur due to shear stresses generated by the rubbing action between particles. This is an important phenomenon since it leads to generation of free graphene sheets and exposing underlying layers of MWNT. The graphene sheets have been shown in Fig. 4.29. The peeling of phenomena does not require much force. Once these sheets are torn

off the tubes the only force required to peel them off would be the force required to overcome the van der Waals forces between the tubes. The van der Waals forces have been found to be very weak ~ 0.035 ev/atom [269] and described by Lennard-Jones potential [270] as shown in equation 2.

$$U(R) = 4\varepsilon\left[\left(\frac{\sigma}{R}\right)^{12} - \left(\frac{\sigma}{R}\right)^{6}\right]$$

Equation 4.10

Where R is the interlayer distance and ε = 0.0556 kcal.mol^{-1} and σ = 0.34 nm are the Lennard-Jones parameters. Cummings and Zettl [28] have demonstrated very low friction between the nanotube layers suggesting their application as frictionless bearings. It was shown that the friction forces calculated based on the van der Waals forces were three orders of magnitude lower than that calculated for conventional materials [271]. Li et al. [272] have produced bulk carbon nanotube materials by spark plasma sintering (SPS). Graphitization and peeling off was observed while polishing the sintered samples. Fig. 4 shows clearly that peeling off of graphene layers is the mechanism of damage or graphitization as a result of application of shear stresses caused due to a rubbing of MWNT between two particles. Peeled graphene layers could reduce the coefficient of friction of MWNT reinforced coatings.

4.7. Mechanical Property Measurements at Multiple Length Scales

Mechanical properties of the coatings were measured at the multiple length scales using different techniques. For cold sprayed coatings, only nanoindentation and nanoscratch studies were performed due to sample limitations. For plasma sprayed coatings, tensile and compression tests were carried out on free-standing bulk samples, in addition to

nanoindentation and nanoscratch testing. Fig 4.59 is a chart of the mechanical property testing carried out.

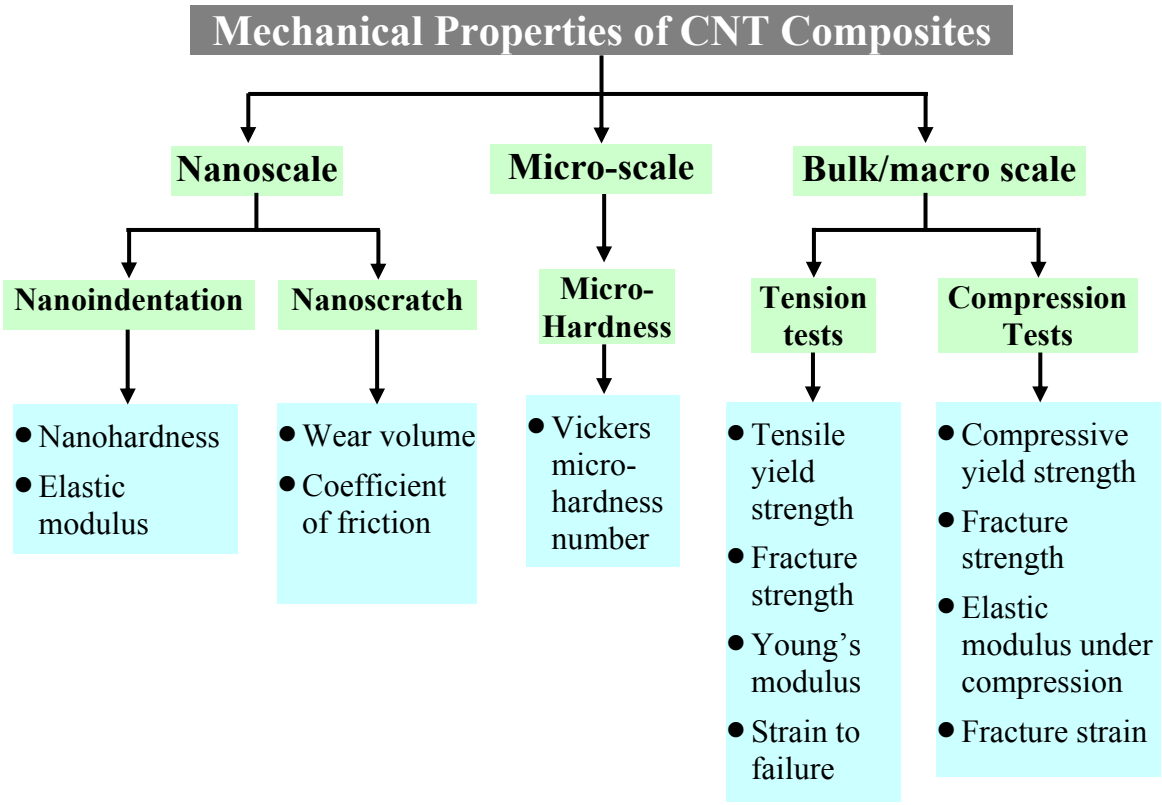

Fig. 4.59: Chart showing the mechanical properties evaluated for the CNT composites in this study

4.7.1. Microhardness of Coatings

Fig. 4.60 shows the variation of microhardness of the cold sprayed Al-CNT coatings. The average value of Vickers microhardness was found to be 56.1±2.6 VHN, 58.7±3.2 VHN and 60.9±2.8 VHN for the Al, Al-0.5CNT and Al-1CNT coatings respectively. These values are high compared to the powder (31.5 GPa [229]). This is due

to the fact that the powders are severely deformed during cold spraying, which causes work hardening.

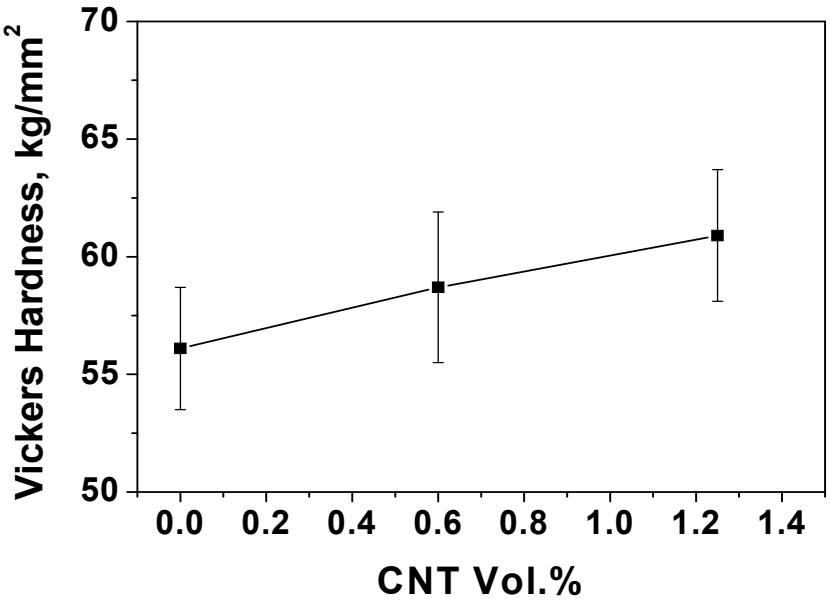

Fig. 4.60: Variation of microhardness of cold sprayed coatings with CNT content

Addition of CNTs does not produce significant increase in microhardness. This is due to the fact that the amount of CNTs added is very small. Also the CNTs are concentrated in the inter-splat regions only leading in less effective hardening.

Figure 4.61 shows the variation of microhardness of the plasma sprayed Al-Si-CNT coatings. It is observed that plasma sprayed Al-Si coating has higher hardness than the cold sprayed Al-CNT coatings due to the present of fine Si. The hardness of 99.999% pure Al is 13 $kg.mm^{-2}$ where as that of silicon on 1127 $kg.mm^{-2}$ (from www.matweb.com). So addition of silicon is expected to increase the hardness. Since in

Al-Si eutectic alloy, the silicon is intimately distributed in the eutectic phase, the hardening effect is even higher.

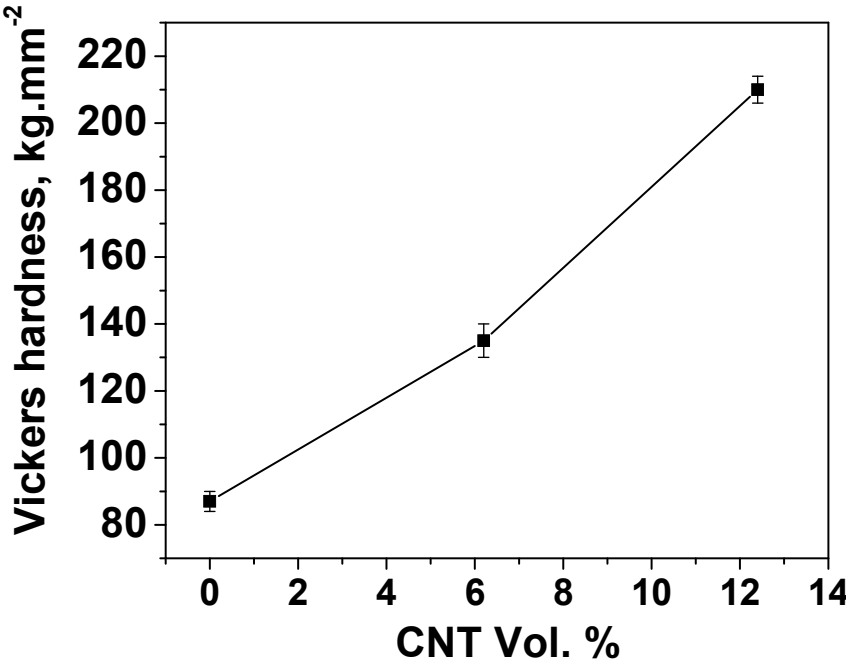

Fig. 4.61: Variation of Vickers hardness of plasma sprayed Al-Si-CNT coatings with CNT content

The hardness values were found to be 87±3, 135±5 and 210±4 VHN respectively for Al-Si, Al-5CNT and Al-10CNT coating respectively. It is observed that addition of CNTs leads to a significant increase in hardness of the coatings. This increase in hardness is attributed to the CNTs in the intersplat regions which restrict the plastic flow and hence deformation of the material. The hardness increase could also be due to presence of Al_4C_3.

4.7.2. Nanomechanical Properties by Nanoindentation

4.7.2.1. Elastic Modulus and Hardness of Plasma sprayed Al-Si CNT coatings

Indentations were carried out on the matrix portion of polished cross section samples at loads of 2000 μN, 3000 μN and 4000 μN using a Berkovich tip of tip radius 100 nm. Nine indents were made for each load on the ***matrix*** part of the nanocomposite coating, which makes it a total of 27 values of hardness and elastic modulus per sample. It was found that the results were consistent and nine values at each load were sufficient to generate an average value for the properties. Figure 4.62 shows the scanning probe microscopy (SPM) images of the indents from Al-Si, Al-5CNT and Al-10CNT coatings, respectively.

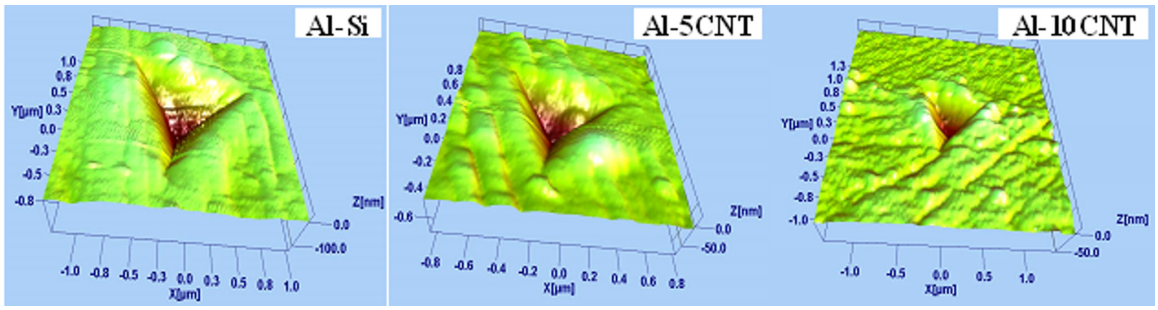

Fig. 4.62: SPM images of the indents on three PSF coatings at 2000 μN load

The decreasing size of the indents suggests strengthening effect due to addition of CNTs. Figure 4.63a shows the representative load displacement curves for the three coatings at a load of 2000 μN. The decrease in maximum displacement (h_{max}) and the residual depth (h_r) indicates strengthening due to addition of CNTs. Figure 4.63b shows the depth profiles taken along the median of the indent. Pile-up of material occurs on the

surface of the indenter and is observed on the edges of the triangle shaped indent. The pile-up height for Al-Si, Al-5CNT and Al-10CNT coating are approximately 19 nm, 15nm and 8 nm, respectively. The reduced depth of the indent and pileup also indicates strengthening effect of CNT addition on the composite.

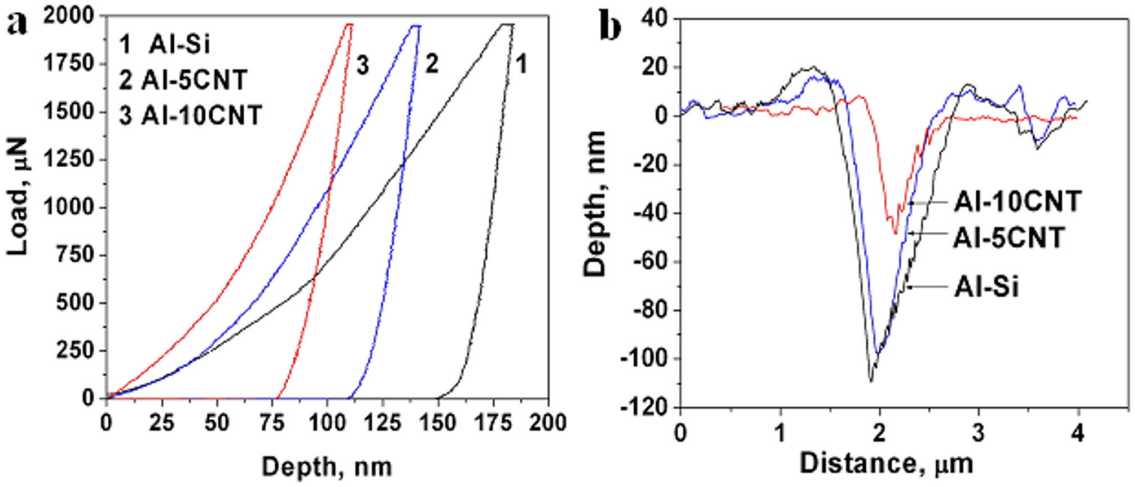

Fig. 4.63: a) Load displacement curves obtained during nanoindentation of plasma sprayed Al-Si-CNT coatings and b) depth profile along a median of the triangular indents

Figure 4.64a shows the variation of hardness and reduced elastic modulus of the coatings, calculated by the Oliver and Pharr method [230], as a function of CNT content. There is a consistent increase in the elastic modulus with CNT addition. The scatter in the data is due to the localized nature of the nanoindentation test in which the values are influenced by the local CNT/Si content. Table 4.6 shows the elastic modulus and hardness values for the coatings. It is seen that the standard deviation of the hardness values obtained by nanoindentation were less than 4% of the average value indicating that the values are consistent.

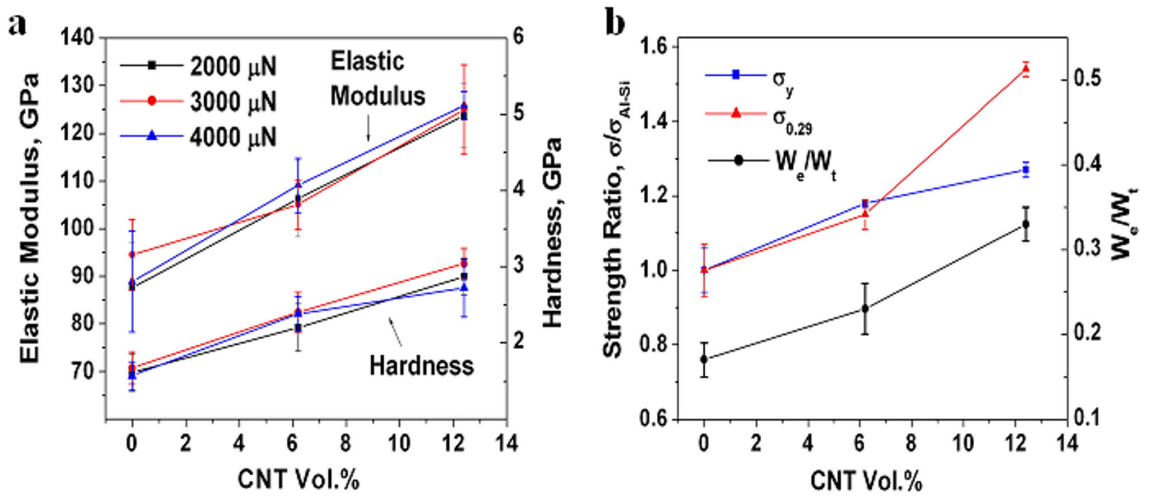

Fig. 4.64 a) Variation of elastic modulus and hardness of the plasma sprayed Al-Si-CNT coatings with CNT content and b) variation of strength ratio and elastic recovery with CNT content

Also the standard deviation of the elastic modulus values of the CNT composites obtained by nanoindentation were less than 6% of the average value indicating consistency in the measured values. The nano-hardness values were found to increase by 45% and 80% by addition of 5 wt.% and 10 wt.% CNT, respectively. The values of hardness obtained by nanoindentation are larger compared to that obtained by microindentation. This is attributed to the localized nature of the nanoindentation test. Values of mechanical properties obtained from microindentation involve several splats and are influenced by several features like inter-splat porosity and splat sliding [273, 274].

Table 4.6: Mechanical properties of plasma sprayed Al-Si-CNT coatings from nanoindentation

Coating	**CNT Vol.%**	**Nanohardness GPa**	**Elastic Modulus GPa**	**W_e/W_t**	**σ_y GPa**	**$\sigma_{0.29}$ GPa**
Al-Si	0	1.61 ± 0.20	90 ± 9.5	0.17 ± 0.02	32.6 ± 2.0	38.3 ± 2.7
Al-5CNT	6.2	2.33 ± 0.2 (45%)	107 ± 6 (19%)	0.23 ± 0.03 (35%)	38.3 ± 1.9	44.1 ± 1.3
Al-10CNT	12.4	2.89 ± 0.27 (80%)	125 ± 7 (39%)	0.33 ± 0.02 (94%)	41.5 ± 1.8	59.1 ± 3.0

Elastic modulus shows an improvement of 19% and 39% by addition of 5 wt.% and 10 wt.% of CNTs, respectively. Further analysis of the load displacement curves was carried out using the method used by Chen et al [275]. The strength and elastic properties of the coatings has been calculated using the following relations:

$$\frac{W_e}{W_t} = 1 - \frac{h_r}{h_{\max}} \qquad \text{Equation 4.12}$$

$$\frac{P_{\max}}{h_{\max}^2} = M_1 \sigma_{0.29} \left(1 + \frac{\sigma_y}{\sigma_{0.29}}\right) \left\{ \ln\left(\frac{E}{\sigma_y}\right) + M_2 \right\} \qquad \text{Equation 4.13}$$

$$\frac{\sigma_{0.29} - \sigma_y}{0.29E} = 1 - 0.142\frac{h_r}{h_{\max}} - 0.957\left(\frac{h_r}{h_{\max}}\right)^2 \qquad \text{Equation 4.14}$$

where W_e and W_t refer to the elastic work and total work done during indentation, h_{max} and h_r are the maximum depth and residual depth, P_{max} is the maximum load, σ_y is the

yield strength, $\sigma_{0.29}$ is the stress at strain of 0.29, E is the elastic modulus and $M_1 = 6.618$ and $M_2 = -0.875$ are constants for Berkovich type indenter. The W_e/W_t ratio provides a measure of the elastic energy recoverable from the material. It can be seen from Table 4.6 that the values of σ_y calculated from nanoindentation are quite large. Strengthening effect is reflected by the increase in the values of σ_y and $\sigma_{0.29}$ on addition of CNTs. The ratio of the strength of the composite coatings to that of Al-Si coating and the W_e/W_t ratio has been plotted in Fig. 4.64b. There is an increase of 17.5% and 27% in σ_y due to addition of 5 wt.% and 10 wt.% CNTs. The increase in W_e/W_t ratio with increase in CNT content indicates improvement of elastic properties of the composites.

4.7.2.2. Elastic Modulus and Hardness of Cold Sprayed Al-CNT Coatings

Nanoindentation was carried out on polished cross section of cold-sprayed Al-0.5CNT and Al-1CNT coatings. A matrix of 7 (x) 7 indentations (49 indents) was made for Al-0.5CNT coating. Each indent was 10 μm apart. Hence these values are obtained from an area of 70 μm x 70 μm. A matrix of 5 (x) 5 indentations (25 indents) representing an area of 50 μm x 50 μm was made for Al-1CNT coating. Fewer indents were required for the Al-1CNT coating because there was a lower spread in the values. Figure 4.26 shows that an area of 50 μm x 50 μm is representative of multiple splats and features present in the coating that includes, pure Al, Al-Si eutectic, porosity and CNTs. In both cases, it was found that there was a distribution in the values of the elastic modulus ranging from 40-220 GPa, though majority of the values ranged between 40-120

GPa. Figure 4.65 shows the load vs. depth curves for the lowest, highest and close to mean values obtained during the tests for the two samples.

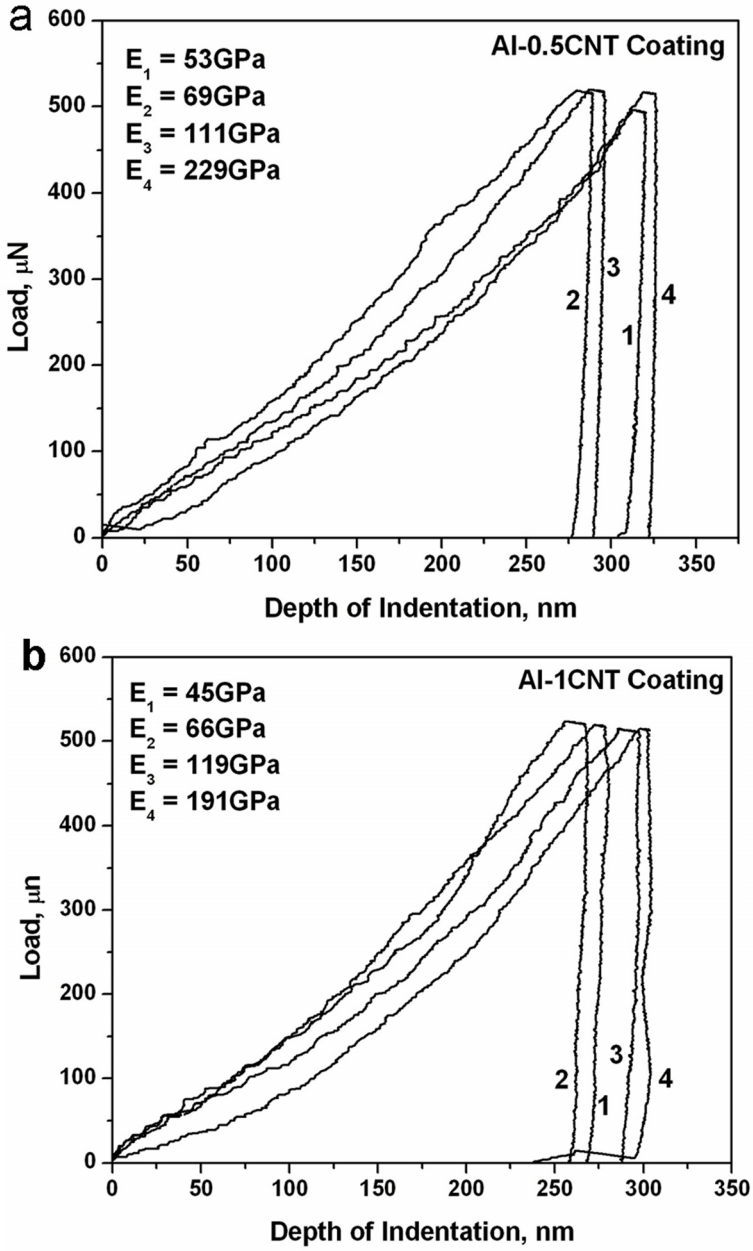

Fig. 4.65: Load vs. depth curve obtained from nanoindentation of polished cross section of a) Al-0.5CNT, and b) Al-1CNT coating

The values obtained by nanoindentation are specific to the local microstructure where the indentation was performed. Figure 4.66 plots the values of the elastic modulus measured at different locations within the coating in the form of histograms. The mean elastic modulus in both cases is close to 69 GPa which is the elastic modulus of polycrystalline aluminum [276] that makes up for most of the coating microstructure. The elastic modulus of polycrystalline silicon is 115 GPa [276] which is close to the maximum value of elastic modulus measured. Thus an indentation on the Al splat will give a value of 69 GPa but on a Al-Si region will yield a value anywhere between 40 and 115 GPa based on the degree of porosity.

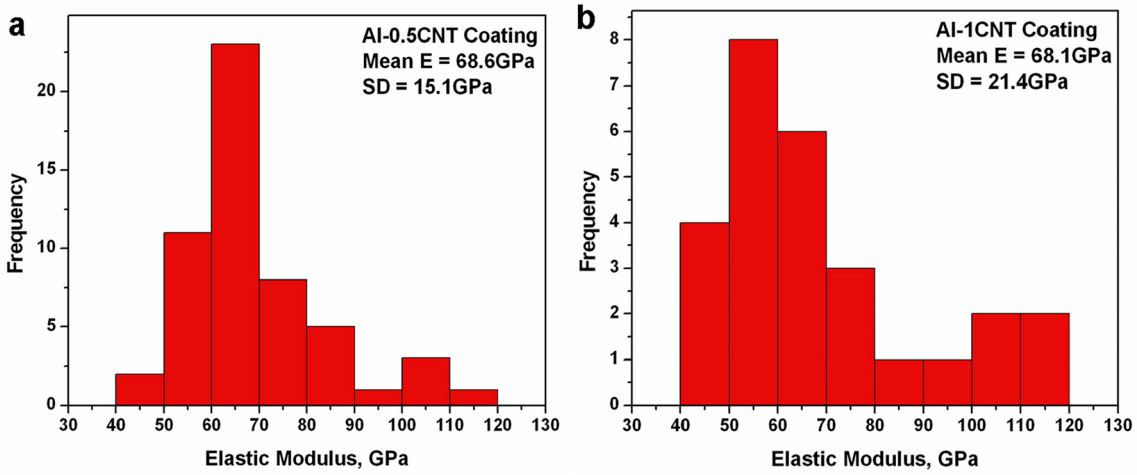

Fig. 4.66: Histogram of measured values of elastic modulus by Nanoindentation for a) Al-0.5CNT, and b) Al-1CNT

It is observed from Fig. 4.66 that a larger fraction of measured values fall between 40 and 60GPa (24% for Al-0.5CNT and 44% for Al-1CNT) and 90 and 120 GPa (9% for Al-0.5CNT and 19% for Al-1CNT) range for 1wt.% CNT containing coating. This is due to the fact that the volume fraction of porous regions as well as Al-Si particles in the 1wt.%

coating is higher. So statistically it is more probable to encounter such regions while carrying out nanoindentation testing in case of 1wt.% CNT containing coating.

Some large values for elastic modulus (155 – 229 GPa for Al-0.5CNT and 141 – 191 for Al-1CNT) were also obtained during nanoindentation of the present coatings. These modulus values are significantly higher than the elastic modulus of pure aluminum or silicon. This is due to the presence and the reinforcement action of CNT present in the region. There are four factors which influence the overall elastic modulus at a given location. They are the volume fraction of Al, Al-Si, CNT and porosity present in the coating. The overall volume fraction of silicon in the composite is 0.014 and 0.028 respectively for 10 wt.% and 20 wt.% addition of Al-Si powder to Al. Considering the rule of mixtures to hold true for the reinforcement due to silicon, the value of the elastic modulus of the matrix without CNT is calculated to be 70 GPa. So the reinforcement is mostly due to the presence of CNTs in the matrix. The elastic modulus of the CNT containing composites calculated using various micromechanical models is presented in Table 4.7. The elastic modulus value for CNT has been assumed as 950 GPa [10]. It is found that the predicted values from Halpin –Tsai equations and the modified Eshelby [220] method are close to the mean of the measured value. Coleman et al. [53] have observed that the Halpin – Tsai equations for random fiber orientation fit the experimentally measured values well at low volume fraction of reinforcement. Some of the measured values of elastic modulus are low compared to the predicted value.

Table 4.7: Elastic modulus of the cold sprayed Al-CNT composite calculated using different micromechanical models

Model used	**Calculated Elastic Modulus of Composite, GPa**	
	Al-0.5CNT	**Al-1CNT**
Rule of Mixture [277]	75	81
Mori Tanaka [278]	85	86
Hashin-Strikman [218]	Lower Bound – 85 Upper Bound – 88	Lower Bound – 86 Upper Bound – 91
Halpin Tsai [53]	72.5	75
Modified Eshelby Method [220]	71.5	73.5

In these calculations the porosity has not been taken into account. The porosity in the present coatings is 1-3 vol. % which is low and is going to have small effect on the overall modulus. However the localized increase in the fractional porosity might have significant effect on values obtained by nanoindentation which is difficult to model. The higher values obtained from nanoindentation reflects the values at different locations which might have an increased concentration of CNTs. Ling and Hou [279] have carried out the nanoindentation of Al_2O_3 – SiC composites and have found a decrease in the average elastic modulus with an increasing SiC content and a large scatter in data due to porosity. Kim et al. [68] have fabricated fully dense CNT reinforced Cu composites by spark plasma sintering of CNT-Cu powders obtained by molecular level mixing. It was observed that Vickers hardness increases almost linearly by 80% for a 10 vol% addition

of CNTs [68]. Salas et al. [143] have reported a decrease in the Rockwell hardness (Scale E) due to addition of CNT in shock consolidated aluminum. It was found that the CNTs formed carbonaceous aggregates which served as easy sites for failure and delamination [143]. These studies have confirmed that dispersion of CNTs and porosity are very important factors determining the extent of reinforcement achieved.

Correlation of Elastic Modulus Distribution with CNT Distribution

One of the purposes of the quantification of CNT distribution is to determine its effect on the mechanical properties of the nanocomposite. The local volume fraction of CNT reinforcement will have an effect on the localized mechanical properties. Models have been proposed for the effect of clustering on the global or macro properties of the composite. Kim et al. [71] have observed two step yielding behavior in copper-CNT composites fabricated by Spark Plasma Sintering of ball milled powders, which was attributed to the two phase microstructure made of CNT clusters and the matrix. Villoria and Miravete [221] have proposed a model to take into account the clustering in CNT composites which can be applied for any fiber reinforced composite showing having a two-phase microstructure. Both the models show that the macroscopic or global properties are determined by the microscopic or local properties of the clusters and the matrix. The localized mechanical properties of the nanocomposite can be measured by nanoindentation. The radius of the elasto-plastic region beneath a Berkovich indent is given by the relation [280]

$$c = \sqrt{\frac{0.3F_{\max}}{\sigma_y}}$$ Equation 4.15

Where ‘c’ is the radius of the elasto-plastic region around the indent, F_{max} is the maximum force used for indentation, σ_y is the yield stress. For a value of F_{max} = 600 μN and σ_y = 125 MPa for 1060 aluminum alloy in H18 condition, the diameter of the elasto-plastic region comes out to be 2.4 μm. The micrographs in Fig. 4.30a, 4.32a and 4.33a were divided into 25 parts so that each cell had an area of approximately 2 μm by 3 μm (similar to the size of elasto-plastic region). CNT percent of each cell was measured. Figure 4.67 shows the distribution of the values of the CNT percent in a cell.

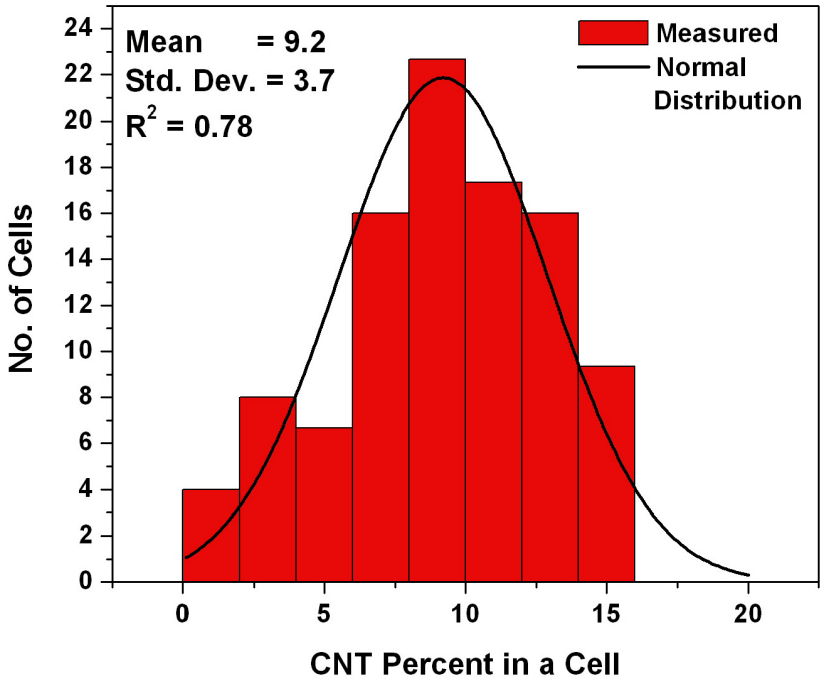

Fig. 4.67: showing the frequency distribution of the values of CNT percent in a cell

A normal distribution given by the following equation was found to fit the data approximately.

$$f(x) = \frac{1}{\sigma\sqrt{2\pi}} \exp\left[-\frac{1}{2}\left(\frac{x-\mu}{\sigma} \right)^2 \right]$$

Equation 4.16

It is seen that the CNT percent values follow the normal distribution curve approximately. Thereafter, elastic modulus of the cells is computed according to the CNT fraction present in them. Halpin-Tsai equations (eq. 2.13) were used to calculate the elastic modulus. For aluminum matrix of elastic modulus E_M = 69GPa and multiwalled CNT as fiber reinforcement with E_F = 970GPa and ζ = 2x800/66 = 24, η_L = 0.34 and η_T = 0.81. Figure 4.68 shows elastic modulus values computed using Halpin-Tsai method utilizing CNT fraction data from the different cells (each cell of size 2 μm by 3 μm).

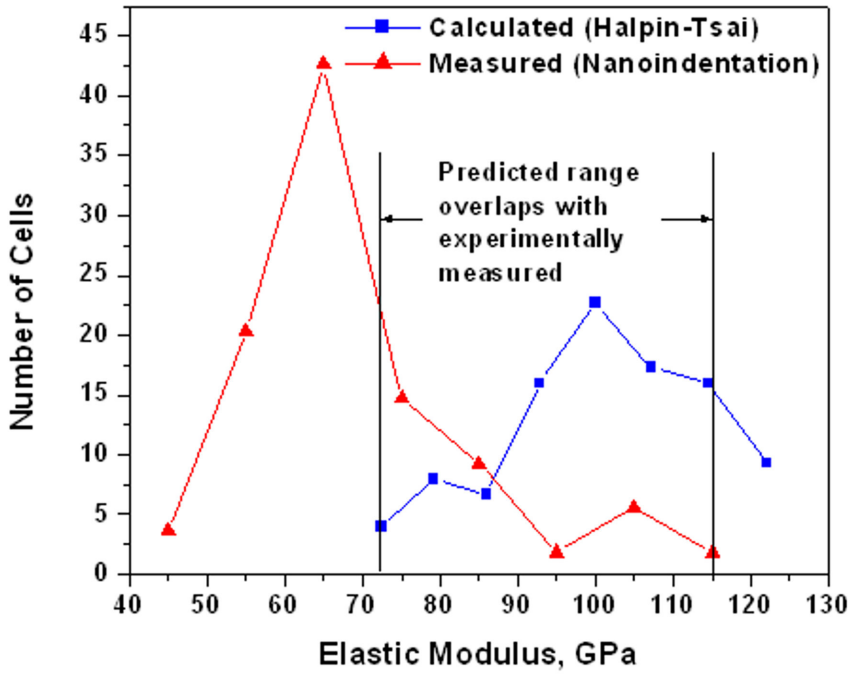

Fig. 4.68: Plot of calculated and experimentally measured frequency distribution of elastic modulus values for the composite

It also shows experimentally measured elastic modulus values using nanoindentation technique. The nanoindentation data shown in Fig. 4.66a was used in 4.68. The values obtained were statistically analyzed which resulted in the curve in Fig. 4.68. In Fig. 4.68, the plots have been normalized for a total of 100 values.

It was observed that even though the overall CNT volume percent was 0.6%, very large values of elastic modulus were obtained by nanoindentation testing. This was attributed to the local nature of the test and to the fact that CNT fraction could be large locally due to clustering effects. It is seen that the current analysis successfully predicts the existence of regions of high stiffness as observed by nanoindentation. This is indicated by the overlap in the values measured and predicted values as shown in Fig. 4.68. But it is seen that the frequencies do not match with computed values. The lower values of elastic modulus obtained by nanoindentation were ascribed to the local variations of porosity and splat interface defects, which are not included in Halpin-Tsai model. Also, most of the composite coating is made up of pure aluminum. It is only at the places where the CNT is present and where the regions are dense that this analysis would hold true. It is also observed that the general nature of the curves is similar. It is believed that if porosity and splat sliding [281] are taken into consideration, the computed values will be lower to provide a better match with experimental values. The current analysis shows how CNT distribution could affect the local mechanical properties of the nanocomposite.

4.7.3. Nanoscratch Measurements

4.7.3.1. Methodology for Computation of Wear Volumes

A novel method was devised to analyze nanoscratch data in terms of nano-scale wear resistance. The nanoindenter measures the instantaneous depth penetrated by the indenter (represented by h_{inst}) as it moves along the surface. So, there is a ***contact volume*** ***(V_C)*** associated with scratching which depends on the instantaneous depth of penetration of the indenter during scratching. But after the indenter passes, elastic recovery processes take place. So the true depth of a scratch (represented by h_{true}) is expected to be smaller than the instantaneous depth of penetration during scratching. Hence, the ***true volume*** ***(V_T)*** of material removed due to scratching depends on the true depth of the scratch which can be measured after the test has taken place. The true depth of a scratch can be measured from the SPM image. Figure 4.69 shows the variation of the instantaneous depth (h_{inst}) during scratching and the true depth (h_{true}) after the scratching for plasma sprayed Al-Si coating using a Berkovich tip. The inset shows the SPM image of the scratch showing the line along which true depth profile was obtained. It is observed that $h_{true} < h_{inst}$, which is attributed to elastic recovery process. The difference between h_{true} and h_{inst} at a given point is a measure of elastic recovery of the material. The Contact wear volume and True wear volume have been calculated according to the methodology described below.

For the Berkovich tip, it is noted that the orientation of the tip with respect to the scratch direction is very important. Figure 4.70 shows the top view of a Berkovich indenter and the scratch direction. As the indenter scratches, total volume swiped by the

indenter will depend on the projected area of the indenter along the scratch axis which is shown as the side view in Fig. 4.70.

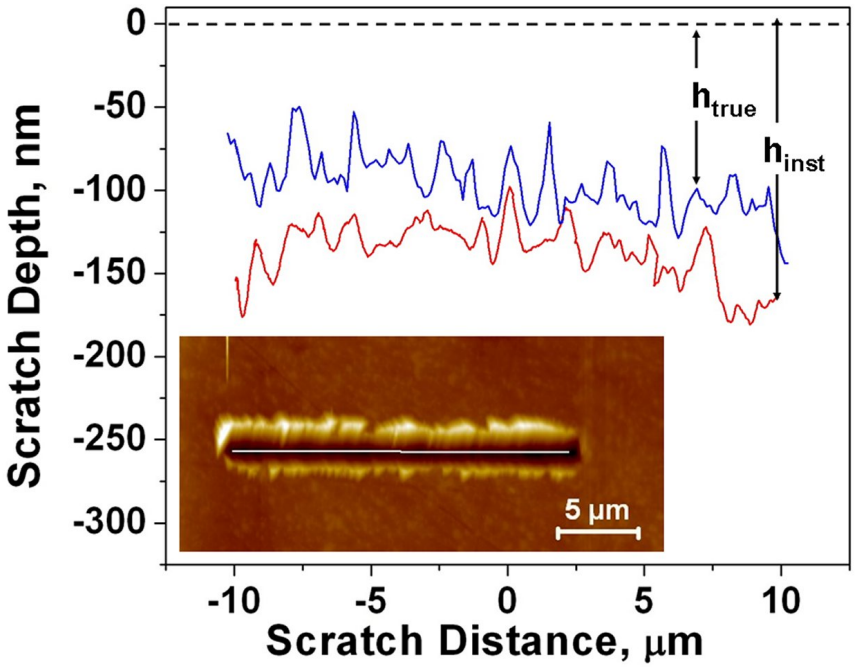

Fig. 4.69: Plot showing the variation of the true and instantaneous depth during nanoscratch of Al-Si coating using a Berkovich tip. The inset shows the SPM image of the scratch along with the line along with the true depth profile was obtained

In case of a perfectly plastic material, the resulting scratch groove will have a cross section equal to the side view of the indenter. The triangular cross section is characterized by the angles θ and ϕ as shown in Fig. 4.70, which in turn are dependent on the tip orientation angle α. The angle α can be experimentally determined from SPM images. The area of cross section is given by

$$A = \frac{1}{2}h\left[h\tan\phi + h\tan(\theta - \phi)\right] = C.h^2 \qquad \text{Equation 4.17}$$

Where $C = f(\alpha) = \frac{1}{2}[\tan\phi + \tan(\theta - \phi)]$ can be defined as the Area factor which varies with angle α. Values of θ and ϕ have been measured for several tip orientations and C was calculated.

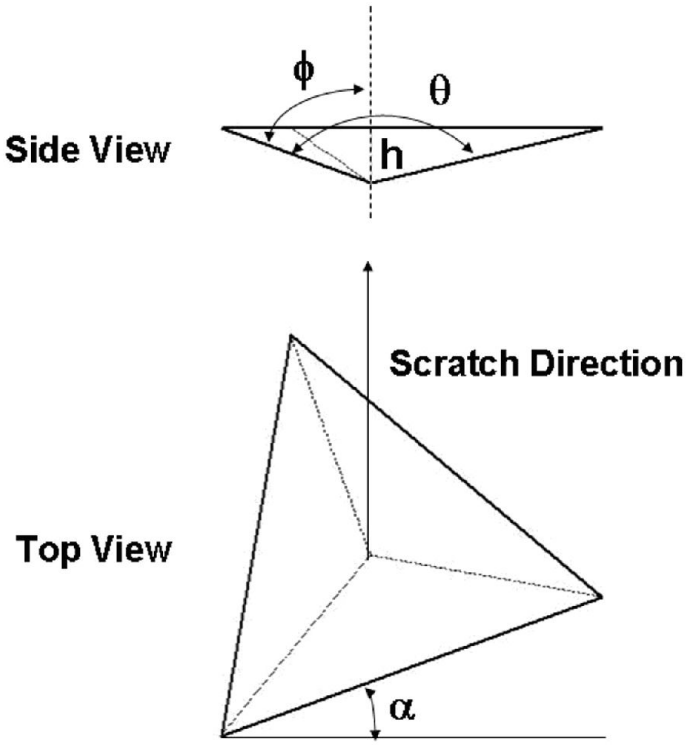

Fig. 4.70: Figure showing the top view and side view of Berkovich indenter

Figure 4.71 shows images of the top view and side view from of a Berkovich indenter with the corresponding values of θ and ϕ.

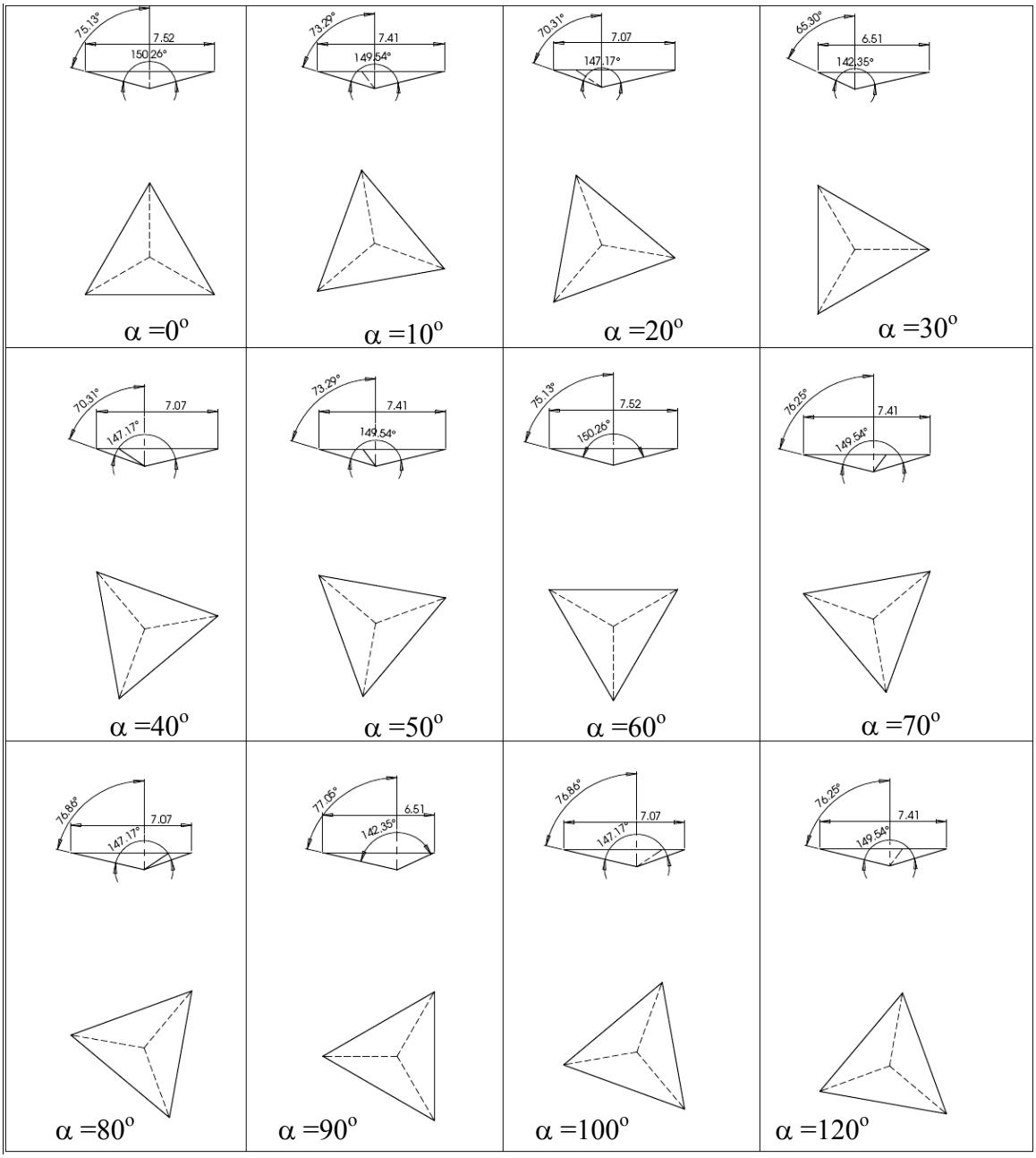

Fig. 4.71: Images showing the top view and side view of the Berkovich tip at various orientation and the corresponding angles

The values of θ, ϕ and C as a function of the orientation angle α has been plotted in Fig. 4.72. It is interesting to note that the values of C and θ have a periodicity of 60° while ϕ has a periodicity of 120° with α which arises from the three fold symmetry of the Berkovich indenter.

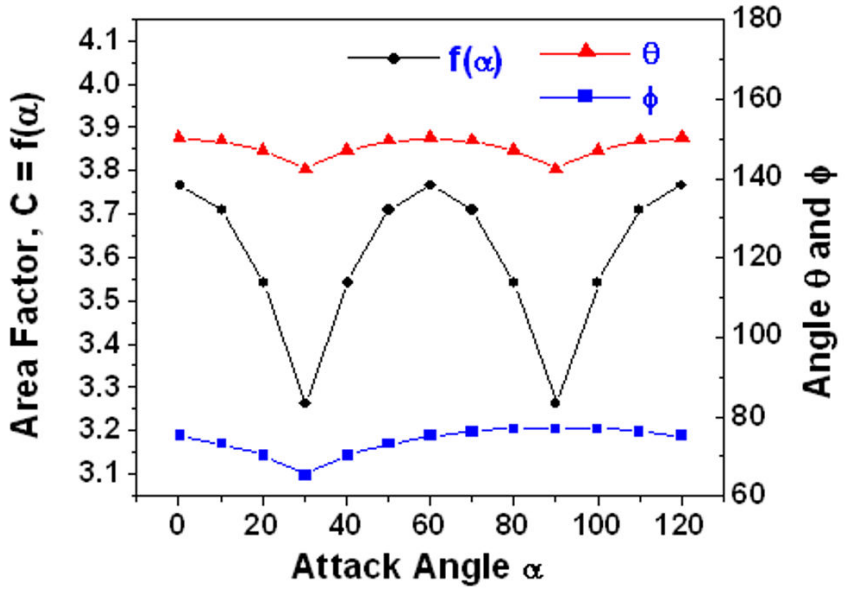

Fig. 4.72: Plots showing the variation of θ, ϕ and C for the Berkovich tip with the orientation angle α

When the indenter is scratching in edge forward (α = 0°) and face forward direction (α = 60°), the scratch groove has the same dimensions but the force required may differ due to the fact that the contact area is different. From the graph above it is seen that C varies between 3.26 and 3.77. Taking C to be mean value of 3.52 will lead to a maximum error of 7.8% in calculation of the cross sectional area of the groove. The

value of θ varies from 142.3 to 150.3 while ϕ varies from 65.3 to 77.1. From known angle α, C can be obtained from Fig. 4.72 and the Contact volume can be calculated by the following equation

$$V_C = \int_{-l/2}^{l/2} A(x)dx = \int_{-l/2}^{l/2} C.h_{inst}^2 dx \qquad \text{Equation 4.18}$$

For calculation of True wear volume (V_T) , the angles the angles θ and ϕ can be determined from the SPM images from the line profile taken transverse to the scratch direction as shown in Fig. 4.73.

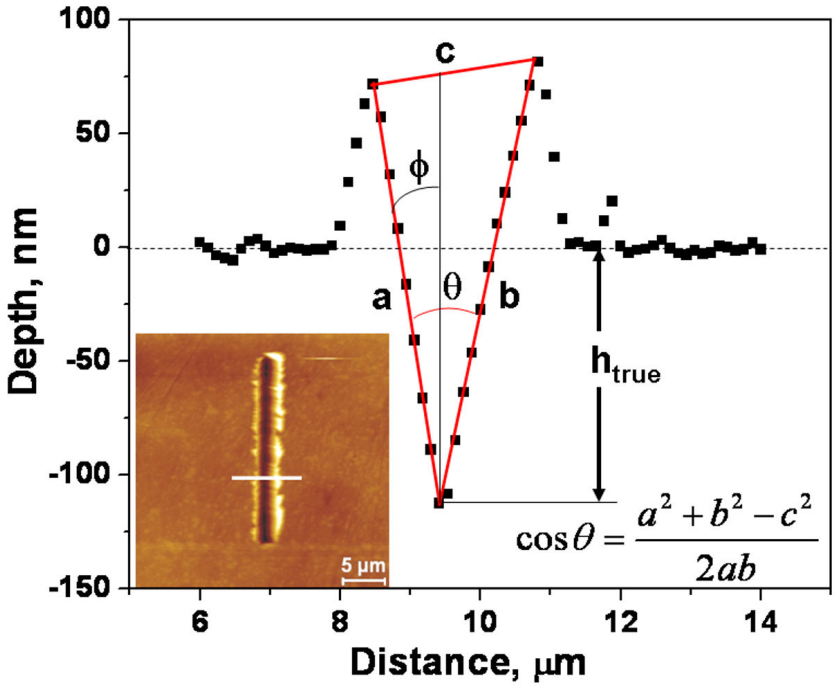

Fig. 4.73: Depth variation along the cross section of the scratch obtained using a Berkovich tip. The depth profile was obtained along the line shown in the SPM image (inset) perpendicular to the scratch length

The line profile shows pile-up on the sides of the scratch and the true depth of the scratch is also indicated. By calculating the dimensions of the triangle, θ and ϕ can be obtained by rule of cosines shown in Fig. 4.73 and C can be calculated. The true volume is then calculated equation 4.16 but using h_{true} values instead of h_{inst}.

4.7.3.2. Nanoscratch Behavior of Plasma Sprayed Al-Si-CNT Coatings

The nanoscratch tests were carried out on the matrix portion of the polished cross sections of the coating approximately perpendicular to the splats. The splat thicknesses range between 1-5 μm. Figures 4.74 shows SPM images of the scratches made with Berkovich tip for different loads and coatings. It can be inferred from the width of the scratches that as load goes on increasing from left to right, the wear volume increases for a particular coating. As we go from top to bottom, for a given load the wear volume goes on reducing with an increase in the CNT content. This clearly shows that addition of CNTs leads to reduction in wear volume at the nano-scale. The orientation angle α for the tip was found to be 3^o which leads to a C value of 3.67. To calculate true volume of the scratches, average of ten values of θ and ϕ were calculated for Al-Si, Al-5CNT and Al-10CNT coatings are tabulated in Table 4.8 where the Area factor C is also tabulated. It is observed that the theta values are almost similar for the three coatings and are larger than that for the Berkovich tip which is due to the elastic recovery processes. Using the values of C from Table 4.68 and the h_{true} values, V_T is calculated from equation 4.16. The arithmetic mean of the contact and true volume for two scratches each made at a load of 1000, 2000 and 3000 μN (total 6 scratches per coating) have been tabulated in Table 4.9.

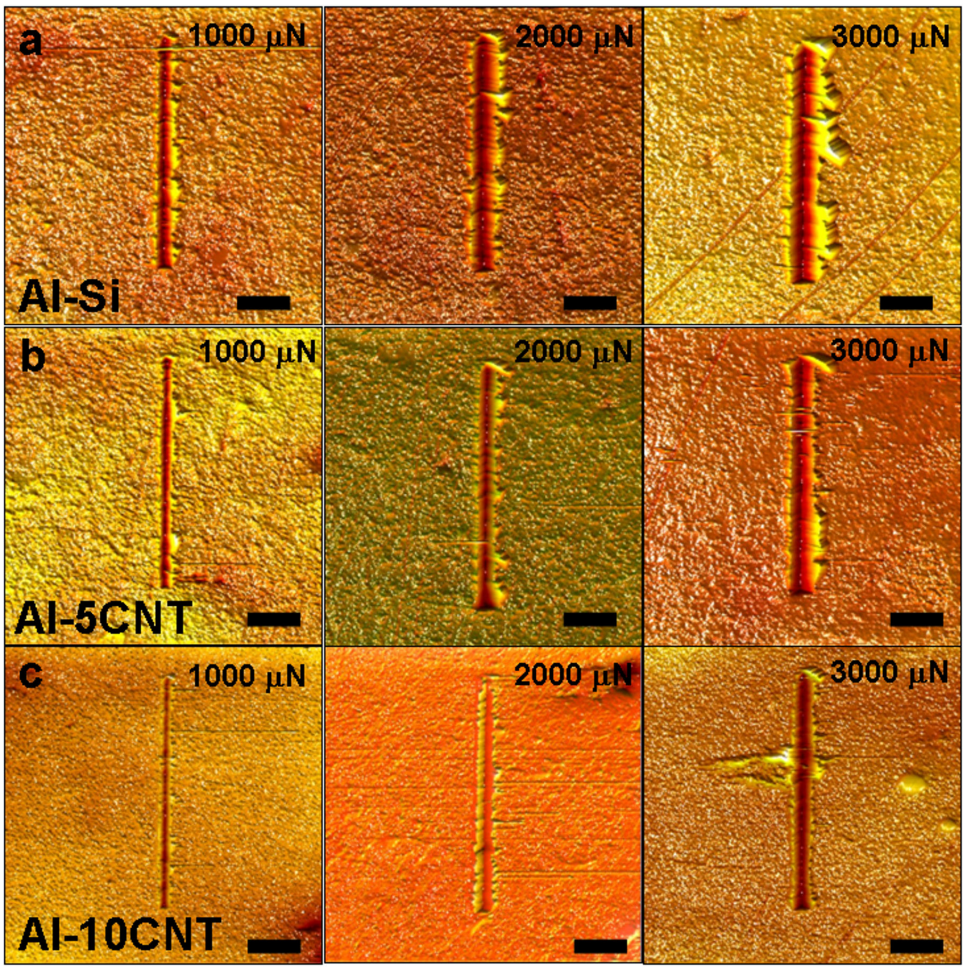

Fig. 4.74: Representative SPM images of the scratches obtained with Berkovich tip for a) Al-Si, b) Al-5CNT and c) Al-10CNT coatings. The scale bar shown corresponds to 5 µm

Table 4.8: Average values of θ and ϕ for scratches obtained with Berkovich tip

Sample	**θ**	**ϕ**	$C = \frac{1}{2}[\tan\phi + \tan(\theta - \phi)]$
Al-Si	162	80	6.4
Al-5CNT	162	80	6.4
Al-10CNT	163	81	6.7

The percentage decrease in the wear volumes as compared to the corresponding values for the Al-Si coating has also been shown. The effect of various factors on the values of V_C and V_T is discussed below.

Table 4.9: Values of the Contact and True wear volume calculated for scratches on the coatings using Berkovich tip. The percentage reduction in wear volume compared to Al-Si coatings is shown in the brackets

Sample	**Load, µN**	**Avg. Wear Volume, µm^3**		**Reduction in Wear Vol. compared to Al-Si (%)**	
		Contact (V_C)	**True (V_T)**	**Contact (V_C)**	**True (V_T)**
Al-Si	1000	0.70±0.06	0.56±0.04	-	-
	2000	2.0±0.15	1.46±0.03	-	-
	3000	2.56±0.10	2.51±0.12	-	-
Al-5CNT	1000	0.43±0.01	0.31±0.01	*38*	*54*
	2000	1.48±0.20	1.14±0.11	*26*	*21*
	3000	2.12±0.14	1.41±0.36	*17*	*34*
Al-10CNT	1000	0.39±0.03	0.21±0.01	*45*	*62*
	2000	0.77±0.07	0.59±0.03	*62*	*60*
	3000	1.28±0.13	0.73±0.07	*50*	*71*

Effect of the CNT Content

Figure 4.75 shows the variation of the contact (V_C) and true wear volumes (V_T) as a function of applied load for scratches. As the load increases, the contact and true volume values increase which is obvious due to the increased depth. It is also observed that the contact and true volumes decrease with increase in CNT content which indicates an improvement in the nano-scale wear resistance. As compared to the Al-Si coating, there is up to 71% decrease in the true wear volume by addition of 10 wt. % CNT which corresponds to an increase in nano-scale wear resistance by almost 4 times. The true volume of the scratches is found to be smaller than the contact volume indicating that elastic recovery processes take place.

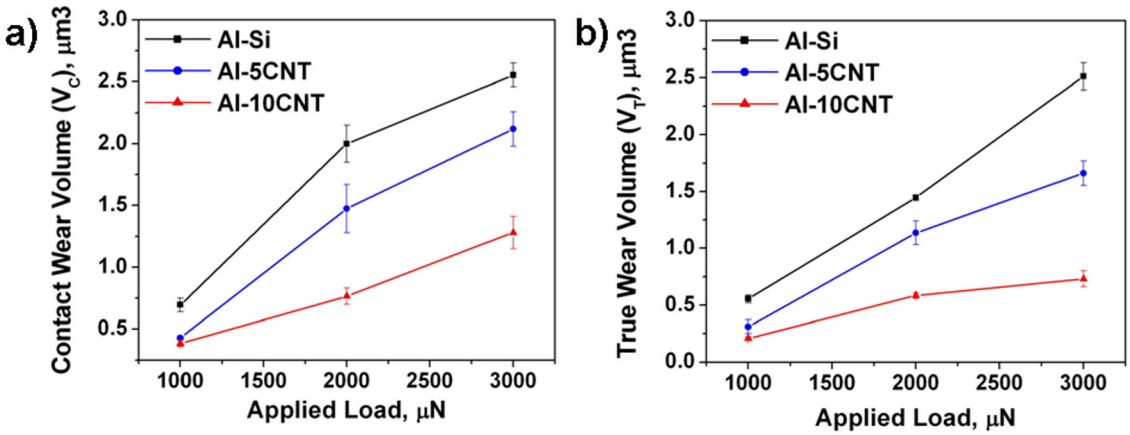

Fig. 4.75: Variation of a) contact volume and b) true volume of the scratches with the applied load for the three coatings

The effect of CNTs on the wear properties is two-fold. The first aspect is that addition of CNTs causes an increase in the hardness of the coatings. The nano-hardness of the Al-Si, Al-5CNT and Al-10CNT coatings was found to be reported to be equal to

1.61 ± 0.20, 2.33 ± 0.27 and 2.89 ± 0.27 GPa respectively. The increase in the hardness with an increase in CNT content results in the reduction of contact depth, and hence, contact and true volumes. The hardness and strength increases because CNTs resist the flow of material and impede dislocation motion. Archard has given a simple theory of mechanical wear relating the wear volume to the load, which can be represented by the simple relation when the average size of the contact area and wear particles are same [282] as

$$\frac{V}{l} = k\left(\frac{P}{H}\right) \qquad \text{Equation 4.19}$$

Where V is the wear volume, l is sliding distance, k is wear coefficient, P is the applied load and H is hardness of material. The wear coefficient (k) is a measure of the probability that a contact event results in material removal thereby causing wear.

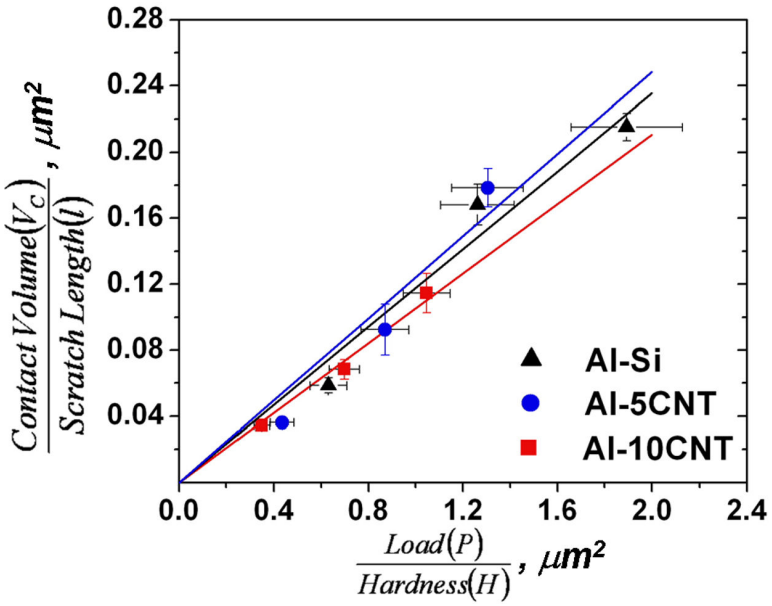

Fig. 4.76: Variation of contact volume per unit scratch length with the ratio of applied load and hardness of the three coatings for the three loads with Berkovich tip

Figure 4.76 shows a plot of the contact wear volume per unit length (V_C/l) as a function of the ratio of load to hardness of the coatings (P/H) for the three loads for Berkovich tip. A straight line was fit to the data on Contact wear volume per unit scratch length and P/H at a given load for the three coatings and the wear coefficient was measured from the slope of the line. The wear coefficient is equal to 0.091, 0.120, and 0.119 for 1000, 2000 and 3000 μN load respectively which are quite large values corresponding to cases of severe wear [282].

The second important effect of addition of CNTs is on the elastic recovery property of the coating. A lot of work has been done in quantification of the elastic response of a material from the load-depth curves obtained from nanoindentation. Most of the work has been in correlating the ratio of elastic work to total work (W_E/W_T) of indentation to the ratio of Hardness to Elastic modulus (H/E_r). Cheng and Cheng [283] have combined finite element simulation and analytical formulation and obtained linear relation between W_E/W_T and H/E_r. Giannakopoulos and Suresh [280] have used $\left(1-h_r/h_{\max}\right)$ as a measure of W_E/W_T where h_r is the residual depth and h_{max} is the maximum depth during nanoindentation. During nanoindentation the actual contact depth is lower than the depth measured by indenter due to elastic deformation of the surface. Bao et al. [284, 285] have derived a recovery resistance parameter based on this elastic response which is given as $R_s = 2.263E_r^2/H$, where R_s is the recovery resistance. Most of the results show a linear relation between W_E/W_T and H/E_r, although recently a nonlinear relation has been derived for the perfect conical tip [286]. The values of various parameters relating to W_E/W_T obtained from nanoindentation have been tabulated in

Table 4.10. From Table 4.10, the increase in H/E_r and $\left(1-h_r/h_{\max}\right)$ values clearly indicates that there is enhancement of elastic properties by addition of CNT. The R_s values are more or less same indicating that it is not a sensitive parameter to CNTs. From Table 4.9, it can be seen that the true wear volumes of the coatings are lower than the contact wear volumes for all the coatings which is due to elastic recovery after the scratching process.

Table 4.10: Variation of the Recovery parameters with CNT content of the coatings

Coating	**H/E_r**	$\left(1-h_r/h_{\max}\right)$	$R_s = 2.263E_r^2/H$
Al-Si	0.018	0.17 ± 0.02	11570±1340
Al-5CNT	0.022	0.23 ± 0.03	11250±2180
Al-10CNT	0.024	0.33 ± 0.02	11880±1680

It is to be noted that, the actual contact depth h_c is lower than the instantaneous depth h_{inst} as in case of nanoindentation and is given by

$$h_c = h_{inst} - h_s \qquad \text{Equation 4.20}$$

where h_s is a displacement of the surface at the perimeter of contact with the indenter as shown in Fig. 13. In case of nanoindentation, we have [230]

$$h_c = h_{inst} - \varepsilon\frac{P}{S} \qquad \text{Equation 4.21}$$

Where P is the applied load, S is the slope at maximum load of the unloading portion of the load-displacement curve during nanoindentation and ε is a factor depending on the geometry of the indenter. The value of ε is equal to 1 for flat punch, 0.72 for a conical

indenter and 0.75 for a paraboloid of revolution [230]. Thus, the actual contact volumes are expected to be lower than those calculated based on h_{inst}.

Experimental Evidence of Increased Recovery

Figure 4.77 shows the SEM images of a scratch on Al-5CNT coating at a load of 2000 μN. The corresponding SPM image of the scratch obtained with the Berkovich tip is shown below the SEM image.

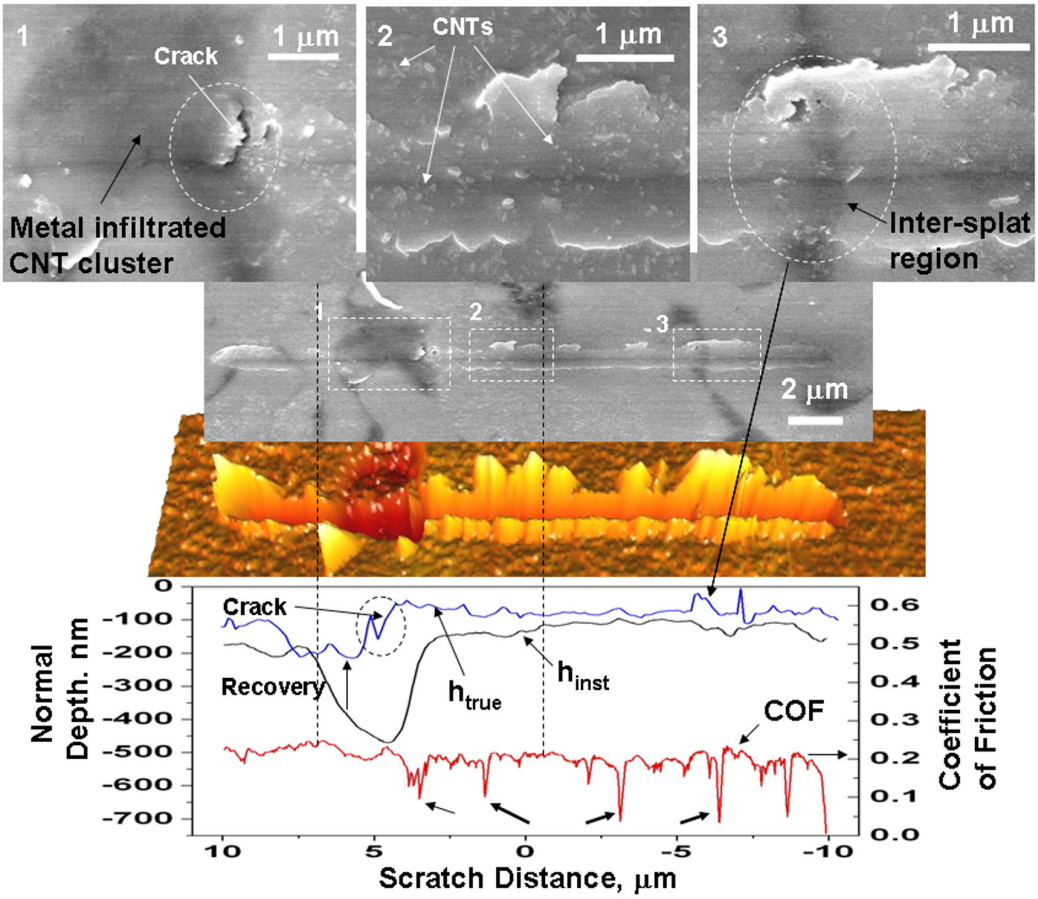

Fig. 4.77: SEM and SPM image of the scratch on Al-5CNT coating made with a Berkovich tip at 2000 μN load. The variation of the instantaneous and true depth is also shown. High magnification SEM images from the wear track are shown

The graphs at the bottom show the variation of the instantaneous depth (h_{inst}) as well as true depth (h_{true}) and the coefficient of friction (COF) along the scratch distance. The scratch is made from right to left and the indenter encounters CNT rich regions in between. A metal infiltrated CNT rich cluster can also be seen towards the end which is darker in contrast to the Al-Si regions. The CNT cluster is soft due to the inter-tube porosity which causes deeper penetration of the indenter tip resulting in generation of crack as seen from the magnified SEM image 1. The true depth as measured from SPM images is lower than the instantaneous depth which is due to elastic recovery processes. It is seen that the elastic recovery is greater for the regions between the two dashed lines. The region between the two dashed lines contains more CNTs as shown in the magnified SEM images 1 and 2. From SEM image 3 which corresponds to an intersplat region where CNTs are present (as evidenced by the darker contrast), the recovery is found to increase in the intersplat region. ***These observations provide direct evidence for increased recovery due to the "presence" of CNTs***. The inverted spike in the variation of coefficient of friction with CNTs (marked by the arrows in Fig. 4.77) will be described later.

Figure 4.78 shows the SEM image of a scratch on Al-10CNT made with 2000 μN load. A large CNT rich cluster which is partially infiltrated with Al-Si (during plasma spraying) is seen at the center of the scratch. The CNT cluster is softer than the matrix due to the inter-tube porosity and the indenter penetrates deeper as compared to the matrix. It is observed that in the area between the dashed lines, there are CNTs as seen in the magnified SEM image 1 the recovery is larger. Compared to Al-5CNT in Fig. 4.77, the true depths are smaller and the recovery is larger in Al-10CNT coating as indicated

by the difference between the true and the instantaneous depth. The recovery is observed to be larger in the CNT cluster. ***These observations indicate recovery increases with "increase" in CNT content.***

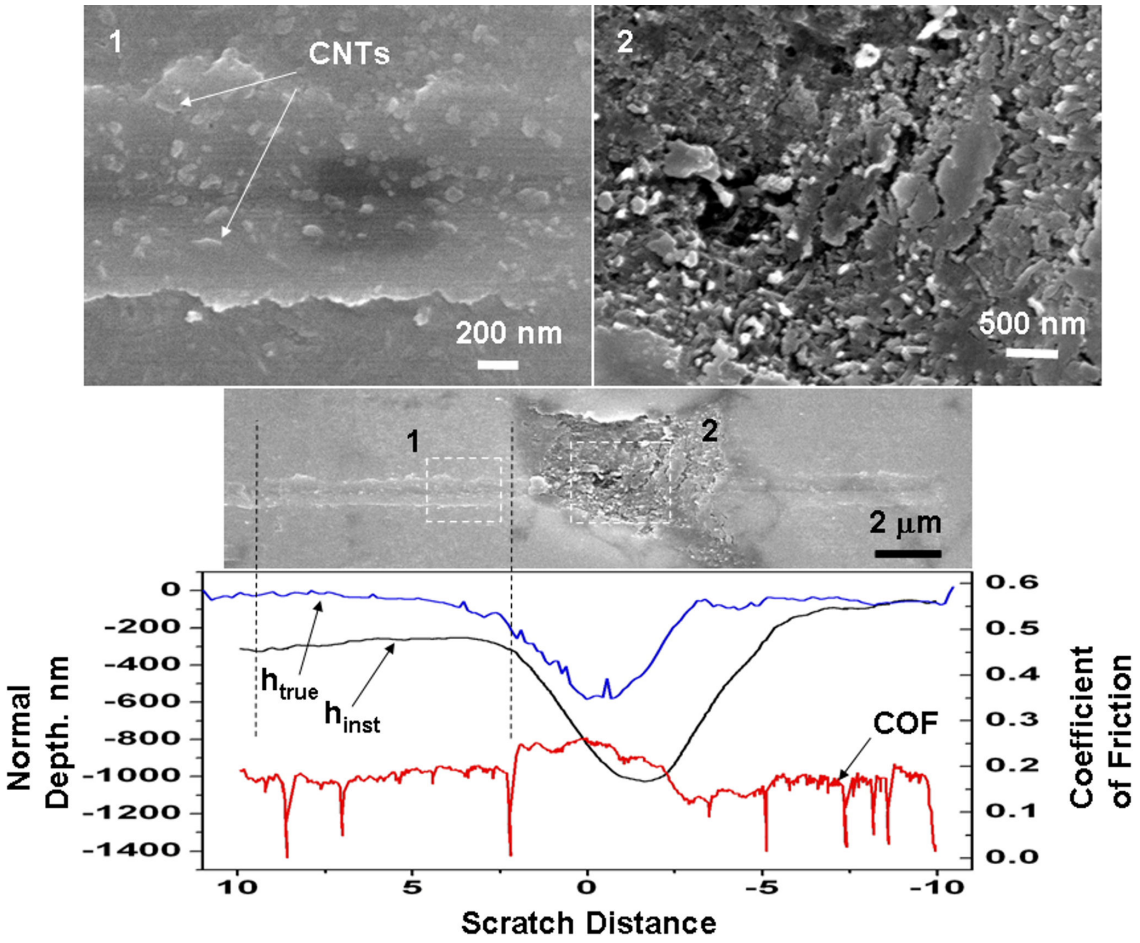

Fig. 4.78: SEM images showing a scratch on Al-10CNT coatings with a Berkovich tip at 2000 μN load. The indenter encounters a CNT cluster

The increase in the elastic recovery at CNT clusters and CNT rich regions are due to the elastic properties of the CNT and interaction with the stress field below the indenter. Figure 4.79 shows a schematic of CNTs present just below the indenter tip.

Depending on the orientation of the CNT, the stress acting on it could cause it to buckle (CNT1), bend (CNT2) or undergo radial compression (CNT3). In case, the tip is over a CNT cluster, some or the other CNTs in the cluster will be undergoing buckling, bending or radial compression.

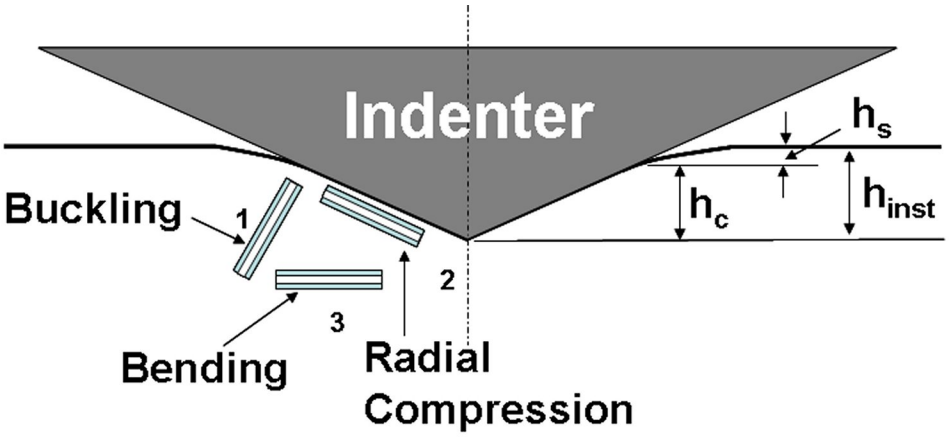

Fig. 4.79: Schematic of indenter tip-CNT interaction in the composite during scratching

Bending of CNTs has been observed to occur by rippling [55]. Bower et al. [259] have observed that the onset strain for rippling was ~5% and that bending completely recovered for strains as high as 8%. Buckling of CNTs under axial load have been studied computationally and experimentally and it has been found to occur by 'column' buckling for long CNTs (L/D ~100) and by 'shell' buckling for shorter nanotubes (L/D < 20) where L/D is the aspect ratio [287-289]. Jeng et al. [288] have measured the critical stress for buckling of individual nanotubes between 12-16 μN, while Waters et al. [289] have measured the force to be 2.5 μN. While the buckling might not result in increase in elastic response of the coatings, it is expected to increase the resistance to deformation. Muthaswami et al. [290] have measured the radial elastic modulus of CVD grown

MWNTs to be between 21±7 GPa using ultrasonic force microscopy, which shows that the radial compression and collapse of nanotubes can happen at smaller loads. Nevertheless, CNTs under radial compression still serve as obstacles to material flow and would help in increasing the hardness. So these mechanisms lead to the increased hardness and elastic recovery due to addition of CNTs.

Coefficient of Friction of Plasma Sprayed Al-Si-CNT Coatings

The other important aspect of wear is the coefficient of friction which is discussed in this section. Figure 4.80 shows the variation of the value of the coefficient of friction with scratch distance for the three coatings. The coefficient of friction (COF) has been calculated by the ratio of the instantaneous lateral force and normal force during scratching. It is observed that the values display localized variation with scratch distance as seen in Figs. 4.77 and 4.78. At some instances the lateral force reduces to very low values making the friction coefficient also very small and resulting in inverse spikes. Inverse spikes in coefficient of friction curve were found at several places where there were micro-cracks on the wear track or fracture of piled-up material. The scratching process happens in a stick-slip fashion with slip occurring at places where there is micro-crack generation or fracture of piled up material. There is sudden decrease in the lateral force during such slip process which results in formation of inverted spike. The coefficient of friction with the Berkovich tip is almost similar for the three coatings. From Figs. 4.77 and 4.78, it is observed that the local COF values at places where dispersed CNTs exist, are slightly lower. At some inter-splat regions where CNTs are

concentrated as in case of SEM images 2 and 3 in Fig. 4.78, small decrease in COF values was observed.

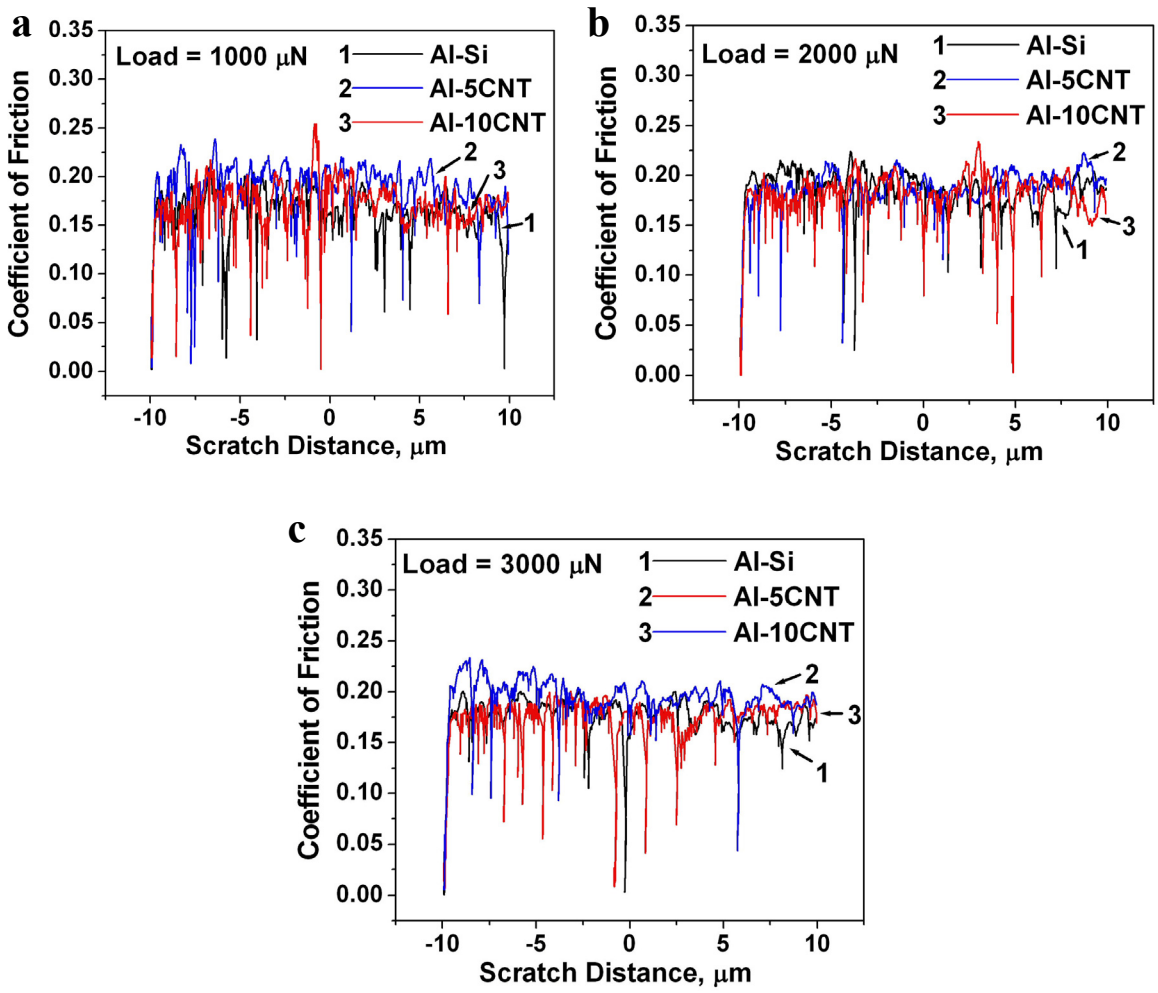

Fig. 4.80: Variation of the friction coefficient with CNT content of the coatings with the scratch distance at various loads of a) 1000 μN, b) 2000 μN, and c) 3000 μN

In general, the COF values are similar for all the loads. This is in accordance with Amonton's law for macro wear [291] which states that the friction coefficient is constant and independent of macroscopic area of contact. With increase in the applied force, the

total contact area between the asperities ($\sum A_{asp}$) increases and this leads to a increase in the fiction force which can be expressed as $F_f = \tau \sum A_{asp}$, where F_f is the friction force and τ is the shear strength. The linear relationship between friction force to the applied load does not hold true for single asperity contact in which A_{asp} is not linearly related to applied load. Recently, Mo et al. [292] have shown that Amonton's law is also valid for nano-scale contacts where atomic scale roughness comes into picture similar to roughness in macro-scale. Deviation from the Amonton's law can occur in the case of adhering surfaces. According to Lafaye and Troyon [293] the frictional forces arise from adhesion between the surfaces in contact and the ploughing action. The friction coefficient can be written as:

$$\mu = \mu_{adh} + \mu_{plough} \qquad \text{Equation 4.22}$$

Adhesion forces between the tip and coating surface play significant role in increasing the frictional forces. According to the Johnson Kendall Roberts theory [294] the adhesive force is given as

$$F_{adh} = -\frac{3}{2}\pi r W_A \qquad \text{Equation 4.23}$$

where r is the contact radius of curvature and W_A is the work of adhesion. Taking W_A to be equal to 1000 $mJ.m^{-2}$, F_{adh} is calculated ~ 1 μN for the Berkovich tip which is very small compared to the applied load (~1000-3000 μN) suggesting that adhesion forces do not play significant role in determining the coefficient of friction values.

From Fig. 4.80 it is seen that the average COF values slightly increases for 5 wt. % CNT and then decreases for 10 wt. % CNT coatings. This is because the effect of

CNTs is two-fold. There is strengthening due to the addition of CNTs which increases the lateral force required for scratching due to increase in the critical shear strength τ. On the other hand, presence of CNTs might lead to lowering of the friction coefficient by acting as lubricant. The possible explanation could be that the increase of COF due to strengthening effect is more pronounced in Al-5CNT coating, while in the Al-10CNT coating the decrease in COF due to lubrication phenomena dominates. This could be due to better dispersion of CNTs in Al-5CNT as was observed in Fig. 4.12. The small effect of CNT content on friction coefficient is due to the fact that the CNTs are intact and lubrication mechanism of graphite are not applicable unless there is extensive damage to CNTs and generation of graphite like debris. This effect is more pronounced in macro-scale wear experiments as in case of Ni-P-CNT [118] and Al_2O_3-CNT composites [295].

4.7.3.3. Nanoscratch Behavior of Cold Sprayed Al-CNT Coatings

Scratches of 10 μm length were made on the polished cross section of the cold sprayed Al-CNT coatings at a normal load of 1000 μN. Figure 4.81 shows the SPM images of the scratches on the three coatings.

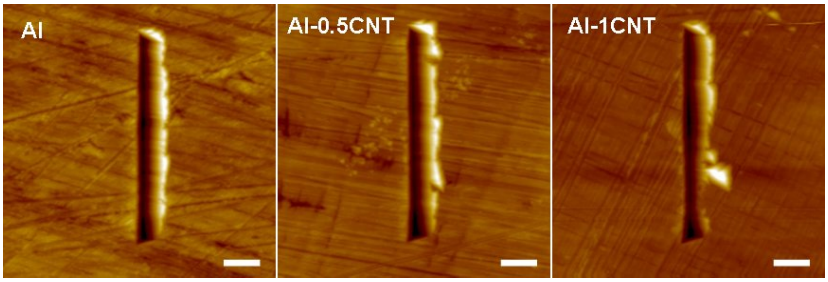

Fig. 4.81: SPM images of the scratches on cold sprayed Al-CNT coatings made using a Berkovich tip at 1000 μN load

Figure 4.82 shows the variation of true depth and instantaneous depth along the scratch distance for the three coatings.

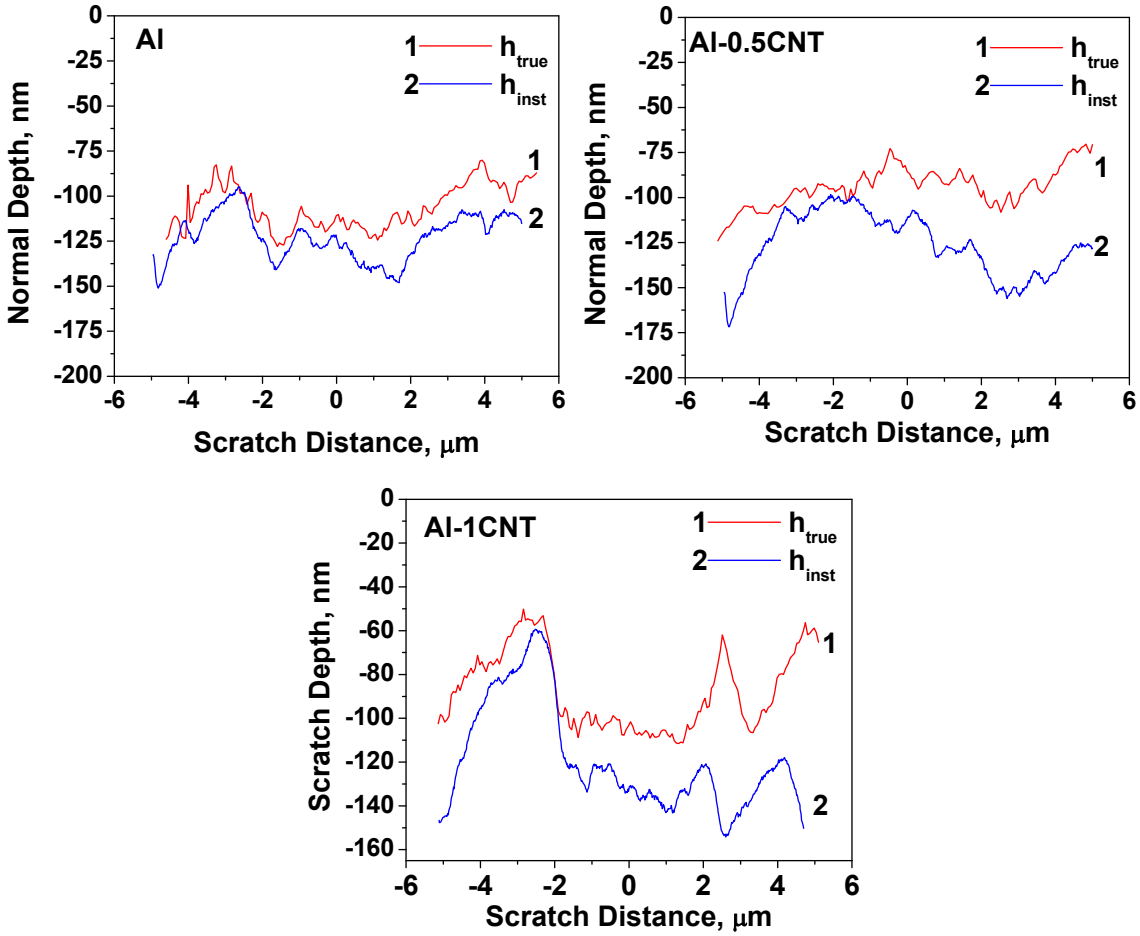

Fig. 4.82: Variation of h_{inst} and h_{true} along the scratch for the cold sprayed Al-CNT coatings

It can be observed that the true depth reduces as the CNT content increases. *Also from the separation between the h_{inst} and h_{true} curve it is observed that the elastic recovery properties also increases with addition of CNTs.* It is seen that the recovery in Al-1CNT is slightly greater than Al-0.5CNT coating. The orientation angle of the tip was

18^o which leads to a value of C = 3.57 from Fig. 4.72. The values of θ and ϕ were calculated from the depth profile of the scratches as described previously. Although the angles θ and ϕ varied from 151-154^o and 71-74^o respectively, the average values were found to be same for all the coatings. The average value of θ, ϕ and C were equal to 152^o, 73^o and 4.21 respectively. The contact volume and true volume have been calculated using the information above and have been tabulated in the Table 4.11. The values reported are the average value of three scratches.

Table 4.11: Calculated values of the contact and true wear volumes for cold sprayed Al-CNT coatings

Coating	**Contact Volume (V_C), μm^3**	**True Volume (V_T), μm^3**	**Reduction in V_T compared to Al coating (%)**
Al	0.49±0.08	0.46±0.02	-
Al-0.5CNT	0.58±0.04	0.40±0.07 (13%)	15%
Al-1CNT	0.50±0.12	0.33±0.02 (28%)	28%

The values of the wear volumes have been plotted in Fig. 4.83 below. It is observed that there is not much difference in the contact wear volume due to addition of CNTs. This is due to the fact that the hardness of the coatings is not significantly affected by the addition of CNTs. The true volume however shows a reducing trend with addition of CNTs. The reason for this is increased elastic recovery of the coatings as shown in Fig. 4.82. Increased elastic recovery reduced the h_{true} values which in turn reduced the true

volume of the scratches. Based on the true volume it can be said that the nano-scale wear resistance of pure Al improves by 40% by addition of 1 wt.% CNTs.

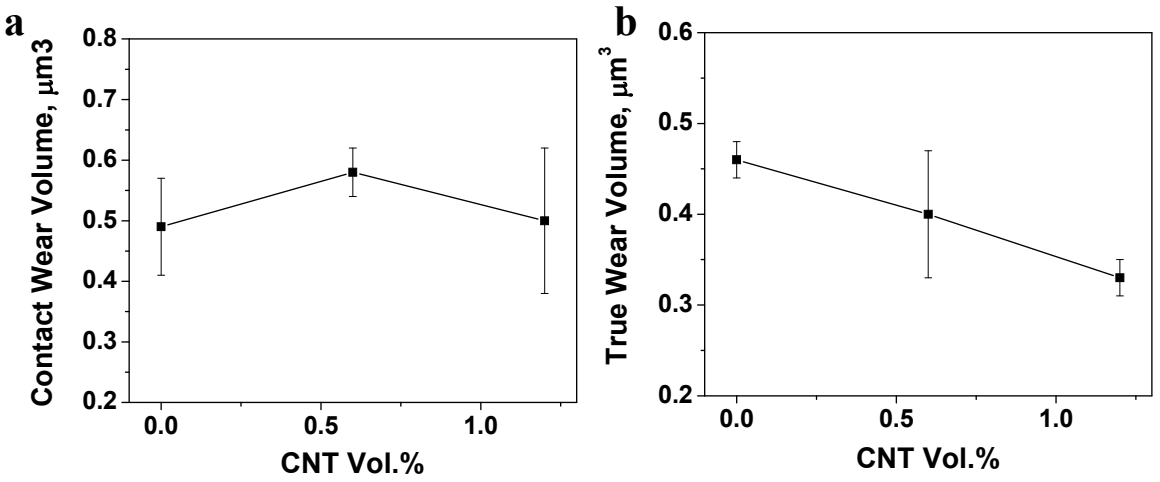

Fig. 4.83: Variation of a) Contact and b) True wear volumes of the cold sprayed Al-CNT coatings as a function of CNT content

Coefficient of Friction of Cold Sprayed Al-CNT Coatings

Coefficient of friction was calculated as the ratio of the instantaneous lateral and normal forces. Figure 4.84 shows the variation of the friction coefficient with CNT content. Figure 4.82 shows that there is not much variation in the coefficient of friction of the coatings. This is partially due to the fact that the CNT content is low and the fact that they are concentrated mainly in the inter-splat regions. The average coefficient of friction was found to be 0.17±0.01, 0.19±0.01 and 0.18±0.02 for Al, Al-0.5CNT and Al-1CNT coating respectively. The coefficient of friction was found to be more or less similar to the plasma sprayed Al-Si-CNT coatings. So it can be said that CNT addition does not bring significant change in coefficient of friction as measured in a nanoscratch test.

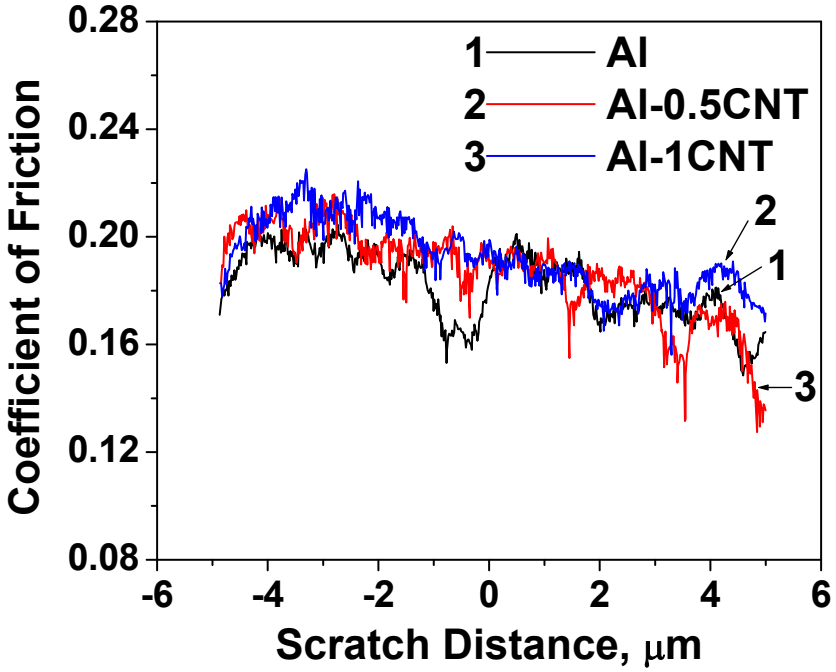

Fig. 4.84: Variation of Coefficient of Friction with CNT content of the coatings

4.7.4. Summary of Nanomechanical Tests

In has been shown that nano-mechanical tests like nanoindentation and nanoscratch are very useful and provide a lot of information of on the mechanical behavior of CNT composites. Due to the localized nature of the tests, the scatter in the data is usually high indicating the anisotropic nature of the plasma sprayed coatings. Scatter in data can also be related to the dispersion of CNTs in the microstructure. Nevertheless, the average values are a good indicator of the strengthening effect of CNTs. Nanoscratch test are very important in quantifying surface wear properties. Comparing the h_{inst} and h_{true} values gives information on the effect of CNT addition on the elastic recovery of the coatings. Also the true volumes of the scratches are a good indicator of the nanoscale wear resistance. SPM and SEM imaging of the scratches can

further provide information in correlating the microstructural features with wear resistance and coefficient of friction.

4.8. Bulk Mechanical Properties of Plasma Sprayed Al-Si-CNT Coatings

Macro scale mechanical properties were measured in tension and compression for large samples machined out of the bulk spray formed cylindrical structure.

4.8.1. Tensile properties of Plasma sprayed Al-Si-CNT composites

Tensile tests were carried out on flat dog bone type samples machined out of the spray deposited cylinder, schematic of which was shown in Fig. 3.5. Figure 4.85 shows the representative pictures of the machined tensile specimen and the fractured specimens. It is observed that the CNT reinforced samples have failed outside the gauge length indicating that they have higher notch sensitivity. The position of failure indicates that the CNT containing samples might be more notch sensitive. Esawi et al. [296] has also reported higher notch sensitivity of Al-2wt% CNT composites prepared by hot extrusion of ball milled Al-CNT powder mixture in the un-annealed condition. It was observed that the samples consistently failed outside the gauge length. Fig. 4.86 shows the representative engineering stress strain curves for the Al-Si-CNT composites in the as- sprayed condition.

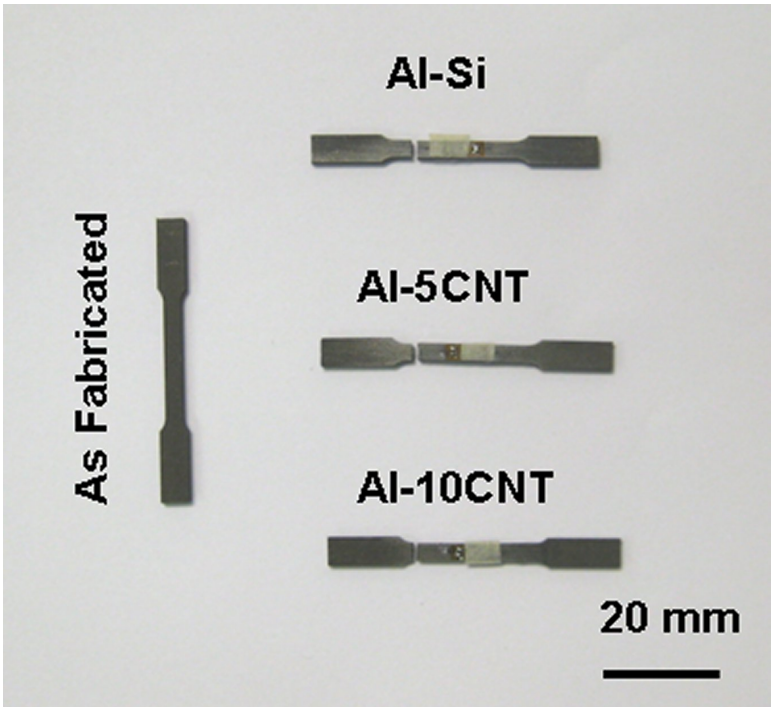

Fig. 4.85: Pictures of the machined and fractured tensile samples made from plasma sprayed Al-Si-CNT composite

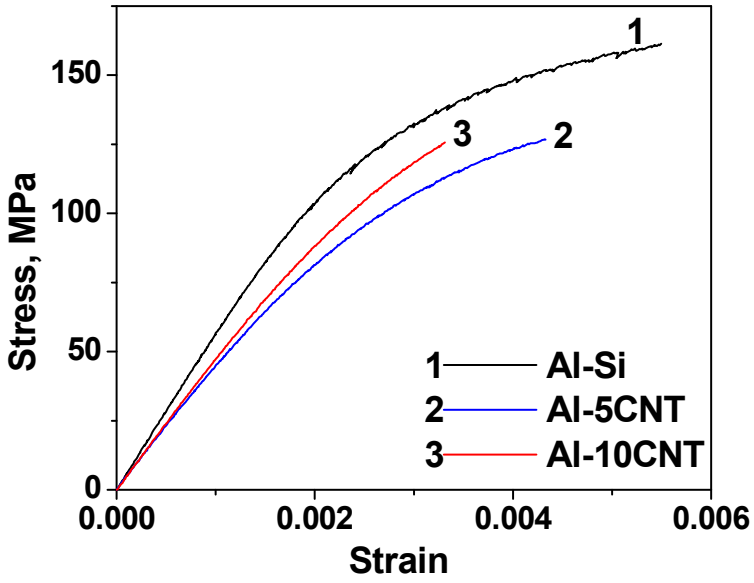

Fig. 4.86: Representative engineering stress strain curves for plasma sprayed Al-Si-CNT composites

The values of elastic modulus, fracture strength and the strain to failure have been tabulated in Table 4.12. The variation of the properties with CNT content has been presented in Fig. 4.87.

Table 4.12: Mechanical properties of bulk Al-Si-CNT composites in as-sprayed condition obtained from tensile test

Sample	**Elastic modulus GPa**	**Average E, GPa**	**Fracture Strength MPa**	**Average σ_f**	**Failure Strain %**	**Average ε_f**
Al-Si	54.6	56.3±1.1	162	162±3	0.65	0.58± 0.06
	57.0		166		0.59	
	56.8		162		0.55	
	56.6		159		0.51	
Al-5CNT	43.2	43.5±0.3 (-23%)	121	123±3 (-24%)	0.4	0.41± 0.02 (-29%)
	43.8		127		0.43	
	43.3		121		0.4	
	43.6		122		0.39	
Al-10CNT	44.5	46.5±1.4 (-17%)	115	121±6 (-25%)	0.31	0.32± 0.02 (-45%)
	47.4		117		0.29	
	46.9		124		0.33	
	47.2		127		0.33	

Tensile tests indicate that there is a 23% and 17% decrease in elastic modulus, 24% and 25% decrease in fracture strength and 29% and 45% decrease in fracture strain by addition of 5 wt.% and 10 wt.% CNTs. Thus addition of CNTs reduces the ductility of the Al-Si alloy and reduces the strength and stiffness by considerable amount. These results are in contradiction with previously reported research from our group where plasma sprayed Al-23 wt.% Si alloy composite reinforced with 10 wt.% CNTs displayed strengthening [181]. To understand this contradiction in context with available studies in the literature, mechanical property testing of bulk Al-CNT samples carried out by others researchers is tabulated in Table 4.13.

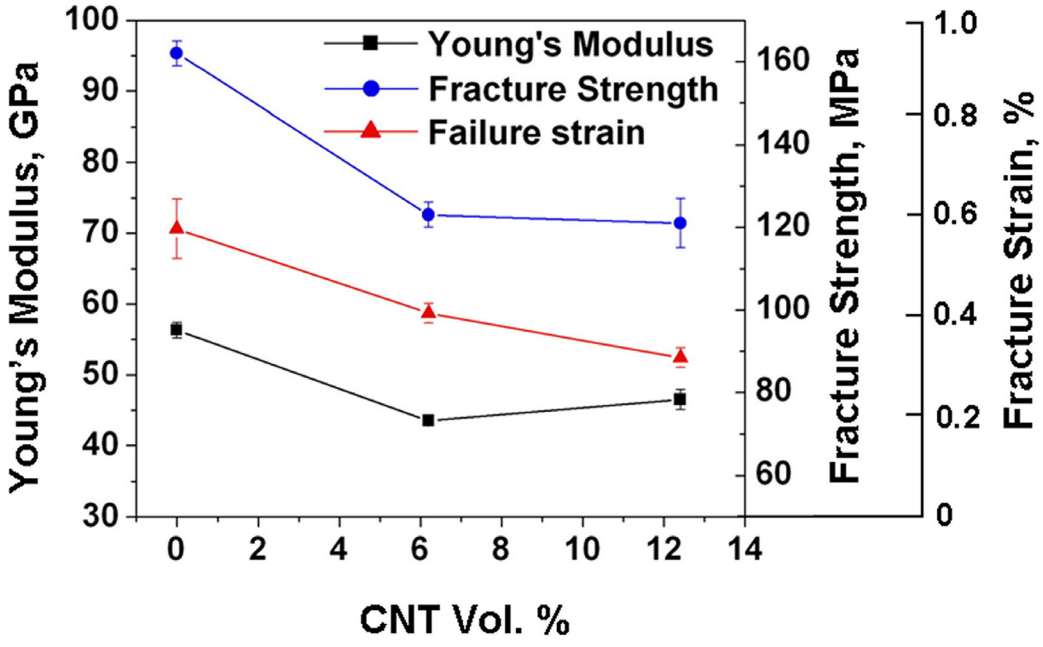

Fig. 4.87: Variation of mechanical properties of bulk plasma-sprayed tensile samples with CNT content

Table 4.13: Bulk mechanical properties of metal matrix CNT composites

Fabrication	**Sample size**	**Microstructure**	**Properties obtained**	**Reference**
Al powders (99.99% pure, 40 μm size) mixed with 5 and 10 vol.% CNT by stirring in ethanol →hot compaction (at 873 K)→ hot extrusion (25:1 ratio at 773 K)	Cylindrical, 3 mm dia. 15mm gauge length,	Clustering observed, no Al_4C_3 formation	*Al:* σ_f = 88 MPa, ε_f = 41%, ρ = 99.6% *Al-5vol.% CNT:* σ_f = 84 MPa, ε_f = 28%, ρ = 94% *Al-10vol.% CNT:* σ_f = 80 MPa, ε_f = 17%, ρ = 96.2%	T. Kuzumaki et al. [29]
Al powders (200 mesh) ball milled with CNT→ compacted and sintered (853K) →hot extrusion (833K)	Bulk sized, but exact dimensions not mentioned	No Al_4C_3 formation, no discussion on clustering	*Al:* E = 70 GPa, σ_y = 80 MPa *Al-0.5vol.% CNT:* E = 78.1 GPa, σ_y = 86 MPa, σ_{UTS} = 134 MPa *Al-2vol.% CNT:* E = 85.85 GPa, σ_y = 99 MPa, σ_{UTS} = 138 MPa	R. George et al. [81]
a) Ni particles (1 wt.%) on Al produced by precipitation calcination→CNT grown by CVD →pressed (600 MPa)→sintered (913 K for 3 hrs)→repressing (2GPa) b) Al-Ni powders and 5 vol.% CNT ball milled→same consolidation as a)	Dog bone shape, 20 mm gauge length, 5.5 mm wide, thickness not mentioned	No Al_4C_3 formation, good Al-CNT bonding, homogeneous dispersion of CNT and Ni particles	*Al:* σ_f = 140 MPa, ρ = 99.6% *Al-5vol.% CNT (a):* σ_f = 398 MPa, ρ = 96.2% *Al-5vol.% CNT (b):* σ_f = 213 MPa, ρ = 95.4%	C. He at al. [21]

1 wt.% CNT (refluxed with HNO_3) ball milled with 2024 Al powders (50 μm size) →cold isostatic pressing (300 MPa) →hot extrusion (733K to 12 mm dia. rods)	Dog bone specimen of 15 mm gauge length, dia. not mentioned	No Al_4C_3 formation, good Al-CNT bonding, homogeneous dispersion of CNT, Al-CNT bonding poor in 2wt.% composite	*Al:* E = 72 GPa, σ_y = 289 MPa, σ_f = 384 MPa, ε_f = 19.8%, ρ = 98.6% *Al-1wt.% CNT:* E = 102.1 GPa, σ_y = 336 MPa, σ_f = 521.7 MPa, ε_f = 18.8%, ρ = 99.1% *Al-2wt.% CNT:* E = 86.5 GPa, σ_f = 351 MPa, ε_f = 3.4%, ρ = 96.4%	C. Deng et al. [82, 84]
500g Al (99.85% pure, 15 μm size), 10g Mg (99.8% pure, 50 μm size) and 20g CNT (dia. 15 nm, length 30 μm) mixed with natural rubber →heat in N_2 at 773K for 2 hr→ Nanoscale dispersed powder →hot extrusion at 673K	Not mentioned, dia. = 4.7 and 3.4 mm for extrusion ratio =10 and 20 respectively	CNT at Al grain boundaries, alignment for extrusion ratio = 20, no Al_4C_3 formation	*Al:* σ_f = 150 MPa, ε_f = 11% *Al-1.6vol.% CNT (extrusion ratio =10):* σ_f = 170 MPa, ε_f = 8% *Al-1.6vol.% CNT (extrusion ratio =20):* σ_f = 230 MPa, ε_f = 6%	J. Yuuki et al. [297]
Al powder (99.7% pure, 75 μm size) –CNT (140 nm dia., 3-4 μm length) mixed in planetary mill (300 rpm) → fill in copper can→cold rolling (50% reduction) →sintering in vacuum (573K for 3 hrs)→sintering in air (823K for 45 min)	Flat tensile specimen, 25mm gauge length, 6mm wide, 0.4 mm thick	CNT uniformly distributed up to 0.5wt.% CNT, cluster-ing in 1 wt.% CNT fracture surface, clustering eliminated for 400 rpm mixing	*Al:* σ_y = 70 MPa, σ_f = 130 MPa, ε_f = 26%, ρ = 98.6% *Al-0.5wt.% CNT:* σ_y = 100 MPa, σ_f = 135 MPa, ε_f = 18%, ρ = 99% *Al-1wt.% CNT:* σ_y = 69 MPa, σ_f = 104 MPa, ε_f = 7%, ρ = 99.2% *Al-1wt.% CNT (400 rpm):* σ_f = 135MPa *Al-2wt.% CNT:* σ_y = 43 MPa, σ_f = 63 MPa, ε_f = 2%, ρ = 97.5%	A. M. K. Esawi et al. [86]

NSD Al-CNT powder→SPS (873K max. temperature for 20 min. at 50 MPa)→hot extrusion (at 673K, extrusion ratio = 20)	3mm dia. samples	CNTs at Al grain boundaries in SPS compact, Al_4C_3 formed, CNT bundles breakdown and alignment on extrusion	*Al:* σ_f = 85 MPa, ε_f = 16.5% *Al-5vol..% CNT:* σ_f = 194 MPa, ε_f = 10.1%	H. Kwon et al. [31]
Al-23wt% Si powder (15-45 μm size) blended with 10wt.% CNT→plasma spray forming	26mm gauge length, 6mm wide, 0.635 mm thick samples, slightly curved	CNT between splats, very thin layer SiC 2-5 nm at interface, good density	*Al-23wt.% Si:* E = 67.5 GPa, σ_f = 79.8 MPa, ε_f = 0.192% *(A-23wt.% Si)l-10wt..% CNT:* E = 120.4 GPa, σ_f = 83.1 MPa, ε_f = 0.088%	T. Laha et al. [33, 35, 181]
Al (99.9% pure, 325 mesh size)-CNT mixture→high energy milling (5hr) →compaction and vacuum sintering (873K for 3hr) →hot extrusion (into 10 mm dia. rods at 773K, extrusion ratio = 16)	Dog bone type, 30mm gauge length	Al_4C_3 formation seen from XRD,	*Al:* σ_y = 105 MPa, σ_f = 160 MPa, ε_f = 19.5% *Al-1wt.% CNT:* σ_y = 150 MPa, σ_f = 192 MPa, *Al-2wt.% CNT:* σ_y = 180 MPa, σ_f = 252 MPa, ε_f = 16%,	R. P-. Busta-mante et al. [298]

Al (99.7% pure, 200 mesh size) mixed with 2 wt.% CNT→ball milled (200 rpm for 3h and 6 h)→cold compaction (475 MPa)→hot extrusion (at 773K, extrusion ratio = 4)→annealing (673K and 773K for 10h)	20 mm gauge length, 4 mm dia.,	No Al_4C_3 from XRD, small crystallite size of annealed Al-2wt.% CNT samples (milled 3h = 93 nm and 6h = 72 nm)	*Al(milled 3hr, annealed 773K):* σ_f = 284.5 MPa, ε_f = 8.6% *Al(milled 6hr, annealed 773K):* σ_f =348.5 MPa, ε_f = 8.4% *Al-2wt.% CNT (milled 3hr, annealed 773K):* σ_f = 345 MPa, ε_f = 5.7% *Al-2wt.% CNT (milled 6hr, annealed 773K):* σ_f = 348 MPa, ε_f = 7.9%	A. M. K. Esawi et al. [296]

Several of the above listed studies found considerable strengthening by addition of CNTs. The contradictory results in the present research work are attributed to several factors: (i) presence of porosity in the coating, (ii) poor inter-splat adhesion, (iii) CNT clustering and (iv) Aluminum carbide (Al_4C_3) formation in significant quantity. The effect of each of these factors is elucidated in detail below.

1) Porosity of the coatings

This is one of the main reasons for reduction in bulk properties. It is observed that most of the studies in Table 4.13 reported significant increase in strength on dense samples produced by extrusion [31, 81, 82, 297, 298] or sintering and repressing [21]. Studies where the density is low have reported poor properties [29]. The density of the plasma-sprayed Al-Si, Al-5CNT and Al-10CNT coatings was found to be 2.44, 2.36 and 2.35 g/cc which correspond to 90%, 88% and 90% of the theoretical density respectively. This is very high porosity as compared to the samples obtained by other methods (density > 96%) shown in Table 4.14. It is also observed that the fracture strain is very small and reduces with addition of CNTs. Plasma sprayed coatings contain macro pores as well as micropores between splats due to splat curvature and insufficient melting and inter-splat bonding. Inter-splat pores act as sharp cracks and weaken the composite considerably. Growth and coalescence of the inter-splat pores with macro pores might cause premature failure of the composite. Figure 4.88 shows the optical micrographs of the Al-5CNT and Al-10CNT coatings. It is observed that the macro porosity is mainly concentrated in the neighborhood of CNT clusters.

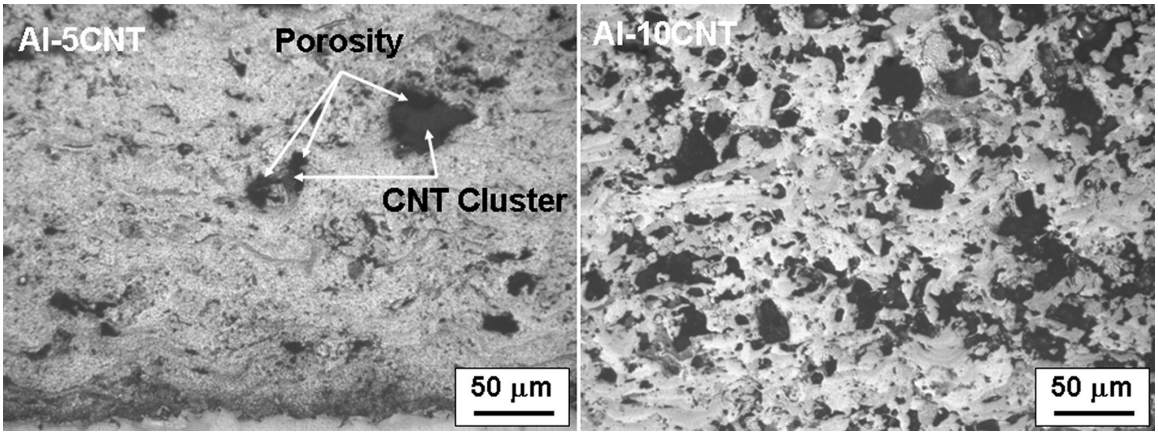

Fig. 4.88: Optical micrographs of plasma sprayed Al-CNT coating cross sections showing CNT clusters and porosity

It is seen that the amount of CNT clusters is more in Al-10CNT. The area fraction of the CNT clusters was calculated for five (5) images and the mean was found to be 10.4% and 18.8% for Al-5CNT and Al-10CNT coating respectively. Fig. 4.89 shows the low magnification SEM images of the fracture surface of the plasma-sprayed composites. It is observed that the porosities on surface act as notches and sites for crack nucleation. Also the coalescence of pores could lead to bulk de-cohesion of the matrix. The porosities reduce the effective area that bears the load under tension. Thus porosity in bulk samples is very much deleterious for the mechanical properties of the composite.

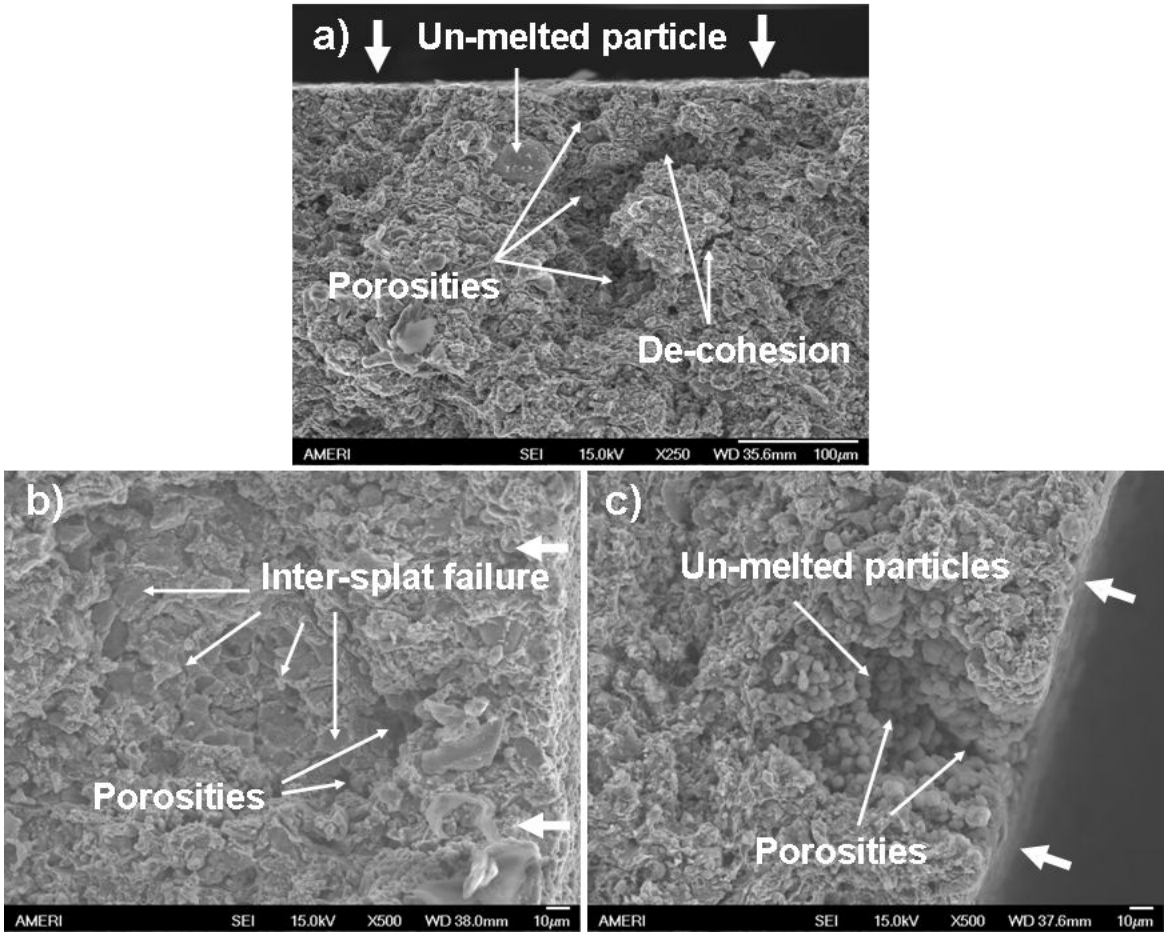

Fig. 4.89: Low magnification SEM images showing various features of the fracture surface of a) Al-Si, b) Al-5CNT and c) Al-10CNT composites. The thick arrows indicate the spray direction and the load was applied perpendicular to the fracture surface

2) Inter-splat Adhesion and Bonding

Fig. 4.89 shows poor inter-splat adhesion and absences of perfectly flat lamella. Un-melted particles seen in the Al-Si and Al-10CNT composite have weak bonding with the matrix and serve as easy paths for pull out and crack propagation. It is seen in Al-10CNT coating (Fig. 4.87c) that the cracking and de-bonding has occurred where fine sized un-melted Al-Si particles are present. In the Al-5CNT coating, fracture occurred in

the inter-splat regions. Tensile samples were fabricated along the length of the cylindrical deposit, and hence the splats are arranged along the longitudinal axis of the tensile specimen. Figure 4.90 shows the schematic of the stress state in the composite and the nanotubes. It is seen that most of the splats are arranged parallel to the axis.

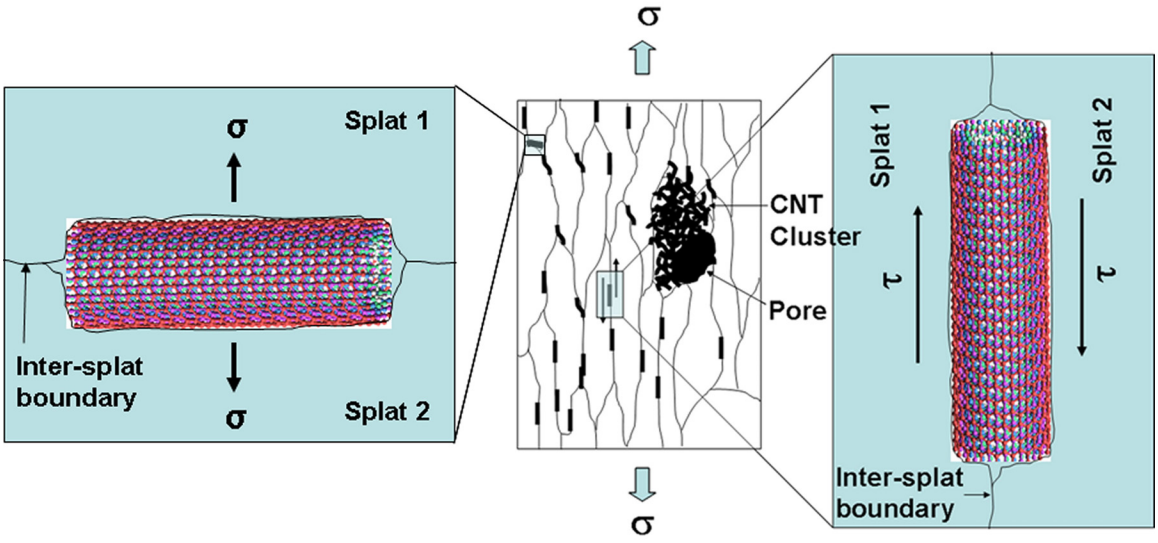

Fig. 4.90: Schematic showing the stresses acting at CNT-splat interfaces under various orientations

The stress is transferred to the CNTs through the interface as shown in the CNT on the right. For effective strengthening, a large interfacial stress (τ) transfer is required which can be brought about if there is some interfacial product layer or mechanical interlocking between the CNT and matrix. However, not all splats in the composite will be arranged parallel to the axis. For CNTs entrapped between splat interfaces which are normal to applied stress the case will be tensile as shown in the CNT on the left. These CNTs act as link between the two splats. Reaction at the interface leading to chemical bonding is

necessary for obtaining a strong bond. Mechanical bonding is possible, but the surface of the CNT must be rough (brought about by oxidation treatment) and the surfaces must be intimately in contact as in case of high density composite. Lack of bonding between CNT and splat will lead to easy inter-splat failure. Figure 4.12 showed the SEM images of fracture surfaces indicating that CNTs are present uniformly on the inter-splat regions. Lack of bonding between CNTs and the splats will translate into poor overall inter-splat bonding. Bonding between CNTs and matrix is brought about by reaction between the prismatic planes or defect sites leading to carbide formation which was discussed in chapter 4.5. Such carbide formation can be helpful in pinning the CNTs to the splats [31]. Figure 4.91 shows the high magnification SEM images fracture surfaces of Al-5CNT and Al-10CNT. Flat fracture surfaces were observed at some places in Al-5CNT and Al-10CNT coatings, which indicate weak regions. Fig. 4.91 shows that some of the flat regions consisted of CNT rich regions and the CNTs are roughly parallel to the fracture surface. Most of the CNTs have a clean surface indicating that they have not reacted. Presence of unreacted CNTs or un-bonded CNTs in the inter-splat region would lead to failure at low strains and stresses.

3) CNT Clustering

Plasma sprayed composites displayed biomodal distribution behavior of CNTs which include (i) dispersed CNTs in the interpslat region and (ii) CNT clusters. CNT clusters are formed due to the interaction of the CNTs with molten Al-Si alloy during plasma spraying.

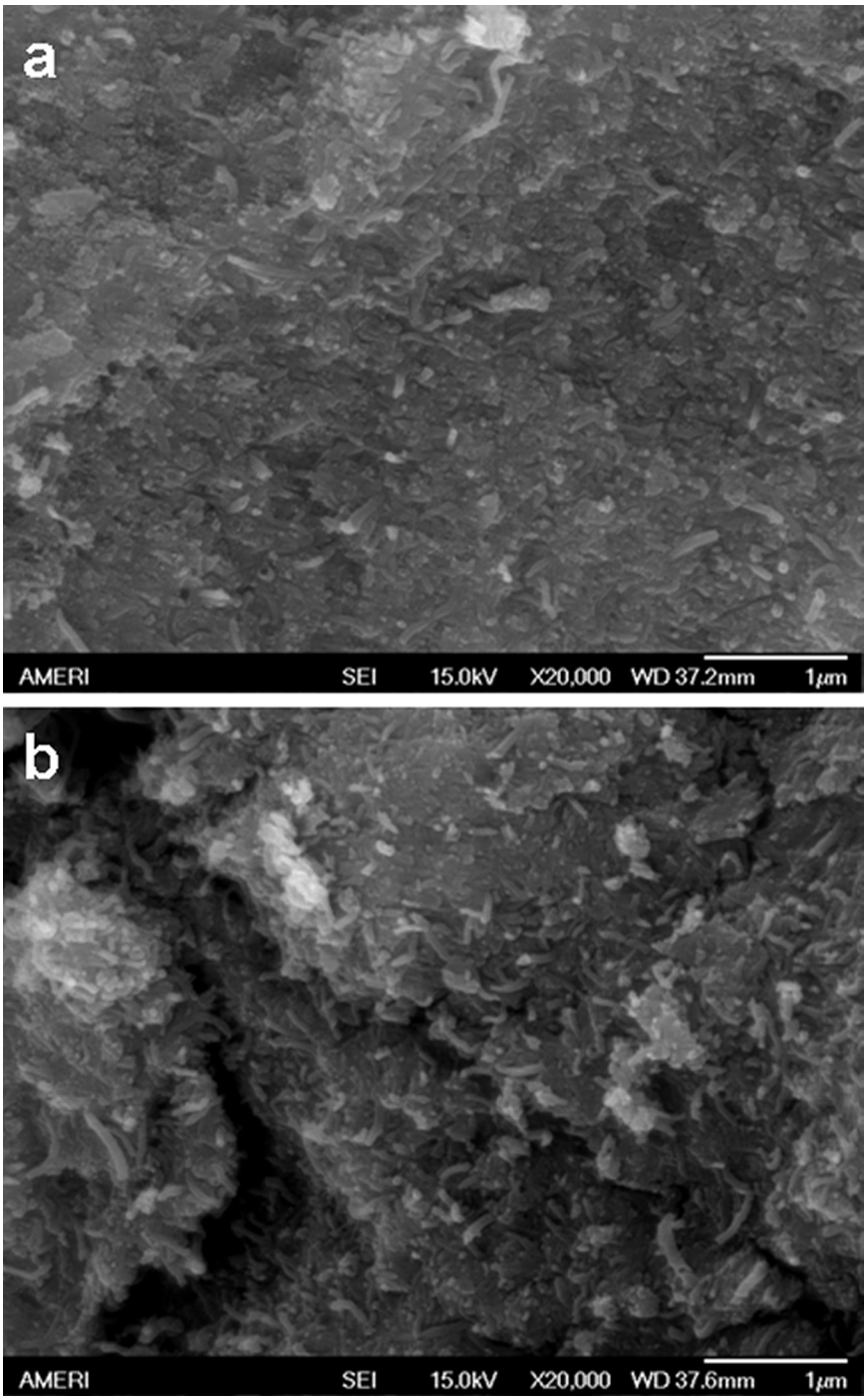

Fig. 4.91: High magnification SEM images of fracture surfaces of a) Al-5CNT and b) Al-10CNT coating showing CNTs parallel to the fracture surface

Porosities are found in the intersplat regions as well as in the CNT clusters. Inter-splat porosities are very fine (1-3 μm) as seen in optical micrographs while ultrafine porosities are not visible in optical micrographs. Region surrounding CNT clusters contain most of the porosity and act a discontinuity. These pores are large in size (5-20 μm) and readily visible in optical micrographs in Fig. 4.86. Clusters and porosities reduce the effective area of cross section and hence the elastic modulus, since they don't contribute to load bearing. Clustering has been previously shown to reduce the density and the strength of Al-CNT composites [29]. Villoria and Miravete have provided a model to take into account clustering of CNTs [221]. The model was briefly mentioned in chapter 2.4.3.2. According to the model, the overall properties of the composite are obtained by considering it as a dilute suspension of the clusters (properties with subscript *dsc*) in matrix.

$$k_{dsc} = k_m + \frac{(k_{Cluster} - k_m)c_c}{1 + \frac{(k_{Cluster} - k_m)}{k_m + 4\mu_m / 3}} \qquad \text{Equation 4.24}$$

$$\mu_{dsc} = \mu_m \left[1 - \frac{15(1-\nu_m)\left(1 - \frac{\mu_{Cluster}}{\mu_m}\right)c_c}{7 - 5\nu_m + 2(4 - 5\nu_m)\frac{\mu_{Cluster}}{\mu_m}} \right] \qquad \text{Equation 4.25}$$

Where c_c refers to the volume fraction of clusters which is related to the overall CNT fraction by $V_f = c_f.c_c$. But this model is suitable for equations where the clusters are infiltrated with the matrix. In the present coatings and composites, it has been shown that

the clusters are not fully infiltrated with metal. They are more or less discontinuities in the matrix and occur in conjunction with the macro pores.

If it is assumed that the CNT clusters do not contribute towards load bearing, then the strength of elastic modulus of the Al-CNT composites can be given by the rule of mixtures as

$$\sigma_C = \sigma_{Al-Si}(1 - V_C) \qquad \text{Equation 4.26}$$

$$E_C = E_{Al-Si}(1 - V_C) \qquad \text{Equation 4.27}$$

Here, $\sigma_{Al\text{-}Si}$ and $E_{Al\text{-}Si}$ are the strength and elastic modulus of the plasma sprayed Al-Si coatings without any CNT clusters and V_C is the CNT cluster volume fraction. The values of $\sigma_{Al\text{-}Si}$ and $E_{Al\text{-}Si}$ are obtained from the tensile test (Table 4.12). $E_{Al\text{-}Si}$ and $\sigma_{Al\text{-}Si}$ is equal to 56.3 GPa and 162 MPa respectively. The volume fraction of the porous CNT cluster region was calculated using image analysis of optical micrographs. The calculated and experimentally obtained values of the mechanical properties of plasma sprayed Al-Si-CNT composites are tabulated in Table 4.14 below.

Table 4.14: Calculated and experimentally measured values of the mechanical properties of plasmas sprayed Al-Si-CNT composites

Sample	**CNT Cluster Fraction, V_C**	**Calculated E, GPa**	**Measured σ_C, GPa**	**Calculated σ_C, MPa**	**Measured σ_C, MPa**
Al-5CNT	0.104	50.4	43.5	145.1	123
Al-10CNT	0.188	45.7	46.5	131.5	121

It is observed that the calculated values of elastic modulus match closely with the measured values. The calculated values of the strength are higher than measured ones. This is due to the fact that intersplat bonding is not taken into account in the calculations. Figure 4.92 shows a SEM image of the fracture surface of Al-10CNT composite showing fracture occurring at a CNT cluster. Such clusters with poor bonding with splats tend to reduce the strength of the composite.

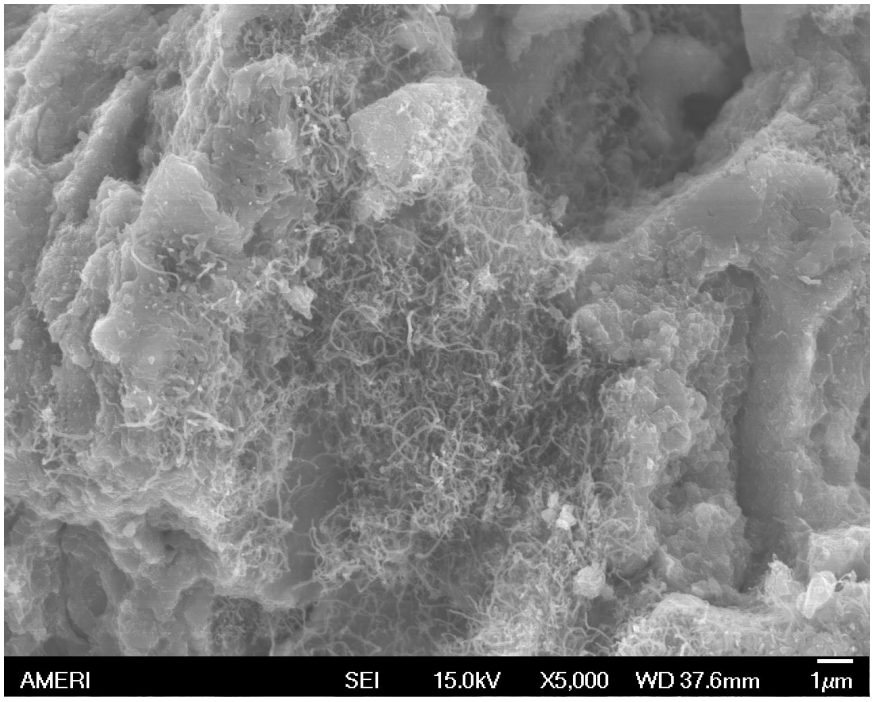

Fig. 4.92: SEM image of fracture surface indicating poor intersplat bonding due to a CNT cluster that has not been metal infiltrated

4) Aluminum Carbide Formation

It is noted that in all the studies mentioned in Table 4.13, significant strengthening was achieved in cases where Al_4C_3 formation was not observed. Al_4C_3 formation is

minimized in solid state processes and the reaction rate between Al and CNTs increases significantly above the melting point of Al [37]. Bustamante [298] and Kwon [31] have observed strengthening in the presence of carbide formation. In those composites, hot extrusion was used which breaks down the CNT clusters and possibly the Al_4C_3 phases formed and distributes them uniformly and aligned to the extrusion direction. This might be alleviating the harmful effects of Al_4C_3 formation. Besides that, a controlled amount (nano layer) of Al_4C_3 formation might help in bonding the CNT with matrix and help in load transfer. This effect has been observed in Al-SiC composites [196].

In the present study, area under the XRD peaks suggested the formation of significantly large amount of Al_4C_3. It was observed that the 7.8% and 15.8% Al_4C_3 by volume was formed in case of Al-5CNT and Al-10CNT coating.

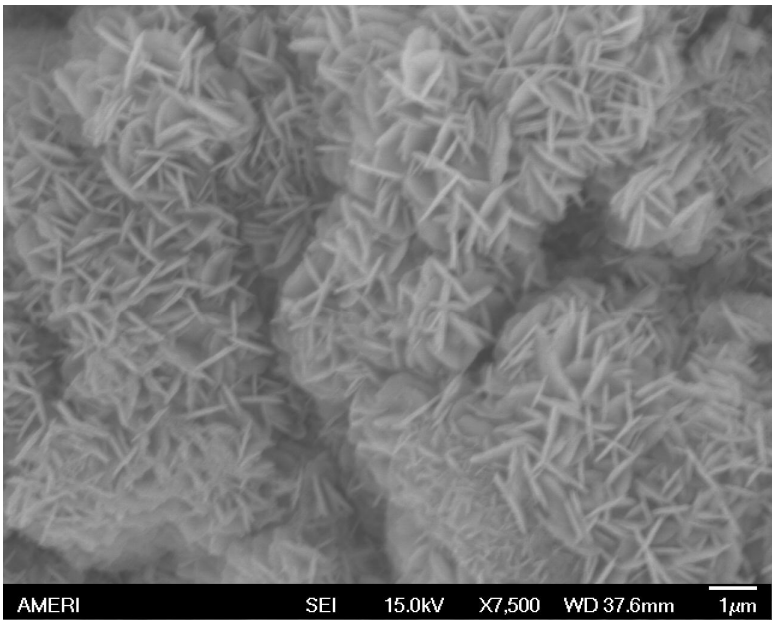

Fig. 4.93: Aluminum carbide needles/platelets forming a flower like morphology on the fracture surface of Al-10CNT composite

Al_4C_3 was also observed on the fracture surface of Al-10CNT coating (Fig. 4.15), in the vicinity of CNTs. Figure 4.93 shows the fracture surface of Al-10CNT tensile specimen showing presence of Al_4C_3. The flower like morphology suggests that it has formed due to reaction of a spray dried particle with the CNTs. Brittle fracture of Al_4C_3 will reduce the strain to failure and will act as sites for crack nucleation.

4.8.2. Compressive Properties

Mechanical properties were tested in compression to study the strengthening effect of CNTs under compressive load. Stresses on CNTs reverse under compression and interfacial bonding between CNT and splats is not as critical since compressive forces lead to crack closure.

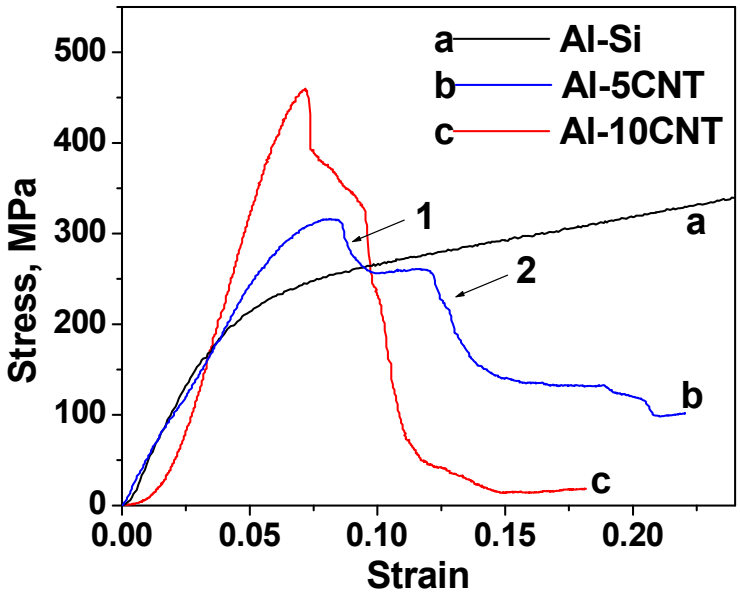

Fig. 4.94: Representative engineering stress-strain curves for plasma sprayed Al-Si-CNT composites under compression

Figure 4.94 shows the representative engineering stress strain curves under compression for plasma sprayed Al-Si-CNT samples and the mechanical properties have been tabulated in Table 4.15. It is observed that the Al-Si sample did not fail under compression. It went on deforming until it was transformed into a flat button and started to crack at the edges due to work hardening. Compressive load was applied parallel to the splats direction. So the loading direction was perpendicular to spraying direction. Initial non-linearity of the stress strain behavior is due to densification occurring due to compaction. Once the pore closure occurs, further deformation occurs by deformation of splats and sliding of the splats past each other. It is observed that there is slight decrease (-6%) in elastic modulus for Al-5CNT composite while the Al-10CNT composite shows 8% increase in compressive elastic modulus compared to Al-Si composite. It can be said that the elastic modulus are more or less the same.

There are two competing effects taking place due to addition of CNTs. There is creation of porosity due to presence of CNT clusters. This has the effect of redcing the stiffness since the closure of pores and compaction of the clusters under the compressive load will lead to large deformations. On the other hand, CNTs between splats in both the cases shown in Fig. 4.12 will serve as obstacles to splat sliding and increase the elastic modulus. It is observed from Fig. 4.12 (b and d) that more CNTs are present within splats in Al-10CNT compared to Al-5CNT. The porosity was measured to be 12% and 10% for Al-5CNT and Al-10CNT coatings respectively.

Table 4.15: Mechanical properties of Al-Si-CNT composites obtained by compression test. The percentage values in the brackets indicate improvement over Al-Si

Sample	**Elastic modulus GPa**	**Average E**	**Yield Strength MPa**	**Average σ_y**	**Fracture Strength MPa**	**Average σ_f**	**Failure Strain %**	**Average ε_f**
Al-Si	5.1	5..25±1.5	196	214±18		-		-
Al-Si	5.4		232					
Al-5CNT	5	4.95±0.05 (-6%)	265	275±10 (28.5%)	294	305±10	11	11.5
Al-5CNT	4.9		284		315		12	
Al-10CNT	6.7	5.65±0.95 (8%)	386	352±34 (64.5%)	386	352±34	10	11
Al-10CNT	4.6		317		317		11	

The values of elastic modulus in compression reflect the effect of porosity. But the volume fraction of porous CNT clusters was found from image analysis to be 10.4% and 18.8%. Based on this it can be said that CNT clusters do no effect the elastic modulus in a significant manner in compression as they do in tension. It is to be noted that the elastic modulus in compression is an order of magnitude lower than that in tension. Compression involves the closure of pores in clusters as well as inter-splat porosity which results in larger displacements/strains for a given amount of stress. Thus the compressive modulus is smaller than the tensile modulus. The deformation behavior of CNT reinforced Al-Si coating is markedly different than Al-Si coating. It is observed that there is a two stage deformation processes. This is marked by 1 and 2 in Fig 4.94. When the sample is deformed, compaction progresses and the porosities are eliminated and CNT clusters get compacted. Splat sliding also occurs till its maximum limit and after that the splats start deforming. Deformation of Al-Si splats is difficult due to their brittle nature and the stress goes on accumulating and when critical limit is reached the composite fails. In some cases, the cracking happens in the maximum shear stress planes oriented at 45^{o} to the normal stress and pieces of the sample chip off along the planes. The load falls drastically as the effective area reduces. This leads to stage 1 of failure. Again the remaining sample starts to get deformed under the load leading to a small plateau in the load displacement curve. Finally, there is total failure of the sample during stage 2 when it crumbles into pieces.

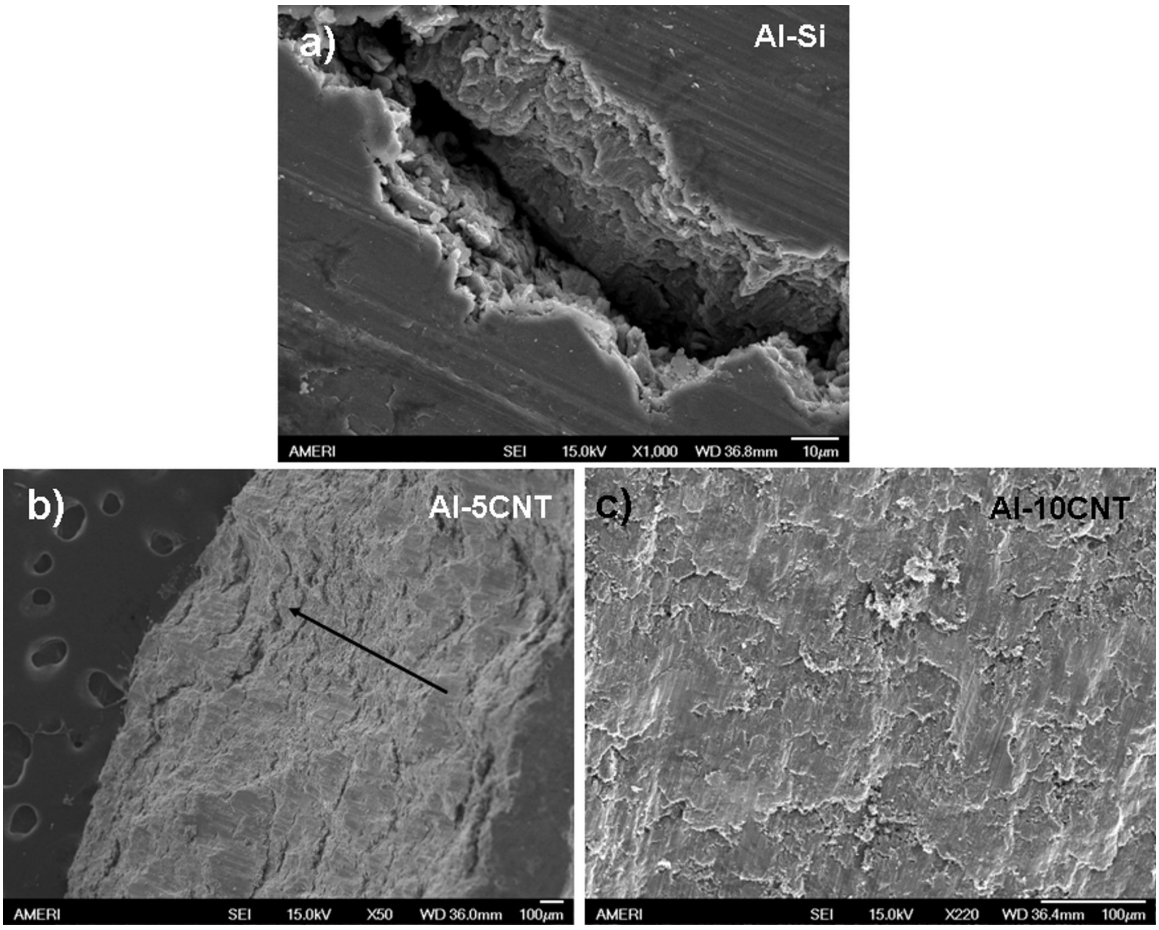

Fig. 4.95: SEM images showing a) edge cracks in Al-Si sample, b) chipping failure at approximately 45^{o} to normal force at maximum load in Al-5CNT composite, and c) fracture surface of chip showing brittle failure in Al-10CNT composite

It is observed that as compared to the Al-Si, the Al-5CNT and Al-10CNT composites have 28.5% and 64.5% increased yield strength in compression which is due to the reinforcement of CNTs. Figure 4.95 shows the fracture surfaces of the plasmas-sprayed composites under compression. Fig. 4.95a shows the edge cracks generated towards the end of deformation in Al-Si sample. Fig. 4.95b shows failure at maximum

load at 45^{o} angle to the applied force in case of Al-5CNT composite. In case of Al-10CNT composite, a chip that has broken under sudden delamination failure is shown in Fig. 4.95c. The crack front is smooth and flat indicating brittle failure. Figure 4.96 shows higher magnification SEM images from fracture surface of Al-5CNT and Al-10CNT composite.

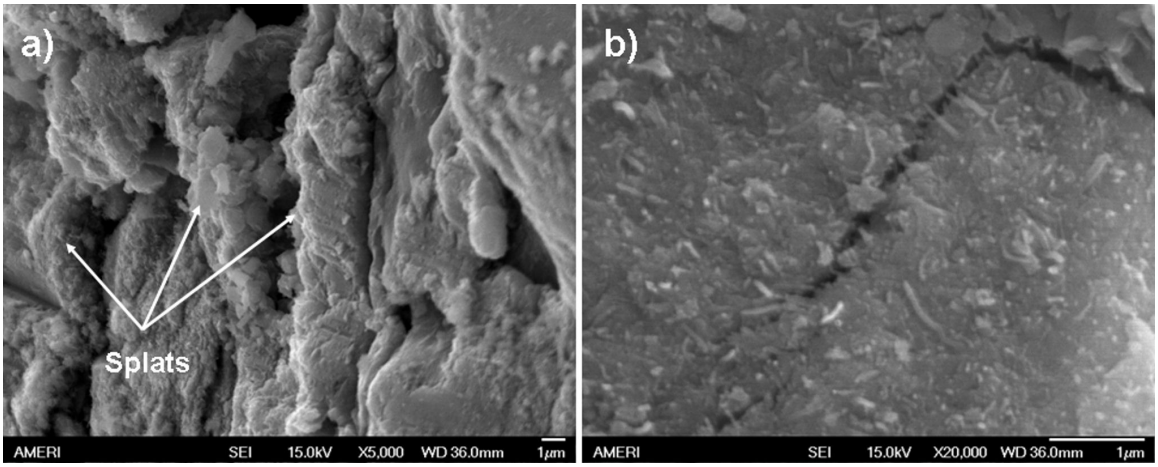

Fig. 4.96: SEM images of fracture surface of a) Al-5CNT showing splat sliding and b) Al-10CNT composite showing crack bridging

Figure 4.96a shows evidence of splat sliding during compression test. Individual splats could be seen which have moved relative to each other and some splat delamination is also observed. Figure 4.96b shows the fracture surface of Al-10CNT composite showing crack closure and bridging by CNTs. This is one of the mechanisms that lead to increased compressive strength of the Al-CNT composite over Al-Si.

4.9. Comparison of Nano and Macro scale Mechanical Properties of Plasma Sprayed Al-Si-CNT Composite

Nanoindentation indicated an ***increase*** in elastic modulus by 19% and 39% in case of plasma sprayed Al-5CNT and Al-10CNT coating over the Al-Si coating. But macro scale bulk tensile testing shows a ***decrease*** in tensile modulus by 23% and 17% for Al-5CNT and Al-10CNT coating respectively. Moreover, the absolute values of elastic modulus obtained by bulk tensile tests were smaller (less than half for CNT containing coatings) as compared to nanoindentation. *It is observed that there is an inversion in mechanical properties with the scale of measurement.* Several factors are responsible for this phenomenon. In nanoindentation, the size of elastic-plastic region beneath the indenter has a diameter of around 5 μm. The depth is limited to a maximum of 300 nm. So the mechanical response is obtained from a few splats. Phenomena like splat sliding and improper bonding do not affect much the results. Also, CNT distribution was found to be uniform in the intersplat region and within the splats. Hence nano-scale strengthening obtained by dispersed CNTs is not nullified by the deleterious effect of CNT clustering and intersplat porosities.

On the other hand, in case of bulk tensile tests, porosity, CNT clustering, inter-splat bonding, CNT splat adhesion, aluminum carbide formation, microstructural anisotropy etc. affect the properties measured. *Nanoscale mechanical properties thus may not reflect the bulk mechanical properties in case of plasma sprayed coatings*. However, several steps can be taken to improve the bulk mechanical properties to match them with the properties at nanoscale. The main idea is to get rid of defects like poor interfaces, porosity, poor bonding etc. Thermo-mechanical treatments are required which not only

will densify the structure but will cause the breakdown of the splat structure. Effective use of CNTs requires there successful integration into the structure with proper bonding for efficient load transfer. Improper bonding may make the same CNTs as defects and cause delamination or serve as sites for nucleation of cracks. Several researchers have obtained properties better than those measured by nanoindentation in this study as shown in Table 4.13. By being able to meet the criteria mentioned above, bulk properties of plasma sprayed composites can also be enhanced.

5. CONCLUSIONS

Several important conclusions could be drawn from the work done in this dissertation. The salient conclusions have been classified in terms of (i) processing, (ii) microstructure (iii) CNT dispersion (iv) mechanical properties (micro scale), (v) mechanical properties (micro scale), and (vi) Mechanical properties (macro scale).

(i) Processing

1. Spray drying is an effective method for dispersing CNTs at the scale of a micrometer size powder. The quality of dispersion obtained is a significant achievement over blending processes.. CNTs tend to form a mesh on the surface of the agglomerate for higher content.
2. Plasma spraying has been successful in fabricating Al-Si, Al-5CNT and Al-10CNT composite coatings and bulk structures with a thickness ranging from 500μm- 5mm. The spraying time for 5 mm thick samples was just 20 minutes indicating the possibility of rapid prototyping of bulk CNT nanocomposites. The Al-Si, Al-5CNT and Al-10CNT composites were 90, 88 and 90% dense.
3. Cold spraying was successfully used in fabricating 500 μm thick Al-CNT coatings from blended mixture of pure Al and spray dried Al-5CNT powders. Two compositions containing overall CNT of 0.5wt.% (Al-0.5CNT) and 1wt.% (Al-1CNT) were prepared. Cold spraying of mixture of Al-Si and spray dried Al-5CNT powders (without pure Al matrix) resulted in coatings of maximum thickness 80 μm due to poor deposition efficiency of Al-Si powders.

(ii) Microstructure

4. Plasma sprayed coatings had a two phase microstructure of a matrix with *uniformly distributed CNTs* and *CNT clusters*. Regions containing clusters contained most of the porosity. CNTs were uniformly distributed in the intersplat region and within splats. CNT clustering occurs due to non wetting nature of Al-Si alloy on nanotube surface. .
5. Cold sprayed coatings had high density (> 98%). The spray dried particles either disintegrated on impact and released the CNTs or were entrapped in between Al splats. Porosity was observed with splats and in entrapped spray dried particles. CNTs were distributed homogeneously in the intersplat region. Some CNTs were entrapped within the Al splats. .
6. Rigorous thermodynamic analysis of the reaction between Al-Si alloys and CNT was carried out using FactSage^{TM}. A pseudo phase diagram was generated which predicts the reaction product that will form for a given silicon content in alloy at a particular processing temperature. It was shown that Al_4C_3 formation is feasible for Al-12 wt.% Si alloy while SiC formation is feasible for Al-23wt.% Si alloy. Also critical thickness calculations at 1700K showed that the critical thickness for Al_4C_3 formation was lower than SiC for Al-12 wt.% Si alloy while the reverse was true for Al-23wt.% Si alloy. XRD and high resolution transmission electron microscopy were used to validate the thermodynamically computed results.
7. Most of the CNTs were retained in plasma sprayed coatings and composites. Some of the CNTs had undergone thermal damage by the exposure to plasma plume. . The extent of CNT damage was more in Al-10CNT coating. The CNT

mesh formed in case of spray dried Al-10CNT powder was more prone to direct interaction with plasma plume.

8. In cold sprayed coatings, length of the CNTs reduced from 1.3±0.6 μm in the SD Al-5CNT powder to 0.8±0.4 and 0.85±0.4 μm in the Al-0.5CNT and Al-1CNT coating. The fracture was due to impact and shear on CNTs between Al-Si particles. Period ripples were formed along CNT length formation due to axial shock waves on impact. Necking kind of failure was also seen for the first time. Shearing of CNTs between deforming particles had a peeling effect leading to generation of graphene sheets. Reaction between CNTs and aluminum was not possible due to the low temperature of the process.

(iii) Carbon Nanotube Dispersion Quantification

9. A new method for the quantification of CNT distribution in a given composite was developed. Two parameters which are complimentary in nature were defined which express the degree of CNT distribution. A Dispersion Parameter (DP) was defined based on the cluster size and was obtained from the image analysis. The larger the value of DP, the better was the distribution. A Clustering Parameter (CP) was defined based on the distances between CNT centers obtained by Delaunay triangulation method. The smaller the value of CP, the better was the distribution. The method was applied to SEM images of the fracture surfaces of cold sprayed Al-CNT and plasma sprayed Al-Si-CNT coatings. The Dispersion parameter was shown to be very effective measure of CNT distribution having better sensitivity that Clustering parameter.

(iv) Mechanical Properties (Micro-scale)

10. The microhardness of plasma sprayed Al-Si, Al-5CNT and Al-10CNT coatings were measured to be 87±3, 135±5 and 210±4 VHN respectively. There is a considerable increase in the microhardness which could be due to indentation resistance produced by CNTs and aluminum carbide formation. Microhardness of cold sprayed Al, Al-0.5CNT and Al-1CNT coatings were 56.1±2.6, 58.7±3.2 and 60.9±2.8 VHN respectively showing that there is only small increase in the hardness. The hardness was considerably higher than that of Al powder (31.5 VHN) due to the severe work hardening during cold spraying.

(v) Mechanical Properties (Nano-scale)

11. Nanoindentation measurements on the matrix portion of the polished cross section indicated that the elastic modulus increased from 90 ± 9.5 GPa for the Al-Si to 107 ± 6 GPa for Al-5CNT and 125 ± 7 GPa for Al-10CNT coating. This corresponds to an increase of 19% and 39% by addition of 5 wt.% and 10 wt.% respectively. Elastic recovery values were calculated from the maximum depth and residual depth of the indentation. There was increase in elastic recovery values by 35% and 94% for Al-5CNT and Al-10CNT coating as compared to Al-Si indicating that there was tremendous improvement in elastic recovery properties due to addition of CNTs. The nanohardness of Al-Si, Al-5CNT and Al-10CNT coatings were found to be 1.61 ± 0.20, 2.33 ± 0.2 and 2.89 ± 0.27 GPa respectively which corresponds to increase of 45% and 80% by addition of 5 and 10wt.% CNT respectively.

12. Elastic modulus measurement of cold sprayed Al-CNT coating indicates a lot of scatter in data with mean value around 69 GPa which is that for pure aluminum. This was explained based on localized nature of the test resulting in values corresponding to areas of different amount of porosity, Si content and CNT content.
13. Nanoscratch experiments were carried out using Berkovich tip. SPM images of the scratch indicated decrease in scratch width and depth with increase in CNT content. Calculations of contact and true wear volumes indicated that the wear resistance of the coatings improves by 4 times for Al-10CNT coating. The reduction in wear volume is ascribed to increase in the hardness and elastic recovery of the coatings due to addition of CNTs. Increase in elastic recovery during scratching in CNT rich regions was shown by correlating the SEM images of the scratch to the true and instantaneous depth as measured by the nanoindenter. Recovery was found to be larger for Al-10CNT coating compared to Al-5CNT coating. The coefficient of friction values were found to be similar for all the three coatings. Correlation with SEM images showed that the friction was slightly lower at regions where CNTs ere concentrated like inter-splat regions.
14. Nanoscratch measurements on cold sprayed coatings indicated up to 40% increase in wear resistance in the Al-1CNT coatings. The contact volumes were more or less similar but the increased recovery property due to CNT addition decreased the true volumes of the scratches for Al-0.5CNT and Al-1CNT coating compared

to Al coating. The coefficient of friction was found to be similar for all the three coatings.

(vi) Mechanical Properties (Macro-scale)

15. Bulk tensile testing on large samples machined from plasma spray formed cylinders showed that the macroscopic mechanical properties of the coatings were poor. The Young's modulus of Al-Si, Al-5CNT and Al-10CNT coatings were found to be 56.3±1.1, 43.5±0.3 and 46.5±1.4 GPa respectively. The decrease in tensile modulus was due to CNT clustering and associated porosity. The volume fraction of the CNT clusters in Al-5CNT and Al-10CNT was found to be 10.4 and 18.8% respectively. The fracture strength reduced from 162±3 MPa for Al-Si to 121±6 for Al-10CNT.. The strain to failure reduced from 0.58±0.06% for Al-Si to 0.32±0.02% for Al-10CNT. r. The decrease in the tensile strength is attributed to porosity,, poor inter-splat adhesion,, CNT clustering and Al_4C_3 formation. Tensile samples consistently failed outside the gauge length indicating that they might be notch sensitive.
16. Compression tests indicated that the yield strength in compression increased from 214±18 MPa for Al-Si to 374±43 MPa for Al-10CNT. The strengthening is due to presence of CNTs in the inter-splat region which obstructs the plastic flow of the material. The elastic modulus was found to be an order of magnitude smaller than in tensile test. The elastic modulus of Al-Si, Al-5CNT and Al-10CNT under compression was equal to 5.25±1.5, 4.95±0.05 and 6.8±2.3 GPa respectively. The

lower values of the elastic modulus were ascribed to collapse of CNT clusters and splat sliding.

Above listed specific conclusions suggest that mechanical properties of CNT reinforced composites can be further enhanced at macro-scale by making improvement and modifications in the processing method to obtain (i) high density (ii) improved CNT dispersion and (iii) improved CNT/matrix interface bonding. Hence, recommendations for the future improvement have been made to further develop the field of CNT reinforced metal matrix composites.

6. RECOMMENDATIONS FOR FUTURE WORK

Several important conclusions were drawn from the research in the previous chapter. The open ended nature of the research suggests that further improvement in macro-scale mechanical properties of metal matrix-CNT composites could be achieved by improving the density, CNT dispersion and CNT/matrix interface bonding. Implementing the knowledge gained through this research work for future studies has been outlined below.

6.1. Optimization of Plasma Spray Parameters

Density of the coatings obtained in this study was low (~88-90%). Although optical microscopy and SEM images indicate that that there was no macro porosity, there could be very fine inter-splat porosity in case of Al-Si coating. These kinds of pores could also be present in Al-Si-CNT coatings. In order to get rid of such pores, plasma processing has to be optimized. A detailed parametric study should be carried out to see if the density of the coatings can be maximized. Based on our recent experiments, it has been found that the plasma power, primary gas flow rate, powder feed rate and the stand-off distance are the most significant parameters that effect the density of the coating. These parameters need to be optimized. This will need lot of experimentation with simultaneous measurement of density and study of microstructure. Table 6.1 summarized the parameters to be played with. If 3 values of plasma power, 3 values of primary gas flow rate, 3 values of powder feed rate and 2 values of stand-off distance are considered the total number of experiments turns out to be 54 experiments.

Table 6.1: Matrix showing plasma spray parameters for optimization experiments

Parameter	Plasma Power	Primary Gas Flow Rate	Powder Feed Rate	Stand-off Distance
Plasma Power	*Variable*	Constant	Constant	Constant
Primary Gas Flow Rate	Constant	*Variable*	Constant	Constant
Powder Feed Rate	Constant	Constant	*Variable*	Constant
Stand-off Distance	Constant	Constant	Constant	*Variable*

Optimization of plasma parameters might lead to improvement in density and mechanical properties.

6.2. Dense Powder Feedstock with Excellent CNT Dispersion

Spray dried powder feedstock had excellent CNT dispersion but suffered with 30-40%porosity. Some of these agglomerates explode during plasma spraying resulting in incomplete melting of Al-Si particles, which cause porosity, poor intersplat adhesion and easy path for crack propagation. A dense powder feedstock with excellent CNT dispersion could result in plasma sprayed coating with similar features.

High density powder with excellent CNT dispersion could be achieved by plasma densification. In plasma densification, the powders are sprayed in a confined column and collected in a container. The particles undergo melting and solidification to form dense powders. Plasma densification could have many advantageous effects. Firstly, use of densified powders could result in dense coatings. Secondly, the reaction between CNTs

and matrix could lead to formation of small amount of Al_4C_3 which will help in pinning the CNTs to the molten metal. This will help in avoiding CNT clustering during subsequent plasma spraying. Plasma densification was tried at our laboratory by air plasma spraying, but it resulted in oxidation of the powders. To avoid oxidation, vacuum plasma spraying needs to be utilized.

An alternate method to produce high density powder feedstock with improved CNT dispersion could be achieved by direct chemical vapor deposition (CVD) growth of CNTs on dense, micron size aluminum powder. Though slow kinetics of CVD process and scale-up limitations could be an impediment to produce large amount of powder feedstock for plasma spraying.

6.3. CNT Pre-treatment

Treatment of CNTs by coating them with metal prior to spray drying could be helpful in many ways. Firstly it may enhance wetting with the molten matrix and hence avoid clustering. Secondly, it will reduce the extent of Al_4C_3 formation which is could bring about drastic improvement in the mechanical properties. Silicon and Nickel coating can be employed. Both the coatings on the CNTs could be applied by chemical vapor deposition. Nickel coatings on CNTs can also be obtained by electro- and electroless deposition techniques. Silicon coatings could result in silicon carbide formation at matrix CNT interface which might enhance the mechanical properties of the composite.

6.4. Manipulating Matrix Composition

The matrix has a strong effect on the interfacial reaction as was shown by thermodynamic calculations. The addition of strong carbide formers like titanium to the Al-Si alloy could retard Al_4C_3 formation. Ti can be added in many ways. CVD routes could be explored for deposition of thin coatings of Ti on Al-Si particles. Alternatively, Ti can be incorporated in the alloy powders during inert gas atomization. Blending of fine Ti powders with Al-Si powders before spray drying could be done. This might lead to preferential reaction of Ti with CNTs leading to formation of TiC, which is not detrimental like Al_4C_3.

6.5. Post –Spray Densification of Plasma-Sprayed Composites

Densification of plasma-sprayed coatings and bulk structures can be done by application of pressure and temperature. Application of pressure is expected to collapse the CNT clusters and align them. Hot-isostatic pressing (HIP) can be used. It has the advantage of application of uniform force which helps in densification through out the composite with complex shapes. The pressure and temperature have to be optimized in order to get good density. Sintering could be used for densification. Sintering would lead to breakdown of splat microstructure which will improve the properties and reduce the anisotropic nature. Sintering might also lead to improvement in bonding between CNT and matrix and lead to strengthening. Another way of consolidation is by hot rolling. Hot rolling could help in densification as well as alignment of the CNT clusters in the rolling direction.

6.6. Exploration of Other Consolidation Processes

Spray dried powders were shown to have very good CNT distribution. In plasma spraying, the CNTs get clustered in the molten droplet and the distribution is lost to a great extent, especially at higher CNT content. The use of other consolidation processes could be explored for spray dried powders. Spark plasma sintering is a rapid sintering technique which can lead to retention of the CNT distribution and can minimize the formation of Al_4C_3. Other methods like hot extrusion of compact can lead to dense structures with minimum formation of Al_4C_3.

6.7. Macro-scale Wear Resistance of Al-Si-CNT coatings

Nanoscratch results showed significant improvement in nano-scale wear resistance of the plasma-sprayed Al-CNT coatings at a nanoscale. It is yet to be established if this nanoscale property improvement translates into macro tribological properties. The effect of splat adhesion and CNT inter-splat bonding on wear resistance has to be studied. Correlation between nano scale and micro scale wear properties should be established similar to mechanical properties.

6.8. Efficacy of CNT Dispersion Quantification Model

A new method for CNT distribution quantification was developed which can be applied to all kinds of CNT composites and to SEM and TEM micrographs. The parameters suggested should be utilized to compare processes or variation of distribution within various samples in a given process. It will establish the efficacy of the CNT dispersion quantification model in the present work.

LIST OF REFERENCES

1. Rohatgi P. *J. Metals* 1991; 43(4): 10-15

2. Kelly A. *J. Mater. Sci.* 2006; 41: 905-912

3. Rawal S. *J. Metals* 2001; April: 14-17

4. Shelly JS, LeClaire R, Nichols J. *J. Metals* 2001; 53(4): 18-21

5. http://scaled.com/projects/ttop/press_release.pdf

6. IIjima S. *Nature* 1991; 354: 56-58

7. Bacon R. *J. Appl. Phys.* 1960; 31(2): 283-290

8. Treacy MMJ, Ebbesen TW, Gibson JM. *Nature* 1996; 381: 678-680

9. Wong EW, Sheehan PE, Lieber CM. *Science* 1997; **277**: 1971-1974

10. Yu MF, Lourie O, Dyer MJ, Moloni K, Kelly TF, Ruoff RS. *Science* 2000; 287: 637-640

11. Yu MF, Files BS, Arepalli S, Ruoff RS. *Phys. Rev. Lett.* 2000; 84(24): 5552-5555

12. Krishnan A, Dujardin E, Ebbesen TW, Yianilos PN, Treacy MMJ. *Phys. Rev. B* 1998; 58(20): 14013-14019

13. Berber S, Kwon YK, Tomanek D. *Phys. Rev. Lett.* 2000; 84: 4613-4616

14. Kim P, Shi L, Majumdar A, McEuen PL. *Phys. Rev. Lett.* 2001; 87(21): 215502

15. Feng Y, Yuan HL, Zhang M. *Mater. Char.* 2005; 55: 211-218
16. Tang Y, Cong H, Zhong R, Cheng HM. *Carbon* 2004; 42: 3260-3262

17. Chen WX, Tu JP, Wang LY, Gan HY, Xu ZD, Zhang XB. *Carbon* 2003; 41: 215–222

18. Shi XL, Yang H, Shao GQ, Duan XL, Yan L, Xiong Z, Sun P. *Mater. Sci. Eng. A* 2006; 457: 18–23

19. Cha SI, Kim KT, Arshad SN, Mo CB, Hong SH. *Adv. Mater.* 2005; 17: 1377-1381

20. Noguchi T, Magario A, Fukazawa S, Shimizu S, Beppu J, Seki M. *Mater. Trans.* 2004; 45(2): 602-604

21. He C, Zhao N, Shi C, Du X, Li J, Li H, Cui Q. *Adv. Mater* 2007; 19: 1128-1132

22. Esawi A, Morsi K. *Composites A* 2007; 38: 646–650

23. Bian Z, Wang RJ, Wang WH, Zhang T, Inoue A. *Adv. Funct. Mater.* 2004; 14(1): 55-63

24. Goh CS, Weia J, Lee LC, Gupta M. *Mater. Sci. Eng. A* 2006; 423: 153-156

25. Li Q, Viereckl A, Rottmeir CA, Singer RF. *Comp. Sci. Tech.* 2009; 10.1016/j.compscitech.2009.02.020

26. Xu CL, Wei BQ, Ma RZ, Liang J, Ma XK, Wu DH. *Carbon* 1999; 37: 855 - 858

27. Hsu CF, Lin HM, Lee PY. *Adv. Eng. Mater.* 2008; 10(11): 1053-1055

28. Kuzumaki T, Ujiie O, Ichinose H, Ito K. *Adv. Eng. Mater.* 2000; 2(7): 1438-1656

29. Kuzumaki T, Miyazawa K, Ichinose H, Ito K. *J. Mater. Res.* 1998; 13(9): 2445-2449

30. Choi HJ, Kwon GB, Lee GY, Bae DH. *Scripta Mater.* 2008; 59: 360-363

31. Kwon H, Estili M, Takagi K, Miyazaki T, Kawasaki A. *Carbon* 2008; doi:10.1016/j.carbon.2008.10.041

32. Laha T, Liu Y, Agarwal A. *J. Nanosci. Nanotech.* 2007; 7(2): 515-524

33. Laha T, Kuchibhatla S, Seal S, Li W, Agarwal A. *Acta Mater.* 2007, 55: 1059-1066

34. Bakshi SR, Singh V, Seal S, Agarwal A. *Surf. Coat. Tech.* 2009; 203: 1544-1554

35. Laha T, Agarwal A, McKechnie T, Seal S. *Mater. Sci. Eng A.* 2004; 381: 249–258

36. Deng CF, Zhang XX, Wang DZ, Ma YX. *Materials Lett.* 2007; 61: 3221–3223

37. Ci L, Ryu Z, Jin-Phillipp NY, Ruhle M. *Acta Mater.* 2006; 54: 5367–5375

38. Laha T, Agarwal A, McKechnie T. *Surf. Eng. Mater. Sci.-III* 2005: 1-10

39. Quang P, Jeong YG, Hong SH, Kim HS. *Key Eng. Mater.* 2006; 326-328: 325-328

40. Quang P, Jeong YG, Yoon SC, Hong SI, Hong SH, Kim HS. *Mater. Sci. Forum* 2007; 534-536: 245-248

41. Quang P, Jeong YJ, Yoon SC, Hong SH, Kim HS. *J. Mater. Proc. Tech.* 2007; 187-188: 318–320

42. Viswanathan V, Laha T, Balani K, Agarwal A, Seal S. *Mater. Sci. Eng. R* 2006; 54: 121-285

43. Glieter H. Acta Mater. 2000; 48: 1-29

44. Mayers MA, Mishra A, Benson DJ. *Prog. Mater. Sci.* 2006; 51: 427-556

45. Taha MA. *Mater. Des.* 2001; 22: 431-441

46. *ASM Specialty Handbook: Aluminum and Aluminum Alloys.* Ed. Davis JR 1993; ASM International

47. Surappa MK. *Sadhana* 2003; 28: 319-334

48. Morgan P. *Carbon Fibers and Their Composites* 2005; Ch. 16: 629-649

49. Oberlin A, Endo M, Koyama T. *J. Crys. Growth* 1976; 32: 335-349

50 Baugman RH, Zakhidov AA, de Heer WA. *Science* 2002; 297: 787-792

51. Lau KT, Hui D. *Composites B* 2002; 33: 263-277

52. Curtin WA, Sheldon BW. *Mater. Today* 2004; November: 44-49

53. Coleman JN, Khan U, Blau WJ, Gun'ko YK. *Carbon* 2006; 44: 1624–1652

54. Lourie O, Wagner HD. *J. Mater. Res.* 1998; 13(9): 2418-2422

55. Poncharal P, Wang ZL, Ugarte D, de Heer WA. *Science* 1999; 283: 1513-1516

56. Salvetat JP, Kulik AJ, Bonard JM, Briggs GAD, Stockli T, Metenier K, Bonnamy S, Beguin F, Burnham NA, Forro L. *Adv. Mater.* 1999; 11(2): 161-165

57. Salvetat JP, Briggs GAD, Bonard JM, Bacsa RR, Kulik AJ. *Phys. Rev. Lett.* 1999; 82(5): 944-947

58. Tu JP, Yang YZ, Wang LY, Ma XC, Zhang XB. *Trib. Lett.* 2001; 10(4): 225-228

59. Yang J, Schaller R. *Mater. Sci. Eng. A* 2004; 370: 512-515

60. Feng Y, Yuan HL, Zhang M. *Mater. Char.* 2005; 55: 211 – 218

61. Eom JY, Park JW, Kwon HS, Rajendran S. *J. Electrochem. Soc.* 2006; 153(9): 1678-1684

62. Huang ZG, Guo ZP, Calk A, Wexler D, Liu HK. *J. Alloys Comp.* 2007; 427: 94-100

63. Chen D, Chen L, Liu S, Ma CX, Chen DM, Wang LB. *J. Alloys Comp.* 2004; 372: 231-237

64. Morsi K, Esawi A. *J. Mater. Sci.* 2007; 42: 4954–4959

65. Hulbert DM, Anders A, Andersson J, Lavernia EJ, Mukherjee AK. *Scripta Mater.* 2009; 60(10): 835-838

66. Kim KT, Lee KH, Cha SI, Mo CB, Hong SH. *Mat. Res. Soc. Symp. Proc.* 2004; 821: 3.25.1-3.25.6

67. Kim KT, Cha SI, Hong SH, Hong SH. *Mater. Sci. Eng.* A 2006; 430: 27-33

68. Kim KT, Cha SI, Hong SH. *Mater. Sci. Eng. A* 2007; 449-451: 46-50

69. Majkic G, Chen YC. *Proc. 47th AIAA Conf.* 2006-2007: 1-5.

70. Pang L, Sun KN, Rena S, Sun C, Fan RH, Lu ZH. *Mater. Sci. Eng. A* 2007; 447: 146-149

71. Kim KT, Cha SI, Hong SH. Hong SH. *Mater. Sci. Eng. A* 2006; 430: 27-33

72. Zhong R, Cong H, Hou P. *Carbon* 2003; 41: 848-851

73. Carreño-Morelli E, Yang J, Couteau E, Hernadi K, Seo JW, Bonjour C, Forró L, Schaller R. *Phys. Stat. Solidi* 2004; 201(8): R53– R55

74. Pang LX, Sun KN, Ren S, Sun C, Bi JQ. *J. Comp. Mater.* 2007; 41(16): 2025-2057

75. Hsu CF, Lee PY. *Mater. Sci. Forum* 2007; 534-536: 865-868

76. Hsu CF, Lin HM, Lee PY. *Adv. Eng. Mater.* 2008; 10(11): 1053-1055

77. Shurong D, Xiaobin Z. *Trans. Nonferrous Met. Soc. China* 1999; 19(3): 1-6

78. Quang P, Jeong YG, Hong SH, Kim HS. *Key Eng. Mater.* 2006; 326-328: 325-328

79. Quang P, Jeong YG, Yoon SC, Hong SI, Hong SH, Kim HS. *Mater. Sci. Forum* 2007; 534-536: 245-248

80. Dong SR, Tu JP, Zhang XB. *Mater. Sci. Eng. A* 2001; 313: 83-87

81. George R, Kashyap KT, Rahul R, Yamadagni S. Scripta Mater. 2005; 53: 1159 - 1163

82. Deng CF, Wang DZ, Zhang XX, Li AB. *Mater. Sci. Eng. A* 2007; 444: 138–145

83. Deng CF, Zhang X, Ma Y, Wang D. *Rare Metals* 2007; 26(5): 450-455

84. Deng CF, Zhang XX, Wang D, Lin Q, Li A. *Mater. Lett.* 2007; 61: 1725–1728

85. Deng CF, Ma YX, Zhang P, Zhang XX, Wang DZ. *Mater. Lett.* 2008; 62: 2301–2303

86. Esawi AMK, Morady MAE. *Comp. Sci. Tech.* 2008; 68: 486-492

87. Bian Z, Xu H, Li MK, Zhang Y, Wang WH. *Appl. Phys. Lett.* 2002; 81(25): 4739-4741

88. Sinian L, Souzhi S, Tianqin Y, Huimin C, Youshou Z, Hong C. *Mater. Sci. Forum* 2005; 488-489: 839-896

89. Goh CS, Wei J, Lee LC, Gupta M. Comp. Sci. Tech. 2008; 68: 1432–1439

90. Goh CS, Wei J, Lee LC, Gupta M. *Nanotechnology* 2006; 17: 7-12

91. Zhou SM, Zhang X, Ding ZP, Min CY, Xu GL, Zhu WM. *Composites A* 2007; 38: 301-306

92. Uozumi H, Kobayashi K, Nakanishi K, Matsunaga T, Shinozaki K, Sakamoto H, Tsukada T, Masuda C, Yoshida C. *Mater. Sci. Eng. A* 2008; 495: 282-287

93. Li YB, Ya Q, Wei BQ, Liang J, Wu DH. *J. Mater. Sci. Lett.* 1998; 17(7): 607-609

94. Hwang JY, Neira A, Scharf TW, Tiley J, Banerjee R. *Scripta Mater.* 2008; 59: 487-490

95. Arai S, Fujimori A, Murai M, Endo M. *Mater. Lett.* 2008; 62: 3545–3548

96. Tan J, Yu T, Xu B, Yao Q. *Trib. Lett.* 2006; 21(2): 107-111

97. Xu Q, Zhang L, Zhu J. *J. Phys. Chem. B* 2003; 107: 8294-8296

98. Chen XH, Peng JC, Li XQ, Deng FM, Wang JX, Li WZ. *J. Mater. Sci. Lett.* 2001; 20: 2057-2060

99. Chen XH, Cheng FQ, Li SL, Zhou LP, Li DY. *Surf. Coat. Tech.* 2002; 155: 274-278

100. Chen XH, Chen CS, Xiao HN, Cheng FQ, Zhang G, Yi GJ. *Surf. Coat. Tech.* 2005; 191: 351-356

101. Arai S, Endo M, Kaneko N. Carbon 2004; 42: 641–644

102. Shi YL, Yang Z, Li MK, Xu H, Li HL. *Mater. Chem. Phys.* 2004; 87: 154–161

103. Tu JP, Zhu LP, Chen WX, Zhao XB, Liu F, Zhang XB. *Trans. Nonferrous Met. Soc. China* 2004; 14(5): 880-884

104. Gang AB, Xang L, Li H. *Trans. Nonferous Met. Soc. China* 2005; 15(5): 1045-1048

105. Arai S, Endo M, Sato T, Atsushi K. Electrochem. Solid-State Lett. 2006; 9(8): 131-133

106. Shi L, Sun CF, Gao P, Zhou F, Liu WM. *Surf. Coat. Tech.* 2006; 200: 4870-4875

107. Arai S, Saito T, Endo M. *J. Electrochem. Soc.* 2007; 154(1): D530-D533

108. Sun Y, Sun J, Liu M, Chen Q. *Nanotechnology* 2007; 18: 505-704

109. Guo C, Zuo Y, Zhao X, Zhao J, Xiong J. *Surf. Coat. Tech.* 2007; 201: 9491–9496

110. Yang YL, Wang YD, Ren Y, He CS, Deng JN, Nan J, Chen JG, Zuo L. *Materials Lett.* 2008; 62: 47-50

111. Guo C, Zuo Y, Zhao X, Zhao J, Xiong J. *Surf. Coat. Tech.* 2008; 202: 3246–3250

112. Dai PQ, Xu WC, Huang QC. *Mater. Sci. Eng. A* 2008; 483-484: 172-174

113. Kang X, Mai Z, Zou X, Cai P, Mo J. *Analytical Biochem.* 2007; 363: 143-150

114. Chai Y, Zhang K, Zhang M, Chan PCH, Yuen MMF. Elec. Comp. Tech. Conf. 2007: 1224-1229

115. Ferrer-Anglada N, Gomis V, El-Hachemi Z, Weglikovska UD, Kaempgen M, Roth S. *Phys. Stat. Sol.* 2006; 203(6): 1082-1087

116. Ngo Q, Cruden BA, Cassell AM, Walker MD, Ye Q, Koehne JE, Meyyappan M, Li J, Yang CY. *Mat. Res. Soc. Symp. Proc.* 2004; 812: 3.18.1-3.18.6

117. Arai S, Endo M, Kaneko N. *Carbon* 2004; 42: 641–644

118. Zhao G, Deng F. *Key Eng. Mater.* 2005; 280-283: 1445-1448

119. Chen XH, Li WH, Chen CS, Xu LS, Yang Z, Hu J. *Trans. Nenferrous Met. Soc. China* 2005; 15(2): 314-318

120. Wang LY, Tu JP, Chen WX, Wang YC, Liu XK, Olk C, Cheng DH, Zhang XB. *Wear* 2003; 254: 1289–1293

121. Ru-jun X, Yu-cheng W. *J. China Univ. Mining Tech.* 2007; 17(3): 424-427

122. Chen X, Zhang G, Chen C, Zhou L, Li S, Li X. *Adv. Eng. Mater.* 2003; 5(7): 514-518

123. Chen X, Xia J, Peng J, Li W, Xie S. *Comp. Sci. Tech.* 2000; 60(2): 301-306

124. Chen WX, Tu JP, Xu ZD, Chen WL, Zhang XB, Cheng DH. *Materials Lett.* 2003; 57: 1256–1260

125. Yang Z, Xu H, Li MK, Shi YL, Huang Y, Li HL. *Thin Solid Films* 2004; 466: 86-91

126. Yang Z, Xu H, Shi YL, Li MK, Huang Y, Li HL. *Mater. Res. Bull.* 2005; 40: 1001–1009

127. Li ZH, Wang XQ, Wang M, Wang FF, Ge HL. *Tribology Int.* 2006; 39: 953–957

128. Chen CS, Chen XH, Yang Z, Li WH, Xu LS, Yi B. *Diam. Rel. Mater.* 2006; 15: 151-156

129. Wang F, Arai S, Endo M. *Carbon* 2005; 43: 1716–1721

130. Chen XH, Chen CS, Xiao HN, Liu HB, Zhou LP, Li SL, Zhang G. *Tribology Int.* 2006; 39: 22-28

131. Liu YM, Sung Y, Chen YC, Lin CT, Chou YH, Ger MD. *Electrochem. Solid-State Lett.* 2007; 10(9): 101-104

132. Deng FM, Chen XH, Chen WX, Li WZ. *Trans. Nonferrous Met. Soc. China* 2004; 14(4): 681-685

133. Chao TC, Shen GR, Cheng YT. *J. Electrochem. Soc.* 2006; 153(1): 98-104

134. Shen GR, Cheng YT, Tsai LN. *IEEE Trans. Nanotech.* 2005; 4(5): 539-547

135. Wu Y, Rong R, Wang F, Yuan Z, Wang T, Hu X. *Mater. Res. Bull.* 2008; 43(12): 3425-3432

136. Kim KT, Cha SI, Hong SH, Hong SH. Mater. Sci. Eng. A 2006; 430: 27-33

137. Ping C, Li F, Jian Z, Wei J. *Propellants, Explosives, Pyrotechniques* 2006; 31(6): 452-455

138. Xu L, Chen X, Pan W, Li W, Yang Z, Pu Y. *Nanotechnology* 2007; 18: 1-4

139. Kim KT, Cha SI, Gemming T, Eckert J, Hong SH. *Small* 2008; 4(11): 1936-1940

140. Chen WX, Lee JY, Liu Z. *Carbon* 2003; 41: 959–966

141. Huang W, Chen H, Zuo JM. *Nanotube Templates* 2006; 2(12): 1418 – 1421

142. Li YH, Housten W, Zhao Y, Zhu Y. *Nanotechnology* 2007; 18: 1-6

143. Salas W, Alba-Baena NG, Murr LE. *Metall. Mater. Trans. A* 2007; 38: 2928-2935

144. Tokunaga T, Kaneko K, Horita Z. *Mater. Sci. Eng. A* 2008; 490: 300-304

145. Morisada Y, Fujii Y, Nagaoka T, Fukusumi M. *Mater. Sci. Eng. A* 2006; 416: 344-348

146. Lim DK, Shibayanagi T, Gerlich AP. *Mater. Sci. Eng. A* 2008; doi:10.1016/j.msea.2008.11.067.

147. Zhang Y, Zhang Q, Li Y, Wang N, Zhu J. *Solid State Comm.* 2000; 115: 51–55

148. Shu J, Li H, Yang R, Shi Y, Huang X. *Electrochem. Comm.* 2005; 8: 51–54

149. Kim T, Mo YH, Nahm KS, Oha SM. *J. Power Sources* 2006; 162: 1275–1281

150. Ishihara T, Nakasu M, Yasuda I, Matsumoto H. *Sci. Tech. Adv. Mater.* 2006; 7: 667–671

151. Wang YH, Li YN, Lu J, Zang JB, Huang H. *Nanotechnology* 2006; 17: 3817–3821

152. Fauchais P. *J. Phys. D* 2004; 37: 86-108

153. Fauchais P, Vardelle A, Dussoubs B. *J. Therm. Spray Tech.* 2001; 10(1): 44-66

154. Meyer WB. *J. Therm. Spray Tech.* 1996; 5(1): 79-83

155. Berndt CC, Lavernia EJ. *J. Therm. Spray Tech.* 1998; 7(3): 411-440

156. Agarwal A, McKechnie T, Seal S. *J. Metals* 2002; September: 42-44

157. Laha T, Agarwal A, McKechnie T, Rea K, Seal S. *Acta Mater.* 2005; 53: 5429-5438

158. Laha T, Agarwal A. *Mater. Sci. Eng. A* 2008; 480: 323-332

159. Alkimov AP, Papyrin AN, Kosarev VF, Nesterovich NI, Shushpanov MM. *US Patent 5302414* 1994

160. Assadi H, Gartner F, Stoltenhoff T, Kreye H. *Acta Mater.* 2003; 51: 4379-4394

161. Grujicic M, Zhao CL, DeRosset WS, Helfritch D. *Mater. Des.* 2004; 25: 681-688

162. Champagne V, Helfritch D, Leyman P, Lempicki R, Grendahl S. *Modell. Simul. Mater. Sci. Eng*. 2005; 13: 1119-1128

163. Grujicic M, Zhao CL, DeRosset WS, Helfritch D. *Mater. Sci. Eng. A* 2004; 368: 222-230

164. Li CJ, Li WY, Wang YY, Yang GJ, Fukanuma H. *Thin Solid Films* 2005; 498: 79-85

165. Balani K, Agarwal A, Seal S, Karthikeyan J. *Scripta Mater.* 2005; 53: 845-850

166. Borchers C, Garner F, Stoltenhoff T, Kreye H. *J. Appl. Phys.* 2004; 96: 4288-4292

167. Van Steenkiste TH, Smith JR, Teets RE, Moleski JJ, Gorkeiwicz DW, Tyson RP, Marantz DR, Kowalsky KA, Riggs WA, Zajchowski PH, Pilsner B, McCune RC, Barnett KJ. *Surf. Coat. Tech.* 1999; 111: 62-71.

168. Li CJ, Li WY. *Surf. Coat. Tech.* 2003; 167: 278-283

169. Li CJ, Li WY, Wang YY. *Surf. Coat. Tech.* 2005; 198: 469-473

170. Balani K, Laha T, Agarwal A, Karthikeyan J, Munroe N. *Surf. Coat. Tech.* 2005; 195: 272-279

171. Ajdelsztajn L, Zuniga A, Jodoin B, Lavernia EJ. *Surf. Coat. Tech.* 2006; 201: 2109-2116

172. Wu J, Yang J, Fang H, Yoon S, Lee C. *Appl. Surf. Sci.* 2006; 252: 7809-7814

173. Li WY, Li CJ, Liao H, Coddet C. *Appl. Surf. Sci.* 2007; 253: 5967-5971

174. Koivuluoto H, Lagerbom J, Vuoristo P. *J. Therm. Spray Tech.* 2007; 16(4): 488-497

175. Kang HK, Kang SB. *Scripta Mater.* 2003; 49: 1169-1174

176. Lee HY, Jung SH, Lee SY, Ko KH. *Appl. Surf. Sci.* 2007; 253: 3496-3502

177. Kim HJ, Lee CH, Hwang SY. *Mater. Sci. Eng. A* 2005; 391: 243-248

178. Phani PS, Vishnukanthan V, Sundararajan G. *Acta Mater.* 2007; 55: 4741-4751

179. Deng CF, Zhang XX, Wang DZ, Ma YX. *Materials Lett.* 2007; 61: 904-907

180. Thakur SK, Kwee GT, Gupta M. *J Mater. Sci.* 2007; 42: 10040–10046

181. Laha T, Chen Y, Lahiri D, Agarwal A. *Composites A* 2009; 10.1016/j.compositesa.2009.02.007.

182. Noguchi T, Magario A, Fukazawa S, Shimizu S, Beppu J, Seki M. *Mater. Trans.* 2004; 45(2): 602-604

183. Nai SML, Wei J, Gupta M. *Mater. Sci. Eng. A* 2006; 423: 166–169

184. Wray PJ, Richmond O, Morrison HL. *Metallography* 1983; 16: 39-58

185. Ghosh S, Nowak Z, Lee K. Acta Mater. 1997; 45: 2215-2234

186. Seidel GD, Lagoudas DC. *Mech. Mater.* 2004; 38: 884–907

187. Luo ZP, Koo. *J. Microscopy* 2005; 225: 118-125

188. Pegel S, Potschke P, Villmow T, Stoyan D, Heinrich G. *Polymer* 2009; doi:10.1016/j.polymer.2009.02.030.

189. Dilandro L, Dibenedetto AT, Groeger J. *Polym. Comp.* 1988; 9: 209-221

190. Piggott MR. Carbon 1989; 27(5): 657-662

191. Chen H, Alpas AT. *Wear* 1996; 192: 186-198

192. Poteet CC, Hall IW. *Mater. Sci. Eng. A* 1997; 222: 35-44

193. Yang M, Scott VD. *Carbon* 1991; 29(7): 877 – 879

194. De Sanctis M, Pelletier S, Bienvenu Y, Guigon M. *Carbon* 1994; 32(5): 925 – 930

195. Vidal-Setif MH, Lancin M, Marhic C, Valle R, Raviart JL, Daux JC, Rabinovitch M. *Mater. Sci. Eng. A* 1999; 272: 321–333

196. Tham LM, Gupta M, Cheng L. *Acta Mater.* 2001; 49: 3243-3253

197. Lin RY. *Key Eng. Mater.* 1995; 104-107: 507-522

198. Aggour L, Fitzer E, Heym M, Ignatowitz E. *Thin Solid Films* 1977; 40: 97-105

199. Himbeault DD. Varin RA, Piekarski K. *Composites* 1989; 20(5): 471-477

200. Zhong Z, Liu B, Sun L, Ding J, Lin J, Tan KL. *Chem. Phys. Lett.* 2002; 362: 135-143

201. Dal H, Wong EW, Lu YZ, Fan S, Lieber CM. *Nature* 1995; 375: 769-772

202. Shi X. Yang H, Sun P, Shao G, Duan X, Zhen X. *Carbon* 2007; 45(9): 1735-1742

203. Landry K, Rado C, Voitovich R, Eustathopoulos N. *Acta Mater.* 1997; 45(7): 3079-3085

204. Nuriel S, Liu L, Barber AH, Wagner HD. *Chem. Phys. Lett.* 2004; 404: 263–266

205. Dujardin E, Ebbesen TW, Hiura H, Tanigaki K. *Science* 1994; 265: 1850-1852

206. Ebbessen TW. *J. Phys. Chem. Solids* 1996; 57(6-8): 951-955

207. Landry K. Eustathopoulos N. *Acta Mater.* 1996; 44(10): 3923-3932

208. Ryu HJ, Cha SI, Hong SH. *J. Mater. Res.* 2003; 18: 2851-2853

209. Coleman JN, Cadek M, Blake R. Nicolosi V, Ryan KP, Belton C, Fonseca A, Nagy JB, Gunko YK, Blau WJ. *Adv. Funct. Mater.* 2004; 14(8): 791-798

210. Yeh MK, Tai NH, Liu JH. *Carbon* 2006; 44: 1-9

211. Anumandla V, Gibson RF. *Composites A* 2006; 37: 2178-2185

212. Lahoz PL, Maser W, Martinez T, Benito A, Seeger T, Cano P, de Villoria RG, Miravete A. *Mech. Adv. Mater. Struct.* 2005; 12: 13-19

213. Zalamea L, Kim H, Pipes RB. *Comp. Sci. Tech.* 2007; 67: 3425-3433

214. Cox HL. *Brit. J. Appl. Phys.* 1951; 3: 72-79

215. Qian D, Dickey EC, Andrews R, Rantell T. *Appl. Phys. Lett.* 2000; 76(20): 2868-2870

216. Halpin JC, Kardos JL. *Polym. Eng. Sci.* 1976; 16(5): 344-352

217. Bakshi SR, Singh V, Balani K, McCartney DG, Seal S, Agarwal A. *Surf. Coat. Tech.* 2008; 202: 5162-5169

218. Hashin Z, Shtrikman S. *J. Mech. Phys. Solids.* 1962; 10: 335-342

219. Hashin Z, Shtrikman S. *J. Mech. Phys. Solids.* 1992; 40(4): 767-781

220. Chen Y, Balani K, Agarwal A. *Appl. Phys. Lett.* 2007; 91: 319031-319033

221. de Villoria RG, Miravete A. *Acta Mater.* 2007; 55: 3025-3031

222. Tu JP, Yang YZ, Wang LY, Ma XC, Zhang XB. *Tribology Lett.* 2001; 10(4): 225-228

223. Chen XH, Li WH, Chen CS, Xu LS, Zhi Y, Hu J. *Trans. Nonferrous Met. Soc. China* 2005; 15(2): 314 - 318

224. Zeng Q, Luna J, Bayazitoglu Y, Wilson K, Imam MA, Barrera EV. *Mater. Sci. Forum* 2007; 561-565: 655-658

225. Kumar KM, Kripesh V, Tay AAO. *J. Alloys Comp.* 2008; 450: 229–237

226. Hong S, Myung S. *Nature Nanotech.* 2007; 2(4): 207-208

227. Praveen BM, Venkatesha TV, Naik YA, Prashantha K. *Surf. Coat. Tech.* 2007; 201: 5836-5842

228. Balani K, Bakshi SR, Chen Y, Laha T, Agarwal A. *J. Nanosci. Nanotech.* 2007; 7(10): 3553–3562

229. Zhang D, Shipway PH, McCartney DG. *J. Therm. Spray Tech.* 2005; 14: 109-116

230. Oliver WC, Pharr GM. *J. Mater. Res.* 1992; 7: 1564-1583

231. Sobolev VV, Guillemany JM. *Materials Lett.* 2000; 42: 46-51

232. Landry K, Kalogeropoulou S, Eustathopoulos N. *Mater. Sci. Eng. A* 1998; 254: 99–111

233. Cordovilli CG, Louis E, Narciso J. *Acta Mater.* 1999; 47: 4461-4479

234. Molina JM, Saravanan RA, Arpon R, Cordovilla CG, Louis E, Narciso J. *Acta Mater.* 2002; 50: 247-257

235. Anson JP, Drew RAL, Gruzleski JE. *Metall. Trans. B* 1999; 30: 1027-1032

236. Dykhuizen RC, Smith MF. J. Therm.Spray Tech. 1998; 7(2): 205-211

237. Thornton C, Yin KK, Adams MJ. *J. Phys. D: Appl. Phys.*1996; 29: 424-435

238. Thornton C, Liu L. *Powder Tech.* 2004; 143-144: 110-116

239. Papyrin A, Kosarev V, Klinkov S, Alkhimov A, Fomin V. *Cold Spray Technology* ed. A. Papyrin 2007: p. 40.

240. Price T. PhD Thesis. University of Nottingham, 2008.

241. Al-Ostaz A, Diwakar A, Alzebdeh KI. *J. Mater. Sci.* 2007; 42: 7016

242. Tempfli SM, Tempfli MM, Piraux L. *Thin Solid Films* 2008; 516: 3735

243. Yang RY; Zou RP, Yu AB, Choi SK. *J. Colloids Inter.* 2006; 299: 719

244. Bale CW, Chartrand P, Degterov SA, Eriksson G, Hack K, Mahfoud RB, Melanqon J, Pelton AD, Petersen S. *CALPHAD* 2002; 26: 189-228

245. Desai P. *J. Phys. Chem. Ref. Data* 1987; 16: 109-124

246. Kaufman L. *CALPHAD* 1979; 3: 45-76

247. Lee JC, Byun JY, Oh CS, Seok HK, Lee HI. *Acta Mater.* 1997; 45: 5303-5315

248. Balani K, Anderson R, Laha T, Andara M, Tercero J, Crumpler E, Agarwal A. *Biomaterials* 2007; 28(4): 618-624

249. Balani K, Agarwal A. *Surf. Coat. Tech.* 2008; 202: 4270–4277

250. Balani K. Zhang T, Karakoti A, Li W, Seal S, Agarwal A. *Acta Mater.* 2008; 56(3): 571-579

251. Hugosson HW, Eriksson O, Jansson U, Ruban AV, Souvatzis P, Abrikosov IA. *Surf. Sci.* 2004; 557: 243-254

252. Solozhenko VL, Kurakevych OO. *Solid State Comm.* 2005; 133: 385-388

253. Tham LK, Gupta M, Cheng L. *Acta Mater.* 2001; 49: 3243-3253

254. Keshri AK, Balani K, Bakshi SR, Singh V, Laha T, Seal S, Agarwal A. *Surf. Coat. Tech.* 2009; 203(16): 2193-2201

255. Nishino H, Yamaguchi C, Nakaoka H, Nishida R. *Carbon* 2003; 41: 2165-2167

256. Chen L, Pang XJ, Zhang QT, Yu ZL. *Materials Lett.* 2006; 60: 241-244

257. Arroyo M, Arias I. *J. Mech. Phys. Solids* 2008; doi:10.1016/j.jmps.2007.10.001.

258. Lourie O, Cox DM, Wagner HD. *Phys. Rev. Lett.* 1998; 81: 1638-1641

259. Bower C, Rosen R, Jin L, Han J, Zhou O. *Appl. Phys. Lett.* 1999; 74: 3317-3319

260. Ugarte D. *Carbon* 1995; 33: 989-993

261. Li YB, Wei BQ, Liang J, Yu Q, Wu DH. *Carbon* 1999; 37: 493-497

262. Wei B, Zhang J, Liang J, Wu D. *Carbon* 1998; 36: 997-1001

263. Yakobson BI, Campbell MP, Brabec CJ, Bernholc *J. Comput. Mater. Sci.* 1997; 8: 341-348

264. *Metals Handbook Desk Edition* Ed. Davis.JR. 1998

265. Wagner HD, Lourie O, Feldman Y, Tenne R. *Appl. Phys. Lett.* 1998; 72: 188-190

266. Hwang GL, Hwang KC. *Nano Lett.* 2001; 1: 435-438

267. Troiani HE. Yoshida MM, Bragado GAC, Marques MAL, Rubio A, Ascencio JA, Yacaman MJ. *Nano Lett.* 2003; 3: 751-755

268. Marques MAL, Troiani HE, Yoshida MM, Yacaman MJ, Rubio A. *Nano Lett.* 2004; 4: 811-815

269. Benedict LX, Chopra NG, Cohen ML, Zettl AL, Louie SG, Crespi VH. *Chem. Phys. Lett.* 1998; 286: 490-496

270. Yao X, Han Q, Xin H. *Comput. Mater. Sci.* 2008. doi:10.1016/j.commatsci.2007.12.019.

271. Cummings J, Zettl A. *Science* 2000; 289: 602-604

272. Wang LJ, He T, Jiang W. *Carbon* 2007; 45: 2636-2642

273. Tang.F, Schoenung J. *Scripta Mater.* 2006; 54: 1587-1592

274. Chen Y, Bakshi SR, Agarwal A. *ACS Appl. Mater. Inter.* 2009; 1(2): 235-238

275. Chen Y, Laha T, Balani K, Agarwal A. *Scripta Mater.* 2008; 58: 1121-1124

276. Warmuzek M. *Aluminum-Silicon Casting Alloys: Atlas of Microfractographs* 2004: 3

277. Dowling NE. *Mechanical Behavior of Materials: Engineering Methods for Deformation, fracture, and fatigue* 1993; 1st ed.: 129, 191-192

278. Mori T, Tanaka K. *Acta Metall.* 1973; 21: 571-574

279. Ling Z, Hou J. *Comp. Sci. Tech.* 2007; 67: 3121-3129

280. Giannakopoulos AE, Suresh S. *Scripta Mater.* 1999; 40: 1191-1198

281. Tang F, Schoenung JM. *Scripta Mater.* 2006; 54: 1587-1590

282. Archard JF. *J. Appl. Phys.* 1953; 24: 981-988

283. Cheng YT, Cheng CM. *Appl. Phys. Lett.* 1998; 73: 614-616

284. Bao YW, Wang W, Zhou YC. *Acta Mater.* 2004; 52: 5397-5404

285. Bao YW, Liu L, Zhou Y. *Acta Mater.* 2005; 53: 4857-4862

286. Chen J, Bull SJ. *J. Mater. Res.* 2009; 24: 590-598

287. Sudak LJ. *J. Appl. Phys.* 2003; 94: 7281-7287

288. Jeng JR, Tsai PC, Fang TH. *App. Phys. Lett.* 2007; 90: 161913

289. Waters JF, Guduru PR, Jouzi M, Xu JM, Hanlon T, Suresh S. *Appl. Phys. Lett.* 2005; 87: 103109(1-3)

290. Muthuswami L, Zheng Y, Vajtai R, Shekhawat G, Ajayan P, Geer RE. *Nano Lett.* 2007; 7: 3891-3894.

291. *Nanotribology and Nanomechanics: An Introduction* 2008; Ed. B. Bhushan: 458

292. Mo Y, Turner KT, Szlufarska I. *Nature* 2009; 457: 1116-1119

293. Lafaye S, Troyon M. *Wear* 2006; 261: 905-913

294. Johnson KL, Kendall K, Roberts AD. *Proc. Roy. Soc. Lond. A* 1971; 324: 301-313

295. Balani K, Harimkar SP, Keshri AK, Chen Y, Dahotre NB, Agarwal A. *Acta Mater.* 2008; 56: 5984-5994

296. Esawi AMK, Morsi K, Sayed A, Gawad AA, Borah P. *Mater. Sci. Eng. A* 2009; 508: 167-173

297. Yuuki J, Kwon H, Kawasaki A, Magario A, Noguchi T, Beppu J, Seki M. *Mater. Sci. Forum* 2007; 534-536: 889-892

298. Bustamante RP, Esparza CDG, Guel IE, Yoshida MM, Jiminez LL,.Garcia SAP, Sanchez RM. *Mater. Sci. Eng. A* 2009; 502: 159-163

APPENDIX

This section provides a list of publication in peer reviewed journals directly related to this study.

List of publications in peer reviewed journals:

1. Srinivasa R. Bakshi, Debrupa Lahiri and Arvind Agarwal, *"Carbon Nanotube Reinforced Metal Matrix Composite - A Review"*, Invited Review Article submitted to ***International Materials Review****, to be published in July 2009*
2. Srinivasa R. Bakshi, Anup K. Keshri, Virendra Singh, Sudipta Seal, Arvind Agarwal, *"Interface in Carbon Nanotube Reinforced Aluminum Silicon Composites: Thermodynamic Analysis and Experimental Verification"*, ***Journal of Alloys and Compounds*** DOI:10.1016/j.jallcom.2009.03.055
3. Srinivasa R. Bakshi, Virendra Singh, Sudipta Seal, Arvind Agarwal, *"Aluminum Composite Reinforced with Multiwalled Carbon Nanotubes from Plasma Spraying of Spray Dried Powders"*, ***Surface and Coatings Technology*** Vol. 203 (2009) 1544-1554
4. Srinivasa R. Bakshi, Virendra Singh, Kantesh Balani, D. Graham McCartney, Sudipta Seal and Arvind Agarwal, "*Carbon Nanotube Reinforced Aluminum Composite Coating via Cold Spraying*", ***Surface and Coatings Technology*** Vol. 202 (2008) 5162-5169
5. Srinivasa R. Bakshi, Virendra Singh, D. Graham McCartney, Sudipta Seal and Arvind Agarwal, "*Deformation and Damage Mechanisms of Multiwalled Carbon Nanotubes Under High Velocity Impact*", ***Scripta Materialia*** Vol. 59 (2008) pp. 499-502
6. Srinivasa R. Bakshi, T. Laha, K. Balani, A. Agarwal and J. Karthikeyan, "Effect of carrier gas on mechanical properties and fracture behaviour of cold sprayed aluminium coatings", **Surface Engineering** Vol. 23[1] (2007) pp. 18-22
7. Yao Chen, Srinivasa R. Bakshi and A. Agarwal, *"Inter-Splat Friction Force for Splat Sliding in Plasma Sprayed Aluminum-alloy Coating During Nanoindentation and Microindentation"* ***ACS Applied Materials & Interfaces*** Vol. 1(2) (2009) 235-238
8. Anup Kumar Keshri, Kantesh Balani, Srinivasa R. Bakshi, Virendra Singh, Tapas Laha, Sudipta Seal and Arvind Agarwal, *"Structural Transformation in Carbon Nanotubes During Thermal Spraying"*, ***Surface and Coatings Technolgy*** Vol. 203 (2009) 2193-2201
9. Srinivasa R. Bakshi, K. Balani, and A. Agarwal, "*Thermal Conductivity of Plasma Sprayed Aluminum Oxide-Multiwalled Carbon Nanotube Composites*", ***Journal of American Ceramic Society*** Vol. 91[3] (2008) pp. 942–947
10. K. Balani, Srinivasa R. Bakshi, D. Lahiri, and Arvind Agarwal, "Grain Growth Behavior of Aluminum Oxide Reinforced with Carbon Nanotubes During Plasma

Spraying and Post-Spray Consolidation", ***International Journal of Applied Ceramic Technology*** *DOI:10.1111/j.1744-7402.2009.02385.x*

11. K. Balani, Srinivasa R. Bakshi, Y. Chen, T. Laha and A. Agarwal, "Role of Powder Treatment and CNT Dispersion in the Fracture Toughening of Plasma-Sprayed Aluminum Oxide – Carbon Nanotube Ceramic Nanocomposite," **Journal of Nanoscience and Nanotechnology** Vol.7[10] (2007) pp.3553–3562
12. *Srinivasa R. Bakshi*, J.E. Tercero, and A. Agarwal, "*Synthesis and characterization of multiwalled carbon nanotube reinforced ultra high molecular weight polyethylene composite by electrostatic spraying technique*", ***Composites: Part A*** Vol. 38 (2007) pp. 2493–2499
13. *Srinivasa R. Bakshi*, K. Balani, T. Laha, J. Tercero, and A. Agarwal, "*The Nanomechanical and Nanoscratch Properties of MWNT Reinforced Ultrahigh-Molecular-Weight Polyethylene Coatings*", ***Journal of Metals*** July 2007 pp. 50-53
14. Anup Kumar Keshri, *Srinivasa R. Bakshi*, Yao Chen, Tapas Laha, Xiaohua Li, Cesar Levy and Arvind Agarwal, *"Nanomechanical Behavior of Plasma Sprayed PZT Coatings"*, ***Surface Engineering*** Vol. 25[4] (2009) 270-275
15. Venkata Pasumarthi, Yao Chen, Srinivasa R. Bakshi and Arvind Agarwal. "Feasibility study of Ti_3SiC_2 Phase Synthesis via Reactive Plasma Spraying" ***Journal of Alloys and Compounds*** doi:10.1016/j.jallcom.2009.04.079

List of Paper Submitted to Peer Reviewed Journals:

1. *Srinivasa R. Bakshi* and Arvind Agarwal, "*Quantification of Carbon Nanotube Dispersion in Randomly Oriented Nanocomposites",* Manuscript submitted to ***Composites Part A*** on Feb 2009
2. Srinivasa R. Bakshi, Debrupa Lahiri, Riken R. Patel and Arvind Agarwal, "Nanoscratch Behavior of Carbon Nanotube Reinforced Aluminum Coatings" Manuscript submitted to ***Acta Materialia*** in Mar 2009
3. Yao Chen, Srinivasa R. Bakshi and A. Agarwal, "Correlation between Nanomechanical and Nanotribological Properties of Carbon Nanotube Reinforced Aluminum Composite Coatings", Manuscript submitted to ***Wear*** in March 2009
4. Debrupa Lahiri, *Srinivasa R. Bakshi*, Anup K. Keshri and Arvind Agarwal, *"Carbon Nanotube Reinforced Aluminum composites prepared by a novel roll bonding technique"* Manuscript submitted to ***Acta Materialia*** in Feb 2009

Book

Srinivasa R. Bakshi, Debrupa Lahiri and Arvind Agarwal Srinivasa R. Bakshi, Debrupa Lahiri and Arvind Agarwal, **"***Carbon Nanotube metal Matrix Composites*", Taylor and Francis Publishers, to be completed by March 2010

Carbon Nanotube Metal Matrix Composites – A Review

Srinivasa R. Bakshi, Debrupa Lahiri and Arvind Agarwal*

Plasma Forming Laboratory
Nanomechanics and Nanotribology Laboratory
Department of Mechanical and Materials Engineering
Florida International University, Miami, FL 33174, USA

Abstract

This review summarises the research work carried out in the field of carbon nanotubes (CNT) metal matrix composites. A lot of research has undergone in utilising CNTs as reinforcement for composite material. However CNT reinforced metal matrix composites has received least attention. These composites are being projected for use in structural applications for their high specific strength as well as functional materials for their exciting thermal and electrical characteristics. The present review focuses on the critical issues of CNT-metal matrix composites that include processing techniques, nanotube dispersion, interface, strengthening mechanisms, and mechanical properties. Processing techniques used for synthesis of the composites have been critically reviewed with an objective to achieve homogeneous distribution of carbon nanotubes in the matrix. The mechanical property improvement achieved by addition of CNTs in various metal matrix systems has been summarized. The factors determining strengthening achieved by CNT reinforcement have been elucidated. The structural and chemical stability of CNTs in different metal matrices and importance of CNT/metal interface has been reviewed. Importance of CNT dispersion and its quantification has been highlighted. Application of CNT metal matrix composites as functional materials has been summarized. Scope for future work that needs attention is addressed.

To be published in July 2009 issue of International Materials Review

G Model
JALCOM-19621; No. of Pages 7
ARTICLE IN PRESS

Journal of Alloys and Compounds xxx (2009) xxx–xxx

Contents lists available at ScienceDirect

Journal of Alloys and Compounds

journal homepage: www.elsevier.com/locate/jallcom

Interface in carbon nanotube reinforced aluminum silicon composites: Thermodynamic analysis and experimental verification

Srinivasa R. Bakshi[a], Anup K. Keshri[a], Virendra Singh[b], Sudipta Seal[b], Arvind Agarwal[a,*]

[a] Plasma Forming Laboratory, Department of Mechanical and Materials Engineering, Florida International University, 10555 West Flagler Street, EC 3464, Miami, FL 33174, USA
[b] AMPAC and Nanoscience Technology Center, University of Central Florida, Orlando, FL 33816, USA

ARTICLE INFO

Article history:
Received 13 January 2009
Received in revised form 10 March 2009
Accepted 11 March 2009
Available online xxx

Keywords:
Metal matrix composites
Surfaces and interfaces
Carbon nanotubes
Thermodynamics
Carbide

ABSTRACT

Interface in carbon nanotubes (CNTs) reinforced aluminium–silicon composites are studied via thermodynamic and kinetic analysis. A pseudo-phase diagram has been generated based on the thermodynamic calculations to predict the type of carbide (Al_4C_3 or SiC) that would form at the matrix–CNT interface as a function of matrix composition and processing temperature. The pseudo-phase diagram is useful in high temperature processes like thermal spray forming. Critical thickness values for carbide nucleation suggest the formation of Al_4C_3 with Al–11.6 wt.% Si alloy and SiC with Al–23 wt.% Si alloy. Thermodynamic calculations show that the amount of Al_4C_3 increases with an increase in the CNT content. The computed results perfectly agree with the results obtained by XRD, SEM of fracture surface and high-resolution transmission electron microscopy (HRTEM) observations on Al–11.6 wt.% Si and Al–23 wt.% Si alloy reinforced with CNT.

1. Introduction

Light weight and high strength metal matrix composites reinforced with carbon fibers have been used for many automobile and space applications [1–3]. In recent years, the focus has shifted to reinforcement of metal matrix composites with carbon nanotubes (CNTs) due to their strengths in excess of 100 GPa and stiffness of 1000 GPa which makes them superior to carbon fibers [4,5]. The major challenge has been to disperse and align the nanotubes in the metal matrix and the fabrication of bulk composites having the above-mentioned characteristics. Cha et al. [6] have shown extraordinary improvement of the yield strength (~200% increase for 10 vol.% CNT addition) in copper–CNT composites fabricated by the molecular mixing method. The increase in the strength was attributed to the uniform dispersion of CNTs. Choi et al. [7] have fabricated aluminium–CNT composites by extrusion of ball milled powders. Young's modulus and yield strength increased by ~49% and ~46%, respectively, for the 4 vol.% CNT containing composite.

The fiber–matrix interface plays an important role in strengthening of the composite. The applied stress is transferred to the high strength reinforcement through the interfacial layer. So a strong interface would make the composite very strong but at the expense of ductility of the composite. A weak interface would lead to lower strength and inefficient utilization of fiber properties by facilitating pullout phenomena at low loads due to interface failure. Interfacial reactions and degree of wetting of the reinforcement (fibers) also affect the properties of the composite [8–10]. Formation of aluminum carbide (Al_4C_3) has been observed at the interface in liquid metal infiltrated aluminum silicon alloy composites reinforced with carbon fibers containing 7 wt.% [11] and 13 wt.% Si [12]. Vidal-Setif et al. have shown reduction in strength and premature failure of 75 vol.% carbon fiber reinforced A357 alloy due to formation of Al_4C_3 and presence of brittle Si particles [13]. So formation of Al_4C_3 needs to be avoided. This can be done by either by controlling the chemistry of the matrix or by using coated carbon fibers [14,15].

Recently there has been a lot of interest in fabrication of aluminum matrix composite reinforced with carbon nanotubes. Bulk aluminium–CNT composites have been fabricated using various processes like cold isostatic pressing followed by hot extrusion [16], pressureless infiltration technique [17] and thermal spraying [18–20] to name a few. *In general, less attention has been devoted to the interfacial reaction between the metal matrix and CNT.* It has been reported by some authors that no reaction product is observed [7,21]. It is very important to understand the interaction between metals and the new forms of carbon namely CNTs, from theoretical and practical viewpoint. Carbon nanotubes are made by rolling a sheet of graphene onto itself and hence outer shell is made up of the basal plane. So they could be quite stable chemically. Zhong et al. have shown from the changes occurring in the intensity of (1 1 1) peak of the XRD pattern of Cobalt, after a 10-h annealing treatment with various forms of carbon at 1000 °C, that the interaction of layered graphite was the lowest followed by single walled CNT,

* Corresponding author. Tel.: +1 3053481701; fax: +1 3053481932.
E-mail address: agarwala@fiu.edu (A. Agarwal).

0925-8388/$ – see front matter © 2009 Elsevier B.V. All rights reserved.
doi:10.1016/j.jallcom.2009.03.055

Please cite this article in press as: S.R. Bakshi, et al., J. Alloys Compd. (2009), doi:10.1016/j.jallcom.2009.03.055

Surface & Coatings Technology 203 (2009) 1544–1554

Contents lists available at ScienceDirect

Surface & Coatings Technology

journal homepage: www.elsevier.com/locate/surfcoat

Aluminum composite reinforced with multiwalled carbon nanotubes from plasma spraying of spray dried powders

Srinivasa R. Bakshi [a], Virendra Singh [b], Sudipta Seal [b], Arvind Agarwal [a,*]

[a] Plasma Forming Laboratory, Nanomechanics and Nanotribology Laboratory, Department of Mechanical and Materials Engineering, Florida International University, Miami, FL 33174, USA
[b] AMPAC and Nanoscience Technology Center, University of Central Florida, Orlando, FL 33816, USA

ARTICLE INFO

Article history:
Received 19 September 2008
Accepted in revised form 4 December 2008
Available online 13 December 2008

Keywords:
Carbon nanotubes
Aluminum composites
Dispersion
Nanoindentation
Spray drying
Plasma spraying

ABSTRACT

Homogenous dispersion of carbon nanotubes (CNTs) in micron sized aluminum silicon alloy powders was achieved by spray drying. Excellent flowability of the powders allowed fabrication of thick composite coatings and hollow cylinders (5 mm thick) containing 5 wt.% and 10 wt.% CNT by plasma spraying. Two phase microstructure with matrix having good distribution of CNT and CNT rich clusters was observed. Microstructural evolution has been explained using single splat and the infiltration of CNT clusters by liquid metal. Partial CNT surface damage was observed in case of the 10 wt.% CNT coating due to CNT mesh formation and smaller size of spray dried agglomerate. Increase in the elastic modulus and improvement in the yield strength and elastic recovery properties due to CNT addition was observed by nanoindentation.

1. Introduction

Metal matrix composites have been proposed for many automobile [1–4] and space applications [4,5] due to their superior mechanical properties like higher specific strength and stiffness, desirable coefficient of thermal expansion and good damping properties [6]. Multiwalled carbon nanotubes (CNTs) possess unique properties like high stiffness (~970 GPa), strength (~63 GPa) [7] and thermal conductivity up to 3000 W m^{-1} K^{-1} [8]. Excellent mechanical and thermal properties of CNTs along with their low density make them ideal as reinforcements for composites. Polymer [9–11] and ceramic [12–15] matrix composites have been prepared with CNTs as reinforcement in order to improve the mechanical and/or thermal properties. Although majority of the research work on development of CNT composites have been carried out using polymers as matrices due to the relative ease of fabrication.

Metal matrix composites with CNT reinforcement have generated significant interest in last five years. Composites have been prepared with metal/alloy matrices of Al [16–19], Cu [20–23], Ni [24–26], Mg [27–29] and metallic glasses [30,31]. Several fabrication routes namely powder metallurgy, ball milling, extrusion, hot pressing, equal-channel angular pressing, spark plasma sintering, electro-deposition, electro-less deposition and thermal spraying have been used to synthesize metal matrix composites with CNTs. Chen et al. [22] have observed a decrease in the wear loss by 80% and coefficient of friction by 40% by addition of CNTs in Ni-P-CNT coatings prepared by electroless deposition technique. Cha and co-workers [21] have observed a 200% increase in the yield strength in 10 vol.% CNT reinforced Cu composites prepared by a molecular level mixing method, highlighting the significance of dispersion in effective strengthening. Noguchi et al. [16] have reported a sevenfold increase in compressive yield strength in 1.6 vol.% CNT reinforced Al composites prepared by a nano-scale dispersion method. Zhou and co-workers [17] have shown a 30% decrease in the wear rate and friction coefficient of Al-CNT alloys by addition of 20 vol.% of CNTs. Tang et al [32] have shown a 65% decrease in coefficient of thermal expansion of aluminum composite reinforced with 15 vol.% single walled CNTs. These studies indicate that there is lot of scope for strengthening and enhancement of properties by addition of CNTs. In the previous work from our research group [13,14,33], it has been shown that plasma spraying can be successfully used to fabricate bulk CNT reinforced metal and ceramic composites. Blending was used by Laha et al. [33] to mix carbon nanotubes and aluminum-23 wt.% silicon alloy powder. However, this lead to poor dispersion and clogging of the powder feeding tubes, due to which the thickness of the cylindrical shell fabricated by plasma spray forming was limited to 0.635 mm [33].

The goal of the present work is to improve the dispersion of the CNTs in the aluminum composite by employing spray dried powders to enable fabrication of thick coatings and bulk freestanding structure. The microstructure evolution of the coatings from spray dried powders is reported with the help of the single splat structure. The change in mechanical properties with CNT addition is also investigated.

* Corresponding author.
E-mail address: agarwala@fiu.edu (A. Agarwal).

0257-8972/$ – see front matter © 2008 Elsevier B.V. All rights reserved.
doi:10.1016/j.surfcoat.2008.12.004

Surface & Coatings Technology 202 (2008) 5162–5169

Contents lists available at ScienceDirect

Surface & Coatings Technology

journal homepage: www.elsevier.com/locate/surfcoat

Carbon nanotube reinforced aluminum composite coating via cold spraying

Srinivasa R. Bakshi [a], Virendra Singh [c], Kantesh Balani [a], D. Graham McCartney [b], Sudipta Seal [c], Arvind Agarwal [a,*]

[a] Department of Mechanical and Materials Engineering, Florida International University, Miami, FL 33174, USA
[b] School of Mechanical, Materials and Manufacturing Engineering and Management, University of Nottingham, University Park, Nottingham, NG7 2RD, UK
[c] AMPAC, Nanoscience and Technology Center (NSTC) and Mechanical, Materials and Aerospace Engineering, University of Central Florida, Orlando, FL 32816, USA

ARTICLE INFO

Article history:
Received 20 February 2008
Accepted in revised form 22 May 2008
Available online 3 June 2008

Keywords:
Cold spraying
Carbon nanotubes
Aluminum
Composites
Elastic modulus

ABSTRACT

Multiwalled carbon nanotube (CNT) reinforced aluminum nanocomposite coatings were prepared using cold gas kinetic spraying. Spray drying was used to obtain a good dispersion of the nanotubes in micron-sized gas atomized Al–Si eutectic powders. Spray dried powders containing 5 wt.% CNT were blended with pure aluminum powder to give overall nominal CNT compositions of 0.5 wt.% and 1 wt.% respectively. Cold spraying resulted in coatings of the order of 500 μm in thickness. Fracture surfaces of deposits show that the nanotubes were uniformly distributed in the matrix. Nanotubes were shorter in length as they fractured due to impact and shearing between Al–Si particles and the Al matrix during the deposition process. Nanoindentation shows a distribution in the elastic modulus values from 40–229 GPa which is attributed to microstructural heterogeneity of the coatings that comprise the following: pure Al, Al–Si eutectic, porosity and CNTs.

1. Introduction

Cold spraying is a relatively new coating technique wherein powder particles are accelerated to supersonic velocities (600–1500 m/s) by a carrier gas flowing under large pressure difference (up to 3.5 MPa) through a de Laval type of nozzle and made to impact onto a substrate [1]. It has unique advantages like minimal effects on the material sprayed like oxidation, grain coarsening or phase changes, produces highly dense coatings and that the substrate is not affected during the coating process. The disadvantage is that a large amount of carrier gas is lost, unless recycled, and that only plastically deformable materials can be deposited. There is no melting of the particles and the bonding is believed to be due to adiabatic shear instabilities arising from thermal softening at the particle/substrate and particle/particle interfaces which have been modeled using finite element method [2,3]. The constitutive relations for plastic flow used in modeling the deformation and bonding take care of the dependence of the flow stress on the strain, strain rate, temperature and pressure. The parameters affecting the process and spraying efficiency are particle size, density of particles, temperature of gas, density of gas and spraying angle, and various models have been proposed for the effect of various parameters [4–6]. Cold spraying has been used to deposit many types of materials including pure metals [7–11], alloys [12–15] and composite materials [16–19]. In all the above cases of spraying composite coatings, it was observed that the second phase was distributed uniformly within the matrix. Recently there has been interest in cold spraying composites containing nanofillers as reinforcements by cold spraying [18,19].

Since the discovery of carbon nanotubes (CNTs) by Iijima in 1991, a lot of interest has been devoted to the application of CNTs as reinforcement for polymer [20–22], ceramic and metal matrix composites. This is due to excellent mechanical properties of CNT like strength and stiffness up to 63 GPa and ~1 TPa respectively [23] and thermal conductivity of up to 3000 W/m K [24]. The use of CNTs as reinforcements increases the strength and stiffness of metals and polymers, while it leads to an improvement in the fracture toughness [25,26] and thermal conductivity [27] of ceramics. Some of the processing techniques used in fabrication of CNT reinforced MMC are conventional powder metallurgy techniques [28,29], electroplating [30] and electroless plating [31] from CNT-containing electrolytic baths, spark plasma sintering [32,33], mechanical alloying [34] and thermal spraying [35,36]. Uniform dispersion and alignment of nanotubes within the metal matrix composites is still a challenge. Recently some success has been obtained in the alignment and dispersion of nanotubes and nanowires in blown bubble films of epoxies containing dispersed CNTs [37].

The overall aim of the work was to utilize the technique of cold gas spraying to investigate microstructure development from a blended feedstock of pure aluminum powder and an agglomerated powder comprising aluminum–silicon eutectic alloy and CNTs prepared by

* Corresponding author.
E-mail address: agarwala@fiu.edu (A. Agarwal).

0257-8972/$ – see front matter © 2008 Elsevier B.V. All rights reserved.
doi:10.1016/j.surfcoat.2008.05.042

Available online at www.sciencedirect.com
ScienceDirect
Scripta Materialia 59 (2008) 499–502
Scripta MATERIALIA
www.elsevier.com/locate/scriptamat

Deformation and damage mechanisms of multiwalled carbon nanotubes under high-velocity impact

Srinivasa R. Bakshi,[a] Virendra Singh,[b] D. Graham McCartney,[c] Sudipta Seal[b] and Arvind Agarwal[a,*]

[a] *Department of Mechanical and Materials Engineering, Florida International University, Miami, FL 33174, USA*
[b] *AMPAC, Nanoscience and Technology Center (NSTC) and Mechanical, Materials and Aerospace Engineering, University of Central Florida, Orlando, FL 32816, USA*
[c] *School of Mechanical, Materials and Manufacturing Engineering and Management, University of Nottingham, University Park, Nottingham NG7 2RD, UK*

Received 28 March 2008; revised 23 April 2008; accepted 24 April 2008
Available online 1 May 2008

Deformation behavior and damage mechanisms of multiwalled carbon nanotubes have been studied under the high strain rate impact during cold spraying. Rippling is suggested as the mechanism for breakdown of nanotubes into smaller nanotubes and possible formation of carbon onions. Necking and cup-and-cone fracture with 70% reduction in area are observed that are comparable to mild steel fracture. Peeling off of outer walls of multiwalled carbon nanotubes is also seen due to shearing action between particles.

Keywords: Cold spraying; MWNT; Deformation; Necking; Rippling

Multiwalled carbon nanotubes (MWNTs) have emerged as potential reinforcement for novel nanocomposites due to their extraordinary strength and elastic modulus [1–4]. Knowledge of the deformation and failure mechanisms of carbon nanotubes is very much essential to understanding the behavior of MWNT-reinforced nanocomposites. Mechanical properties of carbon nanotubes have been experimentally measured by several methods, including thermal vibrations in a transmission electron microscope (TEM) [5], electromechanical resonance [6], micro-Raman spectroscopy [7] and bend tests using an atomic force microscope [8,9]. All of these studies were carried out in the elastic regime. Yu et al. [10] conducted tensile test on individual MWNTs inside a scanning electron microscope. A strain to failure value of 0.12 was observed. It was observed that the sum of the fractured length of the carbon nanotubes (CNTs) was quite a bit larger than the original CNTs. This was attributed to the extra length generated by a "sword in sheath failure" mechanism. It was suggested that the outer layer fractures followed by the pull-out of the inner layer, which is easy since they are attached to each other by weak van der Waals forces. Wagner et al. [11] reported the fragmentation of MWNT in polymer matrix composite with several breaks along the nanotube length. However, high-magnification images were not obtained due to loss of contrast in the presence of the polymer. It was reported that the MWNT failed by telescopic fracture. Hwang et al. [12] observed the fracture of a MWNT inside a TEM, bridging a crack in PMMA matrix, occurring due to tensile forces generated by electrostatic repulsion. A gradual increase in the length of the MWNT with time was observed. This was attributed to the breakage of the outermost layer followed by sliding between the layers to some distance followed by fusion of the outermost layer to the layer below. This breakage, sliding and fusion process continued until the MWNT fractured. It was followed by termination of the broken ends due to cap formation. While this mechanism is significant, it remains to be understood what factors govern the sliding distance and fusion process and the number of tubes that undergo breakage in a single instance. Troiani et al. [13] observed the breakage of a single-walled carbon

* Corresponding author. Tel.: +1 305 348 1701; fax: +1 305 348 1932; e-mail: agarwala@fiu.edu

1359-6462/$ - see front matter © 2008 Acta Materialia Inc. Published by Elsevier Ltd. All rights reserved.
doi:10.1016/j.scriptamat.2008.04.035

Effect of carrier gas on mechanical properties and fracture behaviour of cold sprayed aluminium coatings

S. R. Bakshi[1], T. Laha[1], K. Balani[1], A. Agarwal*[1] and J. Karthikeyan[2]

Two different coatings of 1100 aluminium were cold sprayed onto similar substrates, using He and He–20N_2 (vol.-%) mixture as carrier gases. Three point bend testing was carried out. The elastic moduli of the coatings were found to be close to each other and the substrate. The He processed coating showed higher fracture strength which was attributed to the higher degree of strain hardening. The He–20N_2 processed coating failed at lower stress owing to its strain relaxed structure. The mode 1 fracture of the coating substrate system was found to be higher for the helium processed coating. The toughness was correlated to the microstructure. The delaminated coating showed a higher degree of brittle failure of the interface for the He processed coating.

Keywords: Cold spraying, 1100 aluminium, Fracture surface, Fracture toughness, Three point bend test, Elastic modulus, Brittle fracture, Delamination, Notch, Porosity, Carrier gas, Splats, Dislocation pile up, Subgrain formation

Introduction

Cold spraying is a relatively new coating technique where metallic powder particles are accelerated to very high velocities (600–1500 m s^{-1}) by a carrier gas (He, N_2) flowing at very high pressure (up to 3·5 MPa) and impact the substrate through a converging–diverging de laval nozzle.[1] The carrier gas is preheated to a temperature between 300 and 800°C, partly in order to compensate for the cooling produced by expansion of the gas and to reduce the density which in turn increases the sonic velocity, but below the melting point of the particles. The loss of kinetic energy on impact causes plastic deformation of the particles. This process is also known as cold kinetic spraying. The low temperature solid state coating process eliminates problems owing to oxidation and defects owing to solidification. The disadvantage is that a large amount of carrier gas is lost, unless recycled, and that only plastically deformable materials can be deposited. Many materials have been depostited till date by cold spraying including pure metals,[2–6] alloys[7] and composite materials.[8,9] The exact mechanism of the bonding is not fully understood. It is believed that impact of the particles results in rupture of oxide layers which provides clean surfaces for bonding. Bonding has been attributed to adiabatic shear instabilities at particle/particle and particle/substrate interfaces owing to impact and has been modelled using finite element analysis.[10,11] The parameters affecting the process and spraying efficiency are particle size, density of particles, temperature of gas and density of gas and spraying angle, and various models have been proposed for the effect of various parameters.[12–15]

In the authors' earlier work,[6,16] cold spraying of 1100 Al on 1100 Al substrate was reported. Two different carrier gases, namely He and He–20N_2 (vol.-%), were used to study the effect of carrier gas on the properties of the coating. It was observed that the 100%He processed coating had higher hardness than the He–20N_2 processed coating. TEM analyis revealed dislocation pile-ups and oxide layers in the He processed coating. The He–20N_2 processed coating showed subgrain formation and a relaxed structure.[16] There was more strain hardening in the He processed coating as compared with He–20N_2 processed coatings. Potentiodynamic polarisation experiments in 0·9 pH H_2SO_4 revealed that the corrosion current density was higher for the He processed coating than for the He–20N_2 processed coating indicating superior corrosion resistance of the He–20N_2 processed coating.[6]

The purpose of the present work is to study the effect of the carier gas on the fracture strength and interfacial properties of the coating/subsrate and to establish correlation with the microstructure. Three point bend testing of the samples was carried out. The elastic modulus and fracture properties were studied.

Experimental

The schematic of the three point bend test is shown in Fig. 1. A notch was introduced at the midpoint of the specimen using a diamond saw. The initial crack length was measured by optical microscopy of the cross-section. Table 1 tabulates the dimensions of the samples used.

For the three point bend test geometry the elastic modulus of the coating/substrate system is given by the

[1]Research Student, Department of Mechanical and Materials Engineering, Florida International University, Miami, FL, USA
[2]Director of Research and Development, ASB Industries, Barberton, OH, USA

*Corresponding author, email agarwala@fiu.edu

Published by Maney on behalf of the Institute
Received 24 May 2006; accepted 19 July 2006
DOI 10.1179/174329407X161618

Intersplat Friction Force and Splat Sliding in a Plasma-Sprayed Aluminum Alloy Coating during Nanoindentation and Microindentation

Yao Chen, Srinivasa Rao Bakshi, and Arvind Agarwal*

Department of Mechanical and Materials Engineering, Florida International University, 10555 West Flagler Street, Miami, Florida 33174

ABSTRACT This study computes the friction force during splat sliding in the plasma-sprayed Al−Si coating based on the instrumented depth-sensing nanoindentation and microindentation experiments. A small intersplat friction force ($\sim 10^{-4}$ N) contributes to the occurrence of the splat sliding. As compared with nanoindentation, more and more splat sliding occurs during microindentation because of the increase in the applied load, which accounts for the ~26% loss of the elastic modulus.

KEYWORDS: internal friction • indentation • coating • plasma deposition

1. INTRODUCTION

The plasma spray technique is a versatile process that can deposit a wide range of alloys, ceramics, polymers, and composites as coatings while retaining the benefits of rapid solidification (1). Plasma-sprayed coatings are formed by the stacking of thin splats, which are produced by a stream of molten and semimolten droplets impacting on the substrate followed by flattening and rapid solidification. The typical microstructure of the plasma-sprayed deposit consists of layered splat structures, intersplat pores, microcracks, and fine voids, which often lead to inadequate bond strength between the splats (2). Previous investigations revealed that the elastic moduli of plasma-sprayed coatings are much lower than those of bulk, dense materials (3−9). For example, the elastic modulus (evaluated using the bending test) of an atmosphere plasma-sprayed yttria-stabilized zirconia (YSZ) top coating with ~15% porosity is only 1−2% of that for dense YSZ (4). The elastic modulus of a plasma-sprayed NiCrAlY coating measured by spherical microindentation decreases to 80 ± 12 GPa (8), as compared to 200 GPa for dense NiCrAlY. The relationship between the elastic modulus and porosity, often used in the evaluation of the elastic moduli of porous materials, is (10)

$$E = E_0 \exp(-b_e P) \quad (1)$$

in which b_e is a constant (~2), E_0 the elastic modulus of a dense material, and P the porosity. However, the calculated elastic moduli of plasma-sprayed coatings using eq 1 are much higher than the experimentally measured values (4, 8). The unsatisfactory prediction of the elastic modulus from eq 1 strongly implies that the porosity is not the sole factor in determining the elastic modulus. Consequently, some researchers proposed that the significant decrease in the elastic modulus of a plasma-sprayed coating is ascribed to splat sliding (4) and/or a low effective bonding ratio (5, 6). The bonding ratio is defined as the ratio of the total bonded lamellar interface areas to the total apparent interface areas between flattened splats (5, 6). It should be noted that the intrinsic inhomogeneous microstructure of the as-sprayed coating always leads to anisotropic elastic moduli along the cross-sectional and axial directions of the deposit. Nevertheless, the splat sliding can be activated if the external load is applied along either the cross-sectional or axial direction because of the lower bonding ratio between adjacent splats. However, it has been an unresolved issue for years to estimate the intersplat friction force for splat sliding. In the present study, nanoindentation and microindentation experiments were conducted on the plasma-sprayed Al−Si coating, and the intersplat friction force for splat sliding was estimated using an analytical model.

2. EXPERIMENTAL PROCEDURES

Gas-atomized, prealloyed, spherical Al−11.6 wt % Si alloy (referred to as Al−Si hereafter) powder with a size of 14 ± 9 μm was selected as the precursor powder. Plasma spray was carried out using a SG-100 gun (Praxair, Inc., Danbury, CT), with processing parameters as follows: 40 V; current of 550 A, primary gas argon (42.5 slm), secondary gas helium (30.5 slm), carrier gas argon (11.9 slm), standoff distance of 100 mm, and powder feed rate of 20 g/min. The porosity of the plasma-sprayed coating was estimated by image analysis. To guarantee the measured porosity of the as-sprayed coating, the average of the porosity was calculated based on the image analysis results for five different regions of the as-sprayed coating. Nanoindentation tests were carried out using Hysitron Triboindenter (Hysitron, Minneapolis, MN) with a diamond Berkovich tip. During nanoindentation, the load was applied at the rate of 25 μN/s up to a peak load of 2300 μN, where it was held for 2 s and then unloaded completely at a negative rate of 25 μN/s.

* Corresponding author. Phone: 305-348-1701. Fax: 305-348-1932. E-mail: agarwala@fiu.edu.
Received for review October 12, 2008 and accepted November 14, 2008
DOI: 10.1021/am800114h

Surface & Coatings Technology 203 (2009) 2193–2201

Contents lists available at ScienceDirect

Surface & Coatings Technology

journal homepage: www.elsevier.com/locate/surfcoat

Structural transformations in carbon nanotubes during thermal spray processing

Anup Kumar Keshri [a], Kantesh Balani [a,b], Srinivasa R. Bakshi [a], Virendra Singh [c], Tapas Laha [a,d], Sudipta Seal [c], Arvind Agarwal [a,*]

[a] Mechanical and Materials Engineering, Florida International University, Miami, FL 33174, USA
[b] Materials and Metallurgical Engineering, Indian Institute of Technology, Kanpur, India
[c] Mechanical, Materials and Aerospace Engineering, University of Central Florida, Orlando 32816, USA
[d] Materials and Metallurgical Engineering, Indian Institute of Technology, Kharagpur, India

ARTICLE INFO

Article history:
Received 6 December 2008
Accepted in revised form 9 February 2009
Available online 23 February 2009

Keywords:
Carbon nanotubes (CNTs)
Plasma spraying (PS)
High-velocity oxy fuel spraying (HVOF)
Cold spraying (CS)
Plasma spraying of liquid precursor (PSLP)

ABSTRACT

This study compares the interaction of carbon nanotubes (CNTs) with the flame/energy sources during different thermal spray processes *viz.* plasma spraying (PS), high-velocity oxy fuel spraying (HVOF), cold spraying (CS), and plasma spraying of liquid precursor (PSLP). CNTs were successfully retained as reinforcement in metal and ceramic composite coatings in all thermal spray processes except PSLP. The retention of CNT structure is attributed to micron size metal/ceramic powder which acts as a carrier and thermal shield against high heat in plasma spraying (PS) and high-velocity oxy fuel spraying (HVOF). However, vaporization of CNTs occurred in PSLP under the intense heat of the plasma which is attributed to phase transformation in unshielded CNTs.

1. Introduction

Carbon nanotubes (CNTs) have attracted much attention as reinforcement for composites, by virtue of their remarkable mechanical, electrical and thermal properties [1–4]. This allotrope of carbon possesses almost five times elastic modulus (~1 TPa) and 100 times tensile strength (~150 GPa) than those of high strength steels [5–7]. This ultrahigh strength of CNTs makes them potential reinforcement for composite materials. CNT reinforcement increases the strength and stiffness of metals and polymers, and improves the fracture toughness [8,9] and thermal conductivity [10] of ceramics. Some of the key processing techniques used in synthesis of CNT reinforced metal and ceramic composites are conventional powder metallurgy techniques [11,12], electro and electroless plating from CNT containing electrolytic baths [13,14], spark plasma sintering [15,16], and mechanical alloying [17].

In the last five years, our research group has utilized thermal spray techniques (*plasma spraying, high-velocity oxy fuel spraying, and cold spraying*) to synthesize CNT reinforced metal and ceramic composite coatings [9,18–30]. Laha et al. successfully synthesized CNT reinforced Al–23 wt.% Si composite coating via *plasma* and *HVOF spraying* using blended powder [18]. HVOF deposited coating resulted in improved density (96.8%) and elastic modulus in comparison with plasma sprayed composite [18]. Laha et al. also studied the interfacial phenomena between the Al–Si alloy matrix and the CNT reinforcement in composites synthesized by plasma spraying and HVOF spraying techniques [20]. Formation of SiC as interfacial reaction product was observed in both spraying techniques. However, the thickness of SiC layer in plasma spraying was greater than that of HVOF due to higher processing temperature in plasma spraying. The formation of SiC layer improved the wettability and interfacial adhesion between MWCNT reinforcement and Al–Si matrix [20].

Balani et al. synthesized CNT reinforced Al_2O_3 coating via *plasma spraying* using spray dried composite powder with varying CNTs content [9,21]. Spray dried powder resulted in improved CNTs dispersion and mechanical properties as compared to the blended powder. Addition of 8 wt.% CNTs to Al_2O_3 matrix resulted in fracture toughness of 5.04 ± 0.58 MPa $m^{1/2}$ which is 57% improvement over Al_2O_3 coating without reinforcement [21]. The same coating also displayed improvement in pin-on-disc wear resistance by 49 times as compared to coating without reinforcement [22]. Balani et al. concluded retention of CNT network as anchor indicating the survivals of CNTs in harsh plasma spraying environment. In a separate study, Balani et al. synthesized CNT reinforced hydroxyapatite (HA) bioceramic coating through *plasma spraying* [23]. Fracture toughness improvement of 56% was observed for HA–4 wt.% CNT composite coating which is attributed to CNTs distribution and anchoring of CNTs to form bridge structure. Reinforcement of CNTs showed improvement in precipitation and mineralization of apatite onto CNT surface [23]. Plasma sprayed HA–4 wt.% CNT coating displayed an improvement in wear resistance (1.5 times) as compared to HA coating

* Corresponding author. Tel.: +1 305 348 1701; fax: +1 305 348 1932.
E-mail address: agarwala@fiu.edu (A. Agarwal).

0257-8972/$ – see front matter © 2009 Elsevier B.V. All rights reserved.
doi:10.1016/j.surfcoat.2009.02.013

journal

J. Am. Ceram. Soc., 91 [3] 942–947 (2008)
DOI: 10.1111/j.1551-2916.2007.02081.x

Thermal Conductivity of Plasma-Sprayed Aluminum Oxide—Multiwalled Carbon Nanotube Composites

Srinivas R. Bakshi, Kantesh Balani, and Arvind Agarwal†

Department of Mechanical and Materials Engineering, Florida International University, Miami, Florida

Aluminum oxide nanocomposites reinforced with multiwalled carbon nanotubes (MWNT) were prepared by atmospheric plasma spraying of blended and spray-dried powders. Thermal conductivity was measured using the laser flash technique for temperatures between 25° and 300°C. An aluminum oxide—4 wt% MWNT nanocomposite prepared from the blended powder showed the highest conductivity, followed by aluminum oxide without nanotubes, 8 and 4 wt% MWNT composite prepared from spray-dried powder in that order. The thermal conductivity values obtained are rationalized taking into account the crystallite size, porosity, MWNT content, microstructure, and the interfaces and metastable γ-Al_2O_3 content present in the nanocomposite.

I. Introduction

Thermal conductivity is an important physical property, which is required in modeling heat transfer through solids and structures. It has also been used as a quality control parameter in the production and performance of nuclear fuels[1] and thermal barrier coatings.[2] Carbon nanotubes have shown excellent mechanical, thermal, and electrical properties due to which they have been proposed for a myriad number of applications.[3] Multiwalled carbon nanotubes (MWNT) have also shown[4] very high thermal conductivities in excess of 3000 $W \cdot (m \cdot K)^{-1}$. Hence, they serve as a first choice of materials as fillers for thermal conductivity enhancement in thermal management materials. The thermal conductivity of dense aluminum oxide has been reported[5] to be between 27 and 35 $W \cdot (m \cdot K)^{-1}$. In our previous work,[6] it has been shown that addition of carbon nanotubes to aluminum oxide resulted in a 43% increase in the fracture toughness. Addition of MWNT is also expected to increase the thermal conductivity of the composites, which is beneficial for many applications like electronic packaging. It is generally difficult to predict the thermal conductivity of plasma-sprayed coatings because of its complicated microstructure, which consists of splats, porosity, and interfaces. The goal of this paper is to study the thermal conductivity of plasma-sprayed aluminum oxide—MWNT nanocomposites and rationalize them by taking into account the crystallite size, porosity, MWNT content, matrix microstructure, interfaces, and metastable γ-Al_2O_3 content present in the coatings.

II. Experimental Procedure

(1) Plasma Spraying

The samples were fabricated using DC arc plasma spraying with a Praxair SG-100 gun (Praxair Inc., Danbury, CT). The powders were fed internally into the plasma using argon as a carrier gas. Four types of powders were sprayed. They are (a) a spray-dried nanoaluminum oxide (referred to as nano-Al_2O_3 hereafter), (b) a spray-dried nanoaluminum oxide blended with 4 wt% MWNT (referred to as Al_2O_3—4 wt% MWNT blended hereafter), (c) a spray-dried nanoaluminum oxide 4 wt% MWNT mixture (referred to as Al_2O_3—4 wt% MWNT spray dried hereafter), and (d) a spray-dried nanoaluminum oxide 8 wt% MWNT mixture (referred to as Al_2O_3—8 wt% MWNT spray dried hereafter). Coatings of thickness between 0.5 and 1 mm were sprayed onto a mild steel substrate. The details of the plasma spraying and the microstructure of the coatings are given elsewhere.[6] Carbon nanotubes were found to be well distributed in the partially molten regions and were also found in the intersplat and inter-particle regions.[6] It was also seen that the nanotubes were coated well with Al_2O_3, indicating wetting and better interfacial heat transfer between the two. Undamaged CNTs in the plasma-sprayed coatings were confirmed from scanning electron microscope (SEM, JEOL JSM-633OF, JEOL USA Inc., Peabody, MA) observation of fracture surfaces,[6] micro-Raman spectroscopy,[6] and high-resolution transmission electron microscopy (HRTEM, FEI Tecnai F30, FEI Company, Hillsboro, OR).

(2) Thermal Conductivity Measurement

To fabricate samples for thermal conductivity, the substrate with coating was cut into a 10 mm × 10 mm piece with a low-speed diamond saw (Buehler Isomet 11-1180, Buehler Ltd., Lake Bluff, IL). The diamond saw was used to cut through the substrate. The thin layer of mild steel attached to the coating was then removed by dissolving in nitric acid. Thus, free-standing samples of 10 mm × 10 mm area and 0.5–1-mm thickness were prepared. The bulk density of the samples was measured by the water displacement method using the Archimedes principle. Thermal diffusivity was measured using a Holometrix Micromet-300 Thermal Diffusivity Instrument (Metrisa Inc., Bedford, MA) by the pulse method for a number of temperatures between 25° and 300°C. The thermal diffusivity values were corrected for radiation heat losses using Cowan's method.[7] The nano-Al_2O_3 sample was coated with carbon using a carbon spray, to make it opaque to the laser radiation, and then the edges were ground to ensure that the carbon layer was only at the top and bottom surfaces. The MWNT-containing nanocomposites did not require any carbon coating as they were already opaque to the laser radiation. The error in the measured values of thermal diffusivity was within ±3%. The specific heat capacity of aluminum oxide was taken from the thermodynamic databank FactSage 5.0.[8] The specific heat of carbon nanotubes was taken to be the same as that of graphite and was also obtained from FactSage 5.0. Masarapu *et al.*[9] determined the specific heat capacity of aligned multiwalled carbon nanotubes and found it to be similar to that of graphite. The specific heat capacities of the 4 and 8 wt% MWNT composites were calculated using the Neumann–Kopp additive rule. Finally, the thermal conductivity was calculated from the following equation:

$$k = \alpha \cdot \rho \cdot C_p \tag{1}$$

Here, k is the thermal conductivity, α is the measured value of thermal diffusivity, ρ is the bulk density, and C_p is the specific heat capacity.

K. Watari—contributing editor

Manuscript No. 23313. Received June 6, 2007; approved August 19, 2007.
†Author to whom correspondence should be addressed. e-mail: agarwala@fiu.edu

Int. J. Appl. Ceram. Technol., ■■ [■■] 1–9 (2009)
DOI:10.1111/j.1744-7402.2009.02385.x

International Journal of Applied Ceramic Technology
Ceramic Product Development and Commercialization

Grain Growth Behavior of Aluminum Oxide Reinforced with Carbon Nanotube During Plasma Spraying and PostSpray Consolidation

Kantesh Balani, Srinivasa R. Bakshi, Debrupa Lahiri, and Arvind Agarwal*

Mechanical and Materials Engineering, Florida International University, Miami, Florida-33174

Kantesh Balani

Materials and Metallurgical Engineering, Indian Institute of Technology, Kanpur 208016, India

Grain-boundary mobility of the plasma sprayed aluminum oxide (Al_2O_3)–carbon nanotube (CNT) composites is evaluated in the current work. Grain mobility is evaluated from the grain growth within the spray-dried particles and thermal history experienced during high-temperature plasma processing. CNTs form an interfacial grain boundary layer during thermal exposure, limiting the grain growth of plasma-sprayed coatings. Consequent hot isostatic pressing (HIPing) of CNT-reinforced Al_2O_3 at 1773 K shows differences in grain growth kinetics, degree of densification, and pore shrinkage. Densification of HIPed coatings is observed to be dictated by CNTs, phase transformation, initial grain size, and time of thermal processing. CNTs have shown to impede the Al_2O_3 grain growth by serving as grain pinning obstacles. Impediment of grain-boundary mobility with variation of CNT content, and time and temperature of the heat treatment of aluminum oxide (Al_2O_3)–CNT nanocomposite is addressed in detail.

Introduction

High-temperature strength, wear resistance, and chemical stability of Al_2O_3 inevitably finds application as ceramic liners, heaters, crucibles, etc.[1–3] Low fracture toughness of brittle Al_2O_3 ceramic can be improved by utilizing nano or submicrometer Al_2O_3 powder particles, followed by sintering at high temperatures.[2,4–6] However, high sintering temperature (>1450°C) needed for densification also promotes abnormal grain growth.[2,5–7] Addition of sintering additives and secondary reinforcements have shown to restrict grain growth by acting as barriers.[5] High-temperature sintering of ceramics with additives elicit an inadvertent formation of interfacial grain boundary layer.[8–10] This interfacial layer is observed to be typically in the order of 0.5–2 nm, which acts as a buffer to reduce interfacial stress.[8,11] Interfacial layer becomes critical in deciding the integrity and interactions occurring at the grain boundary.

Grain boundary plays the essential role of "interchanger" controlling the dynamic growth/depletion of grains under specific (thermal/temporal) conditions.

*agarwala@fiu.edu

Journal of
Nanoscience and Nanotechnology
Vol. 7, 1–10, 2007

Role of Powder Treatment and Carbon Nanotube Dispersion in the Fracture Toughening of Plasma-Sprayed Aluminum Oxide—Carbon Nanotube Nanocomposite

Kantesh Balani, Srinivasa Rao Bakshi, Yao Chen, Tapas Laha, and Arvind Agarwal*

Mechanical and Materials Engineering Department, EAS 3464, Miami, FL-33174, USA

Al_2O_3 ceramic reinforced with 4-wt% multiwalled carbon nanotube (CNT) is plasma sprayed for improving the fracture toughness of the nanocomposite coating. Two different methodologies of CNT addition have been adopted in the powder feedstock to assist CNT dispersion in the nano-Al_2O_3 matrix. First, spray-dried nano-Al_2O_3 agglomerates are *blended* with 4 wt% CNT as powder-feedstock, which is subsequently plasma sprayed resulting in the fracture toughness improvement of 19.9%. Secondly, spray dried *composite* nano-Al_2O_3 and 4 wt% CNT powder was used as feedstock for attaining improved dispersion of CNTs. Plasma sprayed coating of composite spray dried powder resulted in increase of 42.9% in the fracture toughness. Coating synthesized from the blended powder displayed impact alignment of CNTs along splat interface, and CNTs chain loop structure anchoring the fused Al_2O_3 melt whereas coating synthesized from composite spray dried powder evinced anchoring of CNTs in the solid state sintered region and CNT mesh formation. Enhanced fracture toughness is attributed to significance of CNT dispersion.

Keywords: Carbon Nanotubes, Nanocomposites, Toughness.

RESEARCH ARTICLE

1. INTRODUCTION

Al_2O_3 (aluminum oxide) ceramic is used for wear and impact resistant coatings, line inserts, heat exchangers, etc., due to its excellent compression strength, high hardness and wear resistance at high temperatures.[1–5] However, the applications of Al_2O_3 are limited due to its brittle behavior.[2–5] Due to their excellent mechanical properties, carbon nanotubes (CNTs) have been used as reinforcing material, largely for polymeric matrices. A very few researchers have added CNTs to ceramic matrices such as SiC, TiO_2, Si_3N_4, hydroxyapatite and Al_2O_3, for improvement of fracture toughness.[6–14] CNT additions in Al_2O_3 matrix has shown bending strength improvement of upto 10%.[15] Zhan et al. have shown three times improvement in the fracture toughness of spark plasma sintered CNT-alumina composite compared to that of pure alumina.[12,16–22] On the contrary, Wan et al claimed that CNT-alumina did not possess high fracture toughness but improved contact-damage resistance.[13] The discrepancy in the fracture toughness data of the two studies could be attributed to the use of different indentation techniques by the two research groups. Hence the absence of a widely accepted fracture toughening mechanism in CNT-ceramic nanocomposite has kept researchers in contradiction. Although it has been observed that fracture toughness is governed by CNT pullout, crack deflection and crack bridging,[23,24] the fundamental reason of attaining the enhanced fracture toughness and its relation to nanotube dispersion still remains unclear.[23]

Importance of CNT as a dispersed phase is already impressed upon by various research works, with dispersion being achieved by sol–gel technique, surface activation, inorganic coating, heterocoagulation, ball milling, solvent incorporation, etc.[25–32] Dispersed CNTs allow interfacial interactions and load-transfers towards attaining improved mechanical properties in ceramic nanocomposites. However, strong agglomeration tendency of CNTs poses the challenge of uniform dispersion.

In the current work, plasma spraying technique has been adopted to synthesize Al_2O_3-CNT nanocomposite coating using two different kind of powder feedstock to obtain improved dispersion of CNTs. Idea of utilizing two strategies is to understand the fracture toughening enhancement of the plasma sprayed coatings as a function of CNT dispersion. Uniform dispersion of CNTs in large scale coatings and bulk structures remains a challenge for researchers.[33–37] Our

*Author to whom correspondence should be addressed.

Available online at www.sciencedirect.com
ScienceDirect
Composites: Part A 38 (2007) 2493–2499
composites
Part A: applied science and manufacturing
www.elsevier.com/locate/compositesa

Synthesis and characterization of multiwalled carbon nanotube reinforced ultra high molecular weight polyethylene composite by electrostatic spraying technique

S.R. Bakshi, J.E. Tercero, A. Agarwal *

Department of Mechanical and Materials Engineering, Florida International University, Miami, FL 33174, United States

Received 6 February 2007; received in revised form 2 July 2007; accepted 1 August 2007

Abstract

In the present work, multiwalled carbon nanotube (MWNT) reinforced UHMWPE composite films were prepared by electrostatic spraying followed by consolidation. X-ray diffraction and differential scanning calorimetry studies showed a decrease in the crystallinity of UHMWPE due to the nature of the fabrication process as well as addition of MWNT. Tensile test showed an 82% increase in the Young's modulus, decrease in stress to failure from 14.3 to 12.4 MPa and strain to failure from 3.9% to 1.4% due to 5% addition of MWNT. Raman spectra showed the presence of compressive stresses in the nanotubes. Fracture surface showed presence of pullout like phenomena in the MWNT reinforced film.

Keywords: A. UHMWPE; A. Multiwalled carbon nanotube; B. Stiffness; C. Mechanical testing

1. Introduction

Ultrahigh molecular weight polyethylene (UHMWPE) has been the choice of material for bio-implants, like artificial hip cups and tibial inserts, since it was first introduced in 1962 [1]. The properties required for such applications include high strength and stiffness, good fatigue and wear resistance, the necessary property being bio-compatibility. UHMWPE has also found application as a structural material in the form of fibers. UHMWPE fibers are commercially available under the trade names Dyneema and Spectra which claim to be up to 40% stronger than Aramid. Strength of the fibers have been specified as 2–4 GPa and they have been measured to be around 2 GPa [2]. They have been proposed for use in bulletproof vests, bow strings, climbing equipment, fishing line and high performance sails in yachting. Various techniques have been used to increase the strength and stiffness of UHMWPE. These include cross-linking [3,4], self-reinforcement with UHMWPE fibers [2], reinforcement with carbon fibers [5], reinforcement with nanoparticles [6,7] and reinforcement with carbon nanotubes [8–12]. UHMWPE reinforced with carbon fibers have shown to be inferior in wear and fatigue resistance in body implants as compared to UHMWPE [5]. Recently Fang et al. have reported UHMWPE composites reinforced with hydroxyapatite nanoparticles, processed by combined swelling/twin-screw extrusion, compression molding and then seems extra hot drawing, having properties comparable to the cortical bone [7].

Since their discovery in 1991, carbon nanotubes have been used extensively as reinforcement for polymers. This has been reviewed in a number of publications [13–15]. Carbon nanotubes (CNTs) have been proposed for a number of applications due to their unique properties [16]. Polymer-CNT composite films have been prepared by many methods some of which include (i) sonicating a mixture of polymer dissolved in a solvent and carbon nanotubes followed by evaporation of solvent or drop casting

* Corresponding author.
E-mail address: agarwala@fiu.edu (A. Agarwal).

1359-835X/$ - see front matter © 2007 Elsevier Ltd. All rights reserved.
doi:10.1016/j.compositesa.2007.08.004

The Nanomechanical and Nanoscratch Properties of MWNT-Reinforced Ultrahigh-Molecular-Weight Polyethylene Coatings

S.R. Bakshi, K. Balani, T. Laha, J. Tercero, and A. Agarwal

Ultrahigh-molecular-weight polyethylene (UHMWPE) and 5 wt.% multi-walled-carbon-nanotube-(MWNT) reinforced UHMWPE coatings were prepared on a steel substrate by electrostatic spraying. Nanoindentation and nanoscratch tests were performed on the coatings to evaluate the mechanical and wear properties at small length scales. The mean values of elastic modulus and hardness were higher for the MWNT-reinforced coating, while the plasticity index of the coatings was unaffected. The lateral force and coefficient of friction was considerably higher in the case of the MWNT-reinforced coating, indicating an increase in resistance to wear due to the addition of MWNT.

INTRODUCTION

Ultrahigh-molecular-weight polyethylene (UHMWPE) has been used in the manufacture of acetabular cups and tibial inserts due to its biocompatibility and strength since it was first introduced in 1962.[1] It has also been used as structural material and as a fiber due to its high strength and stiffness. Thin coatings of polymers and polymer composites find applications in micro-electromechanical systems as a corrosion protective coating, bioactive coatings, and as scaffolds for tissue culture. For special applications where polymer surfaces are in constant motion, wear properties are important. Since the thickness of the coatings is small in comparison to the substrate, conventional methods of testing cannot be employed to assess their tribological properties. Also for these applications the surface nanoscale properties are of special interest. Nanoindentation and nanoscratch tests have been extensively used for the characterization of polymers[2–7] and polymer matrix nanocomposites.[8–13] Nanoindentation is the only method to determine the near-to-surface properties in polymers, which affects their tribological performance.

SYNTHESIS OF THE COATINGS

The UHMWPE powder used in the study was Mipelon™ supplied by Mitsui Chemicals America, Inc., New York. The multiwalled carbon nanotubes (MWNTs) used in the study were ~95% pure and had an outer diameter of 40–70 nm and a length of up to 2 μm. The UHMWPE and MWNT mixture was blended in a rotating jar mill for 4 h. Coatings on the order of 100 μm thick of UHMWPE and UHMWPE reinforced with 5 wt.% MWNT were prepared by electrostatic spraying onto a steel substrate.

The as-sprayed powder film on the substrate was sintered in an oven at 180°C for 30–40 min. The sintering temperature was chosen higher than the melting point of UHMWPE (136°C) because the viscosity of the polymer is very high. H.K. Jen et al.[14] have shown the viscosity of 2 wt.% UHMWPE solution in various solvents to be between 10,000 cP and 30,000 cP at its melting point (viscosity of water ~1 cP at room temperature). Thus, sintering of UHMWPE takes a long time if performed at its melting point.

In Figure 1, the coatings are shown to be wet and covering the steel substrate evenly. The surface of the UHMWPE coatings is shown to be rough compared to the UHMWPE–MWNT coating. Because the thermal conductivity of UHMWPE is very low (0.4 W/m·K),[15] only the outer cores of the large powders become molten during the consolidation process. Due to the high viscosity of UHMWPE, there is improper flow even after melting and the initial surface roughness of the unconsolidated layer of powders is retained. The thermal conductivity of carbon nanotubes is very high, on the order of 3,000 W/m·K,[16] which leads to efficient heat conduction

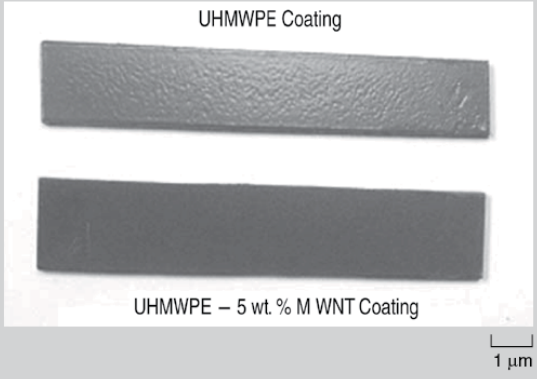

Figure 1. The coated samples.

Nanomechanical behaviour of plasma sprayed PZT coatings

A. K. Keshri[1], S. R. Bakshi[1], Y. Chen[1], T. Laha[1,2], X. Li[1], C. Levy[1] and A. Agarwal*[1]

Nanomechanical properties of the plasma sprayed lead zirconate titanate (PZT) coating have been investigated using nanoindentation technique. PZT coating processed at higher plasma power of 32 kW exhibited lower elastic modulus E of 98 GPa compared with the modulus (113 GPa) of the coating processed at plasma power of 20 kW. The variation in the elastic modulus is attributed to the fine porosity of the PZT coating, which is formed during plasma spraying. Porosity increases by evaporation of PbO phase during plasma spraying. Overall effective elastic modulus of both coatings is computed using micromechanics models and compared with the experimentally obtained values. Hashin–Shtrikman and rule of mixtures models predict values that closely match with nanoindentation values.

Keywords: Plasma spray, PZT, Nanoindentation, Elastic modulus, Porosity

Introduction

Lead zirconate titanate (PZT) is a piezoelectric material, which is widely used as sensors and actuators.[1,2] The miniaturisation of actuators requires fabrication of PZT in the form of thin films and coatings. There are several methods available for the synthesis of PZT coating. Crystalline PZT coatings have been prepared by various methods such as digital metalorganic chemical vapour deposition,[3] vacuum evaporation,[4] aerosol deposition,[5] pulsed laser deposition,[6] radio frequency magnetron sputtering[7,8] and sol–gel deposition.[9–11] PZT films prepared by sol–gel are limited in thickness and usually fall in the range below 1 μm. Deposition of thicker layer usually results in cracks[12] and inferior mechanical properties.

Sherrit *et al.*[13] successfully fabricated PZT glass composite (thickness, 80–250 μm) by plasma spraying technique. Evaporation of lead oxide was a major problem during plasma spraying of PZT, which lead to compositional inhomogeneities. In addition, the presence of porosity (30–40%) in PZT films made poling difficult.[13] Piezoelectric charge coefficient of plasma sprayed PZT film ranged from 0·47 to 1·1 pC/N and dielectric constant from 58 to 20. Plasma sprayed PZT films displayed piezoelectric nature, albeit small. Haessler *et al.*[14] studied the structure and electrical properties of PZT thick films (~200 μm) produced by plasma spraying. Because of the high temperature during the plasma spraying process, the $PbZrO_3$ in the PZT particles melts incongruently and PbO partly evaporates. EDX results showed an inhomogeneous distribution of the phases in the sprayed film due to lead oxide evaporation.

To comprehensively understand the factors influencing piezoelectric coefficients, the mechanical properties of these PZT coatings are extremely important. Elastic modulus is one of the important properties for the membrane structure, which can influence the stiffness of the structure.[15] Bahr *et al.*[16] studied the mechanical deformation of spin coated PZT thin films (600 nm) using continuous indentation technique. PZT film exhibited a hardness value between 5 and 8 GPa, which is slightly lower than the hardness of bulk PZT, ~9 GPa. The elastic modulus of the bulk PZT (~135 GPa) and thin PZT film (130–160 GPa) were also measured by nanoindentation. Zheng *et al.* also studied the nanoindentation behaviour of spin coated $Pb(Zr_{0·52}Ti_{0·48})O_3$ ferroelectric thin films (300–500 nm).[17] Hardness (~12 GPa) and elastic modulus (~150 GPa) of the PZT film were higher than those of the bulk PZT material. PZT coating synthesised using sol–gel process displayed an average elastic modulus and hardness value of ~121 and 13 GPa respectively.[18] Vincent *et al.* fabricated the soft and hard PZT films on alumina substrate by screen printing process.[19] Elastic modulus measured by nanoindentation was 52 ± 8 GPa for soft PZT film and 20 ± 7 GPa for hard PZT film.[19] Elastic modulus values were strongly influenced by porosity in the film.

It is observed that there is much research on nanomechanical properties of PZT film fabricated by sol–gel, screen printing and spin coating processes,[16–19] but nanomechanical properties of plasma sprayed PZT coatings have never been investigated.[13,14] Motivated by these considerations, the objective of the present work is to synthesise PZT coating via plasma spray technique and measure the nanomechanical properties of the plasma sprayed PZT coatings using nanoindentation technique. The correlation

[1]Department of Mechanical and Materials Engineering, Florida International University, Miami, FL 33174, USA
[2]Department of Metallurgical and Materials Engineering, Indian Institute of Technology, Kharagpur, India

*Corresponding author, email agarwala@fiu.edu

Published by Maney on behalf of the Institute
Received 19 August 2008; accepted 5 October 2008
DOI 10.1179/026708408X375307

G Model
JALCOM-19830; No. of Pages 5
ARTICLE IN PRESS

Journal of Alloys and Compounds xxx (2009) xxx–xxx

Contents lists available at ScienceDirect

Journal of Alloys and Compounds

journal homepage: www.elsevier.com/locate/jallcom

Reaction synthesis of Ti_3SiC_2 phase in plasma sprayed coating

Venkata Pasumarthi, Yao Chen, Srinivasa R. Bakshi, Arvind Agarwal *

Department of Mechanical and Materials Engineering, Florida International University, Miami, FL 33174, USA

ARTICLE INFO

Article history:
Received 14 March 2009
Accepted 15 April 2009
Available online xxx

Keywords:
Plasma spraying
Ti_3SiC_2
Reaction synthesis
Coating

ABSTRACT

This investigation focuses on the feasibility of reaction synthesis of Ti_3SiC_2 phase using plasma spraying of powder mixture of Ti, SiC and graphite. In-flight particle diagnostics suggested that dwell (reaction) time of these powder mixture is very short (~10^{-4} s) during plasma spraying. Phase identification and microstructural characterizations of the as-sprayed coatings were conducted using X-ray diffraction (XRD), scanning electron microscopy (SEM), and transmission electron microscopy (TEM). Thermodynamic calculations on Ti–SiC–C system were also made. Reaction mechanism of Ti_3SiC_2 synthesis during plasma spray is proposed. Although relatively lower volume percentage of Ti_3SiC_2 (~15–19%) phase was found in the plasma sprayed coating, reaction synthesis of Ti_3SiC_2 phase using plasma spray provides a potential processing technique to fabricate Ti_3SiC_2 as a protective coating on large engineering components.

1. Introduction

Ternary titanium silicon carbide (Ti_3SiC_2) with a layered hexagonal crystallographic structure has attracted much attention by materials community, because it combines many excellent merits of metals and ceramics [1,2]. For example, it exhibits metal properties such as high electrical and thermal conductivity and is readily machinable [1,2]. It also possesses ceramic like properties such as high elastic modulus of 320 GPa, and high stability to at least 1700 °C in an inert atmosphere or under vacuum [3]. Therefore, Ti_3SiC_2 is expected to be a potential structural material candidate for high temperature applications such as bearings, engine linings, and turbine blades. Ti_3SiC_2 was first synthesized using sintering technique [4] and its structure was determined in the late 1960s. Since then, several processing techniques have been developed to synthesize single-phase, bulk, polycrystalline Ti_3SiC_2. These processing techniques include arc melting [5], direct sintering [6], reactive hot-pressing (HP) [1], hot-isostatic pressing (HIP) [3], spark plasma sintering (SPS) [7], pulse discharge sintering (PDS) [8] and self-propagating high-temperature synthesis (SHS) [9]. A variety of precursor materials viz. Ti–Si–C [4,5,9], Ti–Si–TiC [10,11], Ti–SiC–C [1], Ti–Si–C–SiC [12] and Ti–SiC–TiC [13] have been employed for synthesis of Ti_3SiC_2. Of these processing techniques, most of them are perceived to be energy intensive because of both requirement of high temperature (~1450–1700 °C) and long processing time of approximately 4 h [3,5,6]. SPS and SHS techniques are rapid processing techniques, which have been reported to synthesize Ti_3SiC_2 within 10 min [7] and tens of seconds [9], respectively. From the viewpoint of energy efficiency, development of a novel and rapid processing technique for synthesis of Ti_3SiC_2 compound is of significance.

In addition, the nontrivial properties of Ti_3SiC_2 make it an excellent high temperature *coating* for applications such as jet engines, automobiles, aircrafts, and petrochemical installations. Recently, synthesis of Ti_3SiC_2 as coating has been reported using pulsed laser deposition [14] and dc magnetron sputtering techniques [15,16]. However, Eklund et al. have debated the formation of Ti_3SiC_2 by pulsed laser deposition technique [17]. In addition to slow deposition rate, the pre-requirement for abovementioned two processing methods is high vacuum (10^{-7} Torr), which greatly limits coating deposition on large engineering components for aerospace and automotive applications. Plasma spraying is a well-established, versatile coating technique with high deposition rate, which can deposit a wide range of alloys, ceramics, and composites as functional coatings for thermal protection, oxidation and corrosion resistance, and wear resistance [18]. To the best knowledge of authors, there is little information available in the literature on the synthesis of Ti_3SiC_2 coating using plasma spray technique. One of the reasons could be the lack of commercial availability of Ti_3SiC_2 powder feedstock. Thereby, the objective of the present research is to investigate the feasibility of adopting plasma as the ignition source for the reaction synthesis of Ti_3SiC_2 phase in the coating through the self-propagation reactions in the Ti–SiC–C precursor system. The reaction mechanisms of Ti–SiC–C system under high heating and rapid cooling rate conditions experienced during plasma spraying is also discussed.

2. Experimental procedure

Tribochemically mixed Ti–SiC–C powders with composition of 74 wt.% Ti, 20 wt.% SiC and 6 wt.% graphite in the particle size of 40–50 μm were selected as

* Corresponding author. Tel.: +1 305 348 1701; fax: +1 305 348 1932.
E-mail address: agarwala@fiu.edu (A. Agarwal).

0925-8388/$ – see front matter © 2009 Elsevier B.V. All rights reserved.
doi:10.1016/j.jallcom.2009.04.079

Please cite this article in press as: V. Pasumarthi, et al., J. Alloys Compd. (2009), doi:10.1016/j.jallcom.2009.04.079

VITA

SRINIVASA RAO BAKSHI

EDUCATION

Aug. 1997 – Apr. 2001	: Bachelor of Engineering (**B.E.**) in Metallurgical Engineering, Regional Engineering College (now National Institute of Technology, NIT), Rourkela, India (First Class with Honors)
Aug. 2001 – Jan. 2003	: Masters in Engineering (**M.E.**) in Metallurgy, Indian Institute of Science (IISc), Bangalore, India. (First Class)
Sept. 2005 – Aug. 2009	: Doctoral Candidate (**Ph.D**) in Materials Engineering, Department of Mechanical and Materials Engineering, Florida International University, Miami, GPA **3.975/4.0**

PROFESSIONAL EXPERIENCE

Jan 2007 – Aug. 2009	: Research Assistant, Department of Mechanical and Materials Engineering, FIU
Sept 2005 – Dec 2006	: Teaching and Research Assistant, Department of Mechanical and Materials Engineering, FIU
Sept 2003 – Sept 2005	: Scientific Officer 'C', Post-Irradiation Examination Division, Bhabha Atomic Research Centre (BARC), Mumbai. India

ACADEMIC AWARDS AND HONOURS

1. ***Dissertation Year Fellowship:*** University Graduate School, Florida International University for 2008-2009
2. ***Presidential Enhanced Assistantship:*** University Graduate School, Florida International University, Fall 2005-Summer 2008.
3. Team Leader of the ***Winning FIU team:*** *First National Materials Bowl Competition* organized at TMS annual meeting 2007 in Orlando on Feb. 25, 2007
4. Nominated for membership of ***Sigma Xi*** Honors Society 2007-2008 by Department of Mechanical and Materials Engineering, FIU
5. All India Rank 1 in GATE-2001 in Metallurgy (equivalent to GRE subject test)

6. GE Fund Scholarship for Academic Excellence 2001-2002

PUBLICATIONS AND PRESENTATIONS

1. Srinivasa R. Bakshi, Debrupa Lahiri and Arvind Agarwal, *"Carbon Nanotube Reinforced Metal Matrix Composite - A Review"*, Invited Review Article submitted to ***International Materials Review****, to be published in July 2009*
2. Srinivasa R. Bakshi, Anup K. Keshri, Virendra Singh, Sudipta Seal, Arvind Agarwal, *"Interface in Carbon Nanotube Reinforced Aluminum Silicon Composites: Thermodynamic Analysis and Experimental Verification"*, ***Journal of Alloys and Compounds*** DOI:10.1016/j.jallcom.2009.03.055
3. Srinivasa R. Bakshi, Virendra Singh, Sudipta Seal, Arvind Agarwal, *"Aluminum Composite Reinforced with Multiwalled Carbon Nanotubes from Plasma Spraying of Spray Dried Powders"*, ***Surface and Coatings Technology*** Vol. 203 (2009) 1544-1554
4. Srinivasa R. Bakshi, Virendra Singh, Kantesh Balani, D. Graham McCartney, Sudipta Seal and Arvind Agarwal, "*Carbon Nanotube Reinforced Aluminum Composite Coating via Cold Spraying*", ***Surface and Coatings Technology*** Vol. 202 (2008) 5162-5169
5. Srinivasa R. Bakshi, Virendra Singh, D. Graham McCartney, Sudipta Seal and Arvind Agarwal, "*Deformation and Damage Mechanisms of Multiwalled Carbon Nanotubes Under High Velocity Impact*", ***Scripta Materialia*** Vol. 59 (2008) pp. 499-502
6. Srinivasa R. Bakshi, T. Laha, K. Balani, A. Agarwal and J. Karthikeyan, "Effect of carrier gas on mechanical properties and fracture behaviour of cold sprayed aluminium coatings", **Surface Engineering** Vol. 23[1] (2007) pp. 18-22
7. Srinivasa R. Bakshi, K. Balani, and A. Agarwal, "*Thermal Conductivity of Plasma Sprayed Aluminum Oxide-Multiwalled Carbon Nanotube Composites*", ***Journal of American Ceramic Society*** Vol. 91[3] (2008) pp. 942–947
8. Srinivasa R. Bakshi, J.E. Tercero, and A. Agarwal, "Synthesis and characterization of multiwalled carbon nanotube reinforced ultra high molecular weight polyethylene composite by electrostatic spraying technique", **Composites: Part A** Vol. 38 (2007) pp. 2493–2499

(Listed 8 out of 16 published papers, 4 more papers are under review in peer reviewed journals)

BOOK

Srinivasa R. Bakshi, Debrupa Lahiri and Arvind Agarwal Srinivasa R. Bakshi, Debrupa Lahiri and Arvind Agarwal, **"***Carbon Nanotube metal Matrix Composites*", Taylor and Francis Publishers, to be completed by March 2010